

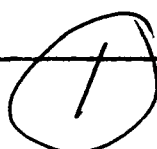
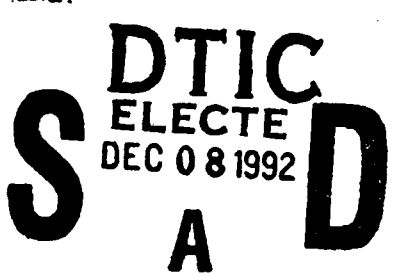
AD-A258 547



IMPLEMENTATION PAGE

Form Approved  
OMB No. 0704-0188

This is estimated to average 1 hour per response, including the time for reviewing instructions, searching existing data sources, gathering and reviewing the collection of information, sending comments regarding this burden estimate or any other aspect of this collection of information, to Washington Headquarters Services, Directorate for Information Operations and Reports, 1215 Jefferson Avenue, Washington, DC 20540, and to the Office of Management and Budget, Paperwork Reduction Project (9704-0188), Washington, DC 20503.

1. AGENCY USE ONLY (Leave blank)		2. REPORT DATE August 1992	3. REPORT TYPE AND DATES COVERED <del>XXXXXX</del> DISSERTATION	
4. TITLE AND SUBTITLE A Method to Predict the Orbital Lifetimes of Free Tethers and Tether-Trailing Satellites using Artificial Neural Networks			5. FUNDING NUMBERS 	
6. AUTHOR(S) Ted W. Warnock, Captain				
7. PERFORMING ORGANIZATION NAME(S) AND ADDRESS(ES) AFIT Student Attending: Auburn University			8. PERFORMING ORGANIZATION REPORT NUMBER AFIT/CI/CIA- 92-017D	
9. SPONSORING/MONITORING AGENCY NAME(S) AND ADDRESS(ES) AFIT/CI Wright-Patterson AFB OH 45433-6583			10. SPONSORING/MONITORING AGENCY REPORT NUMBER	
11. SUPPLEMENTARY NOTES				
12a. DISTRIBUTION/AVAILABILITY STATEMENT Approved for Public Release IAW 190-1 Distributed Unlimited ERNEST A. HAYGOOD, Captain, USAF Executive Officer			12b. DISTRIBUTION CODE	
13. ABSTRACT (Maximum 200 words)				
 <p>DTIC ELECTRONIC SERVICES DEC 08 1992</p>				
14. SUBJECT TERMS			15. NUMBER OF PAGES 245	
			16. PRICE CODE	
17. SECURITY CLASSIFICATION OF REPORT			18. SECURITY CLASSIFICATION OF THIS PAGE	
19. SECURITY CLASSIFICATION OF ABSTRACT			20. LIMITATION OF ABSTRACT	

92-31014



012500

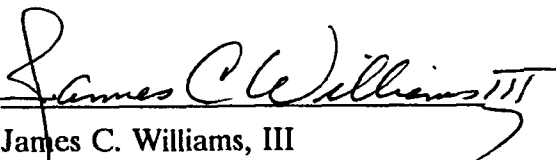
26098

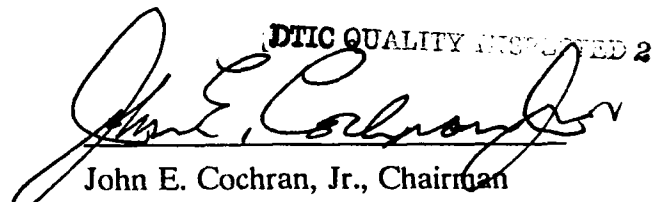
A METHOD TO PREDICT THE ORBITAL LIFETIMES OF  
 FREE TETHERS AND TETHER-TRAILING SATELLITES  
 USING ARTIFICIAL NEURAL NETWORKS

Ted Wesley Warnock

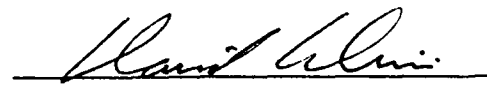
Accession For	
NTIS CRA&I	<input checked="" type="checkbox"/>
DTIC TAB	<input type="checkbox"/>
Unannounced	<input type="checkbox"/>
Justification	
By	
Distribution/	
Availability Codes	
Dist	Avail and/or Special
A-1	

Certificate of Approval:

  
 James C. Williams, III  
 Professor  
 Aerospace Engineering

**DTIC QUALITY INSPECTED 2**  
  
 John E. Cochran, Jr., Chairman  
 Professor  
 Aerospace Engineering

  
 Rhonald M. Jenkins  
 Assistant Professor  
 Aerospace Engineering

  
 David A. Cicci  
 Assistant Professor  
 Aerospace Engineering

  
 Norman J. Doorenbos, Dean  
 Graduate School

A METHOD TO PREDICT THE ORBITAL LIFETIMES OF  
FREE TETHERS AND TETHER-TRAILING SATELLITES  
USING ARTIFICIAL NEURAL NETWORKS

Ted Wesley Warnock

A Dissertation  
Submitted to  
the Graduate Faculty of  
Auburn University  
in Partial Fulfillment of the  
Requirements for the  
Degree of  
Doctor of Philosophy

Auburn, Alabama

August 28, 1992

## VITA

Ted Wesley Warnock, son of William Leroy and Joyce Lee (Davis) Warnock, was born September 2, 1959 in Hialeah, Florida. He graduated from Hialeah Senior High School in June, 1977, and entered Auburn University in September, 1977. He graduated in June, 1981, with a Bachelor of Aerospace Engineering degree, and was commissioned a Second Lieutenant in the United States Air Force. From October, 1981, to December, 1985, he served as a Minuteman II ICBM Missile Launch Officer in Great Falls, Montana. He was promoted to the rank of First Lieutenant in August, 1983, and to Captain in August, 1985. In December, 1984, he completed, by extension, a Master of Science degree in Systems Management from the University of Southern California. In January, 1986, he entered the Graduate Division at Stanford University, under Air Force sponsorship, and graduated in June, 1987, with a Master of Science degree in Aeronautical and Astronautical Engineering. From June, 1987, to August, 1989, he served as an Instructor in the Department of Astronautics at the United States Air Force Academy. He entered the Graduate School at Auburn University in September, 1989, under Air Force sponsorship. He married Margaret Marie Peacock, daughter of Dr. Jimmy Ray and Margaret (Hoadley) Peacock, on January 2, 1982. On December 21, 1990, their first child, Laura Margaret Warnock, was born.

DISSERTATION ABSTRACT  
A METHOD TO PREDICT THE ORBITAL LIFETIMES OF  
FREE TETHERS AND TETHER-TRAILING SATELLITES  
USING ARTIFICIAL NEURAL NETWORKS

Ted Wesley Warnock

Doctor of Philosophy, August 28, 1992  
(M.S., Stanford University, 1987)  
(M.S.S.M., University of Southern California, 1984)  
(B.A.E., Auburn University, 1981)

259 Typed Pages

Directed by John E. Cochran, Jr.

This dissertation deals with the development of a method to predict the orbital lifetimes of uncontrolled free tethers and tether-trailing satellites originating in low-to-moderate altitude Earth orbits. The problem is solved by application of the "empirical method". Two mathematical models to simulate the orbital evolution of tethered systems are developed. In both models the system is discretized into a series of interconnected point masses, orbiting an oblate Earth and transiting an oblate, rotating, temporally and globally averaged atmosphere. For aerodynamic drag calculations, tether segments are modeled as right circular cylinders, and any end-body is modeled as a sphere. Drag coefficients vary as a function of shape and Knudsen

number. In the "multibody model", connections between masses are elastic, and the system is free to assume any orientation. Newtonian equations of motion are numerically integrated. In the "orbital element propagation model", connections between masses are inelastic, and the system is constrained to remain aligned along the local vertical. Gauss' form of Lagrange's Planetary Equations, in terms of equinoctial elements, are used to propagate the orbital elements describing the orbit of the system's center of mass. The element propagation model is shown to provide, for initially unstretched systems aligned along the local vertical, accurate results, very quickly, as compared to those obtained using the multibody model. An algorithm to train feed-forward artificial neural networks, by minimizing the sum of the squares of percent errors, is derived and shown to be invaluable in training networks to represent widely-spread real-valued data. A hybrid training approach, using the derived algorithm in conjunction with the standard backpropagation training algorithm, is described and demonstrated. This approach often reduces network training time, and it is used to train three networks with lifetime data provided by the element propagation model: one to predict the orbital lifetimes of free tethers, one to predict lifetimes of upward-deployed subsatellites trailing a tether, and one to provide correction factors that account for the effects of initial orbit inclination and argument of latitude. The accuracies of network-predicted lifetimes, as compared to those obtained using the multibody model, are demonstrated in 90 cases with randomly chosen initial conditions and system physical dimensions. In all cases, the network's results are shown to be accurate to within  $\pm 20\%$  of results obtained using the multibody model.

## TABLE OF CONTENTS

LIST OF TABLES .....	viii
LIST OF FIGURES .....	x
INTRODUCTION .....	1
MATHEMATICAL MODELS .....	16
External Forces Model .....	17
Environment Model .....	25
Multibody Model .....	27
Orbital Element Propagation Model .....	36
ARTIFICIAL NEURAL NETWORKS .....	49
Overview and Introduction .....	49
The Error Backpropagation Network Training Algorithm .....	58
The Minimum Percent Error Backpropagation Training Algorithm .....	62
Network Training Procedures .....	65
Network Training Example .....	68
RESULTS AND DISCUSSION .....	75
Preliminary Findings and Basic Phenomena .....	76
Element Propagation Model Performance .....	83
Orbital Lifetime Prediction Accuracy .....	90
Predicting Free Tether Orbital Lifetime .....	94
Effects of Initial Inclination, Argument of Perigee, and True Anomaly ...	103
Predicting the Orbital Lifetime of Tether-Trailing Satellites .....	149
Test Case Results .....	173

CONCLUSIONS AND RECOMMENDATIONS .....	199
REFERENCES .....	205
APPENDIX A .....	212
Atmosphere Model .....	212
APPENDIX B .....	224
Drag Coefficient Models .....	224
APPENDIX C .....	229
Network Constants - Free Tether Orbital Lifetime .....	229
APPENDIX D .....	234
Network Constants - Lifetime Correction Factor .....	234
APPENDIX E .....	239
Network Constants - Tether-Trailing Satellite Orbital Lifetime .....	239

## LIST OF TABLES

1. Acceleration magnitudes in 500 km Earth orbit. . . . .	18
2. Lifetime percent difference statistics, $i = 80^\circ$ vs. $i = 28.5^\circ$ . . . . .	107
3. Lifetime percent difference statistics, $\omega = 90^\circ$ vs. $\omega = 0$ . . . . .	109
4. Lifetime percent difference statistics, $\nu = 180^\circ$ vs. $\nu = 0$ . . . . .	111
5. Error limits using 50 km mean percent difference, $i = 80^\circ$ vs. $i = 28.5^\circ$ . . . .	118
6. Error limits using 50 km mean percent difference, $\omega = 90^\circ$ vs. $\omega = 0$ . . . . .	118
7. Error limits using 50 km mean percent difference, $\nu = 180^\circ$ vs. $\nu = 0$ . . . . .	118
8. Argument of perigee and true anomaly data points. (all units degrees) . . . . .	140
9. Argument of perigee and true anomaly data points. (all units degrees) . . . . .	142
10. Mean orbital lifetime correction factors. . . . .	146
11. Center of mass initial orbit radii and parent satellite orbital lifetimes. . . . .	154
12. Maximum lifetime differences caused by subsatellite diameter variations. . . .	165
13. Maximum lifetime differences with 20 km tether. . . . .	166
14. Prediction method performance with free tethers, standard scenario. . . . .	176
15. Initial conditions and tether length, free tethers, $i = 28.5^\circ$ . . . . .	177
16. Prediction method performance with free tethers, $i = 28.5^\circ$ . . . . .	178
17. Initial conds., tether length, MBM life, and EPM accuracy, free tethers. . . . .	180
18. Prediction method accuracies, free tethers. . . . .	181

19. Initial conditions and system dimensions, standard scenario. . . . .	184
20. Calculated and predicted lifetimes and accuracies, standard scenario. . . . .	185
21. Initial conditions and system dimensions, $i = 28.5^\circ$ . . . . .	187
22. MBM life, EPM life, network predicted life, and errors, $i = 28.5^\circ$ . . . . .	188
23. U-i correction factors, predicted lifetimes and errors, $i = 28.5^\circ$ . . . . .	191
24. Initial conditions and system dimensions, upward-deployed satellites. . . . .	193
25. MBM, EPM and network lifetimes and errors, upward-deployed satellites. . .	194
26. Prediction method accuracies, upward-deployed satellites. . . . .	195

## LIST OF FIGURES

1. Ratio of perturbing accelerations to oblateness acceleration. . . . .	19
2. Altitude variation of 2 mm cylinder drag coefficient. . . . .	24
3. Altitude variation of 3 m sphere drag coefficient. . . . .	24
4. Atmosphere mass density curvefit error. . . . .	26
5. Altitude above an oblate Earth. . . . .	27
6. Tethered system lumped-mass model. . . . .	29
7. Rotating coordinate frame. . . . .	31
8. Aerodynamic forces geometry. . . . .	34
9. Equinoctial, Osculating, and GEC coordinate systems. . . . .	46
10. Feed-forward network architecture. . . . .	51
11. Hidden layer neuron operation. . . . .	52
12. Logistic function and its derivative. . . . .	54
13. The effect of multiplicative weights on the logistic function. . . . .	54
14. The effect of a subtracted bias on the logistic function. . . . .	55
15. Selected feed-forward network structure. . . . .	58
16. Function to be learned. . . . .	68
17. Network accuracy evolution. . . . .	70
18. Generalization accuracy after MPE training. . . . .	70

19. Generalization accuracy after standard method training. . . . .	71
20. Network accuracy evolution with combined training. . . . .	72
21. Generalization accuracy after combined training (6172 passes total). . . . .	72
22. Generalization accuracy after combined training (51,534 passes total). . . . .	74
23. Orbital decay with short segments. . . . .	77
24. Orbital decay with long segments. . . . .	77
25. Effect of drag coefficient model on orbital decay. . . . .	78
26. Effect of Earth and atmosphere shape and state on orbital decay. . . . .	80
27. Effect of tether diameter on orbital decay. . . . .	80
28. Effect of tether length on orbital decay. . . . .	82
29. Element propagation model performance with free tethers. . . . .	84
30. Element propagation model performance on "TSS-1". . . . .	85
31. "TSS-1" in-plane libration angle during decay. . . . .	86
32. "TSS-1" out-of-plane libration angle during decay. . . . .	86
33. Element propagation model performance on "SEDS". . . . .	88
34. "SEDS" in-plane libration angle during decay. . . . .	88
35. "SEDS" out-of-plane libration angle during decay. . . . .	89
36. EPM performance on downward-deployed subsatellite. . . . .	90
37. Orbital lifetime prediction curves for 20 km free tether. . . . .	95
38. Orbital lifetime prediction curves for 125 km and 10 km free tethers. . . . .	96
39. Free tether orbital lifetime prediction network structure. . . . .	98
40. Trained network output and orbital lifetime data for 50 km free tether. . . . .	100
41. Error in equivalent sphere orbital lifetimes. . . . .	101

42. Geocentric latitude and angular orbital elements. . . . .	105
43. Effect of initial orbit inclination on lifetime ( $\omega = \nu = 0$ ). . . . .	106
44. Effect of initial argument of perigee on lifetime ( $i = 28.5^\circ \nu = 0$ ). . . . .	108
45. Effect of initial true anomaly on lifetime ( $i = 28.5^\circ \omega = 0$ ). . . . .	110
46. Effect of initial inclination, argument of perigee and true anomaly. . . . .	113
47. Effect of initial true anomaly on lifetime ( $i = 28.5^\circ$ ). . . . .	121
48. Effect of initial argument of latitude on lifetime ( $i = 10^\circ$ ). . . . .	122
49. Effect of initial argument of latitude on lifetime ( $i = 28.5^\circ$ ). . . . .	123
50. Effect of initial argument of latitude on lifetime ( $i = 70^\circ$ ). . . . .	123
51. Error in predicting mean difference lifetime ( $i = 10^\circ$ ). . . . .	126
52. Error in predicting mean difference lifetime ( $i = 28.5^\circ$ ). . . . .	126
53. Error in predicting mean difference lifetime ( $i = 70^\circ$ ). . . . .	127
54. Predicted lifetime accuracy, maximum difference case ( $i = 10^\circ$ ). . . . .	129
55. Predicted lifetime accuracy, minimum difference case ( $i = 10^\circ$ ). . . . .	129
56. Predicted lifetime accuracy, maximum difference case ( $i = 28.5^\circ$ ). . . . .	130
57. Predicted lifetime accuracy, minimum difference case ( $i = 28.5^\circ$ ). . . . .	130
58. Predicted lifetime accuracy, maximum difference case ( $i = 70^\circ$ ). . . . .	131
59. Predicted lifetime accuracy, minimum difference case ( $i = 70^\circ$ ). . . . .	131
60. Error in predicted lifetimes ( $i = 10^\circ \omega = 0^\circ, \nu = 225^\circ$ ). . . . .	133
61. Predicted lifetime accuracy, max. diff. case (100 km tether, $i = 70^\circ$ ). . . . .	134
62. Predicted lifetime accuracy, min. diff. case (100 km tether, $i = 70^\circ$ ). . . . .	135
63. Error in predicted lifetimes (100 km tether, $i = 70^\circ, \omega = 0, \nu = 90^\circ$ ). . . . .	136
64. Error in predicted lifetimes (100 km tether, $i = 70^\circ, \omega = 0, \nu = 180^\circ$ ). . . . .	136

65. Orbital lifetime correction factor network structure. . . . .	141
66. Correction factor network performance at untrained inclinations. . . . .	143
67. ANN representation of orbital lifetime correction factors. . . . .	144
68. Correction factor network performance in "worst case" scenario. . . . .	145
69. Inclination-only orbital lifetime correction factors. . . . .	147
70. Inclination-only correction factor performance in "worst case" scenario. . . . .	148
71. Effect of deployed tethers on satellite orbital decay. . . . .	151
72. Error in equivalent sphere lifetime, downward-deployed 50 km cases. . . . .	156
73. Error in equivalent sphere lifetime, downward-deployed 100 km cases. . . . .	157
74. Error in equivalent sphere orbital lifetime, upward-deployed 20 km cases. . . . .	158
75. Error in equivalent sphere orbital lifetime, upward-deployed 50 km cases. . . . .	158
76. Error in equivalent sphere orbital lifetime, upward-deployed 100 km cases. . . . .	159
77. Effect of tether length on orbital lifetime. . . . .	162
78. Effect of subsatellite mass on orbital lifetime. . . . .	164
79. Upward-deployed tether-trailing satellite lifetime prediction network. . . . .	168
80. Network output and orbital lifetime data for 200 kg, 60 km system. . . . .	170
81. Network lifetime prediction accuracy, 200 kg, 60 km system. . . . .	171
82. Predicted lifetime variations due to changes in $R_a$ and subsatellite mass. . . . .	171
83. Predicted lifetime variations due to changes in $R_a$ and tether length. . . . .	173
84. Errors in free tether lifetime predictions. . . . .	183
85. U-i correction factors and errors in predicted lifetimes, $i = 28.5^\circ$ . . . . .	189
86. Errors in corrected and uncorrected predicted lifetimes, $i = 28.5^\circ$ . . . . .	192
87. Errors in tether-trailing satellite lifetime predictions. . . . .	197

A-1. Atmospheric mass density, 50-75 km. . . . .	215
A-2. Atmospheric mass density, 75-105 km. . . . .	216
A-3. Atmospheric mass density, 105-130 km. . . . .	216
A-4. Atmospheric mass density, 130-200 km. . . . .	217
A-5. Atmospheric mass density, 200-500 km. . . . .	217
A-6. Atmospheric mass density, 50-1000 km. . . . .	218
A-7. Atmospheric mass density curvefit accuracy, 50-1000 km. . . . .	218
A-8. Mean free path, 50-75 km. . . . .	221
A-9. Mean free path, 75-105 km. . . . .	221
A-10. Mean free path, 105-130 km. . . . .	222
A-11. Mean free path, 130-200 km. . . . .	222
A-12. Mean free path, 50-200 km. . . . .	223
A-13. Mean free path curvefit accuracy, 50-200 km. . . . .	223
B-1. Circular cylinder drag coefficient variation. . . . .	226
B-2. Sphere drag coefficient. . . . .	228

## INTRODUCTION

The idea of using tethers in space is not a new concept. In 1895, Tsiolkovsky suggested connecting large masses in space by a long thin string.<sup>1,2</sup> In 1960, Artsutanov envisioned an Earth-based "beanstalk", rooted at the equator and extending to geosynchronous altitude, which would allow one to leave the planet by simply climbing to the top and letting go.<sup>3,4</sup>

The first tether experiments in space were conducted in 1966, during the last two Gemini missions. In both tests, the manned Gemini spacecraft was docked to an unmanned Agena rocket, a 100 foot tether was attached to both vehicles, and the vehicles were separated.<sup>5,6</sup> During Gemini 6, the tethered system was spun about its center of mass, using the Gemini thruster reaction control system, to provide a low artificial gravity. On Gemini 7, the reaction control system was used to orient the vehicles along the local vertical, and passive gravity-gradient stabilization was achieved when the control system was deactivated.

In 1972, M. D. Grossi, a radiophysicist at the Harvard-Smithsonian Center for Astrophysics (SAO), proposed that NASA deploy from the Space Shuttle a 20-to-100 kilometer (km) electrodynamic tether to be used as an antenna to radiate electromagnetic waves in the ULF band.<sup>7</sup> In 1974, SAO gave the project the name SKYHOOK, and made the study of the long antenna's dynamics a top priority.

Professor Guiseppe Colombo, also at SAO, was given the lead in the dynamical analysis, and he quickly realized that a long wire could also serve as a "Shuttle-borne skyhook" to support a scientific satellite.<sup>8</sup> This led to a series of studies at SAO and elsewhere in the United States and Italy on uses for a so-called Tethered Satellite System (TSS). The work culminated in an agreement to develop and fly such a system on the U.S. Space Shuttle.<sup>9</sup>

Currently, NASA plans two experiments to confirm basic tether phenomena and to demonstrate the feasibility of simple tether operational concepts. The first, TSS-1, is devoted to electrodynamics experimentation. It involves a 500 kilogram (kg) satellite, deployed upward (i.e., away from Earth) on a 20 km tether from the Space Shuttle's 300 km altitude orbit.<sup>10</sup> TSS-2 will demonstrate the downward deployment and retrieval of the satellite on a 100 km non-conductive tether.<sup>11</sup>

Shuttle-borne operations are only one item on a growing list of proposed tethered satellite operations categories. Other proposals include<sup>12</sup>

- (a) Using expendable launch vehicles as "parent" craft.
- (b) Using a space station as the tethered parent vehicle for
  - (1) tether initiated reentry or orbit transfer of a subsatellite, and/or
  - (2) local area operations requiring return to the space station.
- (c) Using tethers and/or tethered subsatellite(s) in conjunction with conventional satellites. Possibilities include payload lofting, (parent) satellite maneuvering, electrodynamic thrust and/or power generation, and ULF/ELF/VLF communications.

Many uses of tethered systems have been proposed and studied by the aerospace community in the past decade. Some scenarios include the purposeful cutting of

the tether at the parent satellite and/or the subsatellite. Furthermore, circumstances may require that a tether be cut as an emergency measure, or a tether may be unintentionally cut or broken. Thus, in a number of possible scenarios, a tethered system may be reduced to an uncontrolled distributed mass, with or without an attached end-body, orbiting under the influence of only natural forces. Given that such an occurrence is possible, and may, in fact, be planned, a method of estimating an uncontrolled system's lifetime is needed.

Very little definitive research has been done in this area. In 1987, Bergamaschi and Morana<sup>13</sup> presented an order of magnitude estimate for the orbital lifetime of a free tether (i.e., one with no end-masses) released from either a Shuttle or Space Station orbit. They compared results obtained for a 20 km tether using three models:

- (a) A simple analytical model which treated the tether as a point mass.
- (b) A rigid rod model, which used distributed gravitational and drag forces.
- (c) A hinged rigid rod model, which consisted of two equal length segments, and again used distributed gravitational and drag forces.

In each case only (orbital) planar motion was allowed, and a spherical Earth and non-rotating spherical atmosphere were modeled. The dynamical equations of motion for the rigid rod models were integrated numerically, and the results compared to each other and those of the analytical model. It was learned that there was at least order of magnitude agreement in the results provided by the three models.

In a later study, Bergamaschi<sup>14</sup> used King-Hele's<sup>15</sup> semi-analytical single-mass orbital lifetime methods to calculate the orbital lifetime of a satellite trailing a tether.

To employ King-Hele's methods, the total mass of the system and a representative cross-sectional area were assumed to be located at the satellite's position. Three scenarios were considered:

- (a) A TSS-1 (satellite deployed 20 km upward from Shuttle) freely decaying orbit after the tether was severed at the Shuttle.
- (b) A reentry mission from a Space Station (satellite deployed 20 km below Station).
- (c) Martian atmosphere entry by a free flying probe trailing a tether.

In each case orbit plane orientation was considered constant. Unfortunately, the results were not compared with those of any tethered satellite computer simulations, leaving the validity of using King-Hele's methods in these scenarios in question.

The objective of this research project was to develop a general method for predicting the orbital lifetime of uncontrolled free tethers and satellites trailing a tether. These scenarios currently seem much more likely than an instance of a "complete" tethered system (i.e., parent-tether-satellite) becoming uncontrolled.

The approach used is well known: Compile a database of experimental results, study those results to identify dependent relationships and trends, and derive mathematical expressions to model the relationship between dependent and independent variables. This is known as the "empirical method".<sup>16</sup>

Results obtained using this procedure are successfully employed in many fields. For example, mechanical engineers performing flow analyses routinely use empirically-derived expressions to calculate convection heat transfer coefficients.<sup>17</sup> Another example occurs in aeronautical engineering, where empirically-derived relations are often used to determine the values of various aerodynamic force coefficients for a

given flight vehicle in a configuration of interest. The well-known equation of state for a perfect gas,  $P = \rho RT$ , is another result that may be derived empirically.<sup>18</sup> There are numerous other possible examples, from many areas of science and engineering.

In short, the empirical method is used when the phenomena being investigated is sufficiently complex that mathematical models are either not able to satisfactorily represent the phenomena, or are so complex themselves that they defy analytical solution.

The orbital evolution of an uncontrolled tethered system in Earth orbit is such a phenomena. The system operates in a nonlinear, non-trivial gravity field, experiences aerodynamic forces which are nonlinear in altitude, attitude, and velocity, and is subjected to a variety of additional internal and external forces. A database of historical lifetime data, such as exists for single-mass satellites, is not available for these systems. Furthermore, the orbital decay of these systems cannot be realistically studied experimentally, *per se*.

We can, however, construct a mathematical model of the dynamical situation, solve the mathematical equations numerically for a large variety of cases, thereby creating a "historical database" of sorts, and derive representative expressions from the data. This is the approach used in this research project.

To obtain data for analysis, two mathematical models of an uncontrolled tethered system are developed. The first, a multibody model, includes an extensible, non-conductive tether connecting end-bodies modeled as spheres. It is used as a "truth" model. The second, a more efficient, dynamically simplified model, is based on an orbital element propagation technique.

In both models, the tethered system orbits an oblate Earth and transits an oblate, rotating, temporally and globally averaged reference atmosphere. Aerodynamic forces are calculated using drag coefficients which vary as a function of shape and Knudsen number.

There are many independent variables which will affect the orbital lifetime of a tethered system. These may be grouped under three headings:

- (a) The initial orbit of the system's center of mass.
- (b) The initial motion and orientation of the system about its center of mass.
- (c) The system's physical dimensions and characteristics.

The mathematical description in each of these categories requires several variables. For example, the center of mass' initial orbit can be described by using the six classical orbital elements: the orbit's semi-major axis, eccentricity, inclination, ascending node longitude, argument of perigee, and true anomaly. There are, literally, an infinite number of possible initial configurations and motions of the system about its center of mass. The description and modeling of these characteristics can consequently vary from trivial to nearly impossible. Even the system's physical characteristics offer a multitude of options. These include the tether's length, diameter, mass density, and elastic properties, in addition to the size and shape of any end-body. The location and method used to attach the tether to an end-body may also affect the system's motion.

Clearly, the scope of the present study must be narrowed. This is possible for several reasons. First, the vast majority of planned or proposed Earth-orbiting tethered satellite missions involve deployment in  $28.5^\circ$  inclination orbits, at low to

moderate altitudes - 200 km to 500 km. Second, the missions typically involve tether lengths of either 10-20 km or near 100 km. Third, the parent craft will probably be in a circular or near-circular orbit. Fourth, the deployed tether, with or without an attached subsatellite, will probably be maintained along, or near, the local vertical. These characteristics of probable tethered satellite missions provide natural boundaries for this research project.

First, in this work, tether length is limited to a maximum of 125 km. This is the maximum length discussed in NASA's *Tethers in Space Handbook* for any planned or proposed Earth mission.<sup>19</sup> Tether diameter is assumed to be 2 millimeters, although the general effect of different diameters is investigated. The mass density and elastic properties of the tether are assumed to be those of Kevlar 29. In so doing, the physical properties and diameter assumed here will coincide with those most commonly used in the current literature. Next, the deployed tether, with or without an attached subsatellite, is initially unstretched, aligned along the local vertical, orbiting as a rigid rod. These conditions are the goal of many of the various control schemes which have been proposed for use with tethered systems.<sup>20</sup> We also assume that the tether is connected to the center of mass of any attached end-body, and ignore any tether - end-body aerodynamic interference or interaction effects. We will study only direct orbits, as no uses of tethered systems in retrograde orbits have been proposed. Finally, the radii of perigee and apogee of the center of mass' initial orbit will be limited to 6578 km and 6878 km, respectively (i.e., 200 and 500 km altitude in an equatorial orbit). The upper limit corresponds to the maximum altitude of currently

proposed missions, as discussed earlier, and the lower limit is based on Bergamaschi's finding<sup>21</sup> that the orbital lifetime of tethers, once they reach 200 km altitude, is very short. We will consider a system's orbital lifetime to be complete when the system center of mass reaches 150 km altitude.

Even after applying the constraints just described, a tethered system's orbital lifetime will still depend on several independent variables: the center of mass' initial orbit, the tether's length, and the mass and size of any attached end-body. Although it is theoretically possible for one to analytically identify and express the relationship between each of these variables (or groups of variables) and the orbital lifetime, it is certainly not a task with an assured result. The process is complicated by the interdependence of many of the variables. For example, changing the argument of perigee of the center of mass' initial orbit will alter the latitude, and, consequently, the altitude above an oblate Earth, at which the point of closest approach occurs. This, in turn, will affect the system's orbital energy loss due to aerodynamic drag, thereby altering the system's orbital lifetime. Unfortunately, changing the initial orbit's inclination will affect the variation caused by changes in the argument of perigee. For example, a 90° argument of perigee and a high inclination will result in a much more northerly perigee latitude than the same argument of perigee in a nearly equatorial orbit. Hence, it is clear that we are challenged with deriving a very complicated, nonlinear mapping in a high-dimension space.

Traditional curve fitting techniques - postulating the form of a mathematical expression describing the relationship between one or more independent variables and

the orbital lifetime, and using a least squares method to adjust the expression's coefficients to minimize the error between the calculated and empirical data - may, or may not, yield satisfactory results when applied to the current situation. It is more likely that a solution may be obtained by training an artificial neural network (ANN) to represent the empirical data.

Neural network research dates back to the late 1800's, with some of the initial work being done by Freud.<sup>22</sup> Prior to his psychoanalysis investigations, Freud attempted to "... represent psychical processes as quantitatively determinate states of specifiable material particles ....".<sup>23</sup> The first mechanical implementation of an ANN was a hydraulic device designed by Russell, in 1913.<sup>24</sup> This mechanism simulated the action of nervous discharges, and was able to "learn" by experience.<sup>25</sup> In 1943, McCulloch and Pitts derived the first mathematical model of an ANN.<sup>26,27</sup> In 1949, Hebb developed the first learning algorithm for ANNs.<sup>28,29</sup> Minsky and Edmonds studied the work of McCulloch, Pitts, and Hebb, and are credited with creating the first electronic implementation of an ANN.<sup>30,31</sup> Theirs was a 40 neuron machine, with synapses (i.e., connections between neurons) that adjusted their conductances according to the success of performing a specified task.<sup>32</sup> The device successfully modeled the behavior of a rat in a maze searching for food.<sup>33,34</sup> In the four decades following this 1951 invention, ANN research has experienced periods of great enthusiasm, alternating with times of obscurity and even disfavor.<sup>35</sup> Simpson describes no less than 27 ANN models, which represent, as he says, only a fraction of those that have been, and continue to be, developed.<sup>36</sup>

Without question, feed-forward networks trained using error backpropagation<sup>37</sup> are currently the most widely applied neural network architecture. This popularity revolves around the demonstrated ability of backpropagation networks to learn complicated multidimensional mappings.<sup>38</sup> In fact, it has been said that the primary application of this type of artificial neural network is any situation that requires the acquisition of a complex nonlinear mapping.<sup>39</sup>

Hecht-Nielson<sup>40</sup> offers the following as a general, yet rigorous, definition of an artificial neural system:

"A neural network is a parallel, distributed information processing structure consisting of processing elements (which can possess a local memory and carry out localized information processing operations) interconnected together with unidirectional signal channels called connections. Each processing element has a single output connection which branches into as many collateral connections as desired (each carrying the same signal - the processing element output signal). The processing element output signal can be of any mathematical type desired. All of the processing that goes on within each processing element must be completely local; i.e., it must depend only upon the current value of the input signal arriving at the processing element via impinging connections and upon values stored in the processing element's local memory."

Hecht-Nielson's "processing elements" are also often referred to in the literature as "neurons", in recognition of the fact that artificial neural networks are roughly based on the operating structure of the brain. Essentially, ANNs are adaptive information processing systems that develop transformations or mappings between one or more inputs and outputs. Instead of being given a step-by-step procedure for carrying out the desired transformations, a network can be trained to generate its own

internal rules governing the relationships, and to refine those rules until the transformations are accomplished with acceptable accuracy. This is one of the major benefits of using ANNs to represent multidimensional data -- a priori knowledge of a representative function's form is not required.

Another strength of ANNs is their ability to "generalize" from specific training data to new situations for which the data remains representative. In more familiar terms, this is to say that properly sized and structured networks, after training, provide a smooth nonlinear interpolation of the training data. By adjusting the number of network layers and processing units, a designer can affect the generalization abilities, training time, and final accuracy of a network. Once a network is trained, an operator can disable the learning algorithm, and "freeze" the weights and biases on the neuron connections. This will cause the network to stop adapting itself to new data, and will provide a structure that is ready to process "real world" data. Training can be reenabled at any time, to allow the network to adjust itself for newly acquired data.

In recent years, multilayer neural networks have been increasingly popular for applications in pattern recognition, classification, and function approximation. Neural nets have been successfully used in many areas of activity, ranging from solving scheduling optimization problems, to scoring applications for bank loans, to translating written text to speech and vice versa.<sup>41</sup> The Defense Advanced Research Projects Agency recently reported that ANN methods, still in their infancy, have matched or exceeded the performance of established methods used for the classification of special

sonar and seismic signals, and for automatic target recognition with forward looking infrared sensors, despite the many years of R&D supporting the current technologies.<sup>42</sup> The scientific community has placed less emphasis on studying the ability of ANNs to process floating point numbers, but Lapedes and Farber<sup>43</sup> have shown that neural nets are capable of quite accurately representing real-valued functions.

This is not to suggest that ANNs are without their shortcomings. Although there are many examples of the successful use of ANNs, there are also some important issues that are currently solved in practice only by trial and error. Today, the greatest difficulties are (1) choosing the number and type of training samples required for successful learning, where learning is deemed to have been successful when the system generalizes correctly, and (2) using the proper network structure to solve a given problem. With too few neurons, the network may not be powerful enough for a given learning task. With a large number of neurons, computation becomes expensive, and the network may have the resources to actually "memorize" the training data. The number of layers of neurons used is another structural variable that affects how fast a network may be trained and how well it will generalize. It has recently been suggested that networks with more layers, and fewer units in the early layers, may generalize better than "shallow" networks with many units in each layer.<sup>44</sup> However, narrow networks with many layers are known to be more difficult to train than broad networks with one or two hidden layers.<sup>45</sup>

One of the best examples of the power and usefulness of a feed-forward network composed of just three layers - input-hidden-output - is the "NETTALK"

network, developed by Sejnowski and Rosenberg<sup>46</sup> in 1987. This network was trained, using error backpropagation, to translate segments of English text into phonetic notation for pronouncing the text. The phonetic notation was passed to an electronic speech generator and verbalized. The three layer network had 203 input units, 80 units in the hidden layer, and 26 output units. The size of the hidden layer was chosen after experimenting with as many as 120 units and as few as zero units. The decision to use an 80 unit hidden layer was based on experiments which indicated that 80 units were sufficient for good performance, but not prohibitive in terms of training time.

In studying the ability of neural nets to represent real-valued functions, Lapedes and Farber<sup>47</sup> found that (1) more than two hidden layers are never required, and (2) the accuracy of the approximation is controlled by the number of neurons per layer, not the number of layers.

Hence, relying on the experience and findings of Sejnowski, Rosenberg, Lapedes, and Farber, the plan for this research project is to use feed-forward networks having as few hidden layers, with as few units, as are required to represent and interpolate the orbital lifetime data. This requires an iterative procedure of (1) choosing a network structure, (2) attempting to train the network to represent the training data with only acceptable errors, (3) testing the trained network's generalization ability, and (4) returning to (1) if the results of (2) and/or (3) are not satisfactory. The number of input units used will be dictated by the number of independent

variables. There will be one output unit, which will provide the network's approximation for the orbital lifetime.

A new training algorithm, designed specifically to train feed-forward networks to represent any real-valued function, was derived in this work. This algorithm, used in conjunction with a hybrid training approach, is shown to be invaluable in training networks to represent and interpolate real-valued data which spans several orders of magnitude.

Artificial neural networks are used in this research project to model the relationships between various independent variables discussed earlier and the orbital lifetime of tethered systems. One network provides the orbital lifetime of any free tether, 10 to 125 km in length. A second network provides the lifetime of a spherical satellite, of any mass and diameter up to 500 kg and 5 meters, respectively, trailing a downward-deployed tether of any length between 50 and 100 km. This situation may represent a parent satellite trailing a downward-deployed tether, perhaps after a subsatellite has been released, or it may represent an upward-deployed subsatellite trailing a tether, after it has been either cut, or broken free of, a parent vehicle.

The lifetimes produced by the "prediction networks" assume the center of mass of a system of interest is initially in a  $28.5^\circ$  inclination orbit, with argument of perigee and true anomaly equal to zero. A third network produces a lifetime correction factor, based on the system's initial orbit inclination, argument of perigee and true anomaly. The initial longitude of the orbit's ascending node does not affect the

calculated orbital lifetime, since the assumed shapes of the Earth and atmosphere are symmetric about the polar axis.

A large number of randomly generated test cases are used to (1) demonstrate the accuracy of the simplified dynamical model, (2) test the generalization abilities of the trained networks, and (3) demonstrate the validity of the orbital lifetime prediction technique.

## MATHEMATICAL MODELS

The objective of any mathematical modeling effort is to represent, as simply and efficiently as possible, one or more characteristics of a system of interest. In this chapter, two models developed to numerically simulate the motion of uncontrolled tethered satellite systems in freely-decaying Earth orbits are described. The difference in the models is the way in which a system's dynamics are represented.

The first, a "lumped-mass" or "multibody" model, discretizes a tether into multiple, sequentially connected, elastic segments. This approach is a type of "finite element" method. The nonlinear, ordinary, differential equations describing the motion of the system are numerically integrated in time.

In the second model, an "element propagation" model, the system is discretized into multiple nonelastic segments, and "propagation" or "variational" equations describe the time rates of change of orbital elements due to two-body and non-two-body (perturbing) forces. These equations are used to propagate the orbital elements describing the system center of mass' orbit.

The external forces acting on a system and the environment in which it moves are identical in the two models. Hence the external forces model and the environment model are discussed separately.

### External Forces Model

There are many external forces which may affect the motion of a satellite in Earth orbit. In 1666, Isaac Newton conceived the law of universal gravitation, and used it to show that a satellite moving under the influence of only a more massive, spherical, central body would travel precisely in an elliptical path.<sup>48</sup> In this unperturbed "two-body" scenario, the orbit of a satellite would be an ellipse of constant size and shape, in a plane fixed relative to the "fixed" stars.

In reality, a two-body elliptical orbit is perturbed by the effects of a variety of forces. In general, forces due to the following causes will affect the orbit:

- (a) non-sphericity (oblateness) of the Earth's gravitational field,
- (b) Earth's atmosphere (ie., aerodynamic forces),
- (c) gravitational attraction of the Sun, Moon and planets,
- (d) solar radiation,
- (e) other sources - magnetic fields, Earth-reflected solar radiation, ocean and land mass tides, charged and uncharged particle impact, and the effects of precession and nutation of the Earth's spin axis.

The perturbations in (e) would need to be taken into account in analyzing orbits with observations of very high accuracy.<sup>49</sup> We will ignore their effects. The magnitude of the acceleration resulting from each of the sources listed in (a) through (d) are shown in Table 1. The values were calculated for a 500 kg, 5 meter spherical satellite at the northernmost point of a 500 km (altitude) circular orbit, inclined at 28.5 degrees.

Except for the Earth oblateness and aerodynamics calculations, orbit inclinations and

phase angle differences were ignored. That is, the minimum possible distances between the satellite and the other bodies were used, assuming the bodies were located in coplanar orbits with no phase angle difference.

Table 1. Acceleration magnitudes in 500 km Earth orbit.

Source	Acceleration, m/sec <sup>2</sup>	Source	Acceleration, m/sec <sup>2</sup>
Spherical Earth	8.43	Venus	$2.24 \times 10^{-7}$
Earth oblateness	$1.05 \times 10^{-2}$	Mars	$1.45 \times 10^{-8}$
Aerodynamic drag	$2.34 \times 10^{-6}$	Jupiter	$3.66 \times 10^{-7}$
Solar radiation	$2.04 \times 10^{-7}$	Saturn	$2.66 \times 10^{-8}$
Sun (gravity only)	$6.13 \times 10^{-3}$	Uranus	$8.72 \times 10^{-10}$
Moon	$3.72 \times 10^{-5}$	Neptune	$3.66 \times 10^{-10}$
Mercury	$3.74 \times 10^{-9}$	Pluto	$1.98 \times 10^{-11}$

Hence we see that the accelerations due to the Sun, Moon, and planets are significantly less than those imposed by the Earth and its oblateness. Although the acceleration due to aerodynamic drag, at the reference point, is less than that of the Moon or Sun, we note that drag is a dissipative force, which continually opposes the satellite's motion. Conversely, the gravitational forces imposed by the Sun and Moon are conservative, and their effects will be periodic, varying with the satellite's position in orbit and the orbit's position in space.

As discussed in the **Introduction**, the maximum system center of mass altitude to be included in this project is 500 km. As shown in Figure 1, this choice will limit

the magnitude of the Sun's acceleration to a level below approximately 60 percent of the acceleration due to the Earth's oblateness. Hence, only the perturbations due to aerodynamic drag and the Earth's oblateness are included in this work.

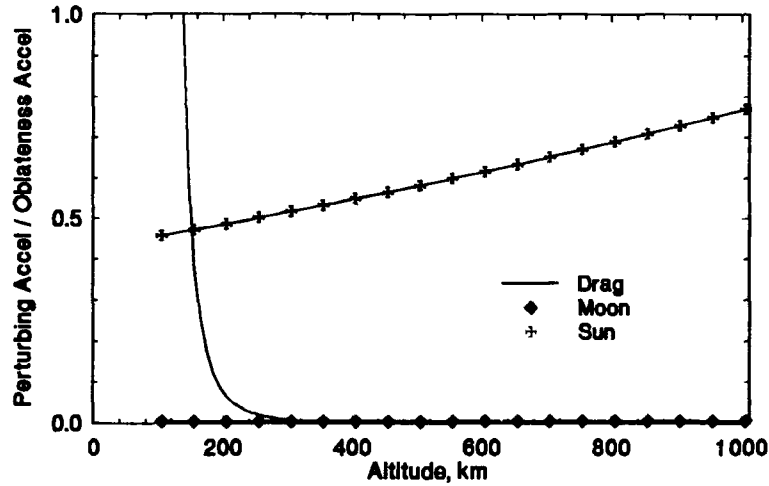


Figure 1. Ratio of perturbing accelerations to oblateness acceleration.

Gravitational Forces. Gravitational forces acting on a tether system are calculated assuming the Earth is symmetric about its polar axis. The external gravitational potential,  $\phi$ , of an oblate, spheroidal Earth may be written as

$$\phi = \frac{\mu_E}{R_E} \left\{ 1 - \sum_{k=2}^{\infty} J_k \left( \frac{R_E}{R} \right)^k P_k(\sin L) \right\} \quad (1)$$

where  $\mu_E$  is the Earth's gravitational parameter,  $R_E$  is the Earth's equatorial radius,  $R$  and  $L$  are the geocentric altitude and latitude of interest, respectively, the  $J_k$  are zonal harmonics of order zero, and the  $P_k$  are Legendre polynomials. Empirically

determined values for the Earth's first seven zonal harmonics are<sup>50,51</sup>

$$\begin{aligned} J_2 &= 1082.63 \times 10^{-6} & J_3 &= -2.54 \times 10^{-6} & J_4 &= -1.61 \times 10^{-6} \\ J_5 &= -0.15 \times 10^{-6} & J_6 &= 0.59 \times 10^{-6} & J_7 &= -0.44 \times 10^{-6} \end{aligned}$$

Since  $J_2$  is over 400 times the magnitude of any of the other coefficients, and because  $(R_E / R)^k$  becomes small as  $k$  increases, we may neglect all harmonic coefficients except  $J_2$ . After expanding the Legendre polynomial ( $P_2$ ), we may write the potential of mass  $i$  in a multimass system as

$$\phi_i = \frac{\mu_E}{R_i} \left\{ 1 - J_2 \left( \frac{R_E}{R_i} \right)^2 \left[ \frac{3}{2} (\sin^2 L_i) - \frac{1}{2} \right] \right\} \quad (2)$$

The acceleration due to gravity acting on mass  $i$  is the gradient of the potential function, and the force due to gravity,  $\underline{F}_{grav_i}$ , is then

$$\underline{F}_{grav_i} = m_i \nabla \phi_i \quad (3)$$

Aerodynamic Forces. Aerodynamic forces are calculated using the expression

$$\underline{F}_{aero} = -\frac{1}{2} \rho |V_{rel_1}| C_D A V_{rel_1} \quad (4)$$

where  $\rho$  is the atmospheric mass density,  $V_{rel_1}$ , sometimes referred to as the "cross-flow" velocity, is the component of velocity relative to the rotating atmosphere that is

perpendicular to the applicable tether segment,  $C_D$  is a drag coefficient, and  $A$  is a reference area.

Atmospheric mass density is modeled using a derived curve fit of the global and temporal average atmosphere defined by the 1986 COSPAR International Reference Atmosphere. The atmosphere model is discussed later in this Chapter.

The numerical value for the drag coefficient is determined by: (a) the shape being modeled, and (b) the flow regime the body is encountering. In this work the tether end-bodies, the "parent" and/or "sub" satellites, are modeled as spheres, and tether segments are modeled as right circular cylinders. The reference area,  $A$ , is the circular cross-sectional area for the end-bodies, and the product of length and diameter for the tether segments.

As explained by Regan<sup>52</sup>, there are at least five distinguishable flow regimes a spacecraft encounters as it "enters" an atmosphere. In order of decreasing altitude they are:

- (a) Free molecular flow
- (b) Near free molecular flow
- (c) Transition flow
- (d) Viscous merged layer flow
- (e) Continuum flow

The similarity parameter that identifies the current flow regime is the Knudsen number,  $Kn$ . The Knudsen number is defined as the ratio of the molecular mean free path,  $\lambda$ , to a characteristic body dimension,  $d$ , so that  $Kn = \lambda / d$ . A very small  $Kn$  indicates continuum flow conditions, while a very large  $Kn$  indicates free molecular flow conditions.

The molecular mean free path is the average distance a molecule travels between collisions with any other molecule. This distance is equal to the ratio of the mean molecular speed and the mean collision frequency, and may be calculated using<sup>53</sup>

$$\lambda \text{ (meters)} = \left[ \frac{R^*}{\sqrt{2} \pi \sigma^2 N_A} \right] \left( \frac{T}{P} \right) = 2.3325083 \times 10^{-5} \left( \frac{T}{P} \right) \quad (5)$$

where  $R^*$  is the universal gas constant,  $\sigma$  is the effective mean collision diameter,  $N_A$  is Avogadro's number,  $T$  is the ambient temperature in degrees Kelvin, and  $P$  is the ambient pressure in Pascals. Hence, given the temperature and pressure at an altitude of interest, the mean free path can be calculated, the Knudsen number formed, and the local flow regime identified.

In continuum flow, Newtonian impact theory can be used to derive, analytically, the drag coefficients for blunt bodies moving at hypersonic speeds.<sup>54</sup> The Newtonian theory assumes the normal momentum of the particles impacting a body's surface is completely absorbed, while the tangential component is preserved. Hence the aerodynamic loads result from "impact pressure" alone.

In the free molecular flow regime, molecules reflected or emitted from a body's surface are assumed to not collide with other molecules. As Harvey<sup>55</sup> explains, this simplifies the solution of the Boltzmann equation, which yields expressions for the normal and tangential momentum flux to an immersed body's surface. In this type of flow, the gas-surface interaction and surface temperature are the most significant parameters, and there are both pressure and shear stress contributions to the aerodynamic loads and coefficients.<sup>56</sup> For example, Koppenwallner and Legge have

shown that shear stress accounts for approximately 25% of the total drag coefficient of uncooled circular cylinders in hypersonic free molecular flow.<sup>57</sup> They also found that the drag coefficient of cooled cylinders in this type of flow is approximately 20% less than that of uncooled cylinders.<sup>58</sup>

Theoretical results which cover the flow regimes between continuum and free molecular flow do not exist.<sup>59</sup> Consequently, empirically derived bridging functions, which provide force coefficients as a function of Knudsen number, are used to link the two bounding regimes.<sup>60</sup>

Empirical  $C_D$  data obtained by Koppenwallner<sup>61</sup> and Legge<sup>62</sup> shows that uncooled spheres and cylinders experience free molecular flow conditions at Knudsen numbers above 10. Continuum flow conditions occur for cylinders at Knudsen numbers below approximately 0.01, and for spheres at Knudsen numbers below approximately 0.001. For this data, Knudsen numbers were calculated by dividing the free stream mean free path by the sphere or cylinder diameter. The cylinder drag coefficients ranged from 2.80 in free molecular flow to 1.24 in continuum flow. The sphere drag coefficients ranged from 0.92 in continuum flow to 2.70 in free molecular flow. Curve fits of Koppenwallner and Legge's data are used to model the drag coefficient variations for spheres and cylinders. The derived equations are presented in **Appendix B**. Figures 2 and 3 show the resulting altitude dependence of the drag coefficients when the  $C_D$  versus  $Kn$  models are used in conjunction with the COSPAR atmosphere model.

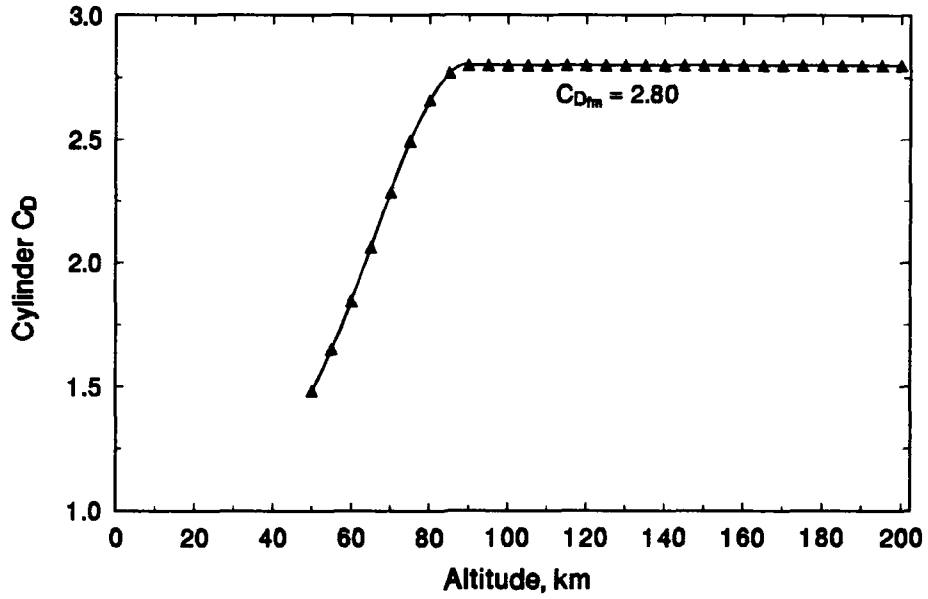


Figure 2. Altitude variation of 2 mm cylinder drag coefficient.

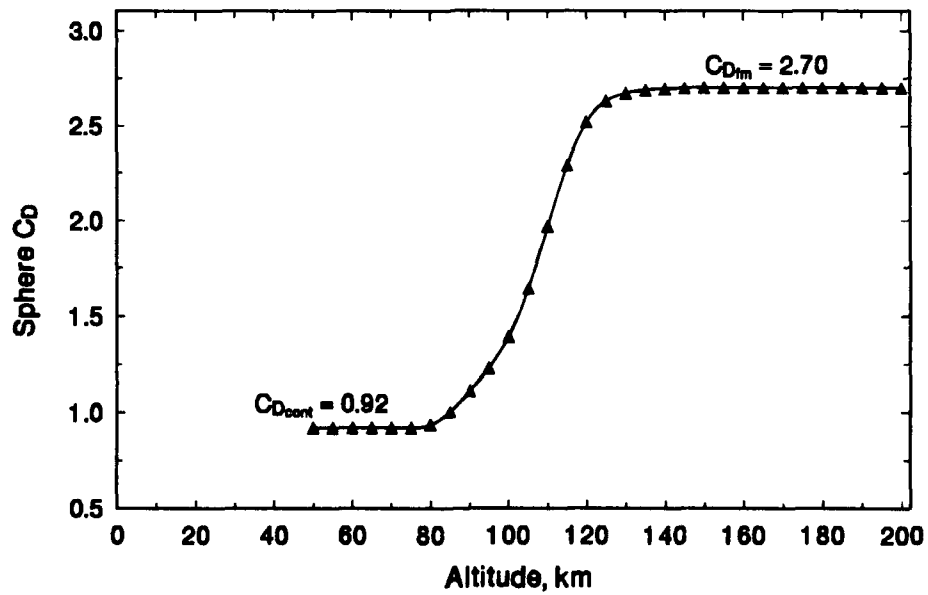


Figure 3. Altitude variation of 3 m sphere drag coefficient.

### Environment Model

Atmosphere Model. The atmosphere mass density and molecular mean free path are modeled using the 1986 COSPAR International Reference Atmosphere.<sup>63,64</sup> This is an empirical model, based on temperature and composition measurements made by a variety of satellites, and by incoherent scatter radar.<sup>65</sup> This Reference Atmosphere, published in 1990, includes algorithms for modeling atmosphere properties for any level of solar and magnetic activity, at any latitude, longitude, year, month, and time of day of interest. A global and temporal average atmosphere, assuming magnetically quiet conditions and an average solar flux, is also defined. This "grand mean" definition was used in this research project. As recommended by The Committee on Space Research, Part II of the COSPAR model is used for altitudes up to 120 km, and Part I is used for altitudes above 120 km.<sup>66</sup>

Curve fits for mass density and mean free path, as functions of altitude, were derived from the COSPAR grand mean data. The curvefit equations are presented in **Appendix A**. As shown in Figure 4, the equations for mass density are accurate to within  $\pm 2\%$  between the altitudes of 50 and 500 kilometers. As shown in **Appendix A**, the curvefit mean free path equations are accurate to within  $\pm 3\%$ .

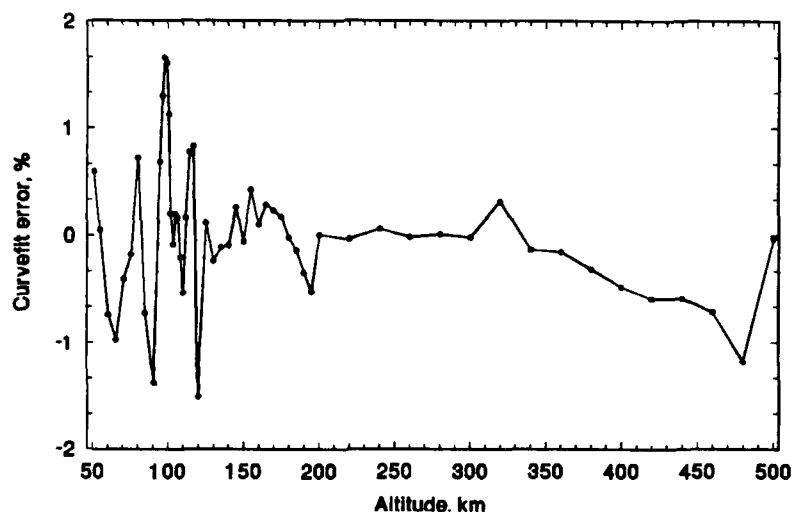


Figure 4. Atmosphere mass density curvefit error.

Altitude Calculation. The altitude of a mass of interest is calculated by determining the perpendicular distance between the mass and the Earth's surface. Because the Earth is not a perfect sphere, this calculation is not a simple matter of differencing the mass' geocentric altitude and the Earth's equatorial radius. As shown in Figure 5, the "geodetic altitude" will equal the difference in  $R_i$  and the Earth's equatorial radius only at the equator. Hence, Gersten's equation<sup>67</sup> is used to calculate the geodetic altitude,  $H$ , where

$$H = R_i - a_E + \frac{1}{2} a_E e_E^2 \sin^2 \phi \left[ (1 + \epsilon) + \sin^2 \phi \left( \frac{1}{4} e_E^2 - \epsilon \right) \right] \quad (6)$$

In this equation,  $a_E$  and  $e_E$  are the Earth's equatorial radius and eccentricity, respectively,  $R_i$  is the mass' geocentric altitude, and  $\phi$  is the mass' geocentric latitude. The

factor  $\epsilon$  is  $a_E e_E^2 / R_i$ . The numerical values for the constants are<sup>68</sup>  $a_E = 6378.137$  km, and  $e_E = 0.08181922$ .

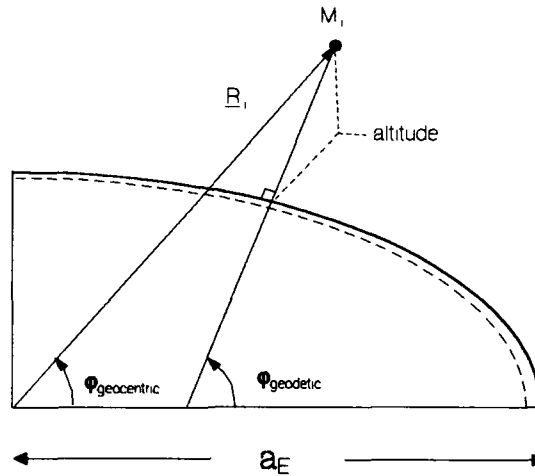


Figure 5. Altitude above an oblate Earth.

Atmosphere Rotation. Following the approach used in many models, the atmosphere is assumed to be rotating, at all altitudes, at the same rate as the solid Earth.<sup>69</sup> Hence the velocity of the atmosphere at any location is calculated from  $\underline{V}_{\text{atm}} = \underline{\omega}_E \times \underline{R}$ , where  $\underline{\omega}_E$  is the Earth's angular velocity. The combination of the altitude calculation method presented earlier, and the atmosphere rotation model described here, means the model atmosphere has the same shape as an ellipsoidal Earth, and rotates with it.

### Multibody Model

As described by Kane<sup>70</sup>, the motions of a spacecraft may be analyzed "... by considering a set of particles placed at the joints of the structure, each particle having a mass equal to one-half the sum of the masses of all truss members meeting at the

joint and the particles being connected to each other with massless springs whose stiffness reflect the elastic properties of the truss members." This is the so-called "lumped-mass" approach to modeling a dynamical system. The dynamical model developed here consists of a non-conductive, extensible, lumped-mass tether, connecting end-bodies modeled as spheres.

System Description. Using the lumped-mass technique, the mass of a tether can be represented mathematically by dividing its length into  $n$  equal length segments, and assuming the mass of each segment is halved into point masses at the segment's ends. Hence, the mass at each segment intersection, referred to here as a "bead", equals the mass of one tether segment. The end-masses,  $M_0$  and  $m_n$ , are equal to the "parent" satellite mass plus one-half of one bead mass, and the "subsattelite" mass plus one-half of one bead mass, respectively.

The mathematical description of the system's dynamics is designed to enhance, as much as possible, the accuracy of results obtained via numerical integration. As shown in Figure 6, the inertial position vector to the parent satellite ( $R_0$ ) is referenced to the origin of the Geocentric Equatorial Coordinate (GEC) system. It is represented in spherical coordinates  $(R_0, \lambda_0, \phi_0)$  to reduce the magnitude change occurring in each variable during numerical integration. The relative position vectors of the remaining masses define the position of each mass relative to its neighbors, in (Cartesian) GEC coordinates. This relative representation reduces the magnitude of the variables involved, thus reducing the effect of roundoff errors on the numerical solution. It also facilitates straightforward specification of system initial conditions.

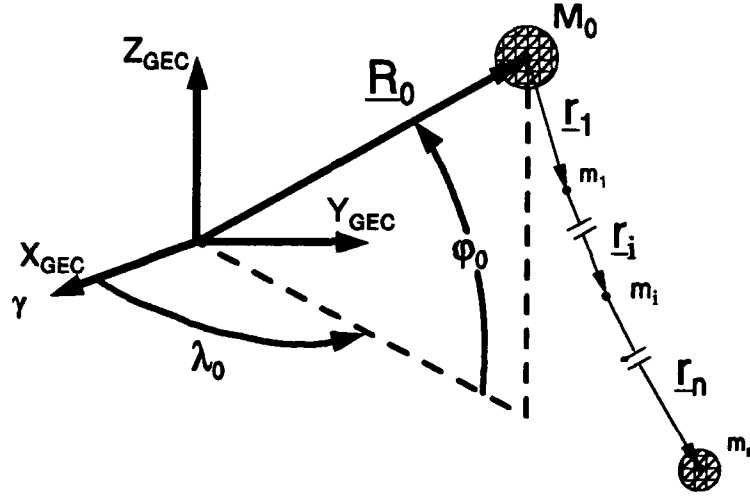


Figure 6. Tethered system lumped-mass model.

System dynamics are described by the state equation

$$\dot{\underline{X}} = F(\underline{X}) \quad (7)$$

where the state vector for the system is

$$\underline{X} = [R_0 \ \lambda_0 \ \phi_0 \ \dot{R}_0 \ \dot{\lambda}_0 \ \dot{\phi}_0 \ x_1 \ y_1 \ z_1 \ \dot{x}_1 \ \dot{y}_1 \ \dot{z}_1 \ \dots \ x_n \ y_n \ z_n \ \dot{x}_n \ \dot{y}_n \ \dot{z}_n]^T \quad (8)$$

The inertial position of the parent satellite is

$$\underline{R}_0 = [R_0 \cos(\phi_0) \cos(\lambda_0)] \hat{\underline{I}} + [R_0 \cos(\phi_0) \sin(\lambda_0)] \hat{\underline{J}} + [R_0 \sin(\phi_0)] \hat{\underline{K}} \quad (9)$$

and the parent's inertial velocity and acceleration vectors are obtained by successively differentiating this vector with respect to time, holding the unit vectors  $\hat{\underline{I}}$ ,  $\hat{\underline{J}}$ , and  $\hat{\underline{K}}$  constant. The inertial position of mass  $i$  is

$$\underline{R}_i = \underline{R}_0 + \sum_{j=1}^i \underline{r}_j \quad (10)$$

and the position of mass  $i$  relative to mass  $i-1$  is

$$\underline{r}_i = x_i \underline{\hat{I}} + y_i \underline{\hat{J}} + z_i \underline{\hat{K}} \quad (11)$$

The inertial velocity and acceleration of mass  $i$  are calculated by taking successive time derivatives of Eq. (10). Since the relative position vectors  $\underline{r}_j$  are written in the inertial frame, there are no vector cross products with which to contend in the kinematic velocity and acceleration expressions for  $\underline{R}_i$ . This is a distinct advantage over writing descriptions in a rotating frame located at some point in the system.

Equations of Motion. To numerically integrate the state equations (Eq. (7)), we require expressions for the time derivatives of the velocity components of the state vector (Eq. (8)). The acceleration of mass  $i$  relative to mass  $i-1$ , obtained by differentiating and rearranging Eq. (10), is

$$\ddot{\underline{r}}_i = \ddot{\underline{R}}_i - \ddot{\underline{R}}_0 - \sum_{j=1}^{i-1} \ddot{\underline{r}}_j \quad (12)$$

Using Newton's Second Law to substitute forces and masses for unknown accelerations, Eq. (12) becomes

$$\ddot{\underline{r}}_i = \frac{\sum \underline{F}_i}{m_i} - \frac{\sum \underline{F}_0}{m_0} - \sum_{j=1}^{i-1} \ddot{\underline{r}}_j \quad (13)$$

where  $\underline{F}_i$  and  $\underline{F}_0$  are forces acting on masses  $i$  and  $0$ , respectively. This equation describes the motion of mass  $i$  relative to mass  $i-1$ , and is used to update the state vector's relative velocity terms incrementally in time. The forces included in the summations are aerodynamic forces, forces due to gravity, and tension forces occurring in the elastic connections with neighboring beads.

Expressions for  $\ddot{R}_0$ ,  $\ddot{\lambda}_0$  and  $\ddot{\phi}_0$  are most easily derived in a rotating coordinate frame attached to  $M_\phi$ , the parent mass. As shown in Figure 7, this coordinate system is defined with mutually orthogonal unit vectors in the  $\hat{R}$ ,  $\hat{\lambda}$  and  $\hat{\phi}$  directions. The system's angular velocity,  $\underline{\omega}$ , is

$$\underline{\omega} = \dot{\lambda}_0 \underline{\hat{K}} - \dot{\phi}_0 \underline{\hat{e}}_\lambda \quad (14)$$

where

$$\underline{\hat{K}} = \sin\phi_0 \underline{\hat{e}}_R + \cos\phi_0 \underline{\hat{e}}_\phi \quad (15)$$

so that the frame's angular velocity, written in rotating coordinates, is

$$\underline{\omega} = \dot{\lambda}_0 \sin\phi_0 \underline{\hat{e}}_R - \dot{\phi}_0 \underline{\hat{e}}_\lambda + \dot{\lambda}_0 \cos\phi_0 \underline{\hat{e}}_\phi \quad (16)$$

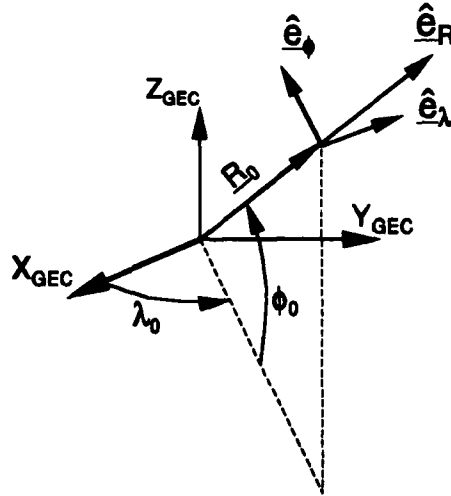


Figure 7. Rotating coordinate frame.

The time rate of change of the angular velocity is

$$\underline{\dot{\omega}} = \ddot{\lambda}_0 \hat{K} - \ddot{\phi}_0 \hat{e}_\lambda - \dot{\phi}_0 (\underline{\omega} \times \hat{e}_\lambda) \quad (17)$$

When written completely in rotating frame components, Eq. (17) becomes

$$\underline{\dot{\omega}} = (\ddot{\lambda}_0 \sin \phi_0 + \dot{\lambda}_0 \dot{\phi}_0 \cos \phi_0) \hat{e}_{-R} - \ddot{\phi}_0 \hat{e}_\lambda + (\ddot{\lambda}_0 \cos \phi_0 - \dot{\lambda}_0 \dot{\phi}_0 \sin \phi_0) \hat{e}_{-\phi} \quad (18)$$

The parent's inertial position, written in the rotating frame, is

$$\underline{R}_0 = R_0 \hat{e}_{-R} \quad (19)$$

The parent's inertial velocity is

$$\begin{aligned} \underline{\dot{R}}_0 &= \dot{R}_0 \hat{e}_{-R} + R_0 (\underline{\omega} \times \hat{e}_{-R}) \\ &= \dot{R}_0 \hat{e}_{-R} + R_0 \dot{\lambda}_0 \cos \phi_0 \hat{e}_{-\lambda} + R_0 \dot{\phi}_0 \hat{e}_{-\phi} \end{aligned} \quad (20)$$

and its inertial acceleration is

$$\underline{\ddot{R}}_0 = \ddot{R}_0 \hat{e}_{-R} + 2 \dot{R}_0 (\underline{\omega} \times \hat{e}_{-R}) + R_0 (\underline{\dot{\omega}} \times \hat{e}_{-R} + \underline{\omega} \times (\underline{\omega} \times \hat{e}_{-R})) \quad (21)$$

After expanding the vector products and grouping like terms, Eq. (21) becomes

$$\begin{aligned} \underline{\ddot{R}}_0 &= (\ddot{R}_0 - R_0 \dot{\lambda}_0^2 \cos^2 \phi_0 - R_0 \dot{\phi}_0^2) \hat{e}_{-R} \\ &+ (2 \dot{R}_0 \dot{\lambda}_0 \cos \phi_0 - 2 R_0 \dot{\lambda}_0 \dot{\phi}_0 \sin \phi_0 + R_0 \ddot{\lambda}_0 \cos \phi_0) \hat{e}_{-\lambda} \\ &+ (2 \dot{R}_0 \dot{\phi}_0 + R_0 \ddot{\phi}_0 + R_0 \dot{\lambda}_0^2 \sin \phi_0 \cos \phi_0) \hat{e}_{-\phi} \end{aligned} \quad (22)$$

This is the parent's inertial acceleration, expressed in the rotating coordinate system.

Using Newton's Second Law, we may relate this expression to the sum of the forces acting on  $M_\phi$ , so that

$$\ddot{\underline{R}}_0 = \frac{\sum \underline{F}_0}{M_0} \quad (23)$$

The forces included in the summation are the aerodynamic forces acting on the parent satellite and one-half of the immediately adjacent tether segment, the force due to gravity acting on mass  $M_0$ , and the tension force occurring in the elastic connection with the first bead. Using Eqs. (22) and (23), we may now solve explicitly for the desired derivatives:

$$\ddot{R}_0 = \frac{F_{0R}}{M_0} + R_0 \dot{\lambda}_0^2 \cos^2 \phi_0 + R_0 \dot{\phi}_0^2 \quad (24)$$

$$\ddot{\lambda}_0 = \frac{F_{0\lambda}}{M_0 R_0 \cos \phi_0} - 2 \frac{\dot{R}_0 \dot{\lambda}_0}{R_0} + 2 \dot{\lambda}_0 \dot{\phi}_0 \tan \phi_0 \quad (25)$$

$$\ddot{\phi}_0 = \frac{F_{0\phi}}{R_0 M_0} - \dot{\lambda}_0^2 \sin \phi_0 \cos \phi_0 - 2 \frac{\dot{R}_0 \dot{\phi}_0}{R_0} \quad (26)$$

In these equations, the subscripts on  $F_0$  indicate the applicable force vector component.

Aerodynamic Forces. Aerodynamic forces are calculated as described earlier.

Forces applied to the end-masses are the resultants of both the drag of the end-body and the drag on one-half of the immediately adjacent tether segment. Forces applied to the tether beads are the resultants of drag forces acting on the tether  $\frac{1}{2}$  segments immediately "above" and "below" the bead. As shown in Figure 8, the aerodynamic

forces will have components along both the drag and lift directions (ie., parallel and perpendicular to  $\underline{V}_{rel}$ ) for any tether segment that is not perpendicular to  $\underline{V}_{rel}$ .

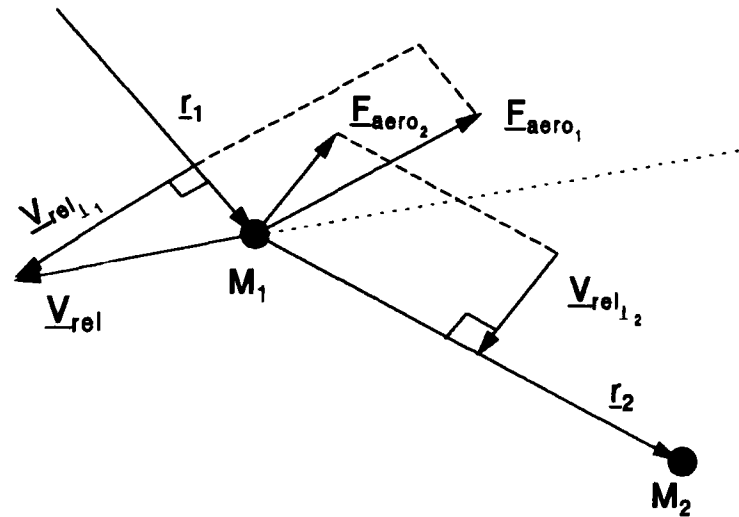


Figure 8. Aerodynamic forces geometry.

The reference cross-sectional area for each segment (length x diameter) will vary as it's length changes, due to elasticity effects. Poisson's ratio,  $\nu$ , is the ratio of the strain in the lateral direction to the strain in the axial direction.<sup>71</sup> Using this material property, the reduced diameter,  $d$ , of a stretched segment is calculated from

$$d = \frac{\nu d_0 (l_0 - l)}{l_0} + d_0 \quad (27)$$

where  $d_0$  is the unstrained (original) segment diameter, and  $l_0$  and  $l$  are the original and stretched segment lengths, respectively. The diameter is assumed to be equal to it's original value for segments that are equal to or less than their unstretched lengths.

**Tension Forces.** Tension forces are calculated by modeling each tether segment as a massless, linearly elastic spring. The equivalent spring constant,  $k_{eq}$ , for the entire tether length is

$$k_{eq} = \frac{EA}{L} = \frac{E\pi d^2}{4L} \quad (28)$$

where  $E$  is the tether modulus of elasticity,  $A$  is the (circular) tether cross-sectional area,  $d$  is the tether diameter, and  $L$  is the total tether length. The equivalent spring constant for each tether segment is  $nk_{eq}$ , where  $n$  is the total number of tether segments being modeled. The total tension force acting on mass  $i$  is determined by the elongation of the springs connecting the mass to its neighbors. The springs are assumed to exert forces in tension, but not in compression. The tension force on mass  $i$  is calculated from

$$\underline{F}_{tens_i} = nk_{eq} \cdot \left[ (stretch_{i+1}) \hat{r}_{i+1} - (stretch_i) \hat{r}_i \right] \quad (29)$$

where  $\hat{r}_{i+1}$  is a unit vector from mass  $i$  to mass  $i+1$ , and  $\hat{r}_i$  is a unit vector from mass  $i-1$  to mass  $i$ . The scalar "stretch" terms are the elongations of the corresponding tether segments. These terms are always greater than or equal to zero. If the current distance between mass  $i$  and one of its neighbors is less than the original segment length, the stretch term is set equal to zero, and there is no spring force applied along that connection.

**Numerical Integration.** The state equations are numerically integrated using a Runge-Kutta-Gil fourth-order method.<sup>72</sup> Eqs. (13), (24), (25) and (26) provide the means by

which to calculate the time derivatives of the state vector's velocity terms at each integration time step. Calculations at each time step begin with the parent mass and proceed sequentially to mass  $n$ , the subsatellite.

### **Orbital Element Propagation Model**

The model described in the previous section involves direct numerical integration of the equations of motion, including all perturbing forces of interest. In the vernacular of perturbation techniques, it is classified as a "special" perturbation technique, and is sometimes referred to as Cowell's Method.<sup>73</sup>

Unfortunately, the method's simplicity is somewhat offset by the time required to simulate a tethered system's orbital decay. A similar, but more efficient technique, which is often used for single-mass satellite orbit simulations, is the "variation of parameters" method. John Bernoulli first used this method in 1697 to solve a linear, first-order, non-homogenous differential equation with non-constant coefficients.<sup>74</sup> Leonhard Euler received prizes from the French Academy in 1748 and 1752 for his use of the method to study the perturbations of Jupiter and Saturn, and J. L. Lagrange made further advances on the subject in 1766.<sup>75</sup> In 1782, Lagrange, for the first time, completely developed the method in a memoir on the perturbations of comets moving in elliptical orbits.<sup>76</sup> As a result, orbital element variational equations derived using this method are usually referred to as "Lagrange's Planetary Equations".

The objective of the method is to describe how a selected set of orbital elements varies with time due to perturbations - non-two body forces acting on the

system. This is done by deriving analytical expressions for the time rates of change of the elements in terms of the perturbations of interest. The expressions are then numerically integrated to find the values of the elements at future times.

In this section, we will summarize the derivation of Lagrange's Planetary Equations, discuss the derivation of, and present, a set of non-singular propagation equations, and, finally, describe the unique perturbations used in the equations to propagate the orbital elements of a tethered system's center of mass. Many of the equations presented are available in various published documents, and are included here only for completeness. However, the application of these techniques to a tethered system's orbital evolution is unique to this work.

Lagrange's Planetary Equations. <sup>77,78</sup> The orbital equation of motion for a perturbed small satellite moving under the influence of a more massive central body is

$$\frac{d^2 \underline{r}}{dt^2} + \frac{\mu}{r^3} \underline{r} = \left[ \frac{\partial R}{\partial \underline{r}} \right]^T \quad (30)$$

where  $\underline{r}$  is the satellite's position relative to the central body,  $\mu$  is the body's gravitational parameter ( $GM$ ), and  $R$  is a potential or "disturbing" function. This formulation requires that the perturbing forces be conservative, neither adding energy nor deleting it from the system, which is an obvious limitation. Although Lagrange derived the variational equations with this restriction, the problem was revisited by Gauss in 1814. He modified the equations to account for an arbitrary perturbing force. In this case, the equation of motion is

$$\frac{d^2 \underline{r}}{dt^2} + \frac{\mu}{r^3} \underline{r} = \underline{a}_d \quad (31)$$

where  $\underline{a}_d$  is the disturbing acceleration. This second-order equation may be written as a system of two first-order equations, with

$$\frac{d\underline{r}}{dt} = \underline{V} \quad \text{and} \quad \frac{d\underline{V}}{dt} + \frac{\mu}{r^3} \underline{r} = \underline{a}_d \quad (32)$$

where  $\underline{V}$  is the satellite's velocity relative to the central body. If there were no disturbing acceleration, the solution to these equations would be

$$\underline{r} = \underline{r}(\underline{\alpha}, t) \quad \text{and} \quad \underline{V} = \frac{d\underline{r}}{dt} = \frac{\partial \underline{r}(\underline{\alpha}, t)}{\partial t} \quad (33)$$

where  $\underline{\alpha}$  is a six-dimensional vector containing the (constant) orbital elements. This is the Keplerian, two-body situation.

The objective of Lagrange's derivation is to reformulate Eqs. (32) into equations for  $\frac{d\underline{\alpha}}{dt}$  while maintaining the form and meaning of Eqs. (33). In so doing, we will be able to compute the instantaneous position and velocity of the perturbed satellite using the well-known Keplerian formulae.

In perturbed motion  $\underline{\alpha}$  is not constant, and the total time derivative of  $\underline{r}$  is

$$\frac{d\underline{r}}{dt} = \frac{\partial \underline{r}(\underline{\alpha}, t)}{\partial t} + \frac{\partial \underline{r}(\underline{\alpha}, t)}{\partial \underline{\alpha}} \frac{d\underline{\alpha}}{dt} \quad (34)$$

Comparing this equation to the second of Eqs. (33), we see that we must require

$$\frac{\partial \underline{r}}{\partial \underline{\alpha}} \frac{d\underline{\alpha}}{dt} = 0 \quad (35)$$

Imposing this "condition of osculation" and differentiating once more, we obtain

$$\frac{d^2 \underline{r}}{dt^2} = \frac{d\underline{V}}{dt} = \frac{\partial \underline{V}}{\partial t} + \frac{\partial \underline{V}}{\partial \underline{\alpha}} \frac{d\underline{\alpha}}{dt} \quad (36)$$

Substituting this expression into the equation of motion yields

$$\frac{\partial^2 \underline{r}}{\partial t^2} + \frac{\mu}{r^3} \underline{r} + \frac{\partial \underline{V}}{\partial \underline{\alpha}} \frac{d\underline{\alpha}}{dt} = \underline{a}_d \quad (37)$$

and we note that, by design,

$$\frac{\partial^2 \underline{r}}{\partial t^2} + \frac{\mu}{r^3} \underline{r} = 0 \quad (38)$$

Hence, we must also require

$$\frac{\partial \underline{V}}{\partial \underline{\alpha}} \frac{d\underline{\alpha}}{dt} = \underline{a}_d \quad (39)$$

Eqs. (35) and (39) are the six scalar differential equations we seek. They are equivalent to the original equation of motion, and must be satisfied by the vector of perturbed orbital elements,  $\underline{\alpha}(t)$ . The equations may now be combined into a more compact form.

The 6x6 skew-symmetric Lagrange matrix,  $\underline{L}$ , is formed by

$$\underline{L} = \begin{bmatrix} \underline{\partial \underline{r}} \\ \underline{\partial \underline{\alpha}} \end{bmatrix}^T \frac{\partial \underline{V}}{\partial \underline{\alpha}} - \begin{bmatrix} \underline{\partial \underline{V}} \\ \underline{\partial \underline{\alpha}} \end{bmatrix}^T \frac{\partial \underline{r}}{\partial \underline{\alpha}} \quad (40)$$

and the matrix equation combining Eqs. (35) and (39) is

$$\underline{L} \frac{d\underline{\alpha}}{dt} = \begin{bmatrix} \underline{\partial \underline{r}} \\ \underline{\partial \underline{\alpha}} \end{bmatrix}^T \underline{a}_d \quad (41)$$

The elements of  $\underline{\underline{L}}$ , called the "Lagrangian brackets", are calculated from

$$[L_i, L_j] = \frac{\partial r}{\partial \alpha_i} \cdot \frac{\partial V}{\partial \alpha_j} - \frac{\partial r}{\partial \alpha_j} \cdot \frac{\partial V}{\partial \alpha_i} \quad (42)$$

where the  $i, j$  bracket is the matrix element in row  $i$ , column  $j$ . Because of the skew-symmetry of  $\underline{\underline{L}}$ , there are only 15 distinct brackets to evaluate. Only six of these are non-zero. After the brackets are evaluated, and the right hand side of Eq. (41) is expanded, the elements of the vector  $\frac{d\alpha}{dt}$  can be determined by algebraic elimination.

Lagrange's Planetary Equations, in Gauss' form, are listed below. The disturbing acceleration must be expressed in an osculating coordinate system. This dextral, orthogonal, Cartesian system has unit vectors in the radial, transverse, and (orbit) normal directions. The unit vector  $\hat{e}_r$  points in the direction of the satellite from the central body's center,  $\hat{e}_n$  is perpendicular to the orbit plane, and  $\hat{e}_t$  lies in the orbit plane, completing the unit vector triad, making an angle less than  $90^\circ$  with the satellite's velocity vector. The orbital elements used here are a classical set:  $a$ , the semi-major axis,  $e$ , the eccentricity,  $i$ , the inclination,  $\Omega$ , the longitude of the ascending node,  $\omega$ , the argument of perigee, and  $\nu$ , the true anomaly. In these equations, the subscripts on  $a_d$  indicate the applicable component of the disturbing acceleration. These terms should not be confused with  $a$ , the symbol for the length of the semi-major axis. The "orbit parameter" ( $a(1-e^2)$ ) is  $P$ ,  $h$  is the satellite's specific (orbital) angular momentum, and  $U$  is the argument of latitude, which is defined as the sum of the argument of perigee and the true anomaly.

$$\frac{da}{dt} = \frac{2a^2}{h} \left( e \sin \nu a_{d_r} + \frac{p}{r} a_{d_U} \right) \quad (43)$$

$$\frac{de}{dt} = \frac{1}{h} \left\{ p \sin \nu a_{d_r} + [(p + r) \cos \nu + r e] a_{d_U} \right\} \quad (44)$$

$$\frac{di}{dt} = \frac{r \cos U}{h} a_{d_U} \quad (45)$$

$$\frac{d\Omega}{dt} = \frac{r \sin U}{h \sin i} a_{d_h} \quad (46)$$

$$\frac{d\omega}{dt} = \frac{1}{eh} \left[ -p \cos \nu a_{d_r} + (p + r) \sin \nu a_{d_U} \right] - \frac{r \sin U \cos i}{h \sin i} a_{d_h} \quad (47)$$

$$\frac{d\nu}{dt} = \frac{h}{r^2} + \frac{1}{eh} \left[ p \cos \nu a_{d_r} - (p + r) \sin \nu a_{d_U} \right] \quad (48)$$

Equinoctial Elements and Non-Singular Propagation Equations. Unfortunately, Eqs. (46) - (48), which model the time rates of change of  $\Omega$ ,  $\omega$ , and  $\nu$ , contain terms including  $e$  and/or  $\sin i$  in their denominators. Consequently, singularities occur when  $i$  and/or  $e$  are zero, and the calculated rates of change of  $\Omega$ ,  $\omega$ , and  $\nu$  for orbits of low inclination and/or small eccentricity will be large despite the fact that the disturbing accelerations may be small.

To avoid this problem, the classical elements may be combined in a way that eliminates the singularities. As shown by Battin,<sup>79</sup> a more reliable set of propagation equations results if five new elements are defined:

$$\begin{aligned}
 P_1 &\doteq e \sin \bar{\omega} & P_2 &\doteq e \cos \bar{\omega} \\
 Q_1 &\doteq \tan \frac{i}{2} \sin \Omega & Q_2 &\doteq \tan \frac{i}{2} \cos \Omega \\
 l &\doteq \bar{\omega} + M
 \end{aligned}$$

In this new set of elements,  $\bar{\omega}$ , the longitude of perigee, is  $\Omega + \omega$ ;  $M$  is the mean anomaly; and  $l$  is the mean longitude. The semi-major axis,  $a$ , is the sixth element in the set. These elements are non-singular for all orbits except those with  $i = 180^\circ$ .

Using the mean longitude to update the satellite's position requires that Kepler's equation be solved after each time step. This requirement can be eliminated by propagating the value for the true longitude,  $L \doteq \bar{\omega} + \nu$ , rather than  $l$ , the mean longitude. Combining the expressions for  $\frac{d\Omega}{dt}$ ,  $\frac{d\omega}{dt}$ , and  $\frac{d\nu}{dt}$ , we obtain

$$\frac{dL}{dt} = \frac{h}{r^2} + \frac{r}{h} \sin U \tan \frac{i}{2} a_{d_h} \quad (49)$$

Substituting equinoctial elements, this expression is

$$\frac{dL}{dt} = \frac{\mu^2 (1 + P_1 \sin L + P_2 \cos L)^2}{h^3} + \frac{h}{\mu} \frac{Q_2 \sin L - Q_1 \cos L}{1 + P_1 \sin L + P_2 \cos L} a_{d_h} \quad (50)$$

The remaining propagation equations are

$$\frac{da}{dt} = \frac{2a^2}{h} \left[ (P_2 \sin L - P_1 \cos L) a_{d_r} + \frac{p}{r} a_{d_U} \right] \quad (51)$$

$$\frac{dP_1}{dt} = \frac{r}{h} \left\{ -\frac{p}{r} \cos L a_{d_r} + \left[ P_1 + \left( 1 + \frac{p}{r} \right) \sin L \right] a_{d_v} - P_2 (Q_1 \cos L - Q_2 \sin L) a_{d_h} \right\} \quad (52)$$

$$\frac{dP_2}{dt} = \frac{r}{h} \left\{ \frac{p}{r} \sin L a_{d_r} + \left[ P_2 + \left( 1 + \frac{p}{r} \right) \cos L \right] a_{d_v} + P_1 (Q_1 \cos L - Q_2 \sin L) a_{d_h} \right\} \quad (53)$$

$$\frac{dQ_1}{dt} = \frac{r}{2h} (1 + Q_1^2 + Q_2^2) \sin L a_{d_h} \quad (54)$$

$$\frac{dQ_2}{dt} = \frac{r}{2h} (1 + Q_1^2 + Q_2^2) \cos L a_{d_h} \quad (55)$$

where

$$h = nab, \quad b = a \sqrt{1 - P_1^2 - P_2^2}, \quad n = \sqrt{\frac{\mu}{a^3}}$$

$$p = \frac{h^2}{\mu}, \quad r = \frac{p}{1 + P_1 \sin L + P_2 \cos L}$$

**Disturbing Acceleration.** The propagation equations listed above are used to update the orbital elements of the tethered system's center of mass. Perturbations of the motion arise from three sources:

- (a) Aerodynamic forces on the tether and end-bodies
- (b) Gravitational forces due to Earth oblateness
- (c) Gravitational forces due to the physical distribution of the system's mass.

Thus, the perturbing force,  $\underline{F}_p$ , may be calculated by differencing the "actual" aerodynamic and gravitational forces acting on each mass in the lumped-mass system

with the two-body gravitational force that would result if all the system's mass was actually concentrated at the center of mass location. In Eq. (56),  $\underline{F}_{grav_i}$  and  $\underline{F}_{aero_i}$  are the gravitational and aerodynamic forces acting on mass  $i$ . They are calculated as described in the **Multibody Model** section of this Chapter.

$$\underline{F}_p = \sum_{i=0}^n \left( \underline{F}_{grav_i} + \underline{F}_{aero_i} \right) - \underline{F}_{grav_{cm}} \quad (56)$$

The two-body gravitational force acting on the system center of mass,  $\underline{F}_{grav_{cm}}$ , is calculated from

$$\underline{F}_{grav_{cm}} = M_{tot} \nabla \phi_{cm} \quad (57)$$

where

$$\phi_{cm} = \frac{\mu_E}{R_{cm}} \quad \text{and} \quad M_{tot} = \sum_{i=0}^n M_i \quad (58)$$

Finally, the disturbing acceleration,  $\underline{a}_d$ , is determined by dividing  $\underline{F}_p$  by the total system mass,  $M_{tot}$ .

It is important to note that only the orbital elements for the system's center of mass are propagated forward in time. Hence, this approach will not yield current position and velocity information for all system constituents, which makes calculation of the "actual" aerodynamic and gravitational forces impossible. As discussed in the **Introduction**, we are interested in studying the orbital evolution of tethered systems released when they are aligned along the local vertical, and orbiting as a rigid rod. In an earlier study, Bergamaschi and Morana<sup>80</sup> found that the in-plane libration angle (i.e., the angle between a straight line approximation for the tether and the local

vertical) of a freely-decaying tether remained very small after it was released from these initial conditions. Hence, for this part of the analysis, we will assume the tether is inextensible and remains aligned along the local vertical during its entire lifetime.

Assuming the tether is inextensible means the position of each mass in the system, relative to the system center of mass, is known for all time. Hence the inertial position of mass  $i$  is

$$\underline{R}_i = \underline{R}_{cm} + \underline{r}_{rel_i}, \quad 0 \leq i \leq n \quad (59)$$

where  $\underline{R}_{cm}$  is the inertial position of the system's center of mass, and  $\underline{r}_{rel_i}$  is the position of mass  $i$  relative to the system's center of mass. The inertial velocity of mass  $i$  is calculated from

$$\dot{\underline{R}}_i = \dot{\underline{R}}_{cm} + \dot{\underline{r}}_{rel_i}, \quad 0 \leq i \leq n \quad (60)$$

where

$$\dot{\underline{r}}_{rel_i} = \underline{\omega} \times \underline{r}_{rel_i}, \quad 0 \leq i \leq n \quad (61)$$

In Eq. (61), the fact that the system is assumed to orbit as a rigid rod is exploited. In this situation there is no relative velocity between any of the masses and the system's center of mass. Hence the "apparent" inertial relative velocity is due only to the inertial motion of a reference frame attached to the system. Correspondingly,  $\underline{\omega}$  is the rotation rate of an osculating coordinate system located at the system's center of mass.

Element Propagation and Coordinate Transformation. An Euler numerical integration technique is used to update the orbital elements, as shown in Eq. (62), where  $\chi$  represents any one of the equinoctial elements.

$$\chi(t + \delta t) = \chi(t) + \left( \frac{d\chi}{dt} \right) \delta t \quad (62)$$

Figure 9 shows the physical relationship between the equinoctial ( $\hat{f}$ ,  $\hat{g}$ ,  $\hat{w}$ ), osculating ( $\hat{e}_r$ ,  $\hat{e}_u$ ,  $\hat{e}_h$ ) and GEC ( $X_{GEC}$ ,  $Y_{GEC}$ ,  $Z_{GEC}$ ) coordinate systems. The fundamental plane of the equinoctial coordinate system coincides with the orbit plane.

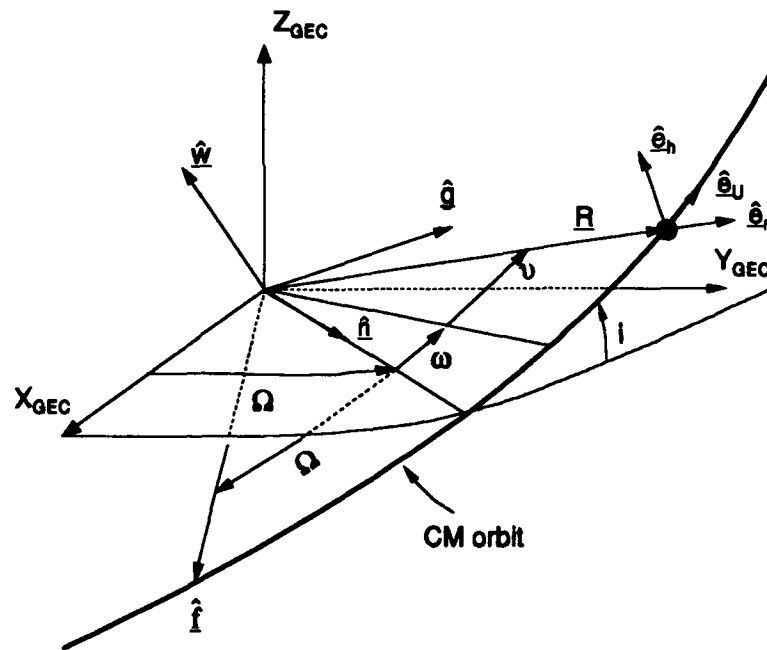


Figure 9. Equinoctial, Osculating, and GEC coordinate systems.

Consequently, the position of the center of mass can be written as

$$\underline{R}_{CM} = (r \cos L) \hat{\underline{l}} + (r \sin L) \hat{\underline{g}} \quad (63)$$

where  $r$  is calculated using the current equinoctial elements, as shown on page 43 (following Eq. (55)). The inertial velocity of the center of mass is

$$\underline{\dot{R}}_{CM} = (\dot{r} \cos L - r L \dot{L} \sin L) \hat{\underline{l}} + (\dot{r} \sin L + r L \dot{L} \cos L) \hat{\underline{g}} \quad (64)$$

After substituting equinoctial element expressions for  $rL$ ,  $\dot{r}$ , and  $\dot{L}$ , we have<sup>81</sup>

$$\underline{\dot{R}}_{CM} = \frac{h}{p} [(-P_1 - \sin L) \hat{\underline{l}} + (P_2 + \cos L) \hat{\underline{g}}] \quad (65)$$

The center of mass' inertial position and velocity vectors may be expressed in GEC coordinates by performing the following transformations:

- (a) a positive rotation about  $\hat{\underline{w}}$  through the angle  $\Omega$ ,
- (b) a negative rotation about  $\underline{n}$  (ascending node vector) through the inclination angle,  $i$ , and
- (c) a negative rotation about  $\hat{\underline{K}}$  ( $Z_{GEC}$ ) through the angle  $\Omega$ .

Hence, any vector expressed in equinoctial coordinates may be transformed into GEC coordinates with the operation

$$\underline{B}_{GEC} = \begin{bmatrix} \cos \Omega & -\sin \Omega & 0 \\ \sin \Omega & \cos \Omega & 0 \\ 0 & 0 & 1 \end{bmatrix} \begin{bmatrix} 1 & 0 & 0 \\ 0 & \cos i & -\sin i \\ 0 & \sin i & \cos i \end{bmatrix} \begin{bmatrix} \cos \Omega & \sin \Omega & 0 \\ -\sin \Omega & \cos \Omega & 0 \\ 0 & 0 & 1 \end{bmatrix} \underline{B}_{fgw} \quad (66)$$

Combining the rotation matrices and writing the result in terms of equinoctial elements yields<sup>82</sup>

$$\frac{B}{GEC} = \frac{1}{1+Q_1^2+Q_2^2} \begin{bmatrix} 1-Q_1^2+Q_2^2 & 2Q_1Q_2 & 2Q_1 \\ 2Q_1Q_2 & 1+Q_1^2-Q_2^2 & -2Q_2 \\ -2Q_1 & 2Q_2 & 1-Q_1^2-Q_2^2 \end{bmatrix} \frac{B}{fgw} \quad (67)$$

## **ARTIFICIAL NEURAL NETWORKS**

As discussed in the **Introduction**, artificial neural networks (ANNs) are used in this research project to represent the mapping between several independent variables and the orbital lifetimes of tethered systems. After an overview and introduction to feed-forward network concepts and architecture, we will describe the "standard" error backpropagation training algorithm, derive a training algorithm specifically designed to train feed-forward networks to represent widely-spread real-valued data, demonstrate the new algorithm's performance, and describe and test a hybrid training approach.

### **Overview and Introduction**

Basic Concepts. Artificial neural networks are not programmed; rather, they "learn" by example. During supervised learning, or "training", a network is presented with a series of input vectors together with corresponding desired output vectors. In response to differences between the network's output(s) and the desired output(s), the network adjusts the values of its internal parameters. Training continues until the network produces the correct output(s) for each input vector in the training set. This process mirrors an important task of the central nervous system: the ability to learn reactions and useful behaviors that permit survival in an often hostile environment.

Networks that provide an optimal reaction or answer to an external stimulus are sometimes referred to as "cybernetic" networks.<sup>83</sup>

The most-studied and popular class of cybernetic networks are the so-called "feed-forward, layered" neural networks. In these networks, information flows along a series of one-way connections between several distinct layers of neurons. At one end is the input layer, which receives external "stimuli", and at the other end is an output layer, which produces, or causes, a desired "reaction". There may be one or more layers of neurons between the input and output layers. These are called "hidden" layers, because they have no direct interface with the "outside world". Rather, they receive inputs from the preceding layer and pass their outputs to the following layer. Figure 10 shows, schematically, the flow of information from inputs to outputs in a network with a single hidden layer. Note that there are no connections between neurons in the same layer, and each layer receives inputs only from the preceding layer.

Each neuron in a network applies a "transfer function" to its input, yielding a result that is passed to each neuron in the following layer. Each connection between neurons has an associated "weight", and each neuron in the hidden and output layers has an associated "bias". These variables are adjusted during the training process, in a manner designed to minimize the error between the desired and actual output value(s). In the following sections, we define a standard terminology, discuss the transfer functions used in this research project, and present a detailed description of

the network structure used in modeling the relationship between the various independent variables and the orbital lifetime of tethered systems.

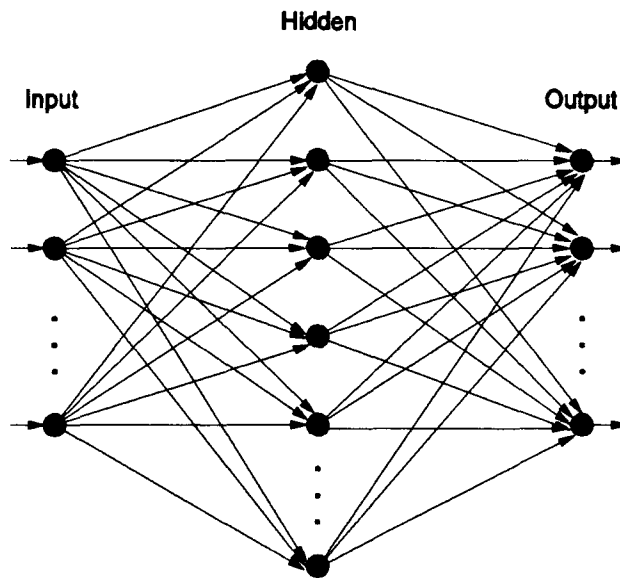


Figure 10. Feed-forward network architecture.

**Terminology.** In this work, input, to any neuron in a network, will be represented by  $X_\alpha$ , where  $\alpha$  is the neuron's "number" in its layer - 1,2,3,4, etc. Output from the neuron is denoted by  $Y_\alpha$ . The weight on a connection between neurons is denoted by  $W_{\beta\alpha}$ , where  $\beta$  is the number of the "transmitting" neuron in the preceding layer, and  $\alpha$  is the number of the "receiving" neuron. The bias on hidden and output neurons is denoted by  $v_\alpha$ , where, as before,  $\alpha$  indicates the neuron's number in its layer. The transfer function applied by a neuron to its input is represented by  $G(X_\alpha)$ .

When writing mathematical formulae describing a network's operation, we use the subscript "i" to refer to the input layer, the subscript "j" to reference the hidden

layer, and the subscript "k" to denote the output layer. (If more than one hidden layer is involved we will use numerical subscripts on "j" to indicate the layer's number.)

Hence, for example, the values of the input vector are  $X_i$ , the outputs from the input layer are  $Y_i$ , the inputs to the (first) hidden layer are  $X_j$ , and the hidden layer's outputs are  $Y_j$ .

Transfer Functions. As shown in Figure 11, each neuron in a hidden layer sums the weighted inputs arriving from neurons in the preceding layer, subtracts a bias value, applies a transfer function to the result, and passes the final result, along weighted connections, to each neuron in the next layer. Neurons in the input layer merely apply a transfer function to a single (external) input, and send the result along weighted connections to the first hidden layer. Neurons in the output layer operate as shown in Figure 11, but provide only a single result,  $Y_k$ , to the "outside world".

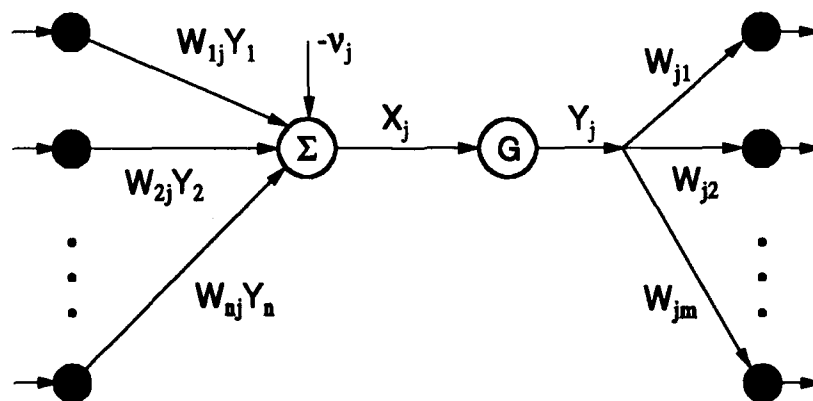


Figure 11. Hidden layer neuron operation.

The transfer function may perform any desired mathematical operation on a neuron's input. Possible candidates include linear, linear-threshold, sigmoid, trigonometric, and even Gaussian functions. The fundamental requirement for employing the error backpropagation training algorithm is that the function and its derivative be monotonic and continuous. Because there are certain mappings which are not "linear separable", preference is usually given to using nonlinear transfer functions. The most commonly used function is the sigmoidal "logistic function",

$$Y = \frac{1}{1 + e^{-x}} \quad (68)$$

This function is one in which the output varies smoothly with the input. The function's derivative is also smooth and continuous. The derivative is

$$\frac{dY}{dX} = \frac{e^{-x}}{(1 + e^{-x})^2} = \left( \frac{1}{1 + e^{-x}} \right) \left( \frac{e^{-x}}{1 + e^{-x}} \right) = Y(1 - Y) \quad (69)$$

Figure 12 shows that the function's output varies in magnitude between zero and one, the so-called "saturation levels". The function's slope is largest when  $X$  is between  $-1$  and  $1$ .

Applying a weight,  $W$ , to the function's result has the effect shown in Figure 13. A positive weight, greater than unity, "stretches" the function along the  $Y$  axis, increasing its slope and maximum magnitude. A positive weight, less than unity, compresses the function along  $Y$ , reducing its slope and maximum magnitude. Negative weights produce the mirror image of these results about the  $X$  axis. The

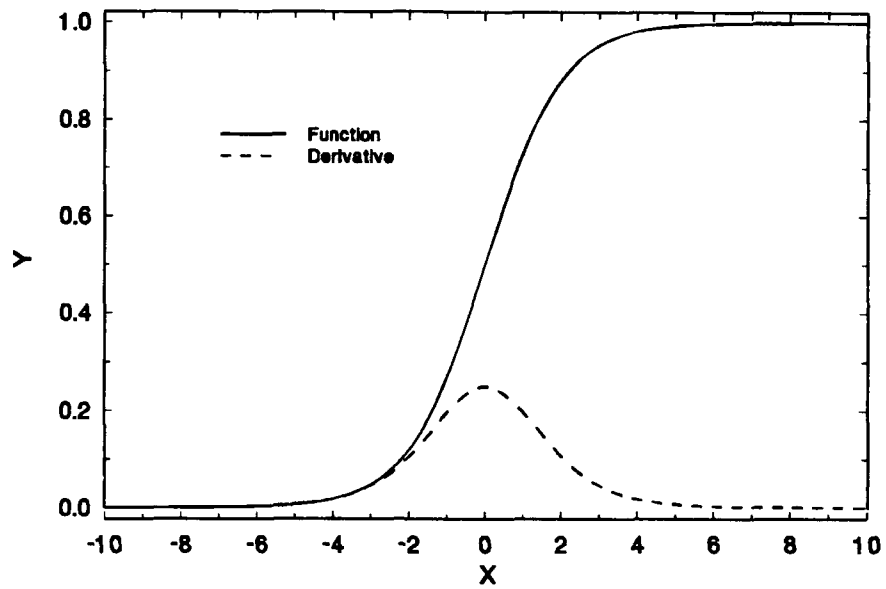


Figure 12. Logistic function and its derivative.

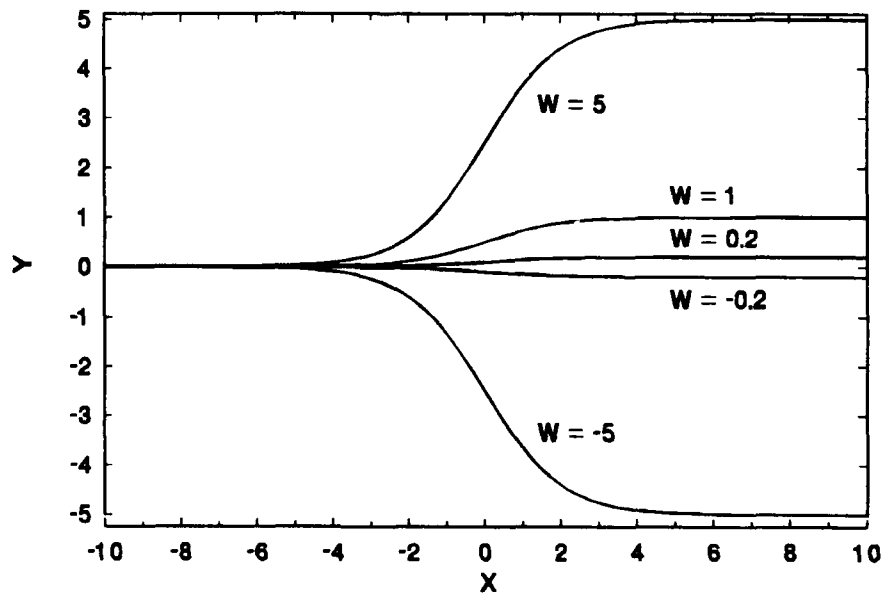


Figure 13. The effect of multiplicative weights on the logistic function.

characteristics illustrated in Figure 13 demonstrate the effect of modifying a neuron's output with a multiplicative weight. Hence, we see that by adjusting the connection weights, during training, a network can control the saturation levels and response characteristics of its many neurons.

As shown in Figure 14, subtracting a bias,  $v$ , from the sigmoid's argument translates the result along the  $X$  axis, without altering the function's slope or magnitude. Positive biases shift the result to the left, and negative biases shift it to the right. We observe that the bias actually serves as somewhat of a "threshold" value, determining the "activation level" at which a neuron's output will begin to transition from zero to the upper saturation level.

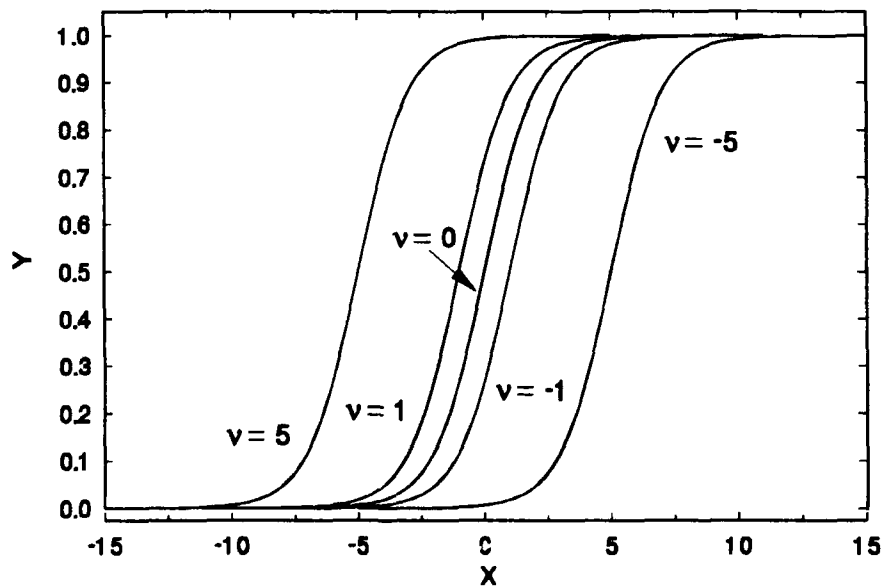


Figure 14. The effect of a subtracted bias on the logistic function.

For a neuron in a hidden or output layer, the sum of the weighted inputs from the preceding layer will be modified by subtracting a bias. The magnitudes of the summation and bias will then determine the output from a sigmoidal (logistic) neuron. A summation result much larger, or, much smaller, than the bias value will yield an output value of one or zero, depending on the signs of the summation and bias, while a summation result nearly equal to the bias value will yield an output between the saturation values. We therefore observe that by learning to employ various bias values, a network can control which neurons are "active", and which are "saturated", at various locations in a data set.

A linear transfer function,  $Y_{\alpha} = X_{\alpha}$ , is also sometimes used for neurons in the input and/or output layers. Applying a weight to this function changes the slope of the resulting line, and subtracting a bias from the function's argument translates the line along the X axis.

Selected Network Structure. Recently, Cybenko<sup>84</sup> showed that finite linear combinations of a single sigmoidal function, such as the logistic function described earlier, can approximate, with any desired accuracy, any arbitrary function. This means that, theoretically, a multilayer feed-forward artificial neural network, with just one hidden layer of sigmoidal neurons, can be used to represent the mapping between the various independent variables and the orbital lifetime of tethered systems. Of course, a suitable number of neurons must be included in the hidden layer, and the correct biases and interconnection weights must be found. The network structure suggested by Cybenko's result is attractive from two perspectives: First, as mentioned

in the **Introduction**, it is known that "broad" networks, with few hidden layers, are easier to train than "narrow" networks with many layers; second, restricting our networks to just three layers of neurons -- input-hidden-output -- will simplify their use by others. This is a significant consideration, as one of the objectives of this research project is to provide computational tools, in the form of trained ANNs, which may be used by others to quickly obtain an approximation of the orbital lifetime of a system of interest.

The size of the input and output layers will be dictated by the problem being solved. For example, if our desired result is an orbital lifetime estimate, we require only one output neuron. The number of neurons in the input layer will be dictated by the number of independent variables. The number of neurons in the hidden layer will determine the accuracy of the mapping, and will be determined experimentally, as discussed previously.

As shown in Figure 15, neurons in the input and output layers will apply the linear transfer function discussed earlier, and hidden layer neurons will apply the logistic function. Hence, we will be using an artificial neural network to implement Cybenko's theorem. The mathematical representation of the network's output is

$$Y_k = \sum_j \frac{W_{jk}}{1 + e^{-(v_j - \sum_i W_{ij} X_i)}} - v_k \quad (70)$$

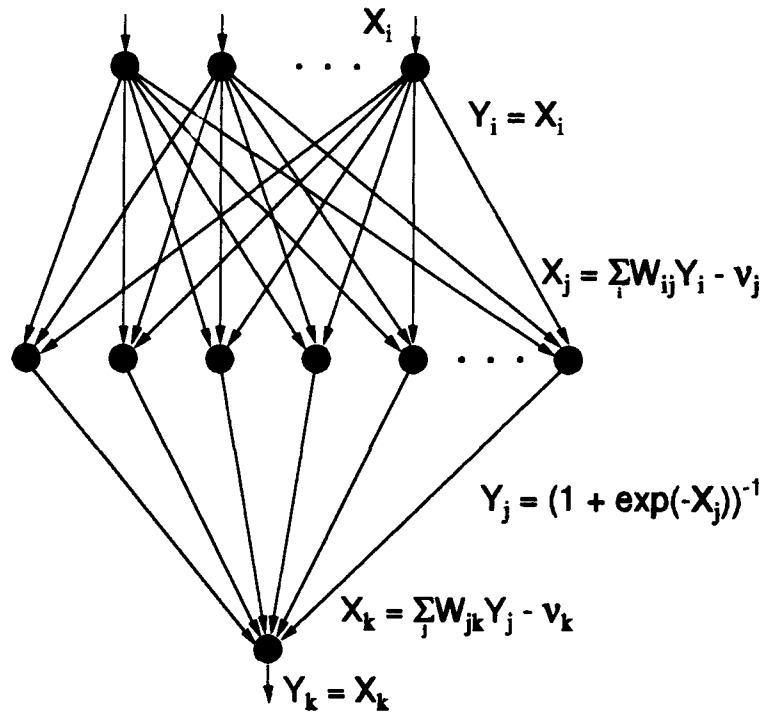


Figure 15. Selected feed-forward network structure.

### The Error Backpropagation Network Training Algorithm

According to Simpson,<sup>85</sup> the error backpropagation training algorithm was independently derived by various individuals and groups, in wide-ranging disciplines, beginning in 1967. In 1986, a group of cognitive and computer scientists -- Rumelhart, Hinton, and Williams<sup>86</sup> -- publicized their derivation of backpropagation training, and demonstrated some of its power and potential. The scientific community took notice, and widespread interest in ANN capabilities and methods has flourished ever since. Consequently, the group led by Rumelhart is usually credited with deriving

the algorithm, although they actually only restated it and demonstrated its usefulness. In any case, the 1986 "discovery" of the backpropagation training algorithm for feed-forward networks is directly responsible for the state of the art today.

The Algorithm. The "standard" error backpropagation algorithm adjusts the weights and biases in a network to minimize the cost function

$$E = \frac{1}{2} \sum_c \sum_k (Y_{k,c} - d_{k,c})^2 \quad (71)$$

where  $E$  represents the total error in a network's performance,  $Y$  is the resultant value provided by an output neuron,  $d$  is its desired value,  $c$  is an index over all training cases presented to the network, and  $k$ , as before, is an index over all output units.

The parameter adjustment procedure is derived by computing the change in the cost function produced by changes in the network's weights and biases. The concept is simple: find the gradient vector of the cost function in parameter space (i.e., in terms of the network weights and biases), and adjust the parameters to reduce the cost. Since the gradient vector points in the direction of the cost function's maximum increase, we move in the opposite direction, to minimize the cost, and hence the error in the network's performance.

The gradient of  $E$ , in parameter space, is calculated using the chain rule of differential calculus. For the output layer, assuming linear output neurons,

$$\frac{\partial E}{\partial W_{jk}} = \frac{\partial E}{\partial X_k} \frac{\partial X_k}{\partial W_{jk}} = \frac{\partial E}{\partial Y_k} \frac{\partial Y_k}{\partial X_k} \frac{\partial X_k}{\partial W_{jk}} = (Y_k - d_k) Y_j \quad (72)$$

$$\frac{\partial E}{\partial v_k} = \frac{\partial E}{\partial X_k} \frac{\partial X_k}{\partial v_k} = \frac{\partial E}{\partial Y_k} \frac{\partial Y_k}{\partial X_k} \frac{\partial X_k}{\partial v_k} = d_k - Y_k \quad (73)$$

where we recall that the input to an output neuron is

$$X_k = \sum_j (W_{jk} Y_j) - v_k \quad (74)$$

For sigmoidal (logistic function) hidden layer neurons,

$$\begin{aligned} \frac{\partial E}{\partial W_{ij}} &= \frac{\partial E}{\partial X_k} \frac{\partial X_k}{\partial Y_j} \frac{\partial Y_j}{\partial X_j} \frac{\partial X_j}{\partial W_{ij}} = \frac{\partial E}{\partial Y_k} \frac{\partial Y_k}{\partial X_k} \frac{\partial X_k}{\partial Y_j} \frac{\partial Y_j}{\partial X_j} \frac{\partial X_j}{\partial W_{ij}} \\ &= \left[ \sum_k (Y_k - d_k) W_{jk} \right] Y_j (1 - Y_j) X_i \end{aligned} \quad (75)$$

$$\begin{aligned} \frac{\partial E}{\partial v_j} &= \frac{\partial E}{\partial X_k} \frac{\partial X_k}{\partial Y_j} \frac{\partial Y_j}{\partial X_j} \frac{\partial X_j}{\partial v_j} = \frac{\partial E}{\partial Y_k} \frac{\partial Y_k}{\partial X_k} \frac{\partial X_k}{\partial Y_j} \frac{\partial Y_j}{\partial X_j} \frac{\partial X_j}{\partial v_j} \\ &= \left[ \sum_k (d_k - Y_k) W_{jk} \right] Y_j (1 - Y_j) \end{aligned} \quad (76)$$

and we recall that the input to a hidden layer neuron is

$$X_j = \sum_i (W_{ij} X_i) - v_j \quad (77)$$

We note that the factor  $Y_j(1-Y_j)$ , the derivative of the logistic function, appears in Eqs. (75) and (76). If the hidden layer neurons are initially saturated, due to large magnitude inputs, this factor will equal zero, and no learning will occur. If the magnitudes of the input vector components are large, this problem may possibly be avoided by using large initial bias values on the hidden neurons, and/or by assigning small initial connection weights between the input and hidden layers. A more reliable approach is to map all input data to the interval (0,1), or perhaps (-1,1), the "sensitive"

range of sigmoidal (logistic function) neurons, and use random initial weights and biases between -1 and 1. These steps provide a reasonable chance for learning to occur.

Since the gradient vector indicates the direction of maximum increase in the cost function, as mentioned earlier, moving in the opposite direction should decrease the total error. Hence, the parameters are adjusted using the relation

$$\Delta \chi(t) = -\epsilon \frac{\partial E}{\partial \chi}(t) + \alpha \Delta \chi(t-1) \quad (78)$$

where  $\chi$  represents either a weight or bias,  $\epsilon$  is the "learning rate", and  $\alpha$  is a "momentum" term that specifies the extent of the influence of the previous change on the current adjustment.

The procedure for network training is to take a small "step" in the direction of maximum decrease of the cost function, by adjusting the weights and biases according to Eq. (78). After a step is taken, we reevaluate the cost function and make another adjustment, hoping to eventually reach a global, or at least acceptable, minimum of the cost function. The "optimal" values for the learning rate and momentum will vary with the topology of the error surface being traversed. An adaptive algorithm for determining  $\epsilon$  and  $\alpha$  is presented later in this Chapter.

The standard backpropagation training approach has been used very successfully in various applications. Unfortunately, it has some difficulty in training networks to represent real-valued functions that span several orders of magnitude, precisely the situation we will encounter with orbital lifetime data for tethered systems.

Problems with the standard approach are discussed in the next section, and an alternative algorithm is derived.

### **The Minimum Percent Error Backpropagation Training Algorithm**

Problem Description. Parameter adjustments are made in the standard backpropagation training algorithm as a result of the magnitude of the (squared) error between the desired and actual outputs. Consequently, a network trained to any chosen accuracy level is likely to produce outputs with percent errors that are larger at small magnitude output values than at large magnitude output values. This occurs because a large percent error at a small value will often be smaller in magnitude than a small percent error at a large value. Thus, a network may approximate large function values quite well, but miss producing the desired output at small values by large percentages.

If the desired output data spans more than one or two orders of magnitude, the network will need to be trained to a very small error level to guarantee close approximation of the smallest values. Reaching an extremely small error level when training a network to represent widely-spread, real-valued data has been shown to be a difficult, if not impossible, task.<sup>87</sup> In such a situation, we sometimes find that a network trained to a very small error level has "memorized" the training data rather than learned the boundaries and trends necessary for effective generalization. One possible solution is to map the output data into a smaller interval.

For example, if a network uses a linear output neuron to represent data ranging in magnitude from 0.5 to 500, we may map the data to the interval (0, 10). (If the output neuron is sigmoidal, the data would need to be mapped into the active range of the sigmoidal function used.) As shown in Eq. (79), the mapping is accomplished by subtracting 0.5 from each desired output data value, and dividing the result by 49.95, one-tenth the range of the original data.

$$d_{scaled} = \frac{d_{unscaled} - 0.5}{49.95} \quad (79)$$

Converting the scaled network output back to the original data range requires the operation

$$Y_{unscaled} = 49.95 Y_{scaled} + 0.5 \quad (80)$$

Hence we see that an unscaled result of 0.5 requires a (scaled) network output of 0.0. Any error will be magnified nearly 50 times. For example, an output of only 0.01, rather than 0.0, would cause a 99.9 percent error in the corrected result (0.9995 vs. 0.5). By comparison, an unscaled result of 500 requires a network output of 10, and an actual output of 10.01 translates to only a 0.1 percent error (500.4995 vs. 500). Clearly, what is needed is some means of weighting the back-propagated error to account for differences in output data magnitude. Such an algorithm is derived in the next section.

**Minimum Percent Error Backpropagation Training.** As illustrated in the previous section, the backpropagation algorithm, in its "standard" form, is not well suited for

network training in the case of widely-spread, real-valued output data. Rather than seeking a minimum of the total output error, we can instead minimize the sum of the percent errors occurring at output. This will put the network's performance at each data point on an equal basis, rather than skewing the trained network's accuracy in favor of the largest magnitude data points.

Let  $E'$  be the new cost function to be minimized, where

$$E' = \frac{1}{2} \sum_c \sum_k \left( \frac{d_{k,c} - Y_{k,c}}{d_{k,c}} \right)^2 \quad (81)$$

This is the sum of squares of the percent errors occurring at output, including the contributions of all output units and data points. Assuming linear output neurons and sigmoidal (logistic function) hidden layer neurons, we may find the parameter space components of the cost function's gradient using the chain rule:

$$\frac{\partial E'}{\partial W_{jk}} = \frac{\partial E'}{\partial X_k} \frac{\partial X_k}{\partial W_{jk}} = \frac{\partial E'}{\partial Y_k} \frac{\partial Y_k}{\partial X_k} \frac{\partial X_k}{\partial W_{jk}} = \left( \frac{Y_k - d_k}{d_k^2} \right) Y_j \quad (82)$$

$$\frac{\partial E'}{\partial v_k} = \frac{\partial E'}{\partial X_k} \frac{\partial X_k}{\partial v_k} = \frac{\partial E'}{\partial Y_k} \frac{\partial Y_k}{\partial X_k} \frac{\partial X_k}{\partial v_k} = \frac{d_k - Y_k}{d_k^2} \quad (83)$$

$$\begin{aligned} \frac{\partial E'}{\partial W_{ij}} &= \left( \sum_k \frac{\partial E'}{\partial X_k} \frac{\partial X_k}{\partial Y_j} \right) \frac{\partial Y_j}{\partial X_j} \frac{\partial X_j}{\partial W_{ij}} = \left( \sum_k \frac{\partial E'}{\partial Y_k} \frac{\partial Y_k}{\partial X_k} \frac{\partial X_k}{\partial Y_j} \right) \frac{\partial Y_j}{\partial X_j} \frac{\partial X_j}{\partial W_{ij}} \\ &= \left[ \sum_k \left( \frac{Y_k - d_k}{d_k^2} \right) W_{jk} \right] Y_j (1 - Y_j) X_i \end{aligned} \quad (84)$$

$$\begin{aligned}
\frac{\partial E'}{\partial v_j} &= \left( \sum_k \frac{\partial E}{\partial X_k} \frac{\partial X_k}{\partial Y_j} \right) \frac{\partial Y_j}{\partial X_j} \frac{\partial X_j}{\partial v_j} = \left( \sum_k \frac{\partial E'}{\partial Y_k} \frac{\partial Y_k}{\partial X_k} \frac{\partial X_k}{\partial Y_j} \right) \frac{\partial Y_j}{\partial X_j} \frac{\partial X_j}{\partial v_j} \\
&= \left[ \sum_k \left( \frac{d_k - Y_k}{d_k^2} \right) W_{jk} \right] Y_j (1 - Y_j)
\end{aligned} \tag{85}$$

We note that the derivative of the logistic function appears in the equations describing the dependence of changes in  $E'$  on changes in  $W_{ij}$  and  $v_j$ . Hence, steps must be taken to avoid initial saturation of the hidden layer neurons, as discussed earlier. We also observe that these equations have an obvious singularity for a desired output value of zero, because  $d_k$  appears in each denominator. The singularity may be avoided by substituting for zero a very small desired output value.

The network parameters are adjusted during training using Eq. (78). Training may continue until the sum of the percent errors is below a desired tolerance, the maximum percent error at every output data point is less than some desired limit, or both. An adaptive algorithm to adjust the learning and momentum rates, and a demonstration of the Minimum Percent Error (MPE) training algorithm, are presented in the following sections.

### **Network Training Procedures**

**"Optimal" Learning and Momentum Rates.** The training process may be visualized in topographical terms. The cost function is represented as a surface in a  $(\xi + 1)$  dimension space, where  $\xi$  is the number of adjustable network parameters (i.e., the weights and biases). The objective of network training is to reach a low elevation

point, on the "error surface", where the cost function is a minimum. The surface is traversed in steps, whose sizes are dictated by the values of the learning rate,  $\epsilon$ , and the momentum,  $\alpha$ , as shown in Eq. (78).

If training time were of no consequence, we would set the momentum to zero and make the learning rate infinitesimally small. This, theoretically, would insure that we eventually reach a low elevation area on the error surface - i.e., a global or local minimum of the cost function. However, for most problems, training time using this approach would be unacceptably long. Hence, we need a way to determine learning and momentum rates that will yield minimum training time for any surface.

Adaptive Learning Rate Algorithm. If the learning rate is too large, a step may overshoot a "valley", "sink hole", or other depression in the error surface.

Additionally, a non-zero momentum rate will hamper progress if the gradient reverses direction, as will occur following an overshoot. However, if a relatively flat area of the error surface is being traversed, the learning rate, and possibly the momentum, may be reliably increased. These observations lead to an adaptive step-size adjustment algorithm, detailed below:

- If the cost function value increases, an overshoot has occurred, and the learning rate should be reduced and the momentum set to zero.
- If the cost function value decreases and the gradient vector changes direction significantly, a "twisted ravine" is being traversed; the momentum should be set to zero and the learning rate reduced.
- If the cost function value decreases, and the gradient vector does not change direction significantly, a relatively flat surface is being traversed; the learning rate and momentum may be increased.

We may detect significant changes in the gradient vector's direction using the vector dot product,

$$\zeta = \underline{A} \cdot \underline{B} = |\underline{A}| |\underline{B}| \cos \theta \quad (86)$$

where  $\theta$  is the angle between vector  $\underline{A}$  and vector  $\underline{B}$ . If  $\theta$  is within  $\pm 90$  degrees,  $\zeta$  will be positive or zero. Hence, if the dot product of the current gradient vector and the previous gradient vector is negative, we know that the direction of greatest decrease in the cost function has changed by more than 90 degrees.

After interactively experimenting with various criteria, in various network training scenarios, the following algorithm was chosen:

- (1) If  $E(t) > E(t-1)$ , then set  $\epsilon(t) = 0.25\epsilon(t-1)$ , and  $\alpha(t) = 0$ .
- (2) If  $E(t) < E(t-1)$ , and  $\zeta(t) < 0$ , then set  $\epsilon(t) = 0.6\epsilon(t-1)$ , and  $\alpha(t) = 0$ .
- (3) If  $E(t) < E(t-1)$ , and  $\zeta(t) \geq 0$ , then set  $\epsilon(t) = 1.1\epsilon(t-1)$ , and If  $\alpha(t-1) \neq 0$ , and  $\alpha(t-1) < 0.9$ , then set  $\alpha(t) = 1.5\alpha(t-1)$ . If  $\alpha(t-1) = 0$ , then set  $\alpha(t) = 0.1$ .

The initial values for  $\epsilon$  and  $\alpha$  are set to 0.01 and 0.009, respectively.

**Parameter Adjustment.** One way of using the gradient vector components is to adjust the network parameters after every input-output case. Using this scheme, a network can only adjust itself to correct for errors in representing the current data point. An alternative approach, more commonly used, is to accumulate the components of the gradient vector over all the input-output cases before changing the parameters. This "batch method" allows the network to adjust itself in a way that will benefit the entire data set, and is the approach used in this research project.

### Network Training Example

Network Structure and Training Requirements. To demonstrate the utility of the MPE algorithm a three layer feed-forward net, following the structure shown in Figure 15, was trained to represent the function

$$Y = (0.5 + 20X^2)^2 \quad (87)$$

This function, as shown in Figure 16, is exponential, with  $Y$  ranging from 0.5 to 420 in the  $X$  interval (0,1). Our goal is to train the network until the maximum percent error at every (training) data point is less than 10%. The network has one linear input neuron, one linear output neuron, and 10 sigmoidal (logistic function) hidden neurons. Eleven input-output pairs were used for training, with  $X$  (input) varying from 0 to 1 in increments of 0.1.

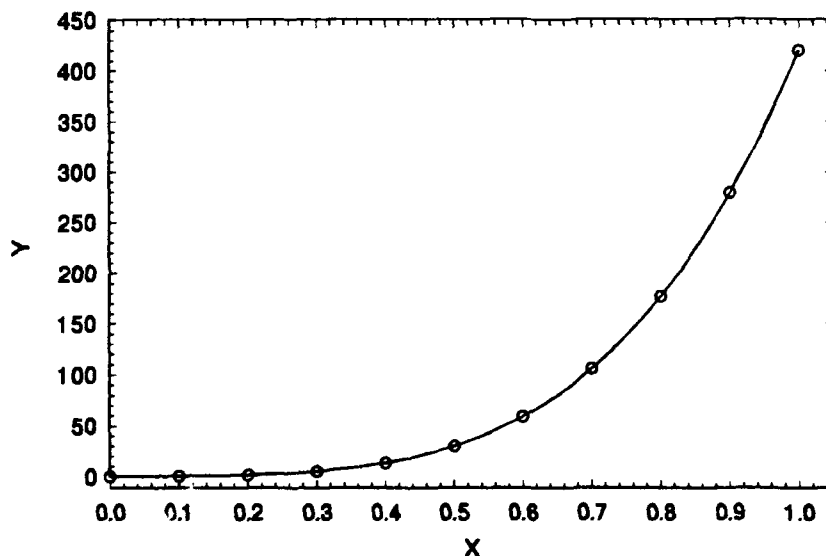


Figure 16. Function to be learned.

Results. The network was trained using the adaptive step size and batch parameter adjustment procedures described previously. Figure 17 shows the accuracy evolution of the network trained using both the standard backpropagation algorithm and the MPE algorithm.

After 51,534 passes through the data, the MPE-trained network had reached a maximum percent error, at any training data point, of slightly less than 10%. The sum of the percent errors was 15.7%. In the same number of training passes, starting with the same initial (random) parameter values, the standard backpropagation algorithm trained the network to a maximum percent error of 25.3%, with a sum of percent errors of 39.4%. Figures 18 and 19 show the interpolation or "generalizing" performance of the networks, in that the networks were tested using  $X$  values in increments of 0.01 to create the figures. The points marked with an "o" indicate the network's accuracy at the training data points, which are in  $X$  increments of 0.1.

Hybrid Training Approach. Figure 17 shows that the standard method, early in the training, produced a larger rate of decrease in the percent errors in the network's output than did the MPE algorithm. This initial success raises the question, what if the two methods were combined? We observe that when using the standard method, the percent errors quickly reached "plateau" values, and their rates of decrease became very small. Hence the decision was made to begin with the standard method, and switch to the MPE method, when the slope of the sum of the percent errors curve became greater than  $-0.1\%$  in 1000 passes.

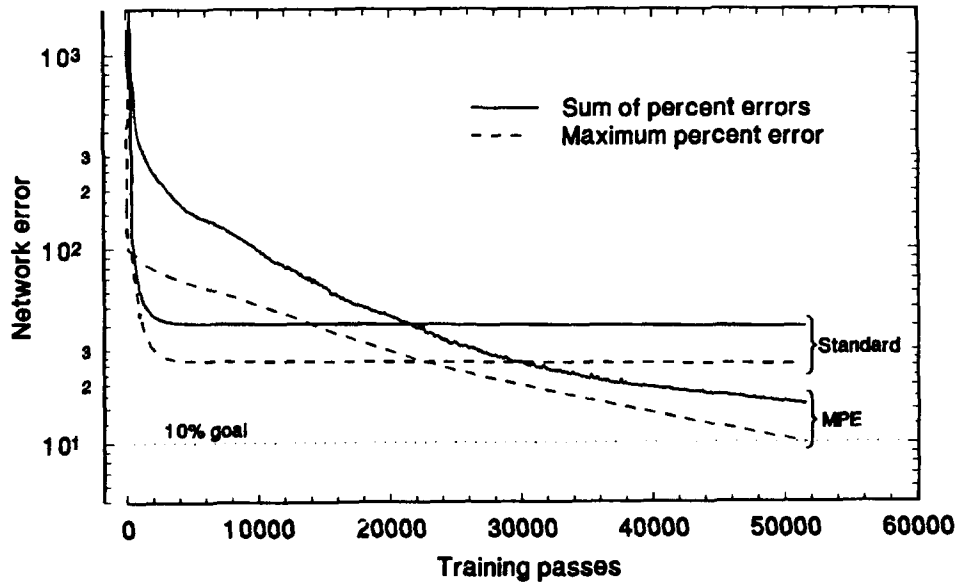


Figure 17. Network accuracy evolution.

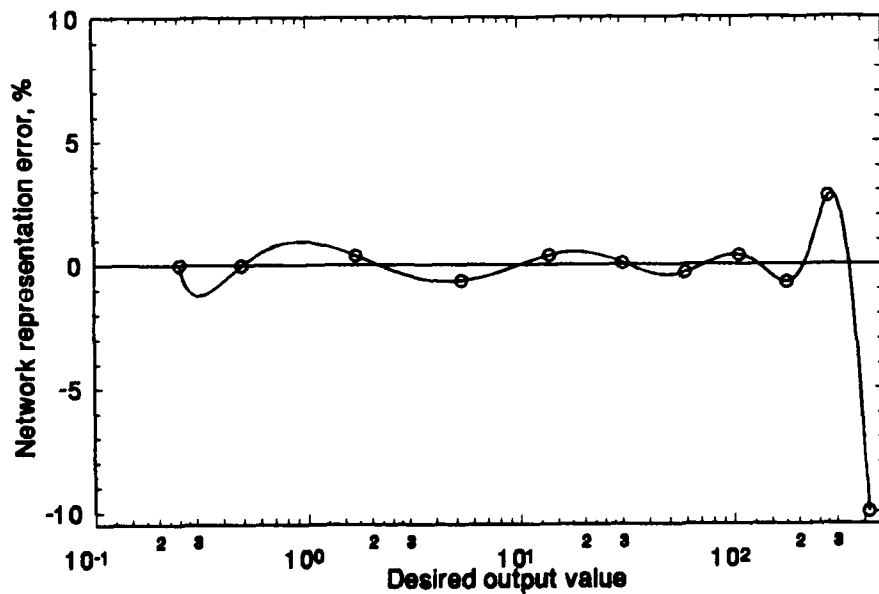


Figure 18. Generalization accuracy after MPE training.

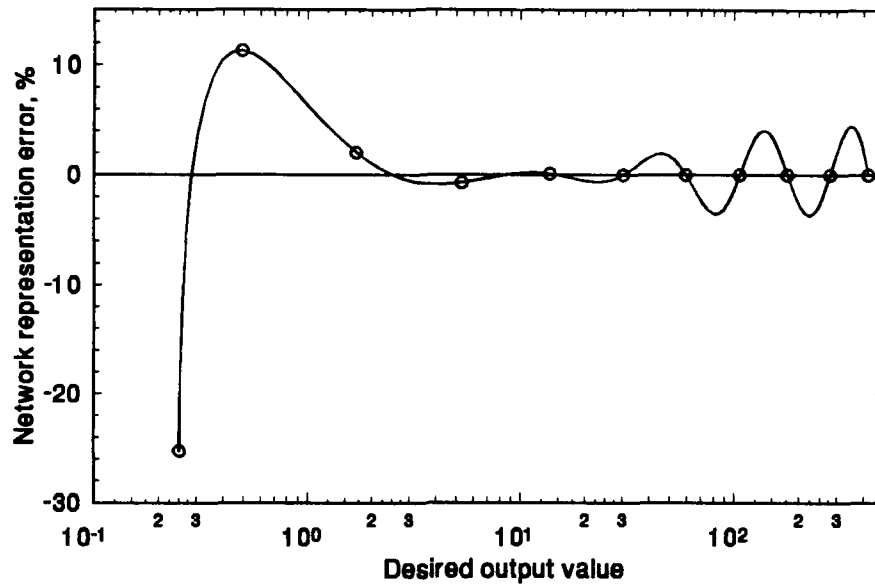


Figure 19. Generalization accuracy after standard method training.

As shown in Figure 20, this approach led to a greatly reduced training time. The training method transition occurred after 6005 passes, when the standard algorithm had trained the network to a maximum percent error in representing the training data of 26.5%, and a sum of percent errors of 41.3%. In only 167 additional passes the MPE algorithm was able to train the network to provide output values within  $\pm 10\%$  of the desired values. The sum of the percent errors at this point was 27.5%, indicating more error occurred than in the MPE-only case.

Figure 21 shows the "hybrid-trained" network's generalization performance. We note that this network does not generalize within the desired  $\pm 10\%$  error envelope. This situation can be rectified with additional training, or by adding more

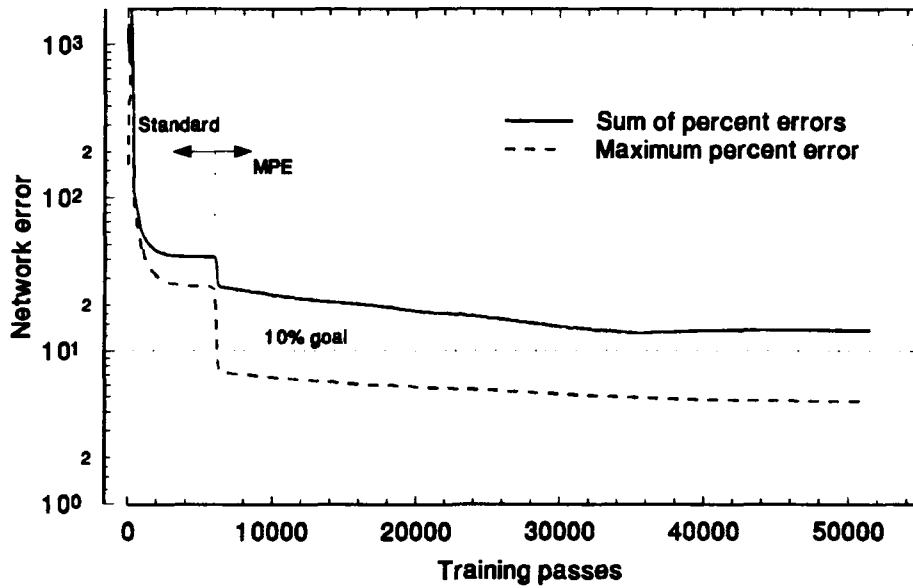


Figure 20. Network accuracy evolution with combined training.

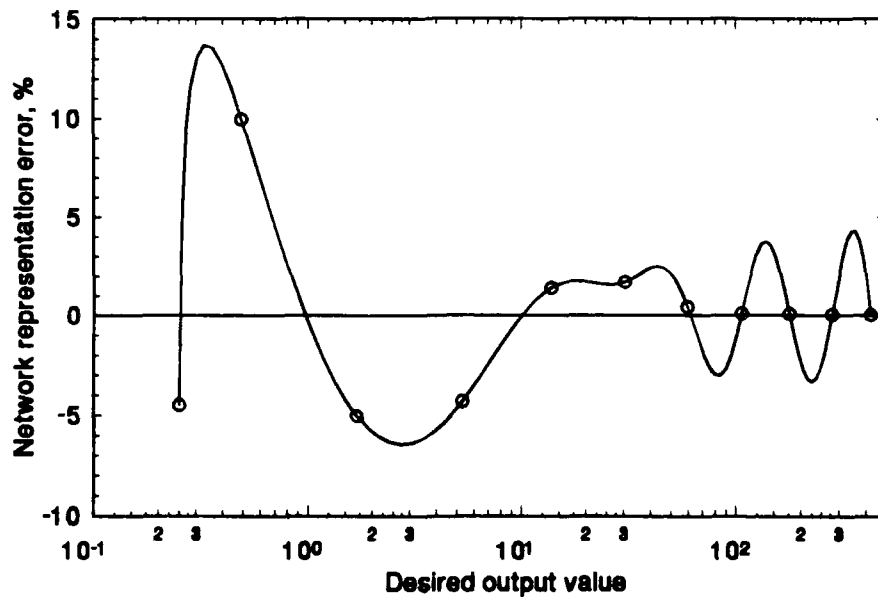


Figure 21. Generalization accuracy after combined training (6172 passes total).

data to the training set. We also note that the network has "inherited" the tendency of networks trained using the standard algorithm to misrepresent the smallest magnitude data points. However, the MPE algorithm was able, in just 167 passes, to reduce the training error to below the desired limit.

Figure 22 shows the generalization accuracy of the hybrid-trained network when we let the MPE phase of the training continue for 45,362 additional passes - to a total of 51,534 passes, the length of the original training session. At this point, the network had a maximum percent error in representing the training data of only 4.7%, and a sum of percent errors of 13.6%. We note from the figure that the network now generalizes within the desired 10 % envelope, although the errors in representing the untrained data are greater than those in representing the trained data. We also see that the tendency to misrepresent the smallest magnitude values has persisted.

Hence we have demonstrated the ability of the MPE backpropagation algorithm to train a feed-forward net to very accurately represent real-valued data which spans several orders of magnitude. We have also shown that a "hybrid" training approach -- standard backpropagation until the slope of the sum of the percent errors curve is greater than -0.1% in 1000 passes, then MPE backpropagation -- can often be used to obtain satisfactory results quicker than using the MPE method alone.

Unfortunately, the hybrid approach is not guaranteed to be the most efficient approach in every case. The topology of the error surface representing the total magnitude error may differ significantly from that of the surface representing the sum of the percent errors. Hence, a low level elevation on one will not necessarily translate

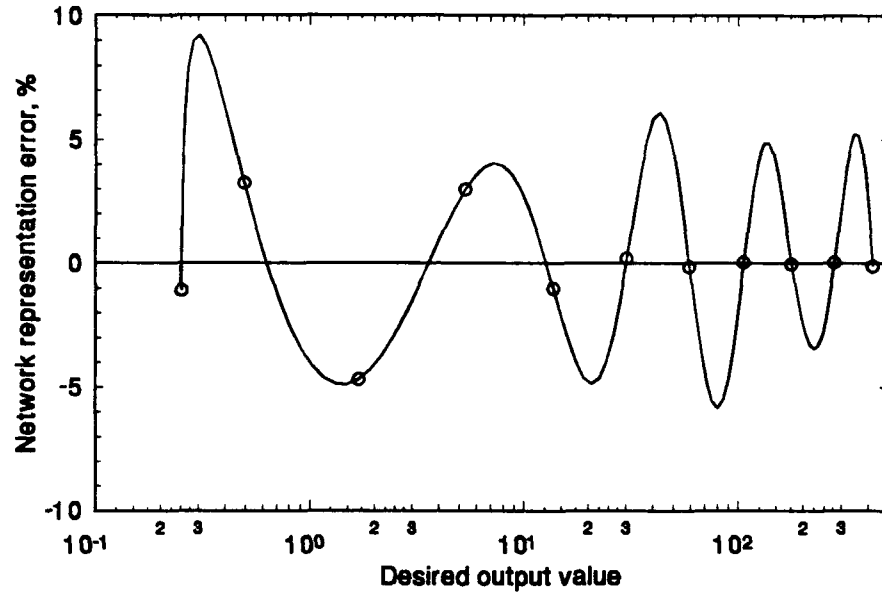


Figure 22. Generalization accuracy after combined training (51,534 passes total).

to a similar level on the other. However, the hybrid approach may be a useful alternative in difficult training situations, or when one wishes to represent the largest magnitude output values with more relative accuracy than is possible with MPE training alone.

## RESULTS AND DISCUSSION

In this Chapter, we illustrate the effect of various assumptions and physical characteristics on tether orbit evolution, demonstrate the accuracy of the orbital element propagation model (EPM) as compared to the multibody model (MBM), and present orbital lifetime results for free tethers and satellites trailing a tether. We will also describe a procedure to modify predicted orbital lifetimes to compensate for initial orbit inclinations other than  $28.5^\circ$ , and nonzero argument of perigee and true anomaly values. In the final section of the Chapter, we demonstrate the reliability and accuracy of the derived orbital lifetime prediction method, by comparing network-produced results for a large number of randomly chosen test cases with those obtained using the MBM.

Unless stated otherwise, the assumptions described in the **Introduction** apply to all presented results. They are listed here for convenience:

1. The tether is 2 mm in diameter, and has the physical properties of Kevlar 29:  $E$  (modulus of elasticity) =  $6.2055 \times 10^{10}$  N/m<sup>2</sup>,  $\rho$  (mass density) = 1440 kg/m<sup>3</sup>,  $\nu$  (Poisson's ratio) = 0.4.
2. The tether is initially unstretched. The system is initially aligned along the local vertical, orbiting as a rigid rod.
3. The system's initial orbit inclination is  $28.5^\circ$ , and the argument of perigee and true anomaly are zero.
4. Orbital lifetime is considered complete when the system center of mass (CM) reaches 150 km altitude.

### **Preliminary Findings and Basic Phenomena**

In this section we use the MBM to investigate the effect of various assumptions and physical properties on free tether orbital decay. We will present results illustrating the effects on orbital lifetime of (1) the length of the segments used to model a tether, (2) the drag coefficient model, (3) the Earth and atmosphere shape and state assumptions, (4) the tether's diameter, and (5) the tether's length. In all but the last of the five sub-sections which follow, we assume a 20 km tether has been deployed downward from a 300 km (altitude) circular equatorial orbit, stabilized along the local vertical, and released. In this case, all points below the "parent" end of the tether are moving at speeds less than that required for circular orbit at their altitude. This means the CM is at apogee of an elliptical orbit, whose apogee radius is 6668.137 km, and whose perigee radius is 6608.129 km (230 km altitude).

Segment Length Effect. Before beginning large scale investigations, we must decide on the number of segments to be modeled in a tether of given length. As shown in Figure 23, there is essentially no difference in the CM altitude-time history when the tether is modeled with one hundred 200 meter segments (99 beads) or six  $3\frac{1}{2}$  km segments (5 beads). Figure 24 shows that acceptable results were obtained even when two 10 km segments were used. Hence, the segment length for all further simulations was conservatively chosen to be 5 km.

Effect of Drag Coefficient Assumptions. Next, we investigated the effect of using the empirically derived drag coefficient model described earlier, as compared to using a

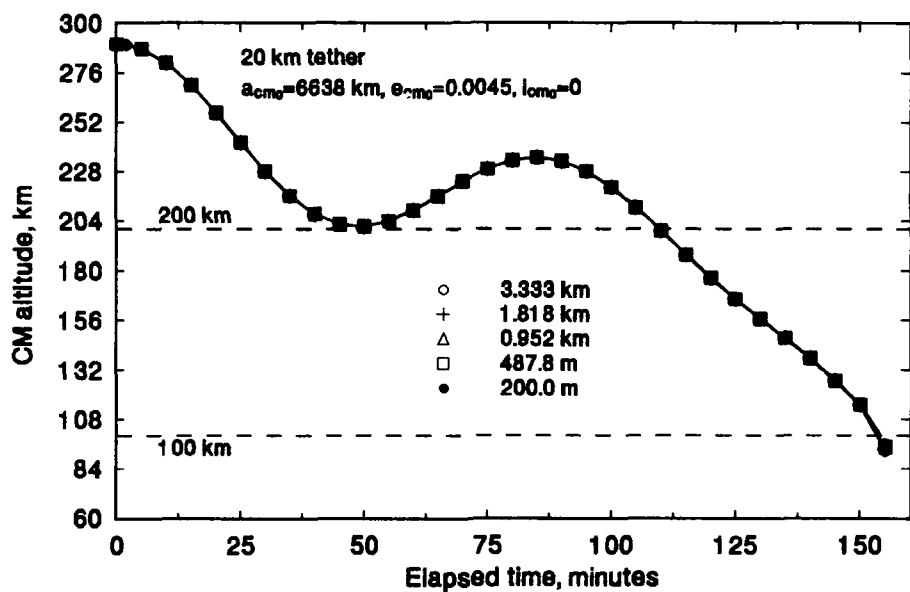


Figure 23. Orbital decay with short segments.

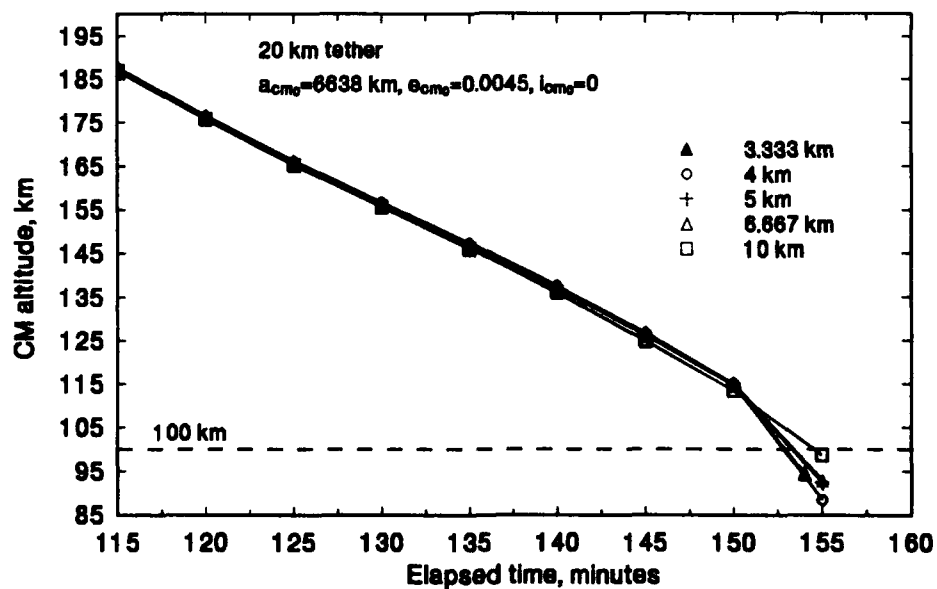


Figure 24. Orbital decay with long segments.

more commonly used constant value of 2.2. As shown in Figure 25, allowing  $C_D$  to vary caused the most difference at low altitudes. This results from two factors: First, the atmospheric mass density is relatively small at the higher altitudes, greatly reducing the magnitude of aerodynamic forces, and hence the effect of the drag coefficient, in that region; and second, a 2 mm diameter circular cylinder experiences free molecular flow conditions (large  $Kn$ ) to an altitude below 100 km, keeping it's drag coefficient at the free molecular value of 2.8. So, the differences in the altitude-time histories shown in Figure 25 actually result from a magnitude difference of 0.6 in the drag coefficient. All further simulations use the empirically derived  $C_D$  model.

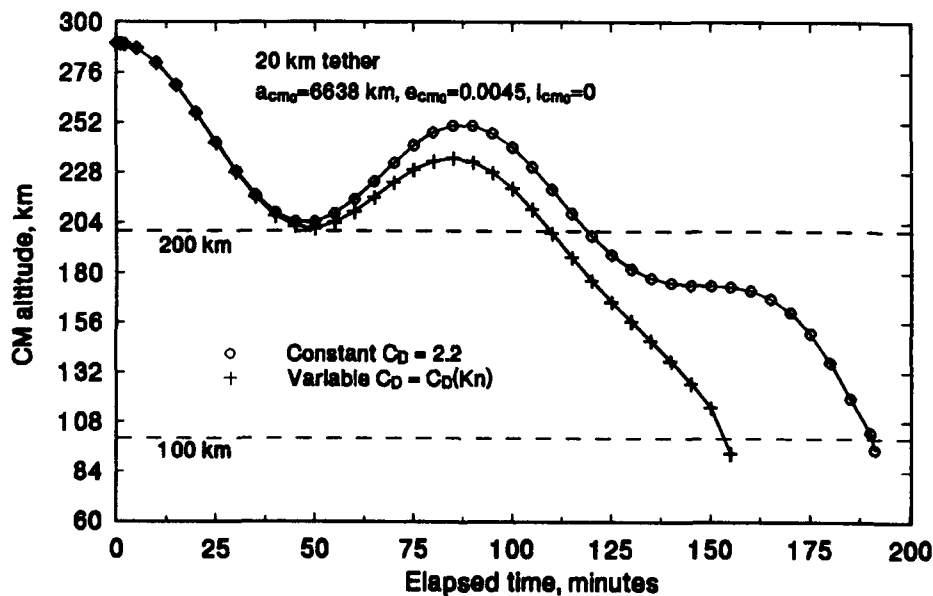


Figure 25. Effect of drag coefficient model on orbital decay.

Effect of Earth and Atmosphere Assumptions. To demonstrate the effects of the assumed shape of the Earth and the shape and state of the atmosphere on a tether's orbital decay, the simulation was run for 3 configurations: (1) assuming a spherical Earth and a non-rotating, spherical atmosphere, (2) assuming a spherical Earth and a rotating, spherical atmosphere, and (3) assuming an oblate Earth and a rotating, oblate atmosphere. As shown in Figure 26, the oblate Earth and rotating, oblate atmosphere model produced the shortest orbital lifetime. The spherical non-rotating model produced an increased lifetime, apparently due to the increase in dissipative drag forces being more than offset by the decrease in gravitational forces. As a validation point, we note that the time required for the tether CM to reach 200 km altitude in this case ( $2^{\text{h}}4^{\text{m}}17^{\text{s}}$ ) is within 20 seconds of the result obtained by Bergamaschi and Morana<sup>88</sup> when they used similar assumptions. Allowing the spherical atmosphere to rotate increased the orbital lifetime, due to decreased drag forces in a posigrade motion, but also caused the greatest departure from the results obtained using the rotating oblate model.

Hence, we see that assuming an oblate Earth and a rotating, oblate atmosphere yields lifetime results which are significantly different from those of the simpler models. In all further simulations, the oblate, rotating models for the Earth and its atmosphere were used.

Tether Diameter Effect. A more surprising result involves the effect of the tether's diameter on its orbital lifetime. One might intuitively believe that increasing a tether's diameter will reduce its lifetime, because the increased area will cause larger drag

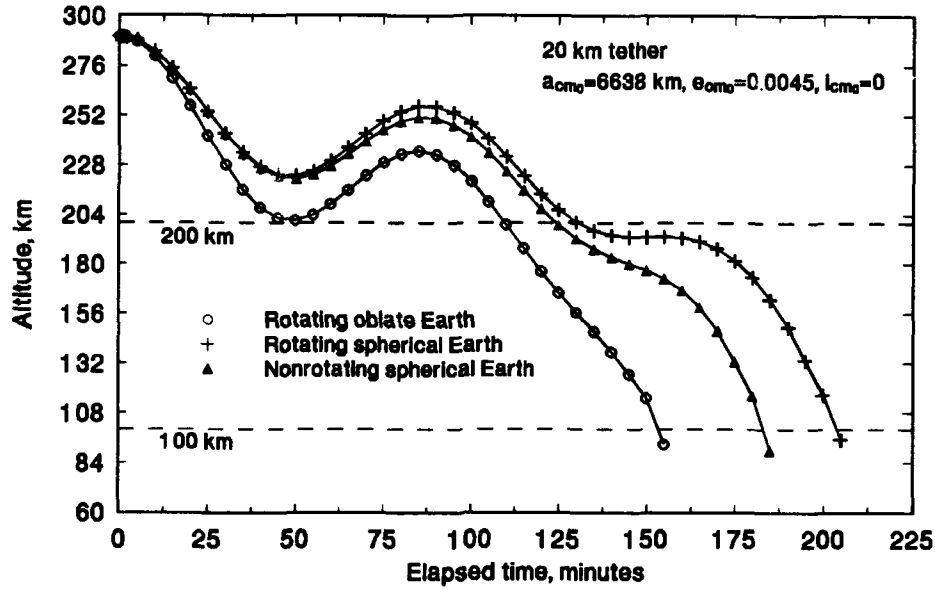


Figure 26. Effect of Earth and atmosphere shape and state on orbital decay.

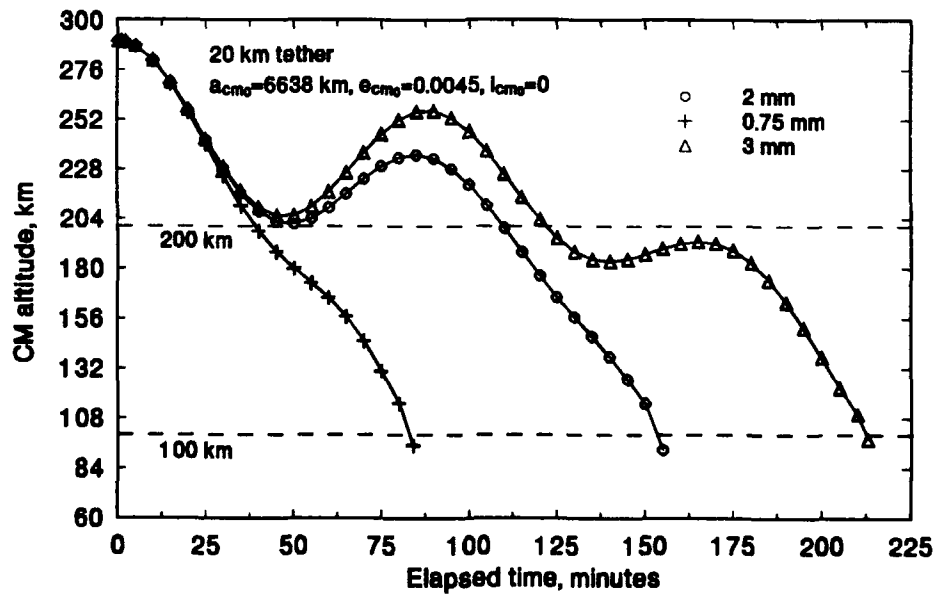


Figure 27. Effect of tether diameter on orbital decay.

forces. However, as shown in Figure 27, increased diameter actually causes increased orbital lifetime. The cross-sectional area and drag force magnitude increase with increased diameter, but, as Eq. (88) shows, the ballistic coefficient,  $\beta$ , actually decreases, since it is inversely proportional to the diameter. In this equation,  $L$  is the tether's length,  $d$  is the tether's diameter,  $A$  is its cross-sectional area ( $L \times d$ ),  $\rho_{\text{tether}}$  is the tether's mass density, and  $M$  is the tether's mass.

$$\beta = \frac{C_D A}{M} = \frac{4 C_D L d}{\pi L d^2 \rho_{\text{tether}}} = \frac{4 C_D}{\pi d \rho_{\text{tether}}} \quad (88)$$

Because the tether's mass is proportional to  $d^2$  and the drag force is proportional to  $d$ , the acceleration due to aerodynamic drag decreases as tether diameter increases.

Consequently, a large diameter tether dissipates less orbital energy per unit mass per unit time than a small diameter tether, and will therefore have a longer orbital lifetime. We assume a 2 mm diameter for all further simulations, and note that this is the most common size proposed in the literature.

Length Effect. Equation (88) shows that a tether's length has no effect on the ballistic coefficient, and hence no effect on the force per unit mass experienced due to drag forces. However, a long vertical, or near vertical, tether will encounter the more dense portions of the atmosphere earlier in its lifetime than a short tether. Thus, a long tether will dissipate orbital energy sooner than a short tether, reducing its lifetime. This characteristic is illustrated in Figure 28, for two tethers of different lengths. The CM of each tether was initially in a circular orbit, with an orbit inclination of  $40^\circ$ , and a semi-major axis length of 6778.137 km.

The results shown in Figure 28 illustrate a potential problem with using orbital lifetime prediction techniques designed for use with single-mass satellites. Various techniques for lifetime prediction and orbit propagation exist, with some of the most well-known having been developed by Sterne<sup>89</sup>, Liu<sup>90</sup>, and King-Hele<sup>91</sup>. Regardless of the approach, the ballistic coefficient, in one form or another, is always an included factor which brings the dissipative effects of aerodynamic drag into the analysis and results. As we have shown, a tether's ballistic coefficient is independent of its length, but the length certainly has an effect on the orbital lifetime. Hence, we conclude that single-mass orbital lifetime prediction methods will not properly account for tether length effects, which may lead to significant errors in predicted lifetimes.

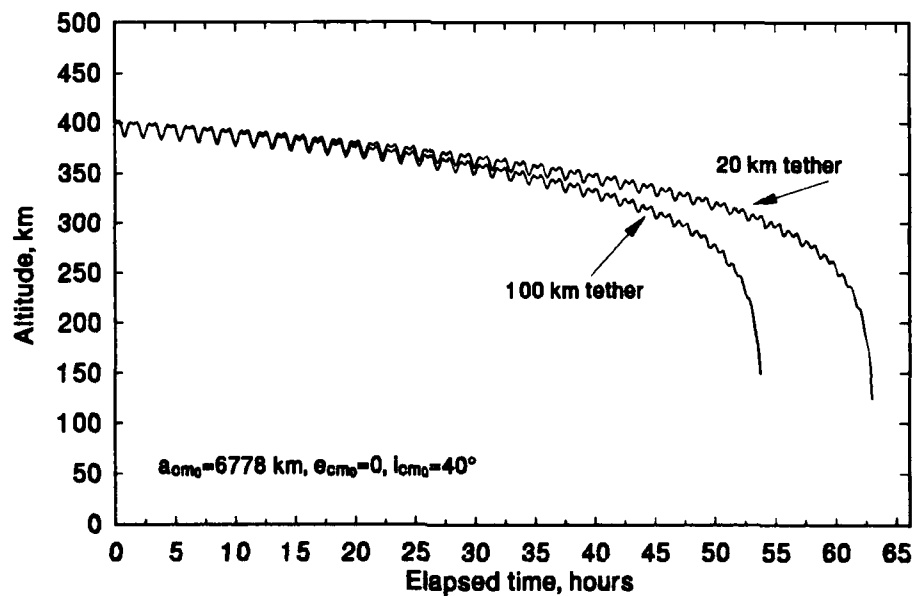


Figure 28. Effect of tether length on orbital decay.

The example results presented in Figure 28 show a length-induced difference in lifetime to 150 km (altitude) of approximately 9.1 hours, which is 15% of the lifetime of the 20 km tether, and 17% of the lifetime of the 100 km tether. We will return to this topic later in this Chapter, and present results showing the general unreliability of single-mass results for most tethered systems.

### **Element Propagation Model Performance**

As discussed in the **Mathematical Models** Chapter, the orbital element propagation model (EPM) relies on the assumptions that the tether is inextensible and aligned along the local vertical at all times. The validity of these assumptions is confirmed in this section by results obtained using the multibody model (MBM), which show that both the in-plane and out-of-plane libration angles, though oscillatory, remain small during orbital decay, even for systems in inclined orbits where out-of-plane accelerations are significant. The libration angles indicate the displacement between a straight line approximation for the tether, and the local vertical, as seen from the parent's location. A positive in-plane angle indicates the upper end (i.e., the initially higher altitude end) of the system leads the lower end (i.e., the initially lower altitude end). A positive out-of-plane angle indicates the subsatellite is currently "north" of (i.e., above) the orbit plane of the parent.

In this section, results showing the accuracy of the EPM, as compared to the MBM, for free tethers, satellites trailing a tether, and a tethered system (parent-tether-subsatellite) are presented.

Free Tether Performance. Figure 29 shows the CM altitude-time history of identical 20 km tethers, released in 3 different equatorial orbits. Each CM orbit was initially circular, and the initial altitudes were 400 km, 450 km, and 500 km. As shown in the figure, the percent differences in lifetime to 100 km between the EPM and the MBM were quite small. These accuracies were obtained using an EPM time step of 1% of an orbit period, and are typical of many other free tether scenarios tested, including longer tethers and/or inclined orbits.

For example, the EPM lifetime of the 20 km tether presented in Figure 28 ( $i_{cmo} = 40^\circ$ ) was only 0.4% less than the MBM result. The EPM lifetime of the 100 km tether in Figure 28 differed by only 0.7% from the MBM result.

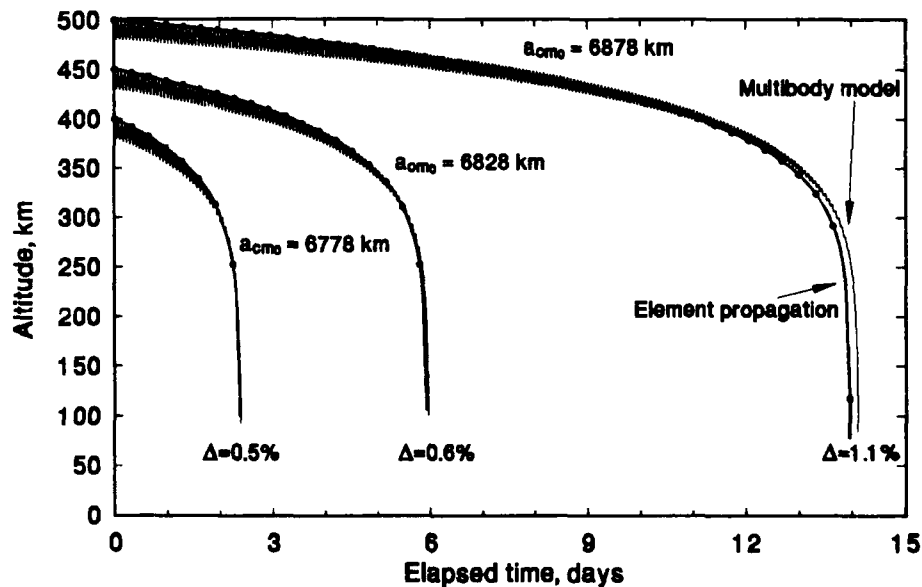


Figure 29. Element propagation model performance with free tethers.

The element propagation technique also dramatically reduced computing time. For example, simulation of the 14-day orbital decay shown in Figure 29 took nearly 5 hours on a Sun SPARC workstation, using the MBM. The EPM was used to simulate the same decay, on the same machine, in just 58 seconds. This is an improvement in the ratio of simulated orbit time to computing time of over 300 to 1.

Upward-Deployed Subsatellite Trailing a Tether. Performance of the EPM was tested on a system composed of a 500 kg mass, 2 m diameter subsatellite, deployed upward on a 20 km tether from a 300 km (altitude) circular orbit, and released. This scenario simulates the behavior of NASA's planned "TSS-1" experiment, if the tether happens to be inadvertently, or purposely, freed from the Shuttle. As Figure 30 shows, the

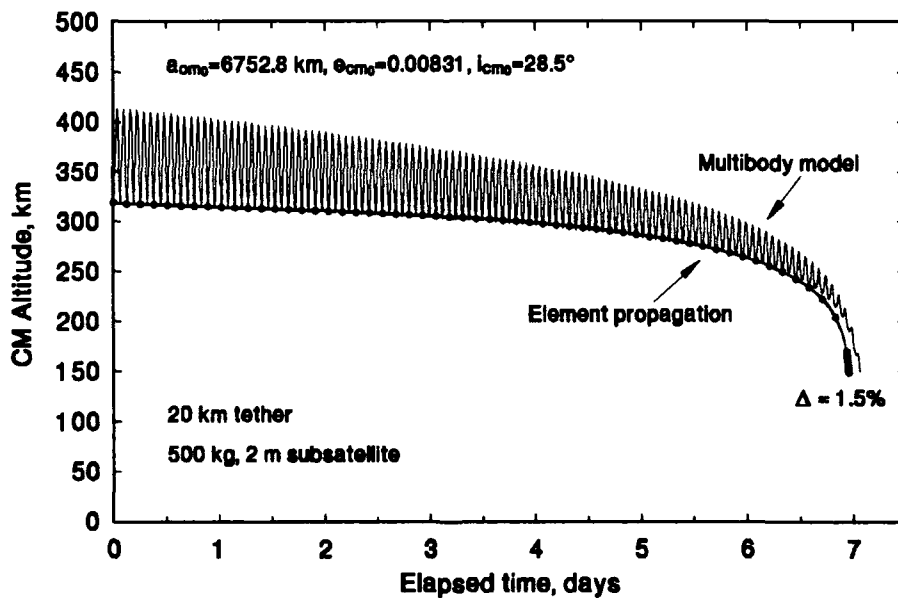


Figure 30. Element propagation model performance on "TSS-1".

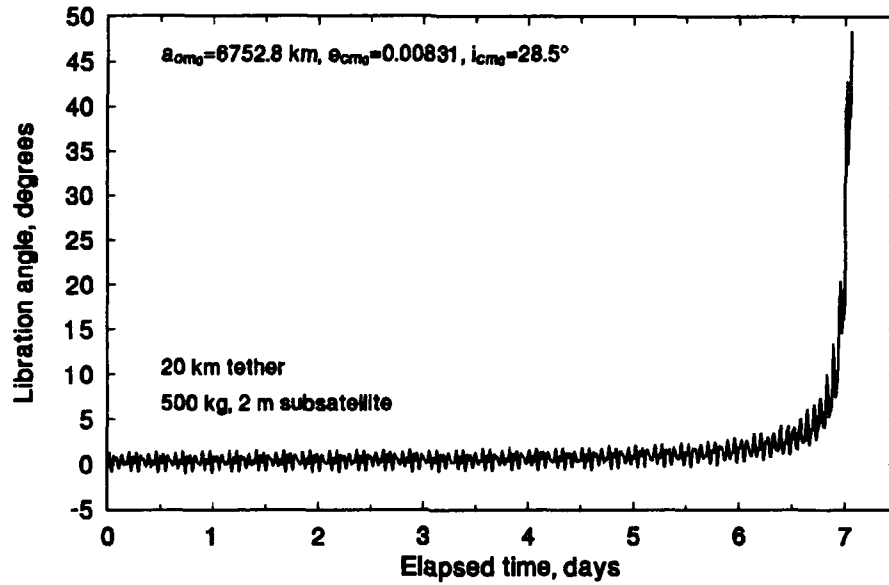


Figure 31. "TSS-1" in-plane libration angle during decay.

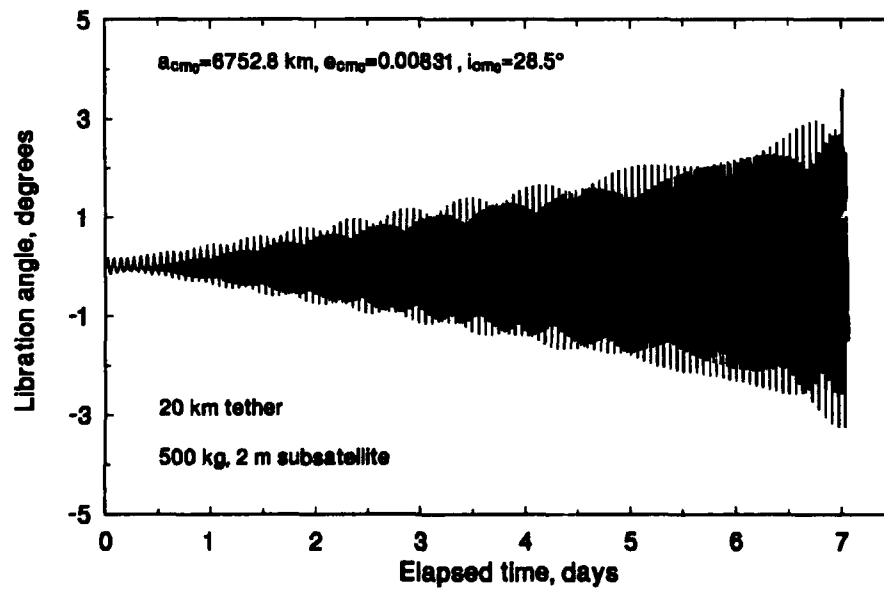


Figure 32. "TSS-1" out-of-plane libration angle during decay.

EPM yielded a result only 1.5% less than that of the MBM. The close agreement between the models is explained by the small libration angles which occurred during most of the orbital lifetime, as shown in Figures 31 and 32.

"SEDS" Orbital Decay. The Small Expendable Deployer System (SEDS) is a lightweight, spinning-reel system designed to deploy a payload attached to a 20 km tether, which is cut after deployment.<sup>92</sup> The first planned experiment with this system involves downward deployment of a subsatellite from a spent Delta rocket upper stage, which serves as the parent vehicle. Although the lifetime prediction methods derived in this research project do not include techniques for "complete" systems (i.e., parent-tether-subsatellite), the performance of the EPM in simulating the orbital decay of such systems is, nevertheless, of interest. Hence, the orbital decay of the SEDS system was simulated, assuming the 20 km tether connecting an 875 kg, 3.048 m parent and a 23 kg, 0.25 m subsatellite, was not cut.

The parent was initially in a 204 km x 704 km, 28.5° inclination orbit, and the subsatellite had been deployed downward, along the local vertical. As shown in Figure 33, the EPM produced a result only 2.8% less than the MBM. The slightly reduced accuracy, as compared to the cases presented previously, is explained by the larger libration angles which occurred in this scenario. Figures 34 and 35 show the in-plane and out-of-plane libration angles during the orbital decay.

Satellite Trailing an Upward-Deployed Tether. The final scenario considered in this section is that of a fairly large subsatellite trailing an upward-deployed tether. We

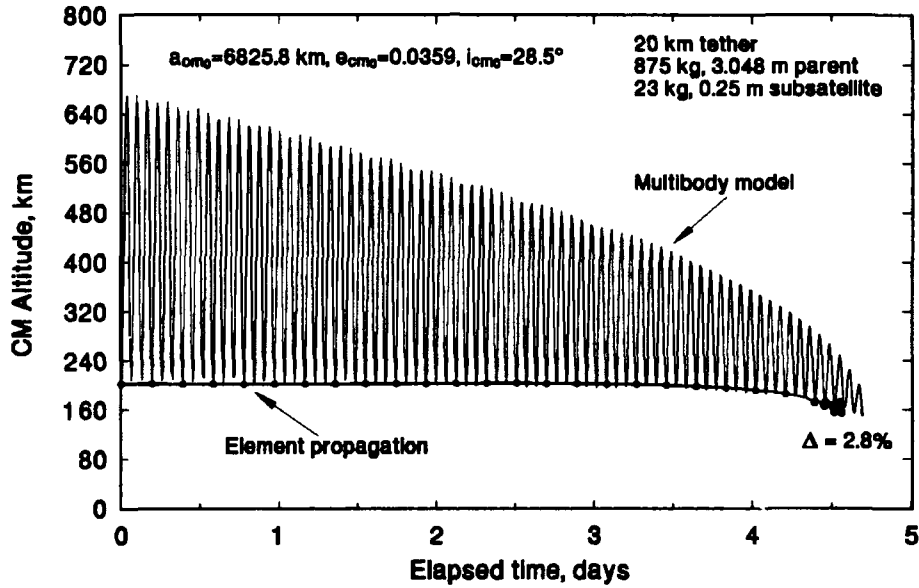


Figure 33. Element propagation model performance on "SEDS".

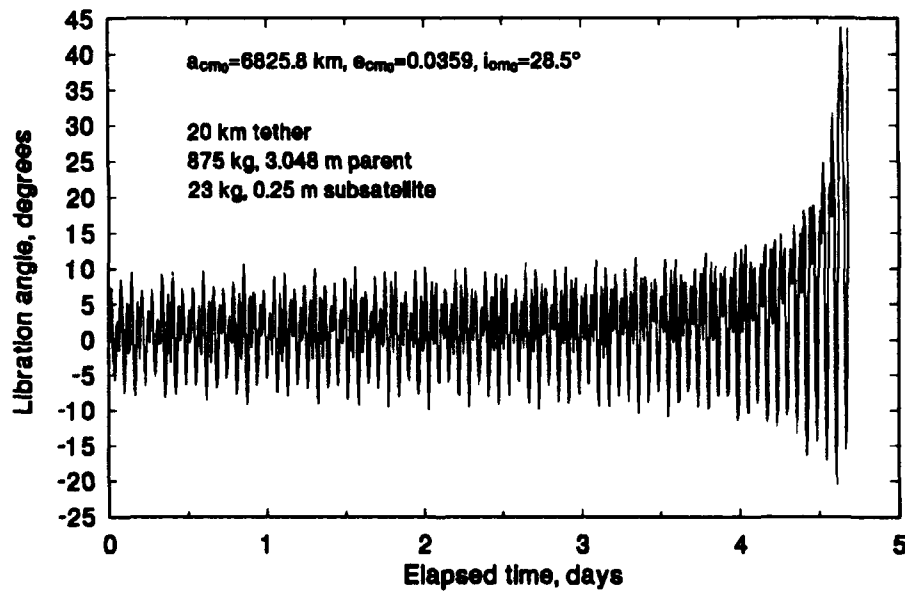


Figure 34. "SEDS" in-plane libration angle during decay.

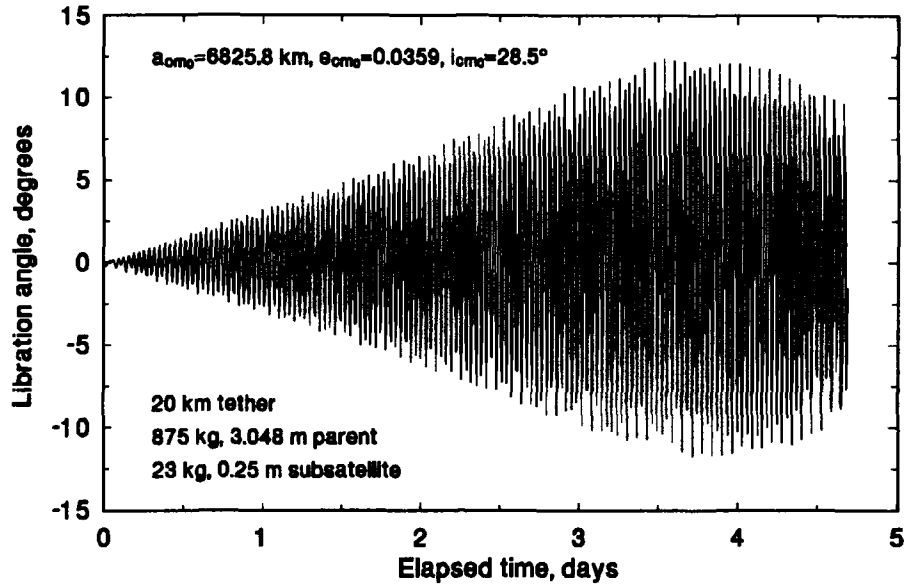


Figure 35. "SEDS" out-of-plane libration angle during decay.

assume a 2000 kg, 3.048 m subsatellite is trailing an upward deployed 20 km tether, whose parent end (i.e., the upper end, 20 km above the satellite) is initially in a circular,  $28.5^\circ$  inclination orbit, with a semi-major axis length of 6778.137 km. Thus, this is essentially a simulation of the orbital decay of a subsatellite deployed downward on a 20 km tether from a space station, or other vehicle, in a 400 km (altitude)circular orbit, and released.

Once again, as shown in Figure 36, the element propagation model performed admirably, yielding a lifetime to 150 km only 1.4% less than the MBM. The libration angle time histories were similar to those in the TSS-1 simulation.

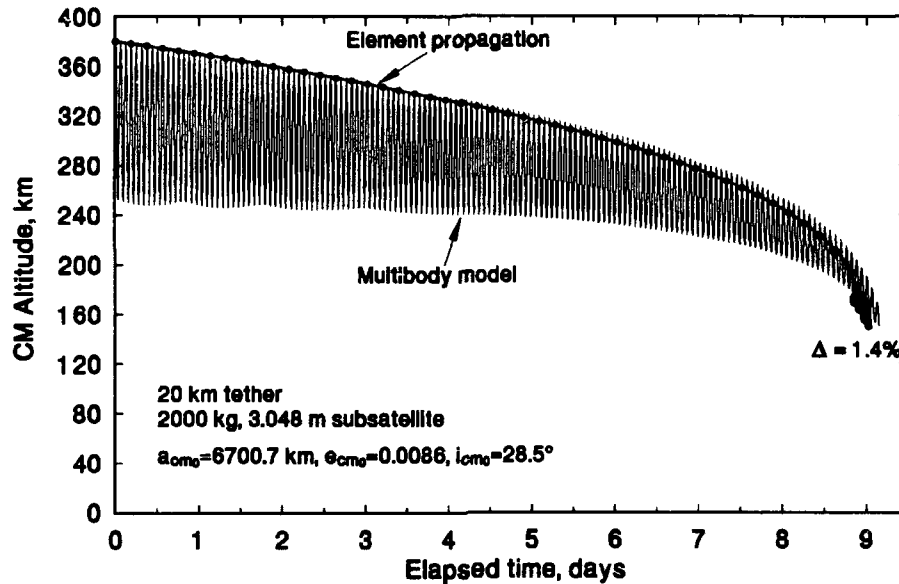


Figure 36. EPM performance on downward-deployed subsatellite.

### Orbital Lifetime Prediction Accuracy

Predicting the orbital lifetime of any satellite, via numerical simulation, or a semi-analytical method, is a process rife with uncertainty. The major uncertainties can be grouped into two categories: attitude and environment.

Attitudinal variables enter the calculations through the ballistic coefficient. The drag coefficient, the current cross-sectional or reference area, and even the current mass may not be precisely known. The current area and mass depend on the constantly varying physical configuration of the spacecraft, and may depend on its orientation relative to the direction of motion. The drag coefficient may vary with the

spacecraft's orientation and configuration, and is also a function of other physical properties, such as the vehicle's surface coating, its temperature, and the temperature and composition of the local atmosphere.

The models developed in this research project include the effects of attitudinal variations on the orbital lifetimes of freely-decaying tethered systems. In the MBM, a tether's cross-sectional area is continually adjusted in response to its elastic behavior, and the drag coefficients of the tether and any end-body are empirically derived, shape-dependent values for uncooled bodies, which vary as a function of the flow regime being encountered. We showed previously that the altitude variation of a tether's drag coefficient can significantly affect lifetime results. The results presented in the previous section demonstrated the accuracy of the EPM, as compared to the MBM, indicating that variations in tether cross-sectional area may be ignored.

The effects of environmental variables on the orbital lifetime of freely decaying systems have also been included in the models developed here. We have shown, for the altitudes of interest, that third body perturbations are insignificant compared to those resulting from aerodynamic drag and the Earth's oblateness. We have also observed that perturbations due to the Earth's oblateness may be many times larger than the drag perturbation, depending on the altitude. Hence, the models developed in this research project include contributions from both sources.

The major effects of the Earth's oblateness are reflected in the generated orbital lifetime results, since  $J_2$  is included in the gravitational potential function. The modeled atmosphere is oblate and rotating, and has the physical properties of a very

recently derived standard atmosphere model, the 1986 COSPAR International Reference Atmosphere.

To remove time and latitude dependency from the calculated lifetime results, globally and temporally averaged atmospheric properties defined by the COSPAR model were used. Rather than finding the average lifetime of a very large number of time and latitude dependent orbital decay cases, for each system and initial orbit of interest, the approach used in this project was to find the lifetimes of interest using average values for the atmosphere's properties.

In a recent study, Hoots and France<sup>93</sup> investigated the effect of environmental uncertainty on orbital lifetime calculations. They used the semi-analytical orbit propagation equations of Liu and Alford<sup>94</sup> to simulate the orbital decay of 18 single-mass satellites originating in various Earth orbits. Atmospheric mass density modeling was based on the Jacchia 1970 model, which provides atmospheric properties as a function of exospheric temperature, and includes corrections for diurnal, geomagnetic, semi-annual, and seasonal-latitudinal effects.<sup>95</sup>

The "prime movers" of the model atmosphere's properties are (1) the value of the solar flux at the 10.7 cm wavelength,  $F_{10.7}$ , and (2) disturbances of the geomagnetic field, as recorded by the Geomagnetic Planetary Index,  $A_p$ . The solar flux disturbs the geomagnetic field, and both variables cause perturbations in the atmosphere's mass density.<sup>96</sup>

The 18 orbital decay scenarios studied had a range of lifetimes from 10 days to one year. For each scenario, Hoots and France calculated 500 Monte Carlo lifetime

predictions, using a random draw from a generic solar cycle to determine values of  $F_{10.7}$  and  $A_p$  at each integration time step. Hence, the calculated result for each scenario was a sample of 500 lifetime predictions, any one of which could have occurred for the satellite of interest. The 500 lifetime predictions for each scenario were analyzed statistically, and it was found that the skewness and kurtosis for each scenario were very close to the theoretical values for normal distributions.<sup>97</sup> Plotting the frequency distribution of the 500 lifetime predictions for a given scenario yields a distribution that appears to be nearly normal.

As Hoots and France report, these results can be related to operational experience at the U. S. Space Command, where, over more than 30 years of experience, a "rule of thumb" has evolved concerning the uncertainty of decay predictions during the final 30 days of a satellite's orbital lifetime. The rule states that the uncertainty in a predicted lifetime during this period will be approximately  $\pm 20\%$ .<sup>98</sup>

An analysis of the results presented by Hoots and France shows that for the five scenarios in which the mean lifetimes were 30 days or less, the average of the three standard deviation levels, in terms of percent difference from the average lifetime for the scenario, was 17.6%, with a maximum three standard deviation level of 22.6%, and a minimum three standard deviation level of 14.6%. These numbers agree very well with the rule derived from Space Command's operational experience.

Including all scenarios having lifetimes of 60 days or less yields an average of the three standard deviation levels of 15.9%, with a minimum of 11.0% and a

maximum of 22.6%. The average of the three standard deviation levels of all 18 scenarios was 10.75%, with a minimum of 3.5% occurring in a scenario whose mean lifetime was 366 days, and a maximum of 22.6%, occurring in a scenario whose mean lifetime was 19 days.

These results have direct bearing on the accuracy required of the lifetime prediction method developed in this research project. Since we assume the numerically generated results are "truth", we have only to set accuracy limits on their functional representation. That is, we may use the results obtained by Hoots and France as a guideline to specify the accuracy with which the trained artificial neural networks must represent the generated orbital lifetime data.

Since almost all of the orbital lifetimes encountered in this project were expected to be less than 60 days, and the vast majority were expected to be less than 30 days, the required ANN accuracy limit was set at  $\pm 20\%$ . The lifetime prediction networks were trained to represent the training data, which spanned the applicable data space, with no more than  $\pm 10\%$  error at each point. In so doing, we attempted to keep eventual (network) generalization errors to within the desired  $\pm 20\%$  limit.

### **Predicting Free Tether Orbital Lifetime**

The EPM was used to simulate the orbital decay of free tethers originating in small eccentricity orbits. Points on a series of "lifetime prediction curves" were determined by varying the perigee and apogee radii ( $R_p$ ,  $R_a$ ) of a given tether's initial CM orbit. The radii included in this study range from 6578.137 km to 6878.137 km,

the limits discussed previously. All "baseline conditions" discussed in previous sections were also applied. Orbital lifetime was considered complete when a tether's CM reached 150 km altitude.

Free Tether Orbital Lifetime Prediction Curves. As shown in Figure 37, plots of the orbital lifetime of a 20 km free tether versus a factor involving the initial CM orbit size and shape ( $R_p$ ,  $R_a$ ,  $e$ ), on a semi-log plot, are fairly straight. The "size and shape factor",  $R_p + (R_a - R_p) / (1 + e)$ , was chosen as the abscissa, and used in a semi-log format, because this combination yields curves that may be easily read, even at points

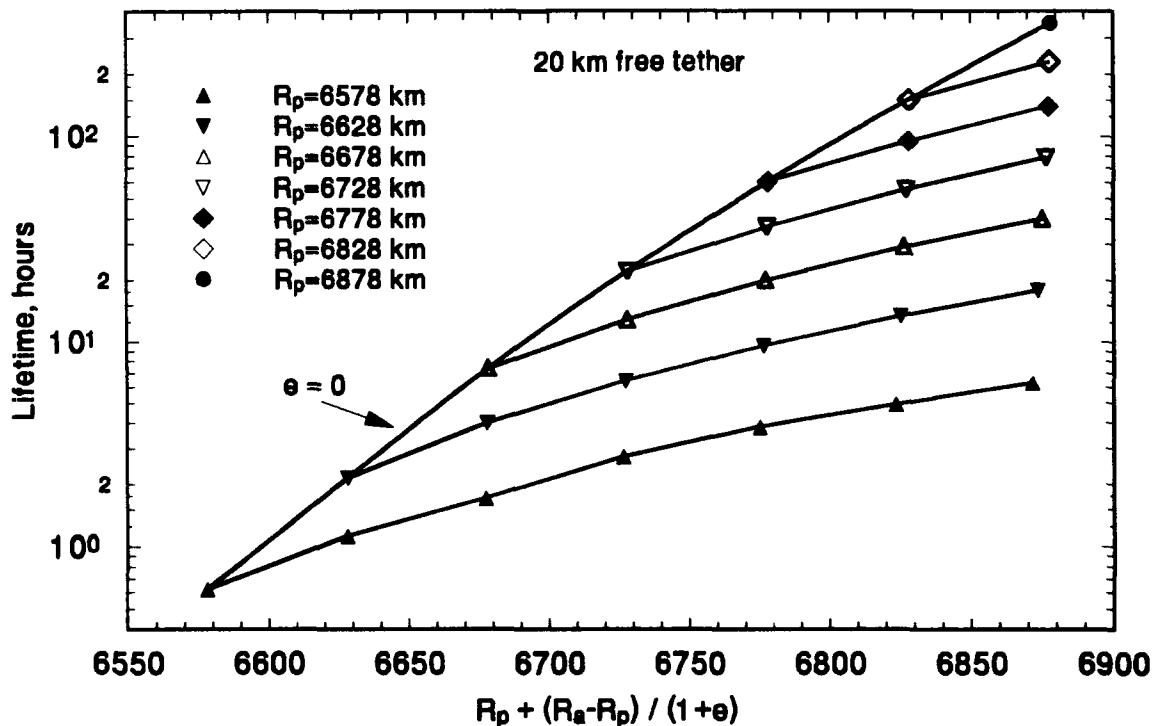


Figure 37. Orbital lifetime prediction curves for 20 km free tether.

other than those generated, to predict the orbital lifetime of the free tether. Initial perigee and apogee radii were varied in increments of 50 km, and each "horizontal" curve represents a fixed initial perigee radius. Predicting the lifetime of a tether having a perigee radius other than one of those shown can be easily accomplished by interpolating between two bounding curves.

The far left point on each horizontal curve is the lifetime of the tether when its CM is initially in a circular orbit ( $R_p = R_a$ ). Hence, the curve running from the

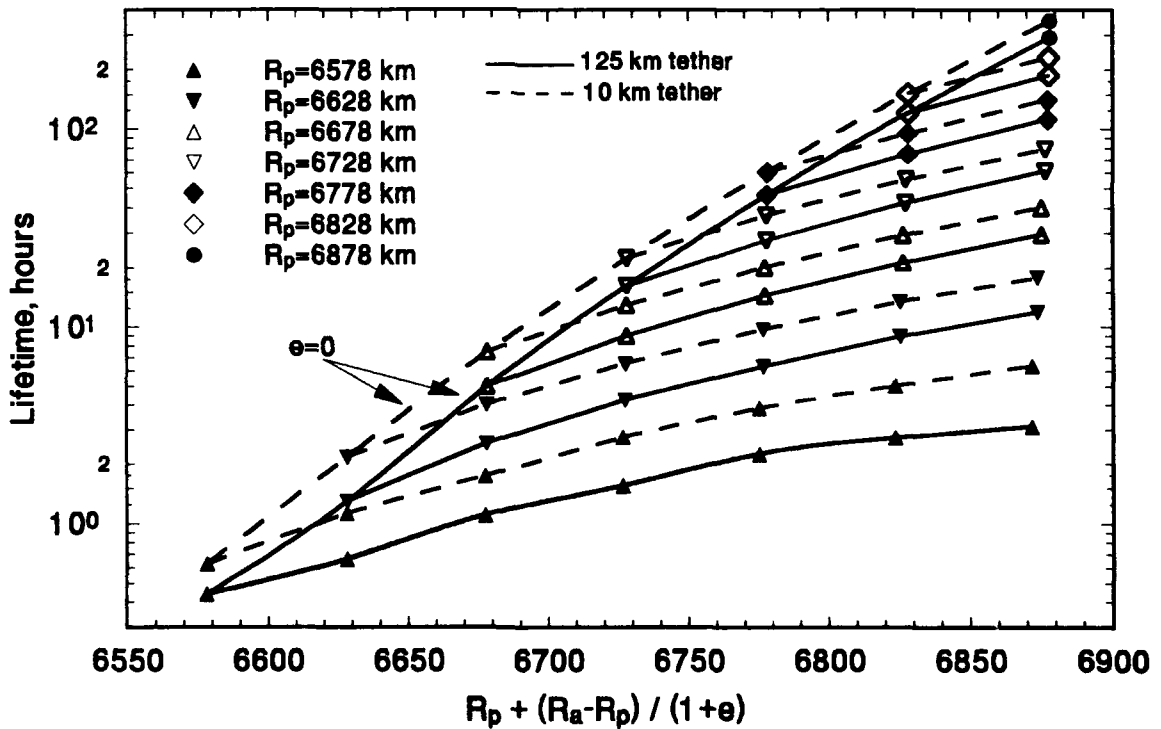


Figure 38. Orbital lifetime prediction curves for 125 km and 10 km free tethers.

lower left corner to upper right corner of the figure is the lifetime prediction curve for a 20 km free tether whose CM is initially in a circular orbit.

Figure 38 shows the lifetime prediction curves generated for 125 km and 10 km free tethers. The effect of tether length on orbital lifetime is demonstrated in this figure, which clearly shows that a "long" tether has a shorter lifetime than a "short" tether. On a percent difference basis, tether length has the most effect on orbits with initially small perigee and large apogee radii. The lifetimes depicted in the figure range from a low of less than 30 minutes for a 125 km tether whose CM is initially in a circular orbit of radius 6578.137 km, to a maximum of nearly 15 days (353.6 hours) for a 10 km tether originating in a circular orbit of radius 6878.137 km.

Neural Network Representation. As shown in the previous section, values for 3 independent variables were chosen to predict the orbital lifetime of a free tether: the CM orbit's initial radius of perigee,  $R_p$ ; the CM orbit's initial size and shape factor, "fac" (i.e., the factor shown below the horizontal axis in Figure 37 and Figure 38); and the tether's length,  $L$ .

An artificial neural network was trained, using the Minimum Percent Error training algorithm, to represent the mapping between the independent variables and the orbital lifetime of free tethers. The feed-forward network was composed of three linear input neurons, 30 hidden sigmoidal (logistic function) neurons, and one linear output neuron. As discussed in the **Artificial Neural Networks** Chapter, the input data values, i.e., the values of the independent variables, were scaled to the interval (0,1). The network output is the orbital lifetime, in units of hours.

As shown in Figure 39, the network requires that a scaled radius of perigee,  $R_p'$ , be provided to the first input neuron, a scaled size and shape factor,  $fac'$ , be provided to the second input neuron, and a scaled tether length,  $L'$ , be provided to the third input neuron. The scaled inputs have magnitudes between zero and one, and exact details of the scaling procedures are included in **Appendix C**.

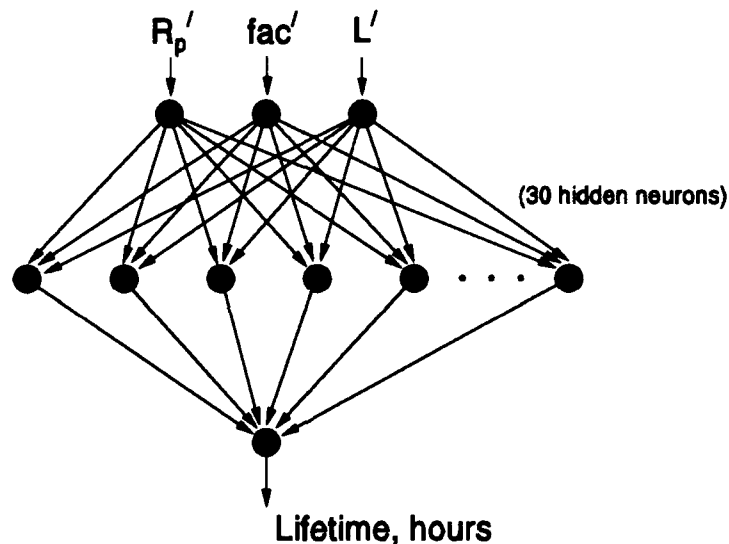


Figure 39. Free tether orbital lifetime prediction network structure.

The network was trained in stages, using data generated with the orbital element propagation model. Initially, lifetime data for 10 km, 60 km, and 125 km tethers comprised the training data set. The data set for each length consisted of 28 points, generated by systematically varying the tether CM's initial orbit radii of perigee and apogee in 50 km increments, which is precisely the procedure used to create each

length case shown in Figure 37 and Figure 38. Thus, the lifetime prediction data points that would be used to create a set of lifetime prediction curves, like those in Figure 37 for a 20 km tether, were used to train the network to represent the mapping for each length of interest.

The training data set was expanded after the network had learned to represent the lifetime data for the 10, 60, and 125 km tethers with less than 20% error at every point. The expanded training data set was composed of lifetime data for 10, 20, 40, 60, 80, 100, and 125 km tethers, a total of 196 points, in a four-dimensional space.

Training with the expanded data set was continued until the network had learned to represent the mapping at each point with less than 10% error. The final weights and biases for the trained network are included in **Appendix C**.

The network's generalization (i.e., interpolation) accuracy was tested by comparing its output with EPM-generated data for tether lengths and/or perigee and apogee radii not included in the training data. In most cases, the network's accuracy was significantly better than the 10% goal, and the maximum error observed in any case was slightly less than 12%.

Figure 40 compares the network's output for a 50 km tether, which was a length not included in the training data set, with data generated using the EPM. The network output was generated by varying the perigee and apogee radii in 25 km and 10 km increments, respectively. The accuracy of the results in this case is typical. The maximum representation error was 9.1%, occurring at the largest magnitude lifetime value.

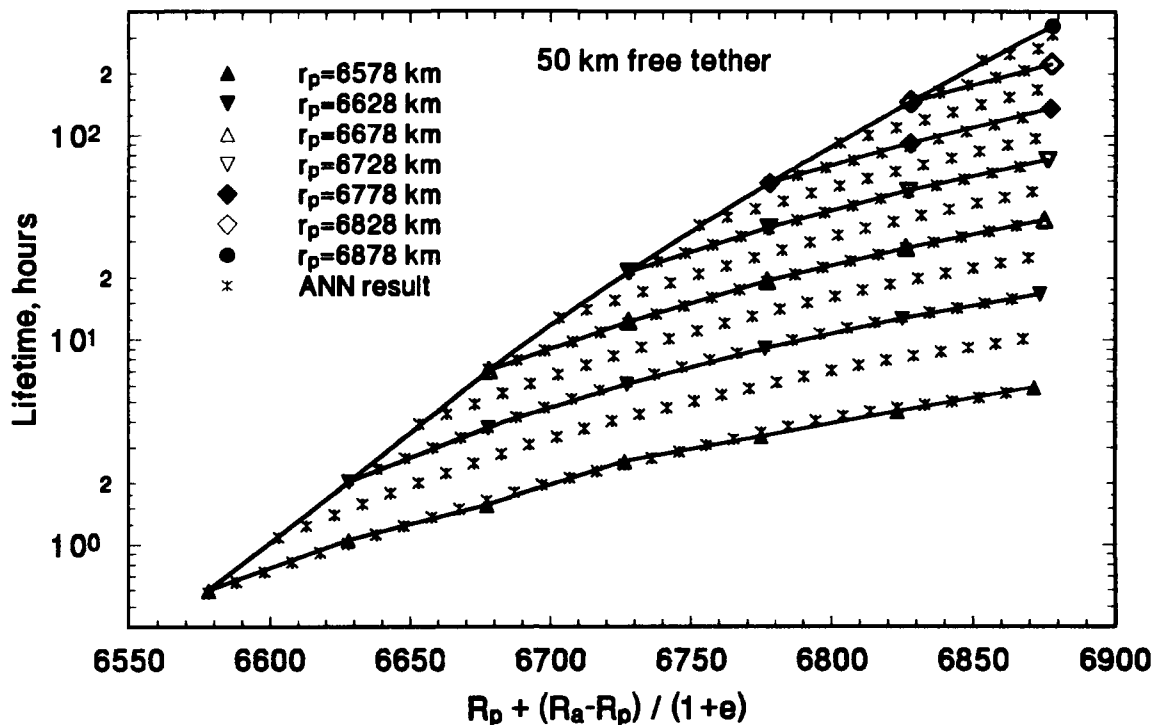


Figure 40. Trained network output and orbital lifetime data for 50 km free tether.

Additional results demonstrating the trained network's accuracy in representing the orbital lifetime of free tethers are presented later in this Chapter.

Comparison with Single-Mass Orbital Lifetime Results. As we noted previously, single-mass orbital lifetime prediction techniques rely on the ballistic coefficient to account for the dissipative effects of aerodynamic drag. Since the ballistic coefficient for a tether is independent of its length, the single-mass techniques will make no distinction between long and short tethers, which may result in significant errors. We

earlier showed one case where reducing the length of a freely decaying tether increased its lifetime by 17%.

To further investigate the errors which may result from using single-mass techniques, the EPM was used to generate lifetime prediction curve data for (single-mass) spheres whose cross-sectional area and total mass were equivalent to that of deployed tethers. Data were generated for spheres representing tether lengths of 10, 20, 40, 60, 80, 100, and 125 km, the lengths included in the "expanded" network training data set.

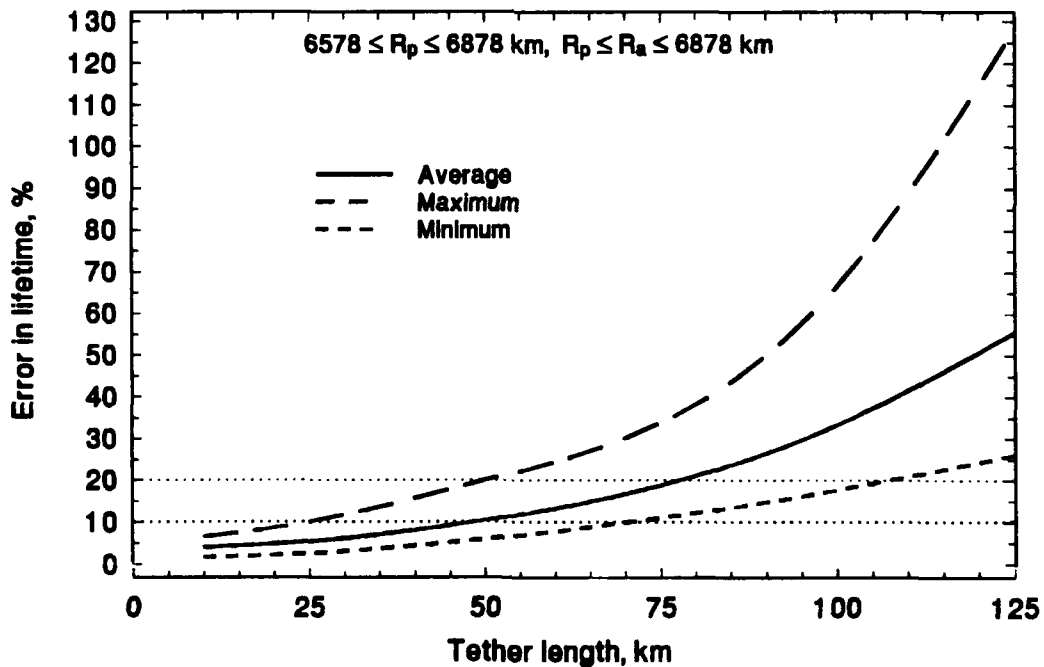


Figure 41. Error in equivalent sphere orbital lifetimes.

The maximum, minimum, and average percent error in the sphere results for each length, as compared to deployed tether results, are shown in Figure 41. The magnitude of the lifetimes represented range from less than 30 minutes, to more than two weeks. The figure shows that the maximum error exceeds 10% for tether lengths greater than approximately 25 km, while the average error exceeds 10% and the maximum error exceeds 20% for tethers longer than approximately 48 km. The average error exceeds 20% for tethers longer than approximately 77 km, and the minimum error is greater than 20% for tethers longer than approximately 105 km.

Thus, we conclude, based on our earlier discussion of desired reasonable accuracy in predicted orbital lifetimes, that single-mass techniques are generally unreliable for free tethers longer than approximately 48 km, although results with less than 10% error may be obtained for tethers as long as 70 km. Single-mass results should never be used for tethers longer than approximately 105 km, as this is the length at which the minimum error exceeds 20%.

Recalling that the free tether lifetime prediction network described earlier provides predicted orbital lifetimes within 10% of those calculated by the EPM, we note that the network's output will, on average, provide a better prediction than a single-mass result, for tethers longer than approximately 48 km. For some cases involving tether lengths between 25 km and 48 km the network's result will be more accurate than single-mass results, since the maximum error exceeds 10% in this region. Finally, we observe that, without exception, the trained network will provide a more accurate result for any tether longer than approximately 70 km.

### **Effects of Initial Inclination, Argument of Perigee, and True Anomaly**

The orbital lifetime prediction results presented in the previous section are based on the assumption that a system's CM is initially in an orbit with an inclination ( $i$ ) of  $28.5^\circ$ , and zero initial argument of perigee ( $\omega$ ) and true anomaly ( $\nu$ ) values. In this section, results illustrating the effects on orbital lifetime of "non-standard" initial values for these variables - i.e., values other than those previously assumed - are presented. (The longitude of the orbit's ascending node ( $\Omega$ ) is of no consequence, since neither the Earth nor atmosphere are modeled with longitudinal variations.) A strategy to account for inclination, argument of perigee, and true anomaly effects on orbital lifetime predictions is derived, and an ANN trained to represent numerically generated data is described. The ANN's generalizing ability is demonstrated, and the performance of the derived "lifetime correction factor" procedure is tested in a "worst case" scenario. We also describe an inclination-only lifetime correction factor procedure, and test its performance in the "worst case" scenario. Demonstration of the abilities of both procedures, in a wide variety of scenarios, is reserved for the last section of this Chapter.

**Basic Phenomena.** In this section we illustrate, separately, the effects on orbital lifetime of initial orbit inclination, argument of perigee, and true anomaly. The inclination dictates the altitude of an object in a given orbit -- high inclination orbits involve higher altitudes than low inclination orbits, due to the Earth's ellipsoidal shape. The value of the argument of perigee, which specifies the angular distance

between the ascending node vector and the eccentricity vector, relates directly to the altitude of the orbit's point of closest approach. A high altitude perigee will result in longer lifetimes than a low altitude perigee, if all other factors are equal. The initial true anomaly value, which specifies a system's initial position relative to perigee, indicates whether the system is inbound to, or outbound from, the point of closest approach. The initial true anomaly value may make a significant difference in the orbital lifetime of a system in a highly eccentric orbit with a small perigee radius.

Figure 42 shows the physical relationship between the angular orbital elements and the geocentric latitude,  $\phi$ . A well-known identity for right spherical triangles<sup>99</sup> may be used to express the latitude as a function of the orbital elements,

$$\sin \phi = [\sin i][\sin (\omega + \nu)] = [\sin i][\sin U] \quad (89)$$

where, as before,  $U$  is the argument of latitude. One interpretation of this relation is that the geocentric latitude equals the orbit inclination, as modified by the sine of the argument of latitude. If  $U$  is  $90^\circ$ , we observe that the inclination equals the geocentric latitude, which is a maximum at this point.

Recalling from the **Mathematical Models** Chapter that altitude above an ellipsoidal Earth increases as  $\sin^2\phi$  increases, we note that the altitude of any point in an orbit will therefore increase as  $\sin^2 i$  increases. Since higher altitudes mean lower atmospheric mass density, and correspondingly lower aerodynamic drag forces, we deduce that a system in a high inclination orbit will have a longer orbital lifetime than an identical system in an identical orbit at a lower inclination. The inclination will also

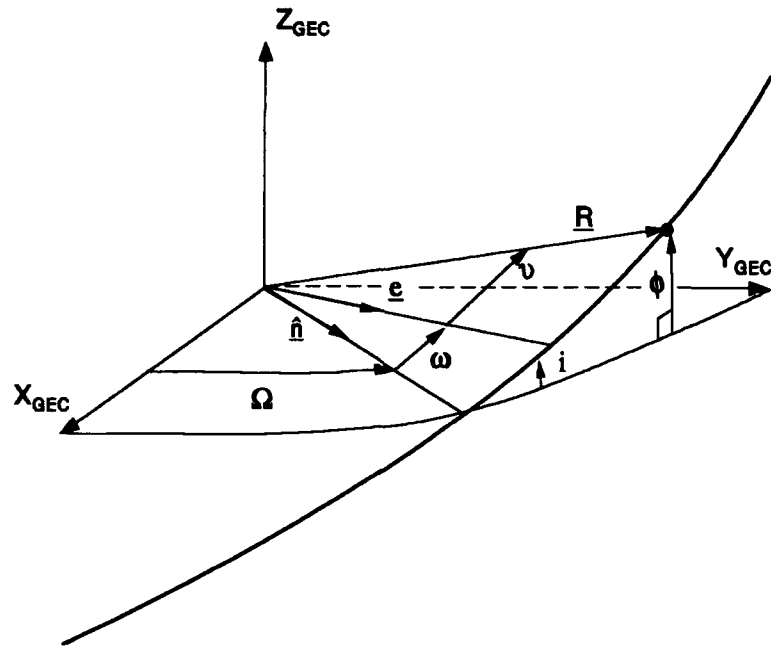


Figure 42. Geocentric latitude and angular orbital elements.

affect the orbit radius at which the lifetime is considered complete, since calculations continue until the system CM reaches 150 km altitude, which is latitude dependent.

To illustrate these effects, lifetime prediction curve data (i.e., 28 points per case,  $6578.137 \text{ km} \leq R_p \leq 6878.137 \text{ km}$ ,  $R_p \leq R_a \leq 6878.137 \text{ km}$ ) was generated, using the EPM, for 10 km, 50 km, and 125 km tethers originating in orbits inclined at  $80^\circ$  and  $28.5^\circ$ , with arguments of latitude equal to zero. The lifetimes at each simulation point are compared in Figure 43, which shows the percent differences of the  $i = 80^\circ$  lifetimes from the  $i = 28.5^\circ$  lifetimes. The percent differences were calculated from

$$\text{Lifetime Difference (\%)} = \frac{\mathcal{L}_{i=80^\circ, \omega=v=0} - \mathcal{L}_{i=28.5^\circ, \omega=v=0}}{\mathcal{L}_{i=28.5^\circ, \omega=v=0}} \times 100 \quad (90)$$

where  $\mathcal{L}$  is the orbital lifetime, to 150 km altitude, of a selected tether. Only lifetimes for equal length tethers are compared.

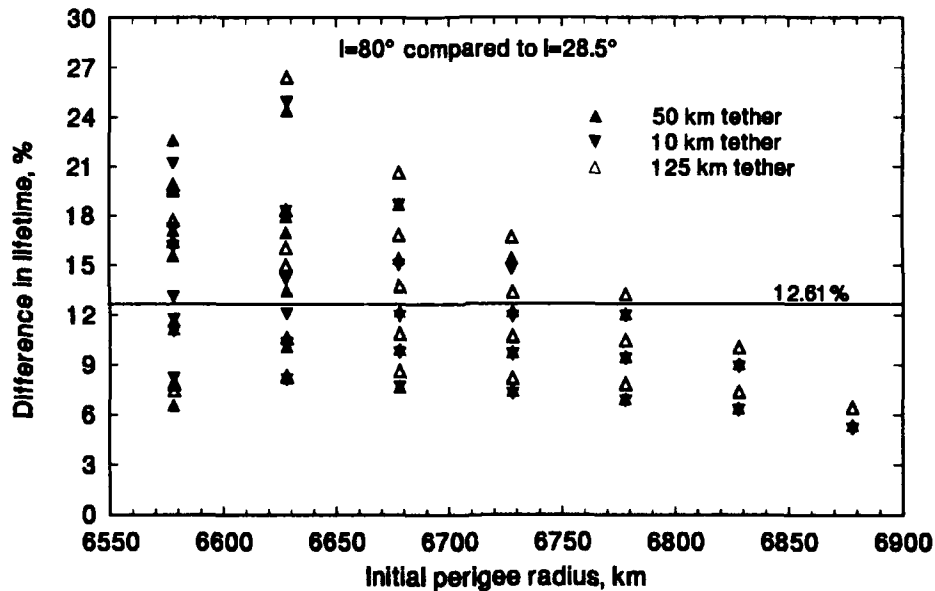


Figure 43. Effect of initial orbit inclination on lifetime ( $\omega = \nu = 0$ ).

Figure 43 illustrates two important characteristics. First, we note that the largest percent differences in orbital lifetime occur for the longest length tether. This is in keeping with the fact that a "long" tether will encounter the more dense portions of the atmosphere sooner than will a "short" tether. Second, we see that the percent

differences in lifetime decrease as the initial radius of perigee increases. This result is also logically expected, since the relative significance of altitude differences, resulting from the Earth's ellipsoidal shape, is reduced with increased orbit radii. The figure also shows the mean of the percent differences in lifetime, 12.61%. As shown in Table 2, this result is identical to the mean of the percent differences for the 50 km tether.

Table 2. Lifetime percent difference statistics,  $i = 80^\circ$  vs.  $i = 28.5^\circ$ .

Tether Length (km)	Mean Difference (%)	Maximum Difference (%)	Minimum Difference (%)
10	12.17	24.9	5.1
50	12.61	24.4	5.4
125	13.06	26.4	6.4

If all orbital elements are held constant while the initial argument of perigee is varied, Eq. (89) shows that the geocentric latitude at which perigee occurs will also vary. As we previously observed, increasing the latitude of the point of closest approach has the result of increasing its altitude, and hence extending orbital lifetime. When  $\omega$  is  $90^\circ$ , perigee occurs at the most northern point in an inclined orbit, which is also the point at which perigee altitude is a maximum. Hence, the orbital lifetime of systems originating in orbits whose argument of perigee is  $90^\circ$  (or  $270^\circ$ ) will have

longer lifetimes than identical systems originating in identically sized and shaped orbits whose initial arguments of perigee have any other value.

Figure 44 shows the percent differences in orbital lifetime for 10, 50, and 125 km tethers originating in orbits which are identical except for their initial arguments of perigee. The EPM was used, as described in the previous example, to generate the lifetime prediction curve data for each of the tethers. In each case, the initial inclination and true anomaly values were  $28.5^\circ$  and zero, respectively.

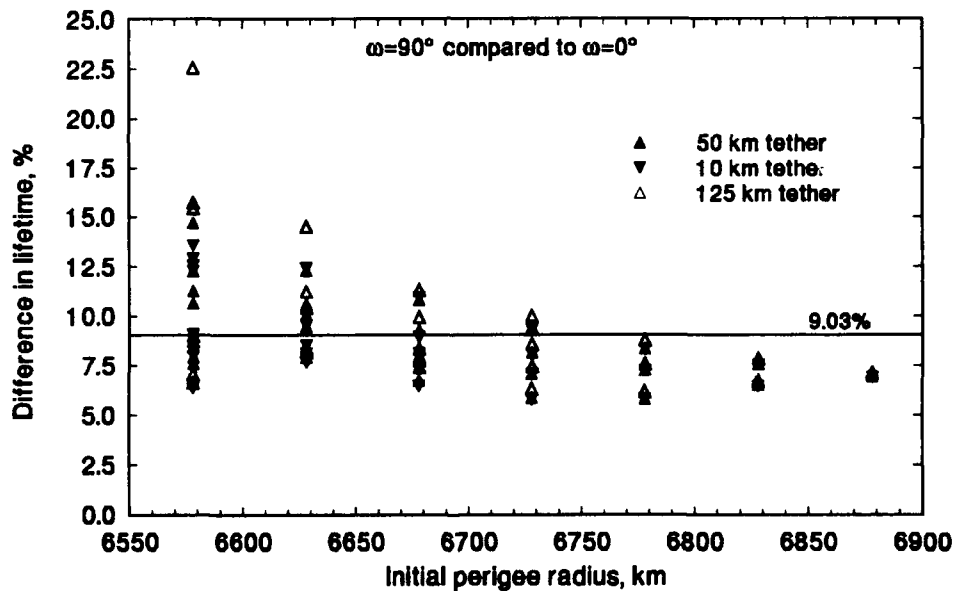


Figure 44. Effect of initial argument of perigee on lifetime ( $i = 28.5^\circ$   $v = 0$ ).

The characteristics noted in the inclination example are again evident. The largest percent differences in the orbital lifetimes occur with the longest length tether,

and the effects of the initial differences in argument of perigee diminish as the radius of perigee increases.

Table 3 lists the mean, maximum and minimum percent differences in orbital lifetimes which occurred for each tether length. Here, we see that the means of the lifetime differences are separated by less than one percentage point. We also note that the mean for the 50 km tether is close to the mean of all the cases, 9.03%, shown in Figure 44.

Table 3. Lifetime percent difference statistics,  $\omega = 90^\circ$  vs.  $\omega = 0$ .

Tether Length (km)	Mean Difference (%)	Maximum Difference (%)	Minimum Difference (%)
10	8.73	13.6	5.8
50	8.81	14.7	5.8
125	9.55	22.6	6.2

The initial true anomaly value indicates a system's starting location in its orbit. Values between zero and  $180^\circ$  indicate the system is outbound from perigee, approaching apogee, while values greater than  $180^\circ$  mean the system has passed through apogee and is approaching perigee.

Figure 45 shows the percent differences in the lifetimes of 10, 50, and 125 km tethers released at apogee ( $\nu = 180^\circ$ ), as compared to systems released at perigee

( $v = 0$ ). The EPM was used to generate the lifetime data, and the initial orbit inclination and argument of perigee were  $28.5^\circ$  and zero, respectively, for each case.

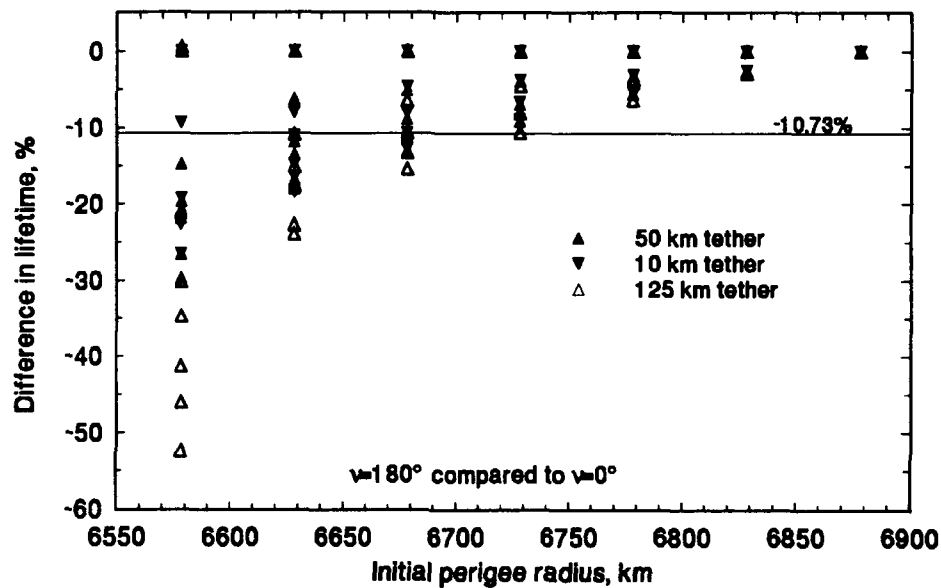


Figure 45. Effect of initial true anomaly on lifetime ( $i = 28.5^\circ$   $\omega = 0$ ).

Once again, we note that the percent differences in lifetime are largest for the 125 km tether. We also observe that the difference in true anomaly has an essentially negligible effect on orbits whose initial radius of perigee is greater than approximately 6828 km. This fact, along with the large percent differences which occur when the radius of perigee is 6578.137 km, indicates that differences in true anomaly have significant effects on orbit decay only in the first few orbit revolutions.

Table 4. Lifetime percent difference statistics,  $\nu = 180^\circ$  vs.  $\nu = 0$ .

Tether Length (km)	Mean Difference (%)	Maximum Difference (%)	Minimum Difference (%)
10	-9.18	0.0003	-26.5
50	-9.60	0.0003	-29.6
125	-13.42	0.6	-52.4

As shown in Figure 45, the mean of all the percent differences in this scenario was -10.73%. We see in Table 4 that the mean of the percent differences for the 50 km tether is the closest of the means of the three lengths to this value. The figure and table show that lifetime differences greater than 20% in magnitude occurred for each of the tether lengths considered. The largest differences occurred when the initial radius of perigee was 6578.137 km, but these quickly diminished as initial perigee radius was increased.

Combined Effects. In the previous section, we demonstrated, separately, the effects of initial orbit inclination, argument of perigee, and true anomaly on the orbital lifetime of free tethers. If the non-standard initial values occur simultaneously for all three variables, we expect to obtain lifetime results which are significantly different from those of the "standard" scenario,  $i = 28.5^\circ$ ,  $\omega = \nu = 0$ .

Figure 46 shows the percent differences in orbital lifetimes for a 125 km tether whose initial angular orbital elements are a combination of the scenarios presented earlier:  $i = 80^\circ$ ,  $\omega = 90^\circ$ ,  $\nu = 180^\circ$ . As before, data the figure was created using

lifetime prediction curve data generated by the EPM. The percent differences between the "standard" and "actual" lifetimes were calculated from

$$\text{Lifetime Difference (\%)} = \frac{\mathcal{L}_{\text{standard}} - \mathcal{L}_{\text{actual}}}{\mathcal{L}_{\text{actual}}} \times 100 \quad (91)$$

where  $\mathcal{L}_{\text{actual}}$  is the 125 km tether's orbital lifetime when initially  $i = 80^\circ$ ,  $\omega = 90^\circ$ ,  $\nu = 180^\circ$ , and  $\mathcal{L}_{\text{standard}}$  is the same tether's lifetime when initially  $i = 28.5^\circ$ , and  $\omega = \nu = 0$ .

The initial conditions applied in the "actual" scenario essentially represent a "worst case". The initial orbit inclination is much larger than that of the standard case, implying significant altitude differences between the two. The  $90^\circ$  argument of perigee places the point of closest approach at the most northern point of the orbit, where the altitude of perigee is greatest. The  $180^\circ$  true anomaly value indicates the system CM is initially at apogee, which means the system is bound for perigee, and the most dissipative region of the orbit.

As Figure 46 shows, the percent differences between the lifetimes in the standard cases, and those which result when the 125 km tether originates in the combined effects, "actual" orbits, are quite large. The mean of the differences is -46.3%, with a maximum difference of -66.1%, and a minimum of -29.5%. In other words, on average, the lifetime of a 125 km tether originating in an orbit with  $i = 28.5^\circ$ , and  $\omega = \nu = 0$ , will be only 53.7% of the tether's lifetime when it originates in an identically sized and shaped orbit with  $i = 80^\circ$ ,  $\omega = 90^\circ$ , and  $\nu = 180^\circ$ .

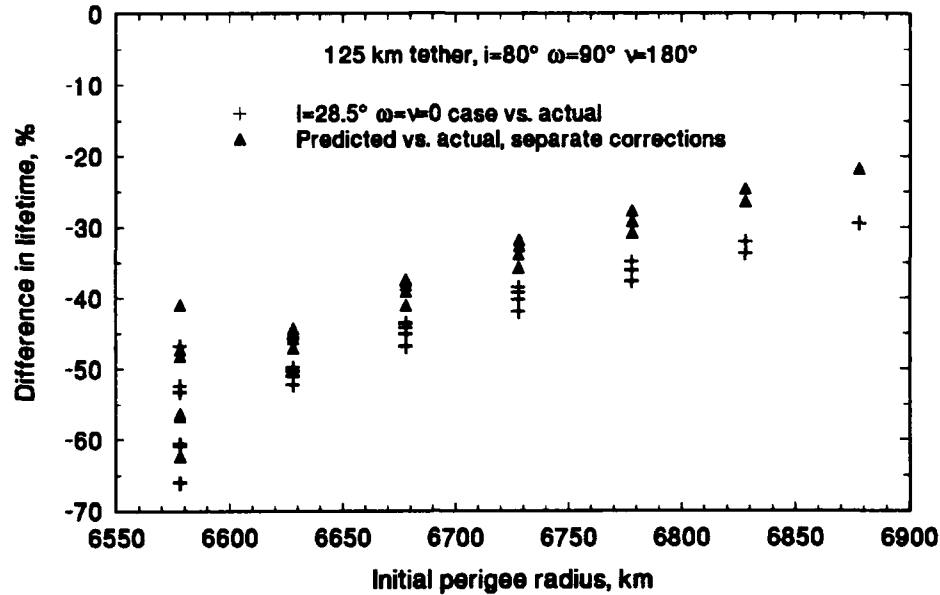


Figure 46. Effect of initial inclination, argument of perigee and true anomaly.

Figure 46 also shows the percent differences in lifetime which result if a correction factor equal to the sum of the means obtained in the separate effects scenarios is applied. The sum of the percent difference means obtained for the 125 km tether is 9.19% (13.06% + 9.55% - 13.42%), and the predicted lifetimes are calculated from

$$\mathcal{L}_{\text{predicted}} = 1.0919 \mathcal{L}_{\text{standard}} \quad (92)$$

The percent differences in the orbital lifetimes are calculated from

$$\text{Lifetime Difference (\%)} = \frac{\mathcal{L}_{\text{predicted}} - \mathcal{L}_{\text{actual}}}{\mathcal{L}_{\text{actual}}} \times 100 \quad (93)$$

The mean of the percent differences between the lifetimes obtained using Eq. (92) and those which result when the 125 km tether originates in the combined effects, "actual" orbits, is -41.4%, with a maximum difference of -62.4% and a minimum of -21.8%.

The poor performance of the summation correction factor is not surprising. As we noted previously, geodetic altitude varies with the square of the sine of geocentric latitude, which is the product of the sines of the orbit inclination and argument of latitude. The altitude specifies an atmospheric mass density, whose altitude variation is exponential, which is a key factor in the calculation of aerodynamic drag. Hence, we see that the effects of the initial angular orbital elements are interrelated, and highly nonlinear.

Nevertheless, the idea of predicting the orbital lifetime of a tether originating in a "non-standard" orbit, by applying a correction factor to lifetime results obtained for a "standard" case, is an approach we will pursue. In the next section, we will derive and implement a strategy, based on a system's initial angular orbital elements, to obtain appropriate lifetime correction factors.

Deriving Lifetime Correction Factors Using An Averaging Approach. As the results in the previous section's scenarios suggest, it may be possible, by shifting the center of the lifetime percent difference error band, to predict, adequately, orbital lifetimes by applying a correction factor to "standard" lifetime results ( $i = 28.5^\circ$   $\omega = \nu = 0$ ). To minimize simulation cases and numerical representation complexity, an "averaging" approach was used. The objective was to find correction factors that apply to groups

of cases, i.e., those which occur in similar "scenarios", rather than attempting to find specific corrections for each possible case.

The analyses and results presented in the previous section show that initial values of three angular orbital elements have potentially significant effects on orbital lifetime: orbit inclination, argument of perigee, and true anomaly. Additionally, the results show some dependence on tether length.

We may evaluate the significance of the spread of the minimum, maximum, and mean percent differences shown in Table 2, Table 3, and Table 4 by converting the percentages to lifetimes, in terms of the "standard" case lifetimes,  $\mathcal{L}_{\text{standard}}$ . Our objective is to determine whether or not using the mean percent difference for a given scenario will yield acceptable approximations for the lifetimes of all, or at least most, of the cases possible in the scenario.

If the mean percent difference is to be used to provide reliable lifetime estimates, it must yield results within  $\pm 20\%$  of the value of any "actual" lifetime occurring in a scenario (recall that each "scenario" is composed of many individual "cases"). We can determine the mean percent difference's relationship to all cases in a given scenario by comparing the lifetimes produced using the mean percent difference as a "correction factor", with the lifetimes occurring in the maximum and minimum percent difference cases. If the estimated lifetimes are within  $\pm 20\%$  of the lifetimes in the extreme cases, the mean percent difference will yield acceptable results for all cases in the scenario. The percent error between the estimated and actual lifetimes, in the maximum percent difference case, is

$$\text{Max Value Error (\%)} = \frac{\mathcal{L}_{\text{mean}} - \mathcal{L}_{\text{max}}}{\mathcal{L}_{\text{max}}} \times 100 \quad (94)$$

and the error in the minimum percent difference case is

$$\text{Min Value Error (\%)} = \frac{\mathcal{L}_{\text{mean}} - \mathcal{L}_{\text{min}}}{\mathcal{L}_{\text{min}}} \times 100 \quad (95)$$

where  $\mathcal{L}_{\text{max}}$  is the lifetime occurring in the maximum percent difference case,  $\mathcal{L}_{\text{min}}$  is the lifetime occurring in the minimum percent difference case, and  $\mathcal{L}_{\text{mean}}$  is the estimated lifetime which results from applying the mean percent difference as a correction factor to the system's lifetime in the applicable standard-scenario case.

For example, the mean percent difference in orbital lifetime shown in Table 2, for a 50 km tether, is 12.61%. This indicates that on average, the orbital lifetime when  $i = 80^\circ$ , and  $\omega = \nu = 0$ , is 1.1261  $\mathcal{L}_{\text{standard}}$ . In other words, on average, the orbital lifetime in the "non-standard" case ( $i = 80^\circ$ ,  $\omega = \nu = 0$ ) is 1.1261 times the lifetime of the same tether, released in an identical size and shape "standard" orbit ( $i = 28.5^\circ$ ,  $\omega = \nu = 0$ ). The largest difference between 50 km tether lifetimes in the standard and non-standard cases was 24.4%, or 1.244  $\mathcal{L}_{\text{standard}}$ . Similarly, the minimum difference was 1.054  $\mathcal{L}_{\text{standard}}$ . Checking the maximum and minimum percent difference cases, we obtain

$$\text{Max Value Error} = \frac{1.1261 - 1.244}{1.244} \times 100 = -9.48\%$$

$$\text{Min Value Error} = \frac{1.1261 - 1.054}{1.054} \times 100 = 6.84\%$$

These results show that, for the 50 km tether, using the mean percent difference in lifetimes as a "correction factor" to predict non-standard lifetimes from standard lifetimes, will yield results within  $\pm 10\%$  of the lifetime value for any non-standard orbit encompassed by the lifetime prediction curve data.

The individual effects scenarios presented in the previous section indicate some dependence on tether length. However, the mean percent differences in lifetime for the 50 km tether, in each of the individual effects scenarios, were very close to the means of the combined data for the 10, 50, and 125 km tethers. Hence, we made the simplifying assumption that results for a 50 km tether are indicative of those for all tether lengths from 10 km to 125 km. Table 5 shows, for each of the three tether lengths, the results of using Eqs. (94) and (95) to compare lifetimes obtained using the 50 km tether's mean percent difference with those occurring in the maximum and minimum percent difference cases. Clearly, using the 50 km tether's mean percent difference as a correction factor between the standard and non-standard cases, in this scenario, will yield acceptable approximations for the lifetime of any length tether (10-125 km). Tables 6 and 7 show the results of performing the same procedure on results obtained in the argument of perigee and true anomaly individual effects scenarios.

Table 5. Error limits using 50 km mean percent difference,  $i = 80^\circ$  vs.  $i = 28.5^\circ$ .

Tether Length (km)	Max Value Error (%)	Min Value Error (%)
10	-9.84	7.15
50	-9.48	6.84
125	-10.91	5.84

Table 6. Error limits using 50 km mean percent difference,  $\omega = 90^\circ$  vs.  $\omega = 0$ .

Tether Length (km)	Max Value Error (%)	Min Value Error (%)
10	-4.22	2.85
50	-5.14	2.85
125	-11.25	2.46

Table 7. Error limits using 50 km mean percent difference,  $\nu = 180^\circ$  vs.  $\nu = 0$ .

Tether Length (km)	Max Value Error (%)	Min Value Error (%)
10	-9.60	23.00
50	-9.60	28.41
125	-10.14	89.92

With the exception of the true anomaly scenario, the tables on the previous page show that using the 50 km tether's mean percent difference as a lifetime correction factor yields acceptable results. For the true anomaly scenario, Figure 45 shows that the largest percent differences, for each of the tether lengths, occur when the systems originate in orbits with  $R_p = 6578.137$  km. If this radius of perigee is eliminated from the analysis, the largest percent difference, including the 125 km tether, is approximately -24%, for which the *Min Value Error* is only 18.9%. We also note that with a 6578.137 km initial perigee radius, the maximum orbital lifetime for a 10 km tether is approximately seven hours, and the maximum lifetime for a 125 km tether is less than three hours. Hence, we see that although the percent differences between the predicted and actual lifetimes may be large in these cases, the magnitude differences are rather small. We can tolerate this type of error, and also note that it only occurs for systems originating in orbits with relatively small initial perigee radii.

Based on these results, we continue to assume that results for a 50 km tether are indicative of those for all tethers. This allows us to use data generated for just one length in deriving lifetime correction factors. We demonstrate the accuracy of this approach later in this Chapter.

Next, we turn our attention to the problem of devising some method to account for the effects of the nearly endless possible combinations of initial orbit inclination, argument of perigee, and true anomaly. As before, our objective is to find some way to predict adequately the orbital lifetimes of groups of possible cases.

Figure 47 shows the variation of orbital lifetimes of a 50 km tether with variations in initial true anomaly. Each point in the figure is the average percent difference between the 28 lifetime prediction curve data points for a particular  $(\omega, \nu)$  (non-standard) scenario and the 28 lifetime prediction curve data points for the  $\omega = \nu = 0$  (standard) scenario. Hence, 1008 EPM-generated orbital lifetimes were used to create the figure. Initial orbit inclination was  $28.5^\circ$  in each case. The percent differences were calculated from

$$\text{Lifetime Difference (\%)} = \frac{\mathcal{L}_{\text{actual}} - \mathcal{L}_{\omega=\nu=0}}{\mathcal{L}_{\omega=\nu=0}} \times 100 \quad (96)$$

Because the Earth and atmosphere models are symmetric about the equatorial plane, effects of initial arguments of perigee between  $180^\circ$  and  $360^\circ$  will be identical to those occurring between  $0^\circ$  and  $180^\circ$ . Hence, Figure 47 only shows data for initial arguments of perigee between  $0^\circ$  and  $135^\circ$ .

When the initial true anomaly is zero, Figure 47 clearly shows the effect of the initial argument of perigee on orbital lifetimes. We see that the average percent difference in lifetime, when  $\omega = 45^\circ$ ,  $\nu = 0^\circ$ , is larger than the  $\omega = \nu = 0$  difference. This results because the  $45^\circ$  situation places perigee at a more northerly latitude, and hence higher altitude, than the  $0^\circ$  scenario. The same is true of the  $\omega = 90^\circ$ ,  $\nu = 0^\circ$  scenario as compared to the  $\omega = 45^\circ$ ,  $\nu = 0^\circ$  scenario. The average percent difference in the  $\omega = 135^\circ$ ,  $\nu = 0^\circ$  scenario is less than that of the  $\omega = 90^\circ$ ,  $\nu = 0^\circ$  scenario, because the altitude of perigee is less than that of the  $\omega = 90^\circ$  scenario. The average percent difference in the  $\omega = 135^\circ$  scenario is less

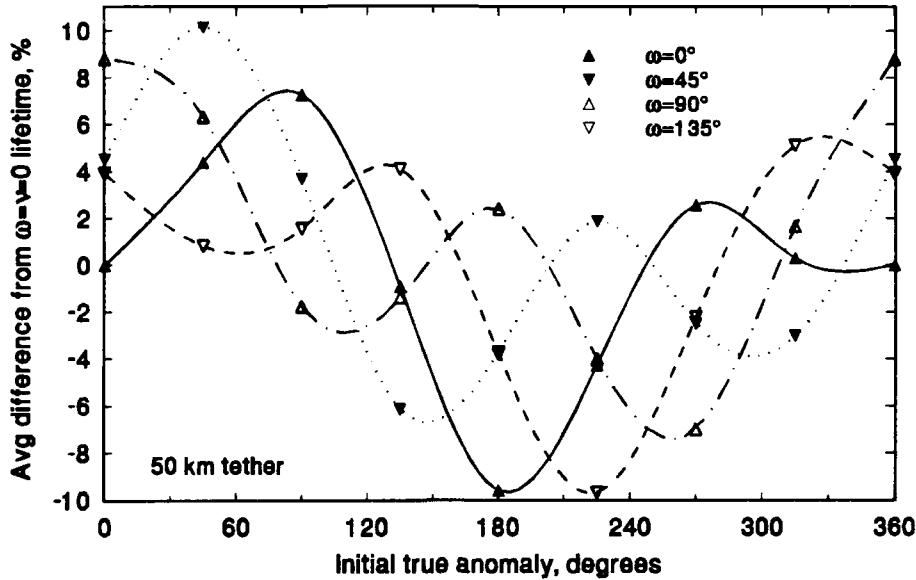


Figure 47. Effect of initial true anomaly on lifetime ( $i = 28.5^\circ$ ).

than that of the  $\omega = 45^\circ$  scenario, because the system is initially southbound, and will cross the equator, where the Earth's radius is largest, sooner than in the  $\omega = 45^\circ$  scenario. The  $\omega = 180^\circ$  scenario would be identical to the  $\omega = 0^\circ$  scenario.

Similar reasoning can be applied to explain the relationships between the data points at each true anomaly value. A clearer picture emerges if the average percent differences in orbital lifetime are plotted as a function of the initial argument of latitude.

As shown in Figures 48, 49, and 50, this procedure yields families of sinusoidal curves, with various amplitudes. For each inclination, the values of the extrema are

the result of two effects: the altitude of perigee, and the system's initial position, relative to perigee and the equator.

We notice, in Figure 48, that the curves for the  $i = 10^\circ$  case are not nearly as "tri-modal" as curves in the other inclination cases. Rather, the extrema have nearly identical magnitudes, and the curves are obviously not in-phase. These differences are due to the fact that changes in perigee altitude, via changes in the initial argument of perigee, have only a minimal effect in low inclination orbits, since the maximum latitude attained by these orbits is small. If the  $i = 10^\circ$  data were plotted as a function of true anomaly, the curves would appear to be nearly in-phase, illustrating the significant effect of initial true anomaly in low inclination scenarios.

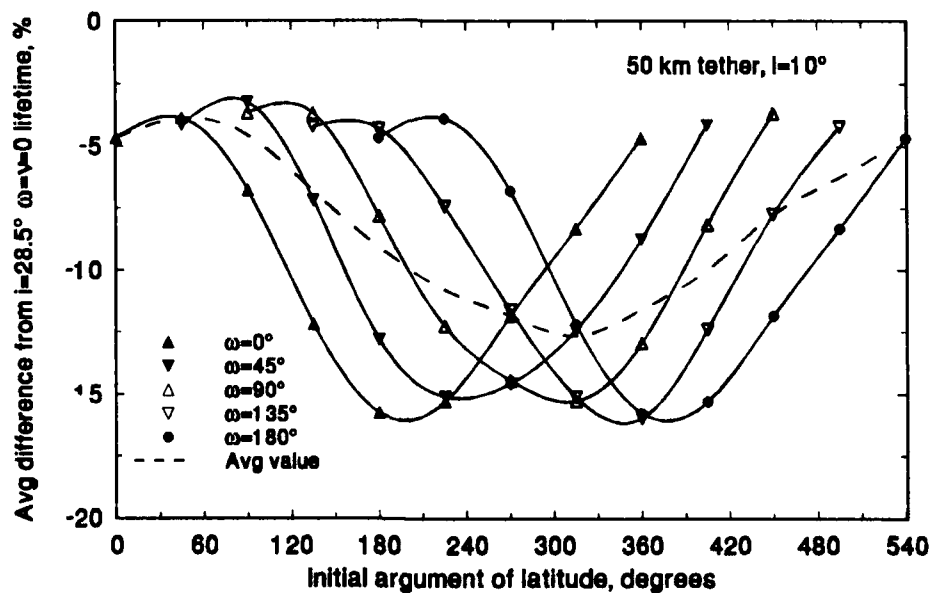


Figure 48. Effect of initial argument of latitude on lifetime ( $i = 10^\circ$ ).

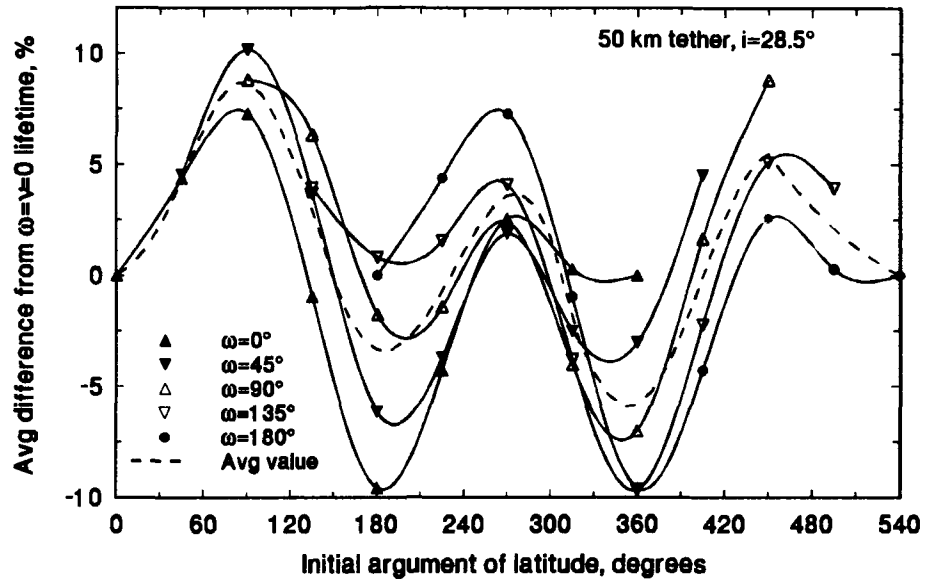


Figure 49. Effect of initial argument of latitude on lifetime ( $i = 28.5^\circ$ ).

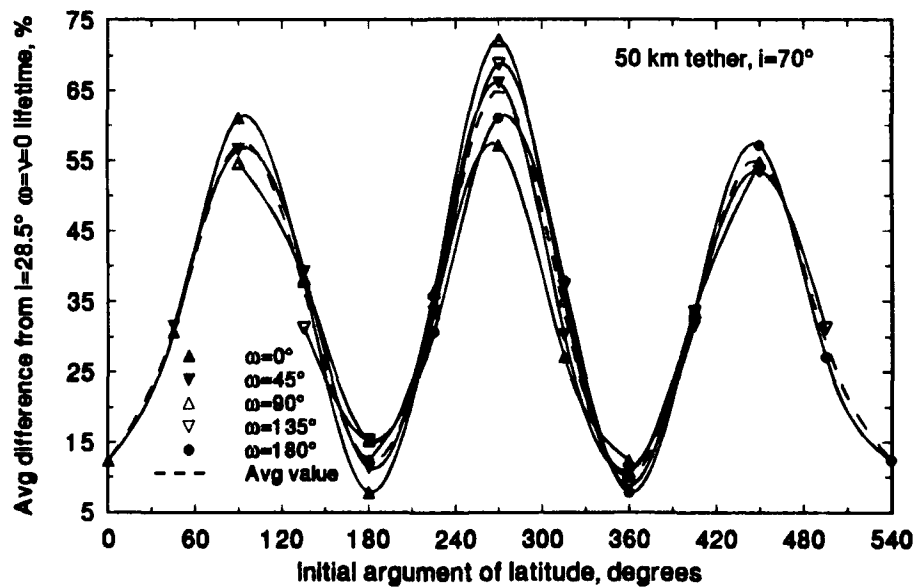


Figure 50. Effect of initial argument of latitude on lifetime ( $i = 70^\circ$ ).

Each Figure also shows an "average value" curve, which is a plot of the average of the inclination family's curves. For most scenarios shown in the figures, the individual mean values are generally not too far removed from those of the average value curve. Hence, a strategy for deriving orbital lifetime correction factors begins to emerge. We may be able to use the corrections indicated by the average value curves to approximate the mean percent differences calculated in each  $i/\omega/v$  scenario. In so doing, the problem's degrees of freedom are reduced by one. That is, a four dimensional problem - correction factor versus  $(i, \omega, v)$  - is reduced to three dimensions - correction factor versus  $(i, U)$ .

The effects of two possible problems must be considered. These are (1) the dispersion of scenario means about the applicable average value curve, and (2) the dispersion of individual case differences about their scenario's mean. If a scenario's mean value differs greatly from the correction factor indicated by the applicable average value curve, the resulting predicted lifetime values may misrepresent "actual" lifetime(s) by more than the desired  $\pm 20\%$ . The average value curve's accuracy in predicting the lifetime of a scenario's mean difference case is calculated from

$$\text{Avg Value Accuracy}(\%) = \frac{\mathcal{L}_{\text{Avg Value}} - \mathcal{L}_{\text{Scenario Mean}}}{\mathcal{L}_{\text{Scenario Mean}}} \times 100 \quad (97)$$

where  $\mathcal{L}_{\text{Avg Value}}$  is the orbital lifetime predicted using the correction factor indicated by the average value curve, and  $\mathcal{L}_{\text{Scenario Mean}}$  is the lifetime for the mean difference case.

For example, Figure 48 shows that the mean lifetime difference for the 50 km tether when  $i = 10^\circ$ ,  $\omega = 0$ ,  $v = 180^\circ$  is approximately -15%, while the average

value curve indicates a correction factor of approximately -9%. The average value curve's accuracy for the mean difference case in this scenario is then

$$\text{Avg Value Accuracy} = \frac{0.91 - 0.85}{0.85} \times 100 = 7.1\%$$

which means that using the average value curve correction factor of -9% will misrepresent the lifetime of the mean difference case by only 7.1%, an acceptable error.

The results of carrying out similar calculations for each mean percent difference in the  $i = 10^\circ$ ,  $i = 28.5^\circ$ , and  $i = 70^\circ$  scenarios are presented graphically on the following pages. Figures 51 - 53 show that correction factors resulting from the average value curves in the  $10^\circ$ ,  $28.5^\circ$ , and  $70^\circ$  initial inclination scenarios are able to predict the mean difference lifetimes, in every scenario, with acceptable accuracy.

The maximum error in predicting the mean difference lifetimes occurs when  $\omega = 0^\circ$ ,  $\nu = 180^\circ$  in the  $10^\circ$  and  $28.5^\circ$  inclination scenarios. For the  $i = 70^\circ$  scenarios, the maximum prediction error occurs when the initial true anomaly is  $270^\circ$  and  $315^\circ$ . All of these occurrences are expected however, as these are the scenarios whose means deviate most from the applicable average value curves. Fortunately, even the lifetime predictions in these "maximum error" scenarios are well within our desired accuracy limits. We must now investigate the effects of the dispersion of individual case differences about their scenario means. Our objective is to determine if all lifetimes predicted using the average value curves are acceptably accurate.

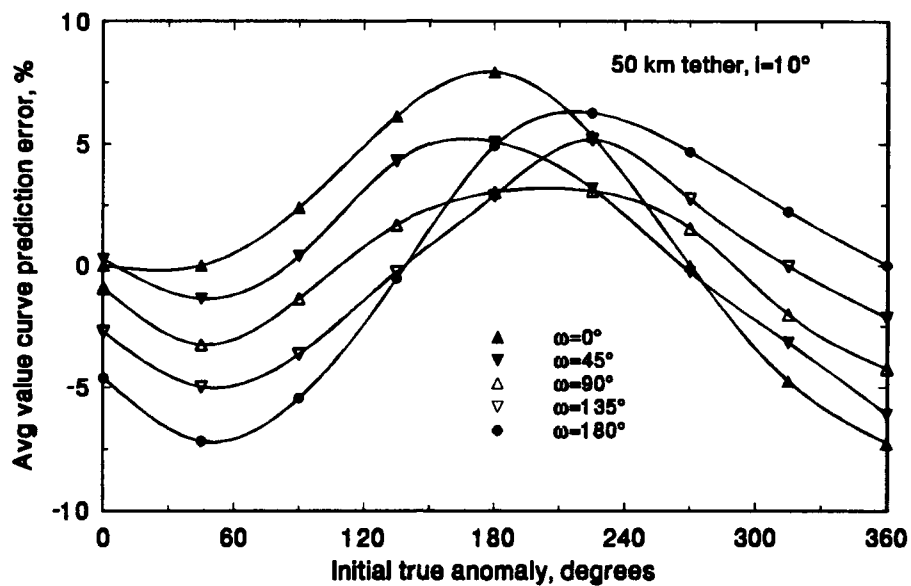


Figure 51. Error in predicting mean difference lifetime ( $i = 10^\circ$ ).

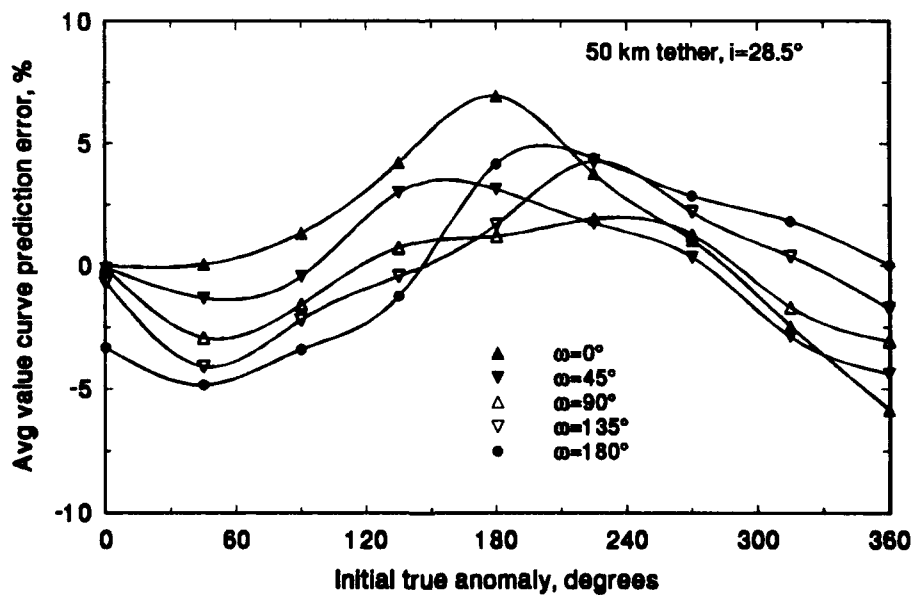


Figure 52. Error in predicting mean difference lifetime ( $i = 28.5^\circ$ ).

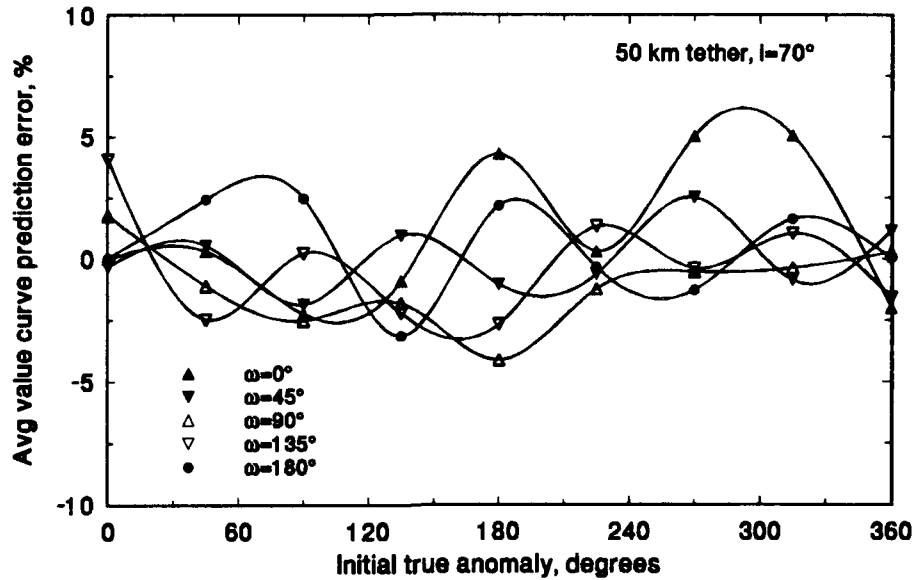


Figure 53. Error in predicting mean difference lifetime ( $i = 70^\circ$ ).

The distribution of the 28 case differences about the applicable scenario's mean will result in predicted lifetimes with errors either greater than or less than the error in the mean difference lifetime prediction. That is, some cases will have smaller magnitude percent differences than the scenario's mean, while others will have larger magnitude percent differences. The smaller differences will be closer to the average value curve than their scenario's mean, indicating reduced errors in predicted lifetime, while larger differences will be farther from the average value curve, leading to increased error in predicted lifetime.

In any given scenario, we may characterize the accuracy of average value curve correction factors by determining the accuracy of lifetimes predicted in the scenario's

maximum and minimum percent difference cases. That is, for each  $i/\omega/v$  scenario there will be one case in which the ratio of actual to standard lifetime,  $\mathcal{L} / \mathcal{L}_{\text{standard}}$ , is largest, and one case in which  $\mathcal{L} / \mathcal{L}_{\text{standard}}$  is smallest (recall that  $\mathcal{L}_{\text{standard}}$  is the system's lifetime when initially  $i = 28.5^\circ$ ,  $\omega = v = 0$ ). If the correction factor indicated by the applicable average value curve yields a predicted lifetime within  $\pm 20\%$  of the actual value, in both the maximum and minimum difference cases, then the lifetimes of all cases in the scenario will be predicted with acceptable accuracy.

The  $\omega = 0$  scenarios have great potential for large errors in predicted lifetimes, as we have previously seen that they involve the largest differences between scenario means and the applicable average value curve. The six figures which follow show, for  $\omega = 0$ , the relationships between the lifetimes predicted using the average value curves, and those of the maximum and minimum difference cases. In each figure, vertical "error bars" indicate the  $\pm 20\%$  accuracy limits about the extremum values. If the error bars for a scenario do not overlap, or at least intersect, the predicted lifetime curve, the scenario has one or more cases whose predicted lifetime is outside the desired  $\pm 20\%$  accuracy limits.

Figures 58 and 59 show that when  $i = 70^\circ$  and  $\omega = 0$ , the lifetimes of all cases are always adequately predicted using the correction factor specified by the average value curve. Figures 54 - 57 show that when  $i = 10^\circ$ , or  $i = 28.5^\circ$ , the average value curves lead to errors in predicted lifetime that are larger than 20%, for the minimum difference cases in several scenarios. The predicted lifetimes are always sufficiently accurate in the maximum difference cases. In the large majority of scenarios, using

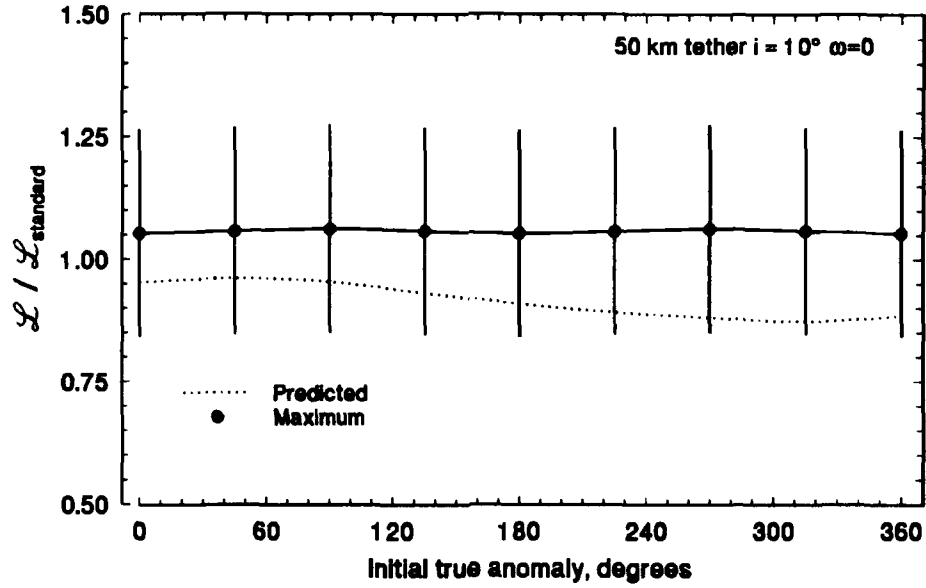


Figure 54. Predicted lifetime accuracy, maximum difference case ( $i = 10^\circ$ ).

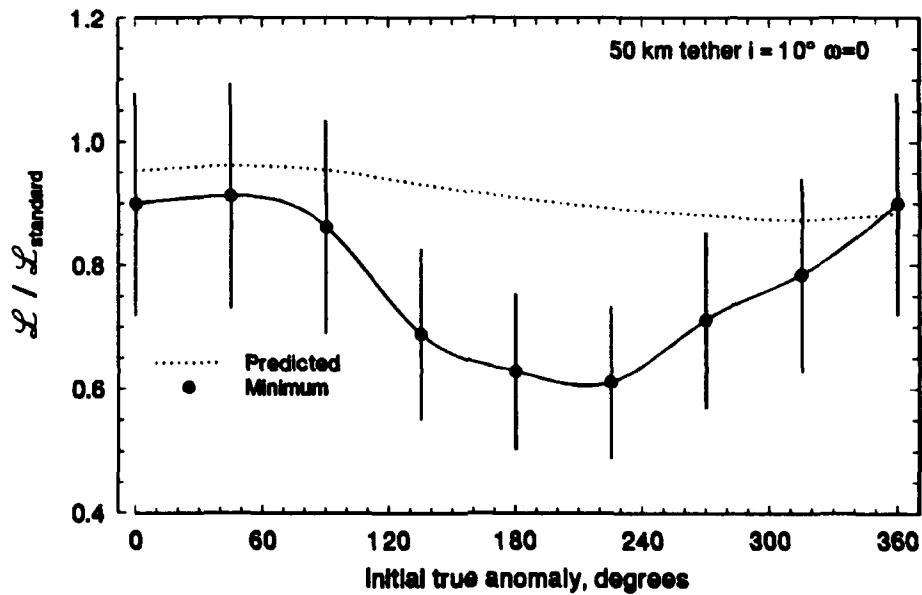


Figure 55. Predicted lifetime accuracy, minimum difference case ( $i = 10^\circ$ ).

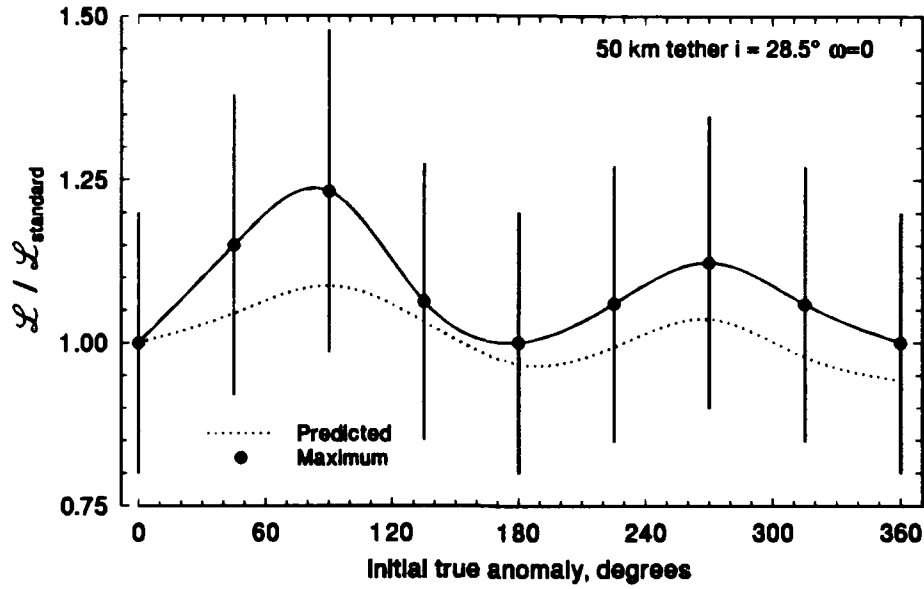


Figure 56. Predicted lifetime accuracy, maximum difference case ( $i = 28.5^\circ$ ).

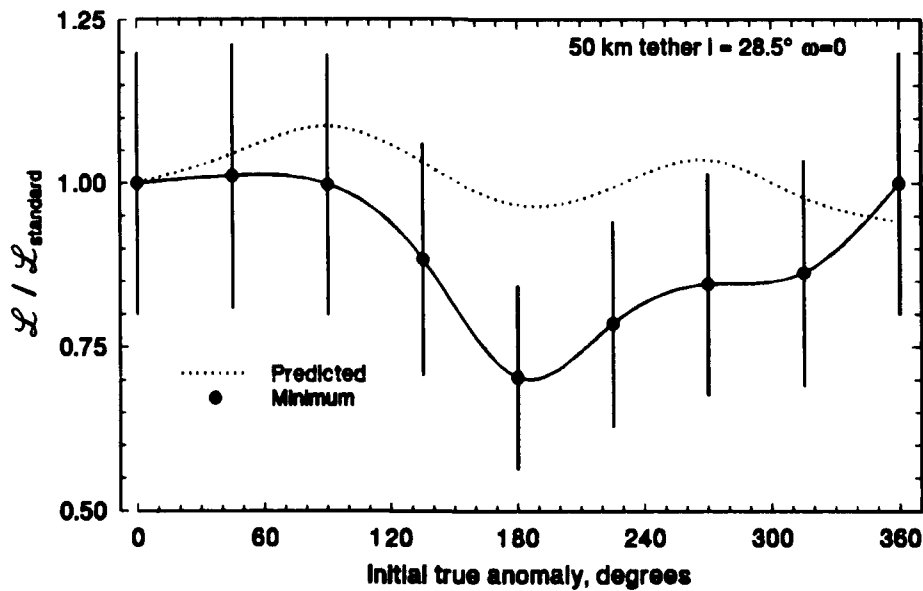


Figure 57. Predicted lifetime accuracy, minimum difference case ( $i = 28.5^\circ$ ).

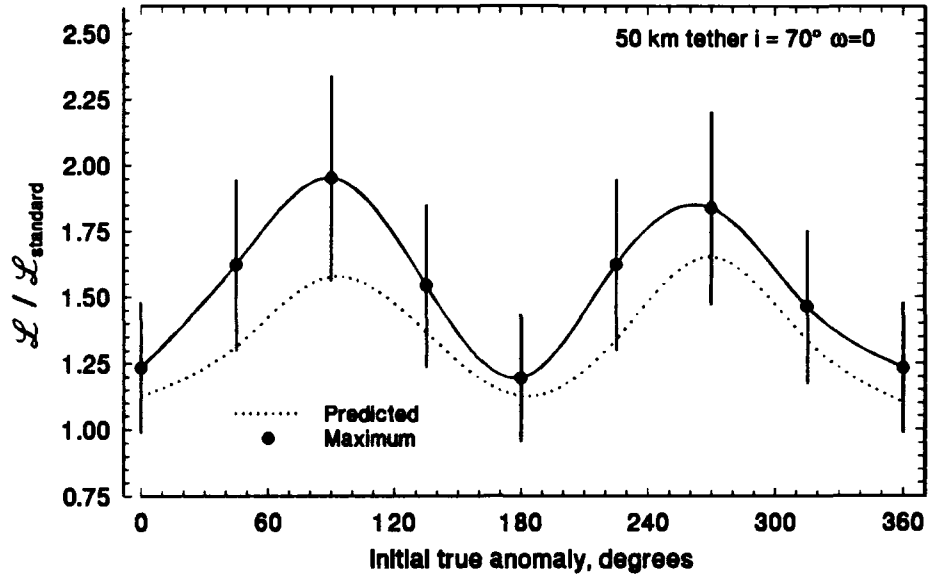


Figure 58. Predicted lifetime accuracy, maximum difference case ( $i = 70^\circ$ ).

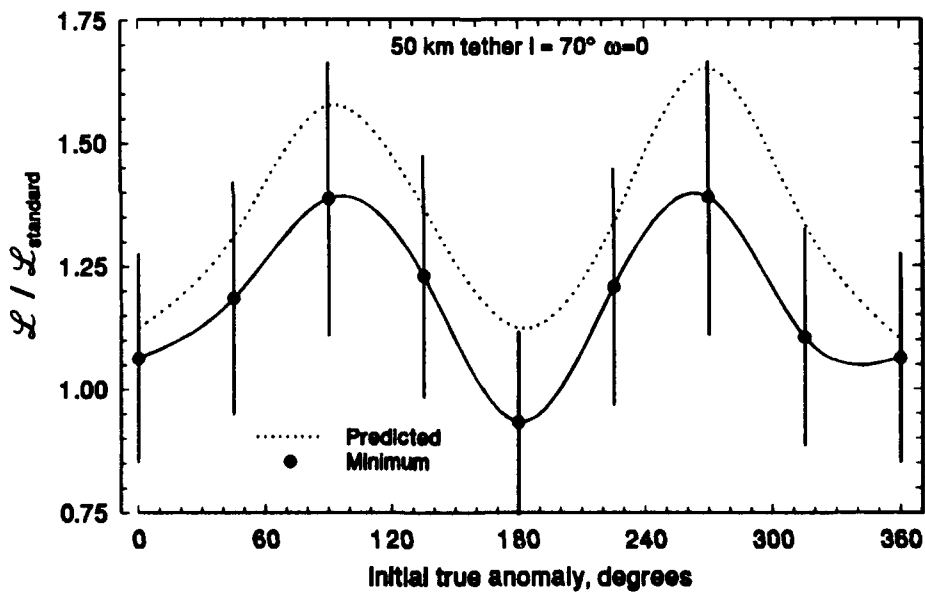


Figure 59. Predicted lifetime accuracy, minimum difference case ( $i = 70^\circ$ ).

the average value curve yields predicted lifetimes closer to the actual values than would be obtained if no correction factor was applied. In only very few instances do we see scenarios in which lifetimes occurring in the standard scenario (i.e.,  $\mathcal{L} / \mathcal{L}_{\text{standard}} = 1$ ) would have been a better approximation for non-standard lifetimes than applying a correction factor indicated by the applicable average value curve.

One of the largest prediction errors shown in Figures 54 - 57 occurs in the minimum difference case, when  $i = 10^\circ$ ,  $\omega = 0$ ,  $\nu = 225^\circ$  (Figure 55). In this case, the minimum percent difference, in actual lifetime as compared to the corresponding standard scenario lifetime, is -38.87%. The average value curve indicates a correction factor of only -10.79%, leading to an error in predicted lifetime of 45.9%. Figure 54 shows that the lifetime of the maximum difference case is adequately predicted in this scenario. The question then becomes, which cases, in addition to the minimum difference case, will have errors greater than 20% in predicted lifetime?

To answer this question, we consider Figure 60, which shows the errors in predicted lifetimes for all cases in the scenario. Here we see that using the correction factor indicated by the average value curve results in acceptably accurate lifetime predictions in all cases except those whose initial perigee radius is 6578.137 km. As we observed previously, the orbital lifetimes in such cases tend to be small, and those occurring in this scenario are no exception - the maximum lifetime when  $R_p = 6578.137$  km is 3.7 hours. Hence we see that although the percent differences are large, the magnitudes of the prediction errors are small. As we stated previously, this type of error is acceptable.

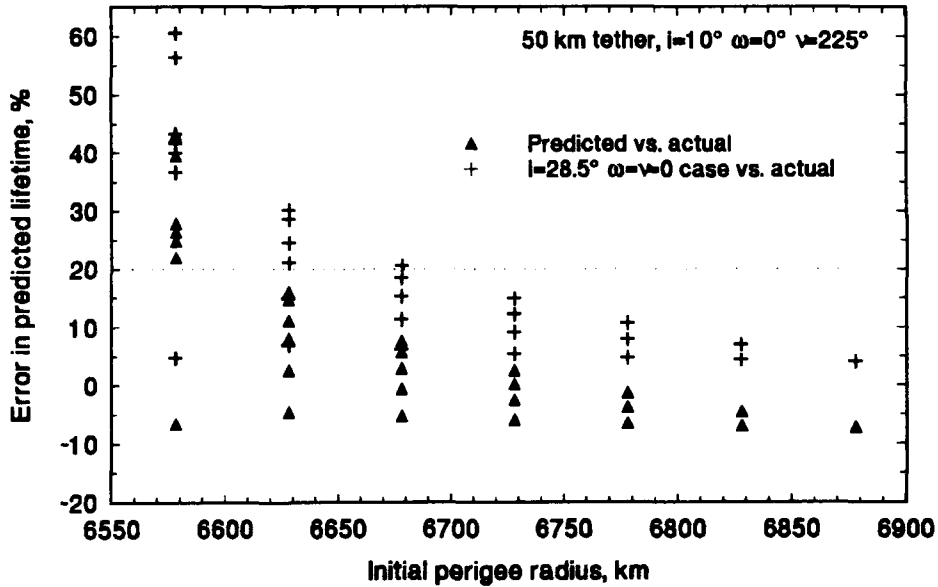


Figure 60. Error in predicted lifetimes ( $i = 10^\circ$   $\omega = 0^\circ$ ,  $\nu = 225^\circ$ ).

Figure 60 also shows the errors in predicted lifetimes which occur if the standard scenario lifetimes are used, with no correction factor applied. The lifetimes in 11 of the 28 cases in the scenario are predicted with errors greater than 20%, and the misrepresented cases are not restricted to those with  $R_p = 6578.137$  km (the actual lifetime in one of these cases is over 31 hours). The largest error is 60.5%, and the mean of all the errors occurring in the scenario is 20.1%. In comparison, the maximum prediction error which occurs when the correction factor is applied is 43.2%, and the mean of the absolute values of all the errors is only 11.1%.

We previously observed, in the "separate effects" investigations described earlier in this Chapter, that tether length has an effect on errors in predicted lifetimes.

Specifically, the data show that increased tether lengths lead to increased magnitude percent differences between non-standard and standard scenario lifetimes.

The results shown in Figure 61 and Figure 62 demonstrate this behavior. Recall that we previously showed that all predicted lifetimes are within the acceptable accuracy range for a 50 km tether, when initially  $i = 70^\circ$ ,  $\omega = 0$  (Figure 58 and Figure 59). The new figures show that, in this scenario, increasing the tether's length to 100 km results in errors in predicted lifetimes, when  $v = 90^\circ$  or  $180^\circ$ , of greater than 20%. We should note, at this point, that although the results cited here are for discrete values of true anomaly, inclination, and argument of perigee, they are actually indicative of results in "bands" of values. For example, Figure 61 clearly shows that the lifetime of the maximum difference case is predicted with greater than 20% error

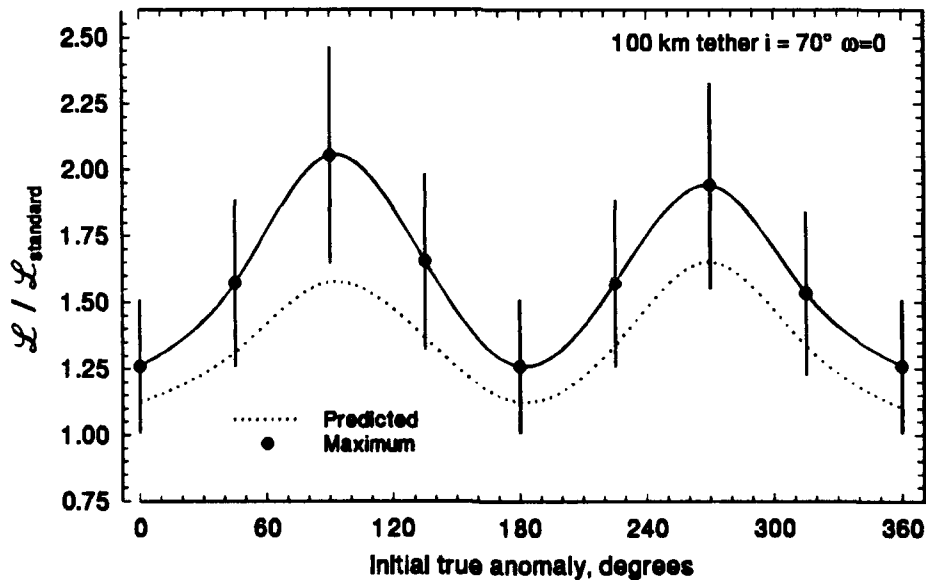


Figure 61. Predicted lifetime accuracy, max. diff. case (100 km tether,  $i = 70^\circ$ ).

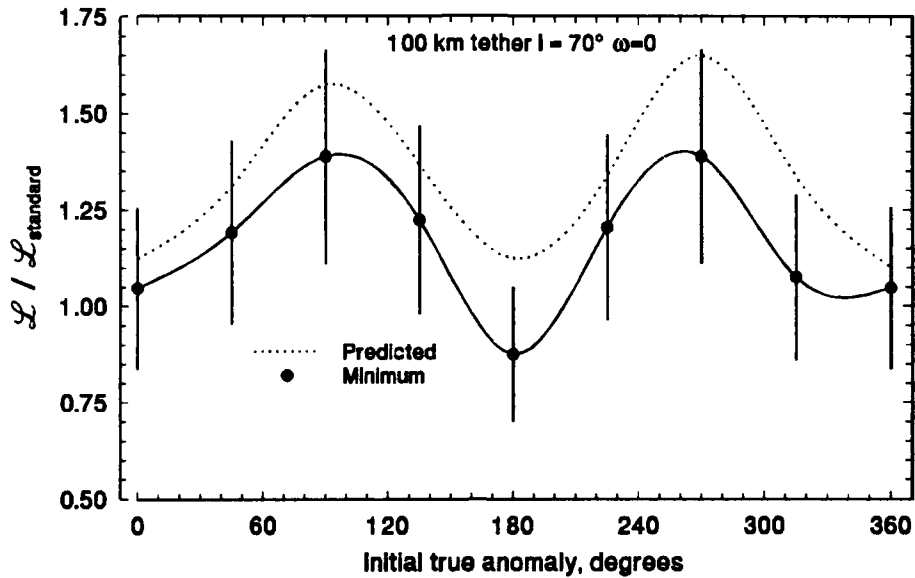


Figure 62. Predicted lifetime accuracy, min. diff. case (100 km tether,  $i = 70^\circ$ ).

in the scenario where a system's initial true anomaly is  $90^\circ$ . However, a closer examination of the plot shows that the downward projected error bars will not intersect the predicted lifetime curve, for some range of true anomaly values around  $90^\circ$ . Hence, results for the specific scenario with  $\nu = 90^\circ$  are merely indicative of results in a range of values.

Figure 63 shows the errors in predicted lifetimes for a 100 km tether, in cases with  $\nu = 90^\circ$ . The figure also shows the errors which would result if the lifetimes of the 100 km tether, in the standard scenario, were assumed to accurately represent those in this non-standard scenario. The mean error using this procedure is -38.4%, with the smallest error being -27.9%, and the largest -51.3%. All lifetimes "predicted"

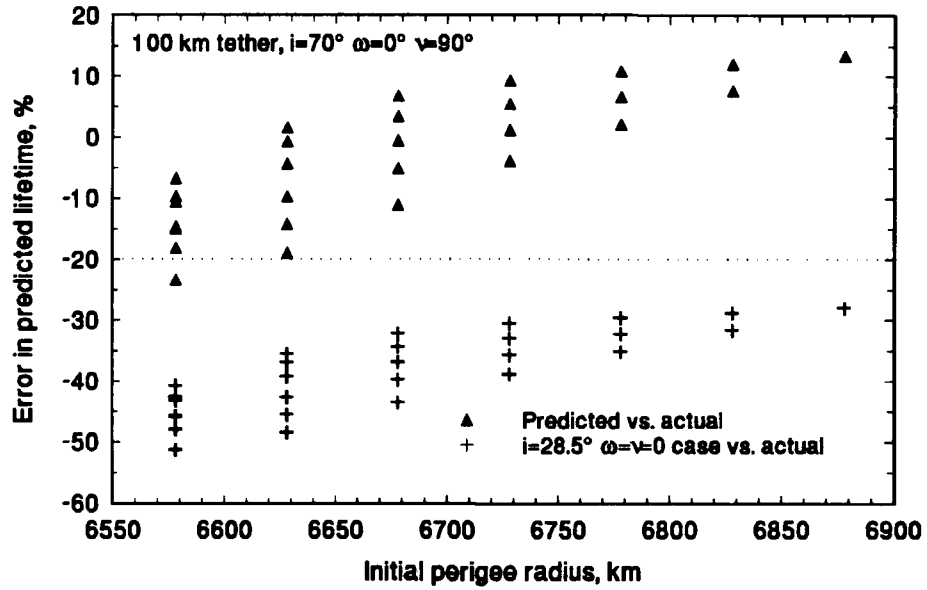


Figure 63. Error in predicted lifetimes (100 km tether,  $i = 70^\circ$ ,  $\omega = 0$ ,  $\nu = 90^\circ$ ).

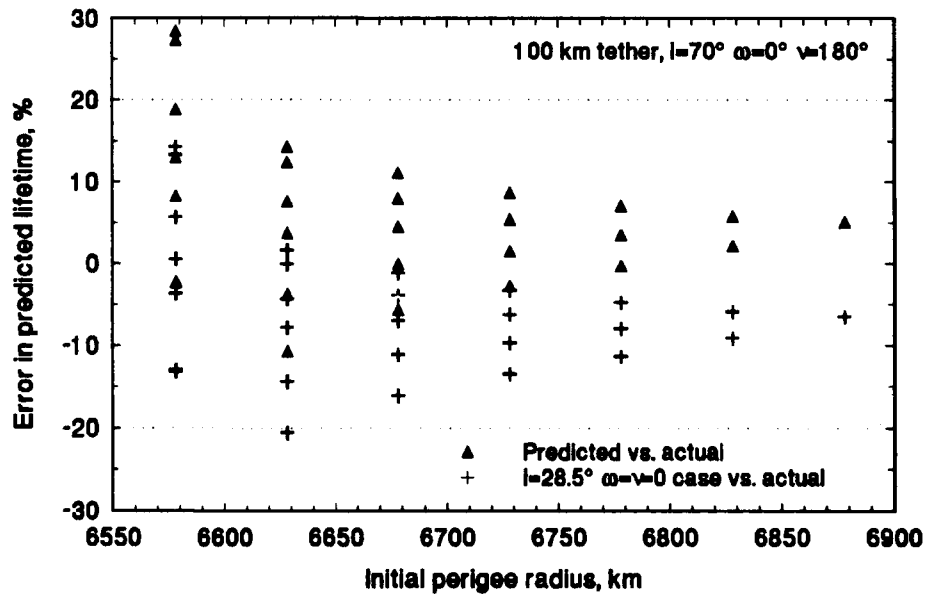


Figure 64. Error in predicted lifetimes (100 km tether,  $i = 70^\circ$ ,  $\omega = 0$ ,  $\nu = 180^\circ$ ).

using this procedure are more than 20% in error. In contrast, applying the correction factor indicated by the average value curve, 1.5743, yields, with one exception, predicted lifetimes within the  $\pm 20\%$  accuracy limits. The maximum error occurs in a case with  $R_p = 6578.137$  km, where the predicted lifetime is 2.7 hours, as compared to an actual lifetime of 3.5 hours.

Similarly, Figure 64 shows the errors in predicted lifetimes for the same system, in cases where the initial true anomaly is  $180^\circ$ . In this scenario, we see that simply using the system's uncorrected lifetimes in the standard scenario as approximations for actual values yields results that are, in all but one case, accurate to within  $\pm 20\%$ . This situation correlates with the relationship shown in Figure 62, between the minimum difference case and the predicted lifetime curve, at  $v = 180^\circ$ ; the upward error bar does not intersect the predicted lifetime curve, but it does cross an imaginary line at  $\mathcal{L} / \mathcal{L}_{\text{standard}} = 1.0$ .

Fortunately, the lifetimes predicted by applying the correction factor of 1.1242 are also generally acceptable. The maximum prediction error is 28.5%, in a case whose actual lifetime is less than 4 hours. The mean of the absolute value of the errors is 8.02%, as compared to 8.22% if the standard scenario lifetimes, with no correction factor applied, are used as "predictions".

By studying the results obtained in many other scenarios, we know that the accuracy of lifetime predictions demonstrated in these cases is typical. In the very vast majority of observed cases, the correction factor approach derived in this work yields results that are well within the desired  $\pm 20\%$  accuracy limits. If errors larger

than 20% occur at all, they most often occur in cases whose initial perigee radius is 6578.137 km. Occasionally, an error of 21% to 22% occurs in longer lifetime cases; while this violates, technically, our desired accuracy limit of 20%, it is not excessive, and is certainly within the region of acceptability. Hence, we conclude that the "averaging approach" derived in this section appears, in the vast majority of cases, to provide a means of adequately predicting the orbital lifetimes of tethered systems originating in orbits whose initial inclination, argument of perigee and true anomaly are non-standard. We will describe a neural network trained to represent the average value curves in the next section. Additional results demonstrating the performance of the averaging approach will be presented later in the Chapter.

ANN Representation. Having satisfied ourselves that the "averaging" approach will yield acceptable results, we turn to generating data to be used in training an orbital lifetime correction factor network. Our objective is to train an ANN to represent the "average value curve" for each possible initial orbit inclination. Hence, we have two independent variables:  $i$ , the initial orbit inclination, and  $U$ , the initial argument of latitude. The network's output will be a lifetime correction factor, which is used to predict the orbital lifetime of a system originating in an orbit whose initial inclination, argument of perigee, and/or true anomaly are different from  $28.5^\circ$ , zero, and zero, respectively.

We define the boundaries of possible initial orbit inclinations to be  $0^\circ$  (i.e., equatorial) and  $80^\circ$  (i.e., near polar). Since the argument of latitude is the sum of the argument of perigee and the true anomaly, we must consider the possible ranges

of both variables. As we mentioned earlier, results obtained for initial arguments of perigee between  $180^\circ$  and  $360^\circ$  will be identical to those occurring when  $\omega$  is between  $0^\circ$  and  $180^\circ$ . Initial true anomaly values range from  $0^\circ$  to  $360^\circ$ , with no possible symmetry simplifications. Hence, we see that the possible range of initial arguments of latitude,  $U$ , is  $0^\circ$  to  $540^\circ$ .

We will attempt to exploit the generalization capabilities of ANNs, to minimize data generation requirements. We will provide training data in  $20^\circ$  inclination increments,  $i = 0^\circ, 20^\circ, 40^\circ, 60^\circ, 80^\circ$ , and  $45^\circ$  argument of latitude increments,  $U = 0^\circ, 45^\circ, 90^\circ, \dots, 540^\circ$ .

To determine argument of perigee and true anomaly values for each argument of latitude, we use the average value curve for  $i = 28.5^\circ$  (Figure 49). Table 7 shows the specific  $\omega$  and  $\nu$  values derived from the average value curve. At each argument of latitude of interest, an approximate argument of perigee was determined graphically; the corresponding true anomaly is then the difference between  $U$  and  $\omega$ .

Since there are 13 data points for each of five inclinations, the network training data set was composed of 65 points. Each point is the average percent difference between the 28 lifetime prediction curve data points for a particular  $(i, \omega, \nu)$  case and the 28 lifetime prediction curve data points for the corresponding  $i = 28.5^\circ, \omega = \nu = 0$  case. Hence, 1,848 EPM-generated orbital lifetimes are used to determine the training data points.

The chosen ANN structure is shown in Figure 65. The feed-forward network is composed of two linear input neurons, 30 hidden sigmoidal (logistic function)

Table 8. Argument of perigee and true anomaly data points. (all units degrees)

$U$	$\omega$	$\nu$	$U$	$\omega$	$\nu$
0	0	0	315	45	270
45	0	45	360	70	290
90	90	0	405	112	293
135	45	90	450	135	315
180	70	110	495	158	337
225	110	115	540	180	360
270	125	145			

neurons, and one linear output neuron. As discussed in the **Artificial Neural Networks** Chapter, the input data values, i.e., the values of the independent variables, are scaled to the interval (0,1). The network requires that a scaled argument of latitude,  $U'$ , be provided to the first input neuron, and a scaled orbit inclination,  $i'$ , be provided to the second input neuron. Exact details of the scaling procedures are included in **Appendix D**. The network's output is a lifetime correction factor percentage, which is the percent difference between the lifetime of interest and the lifetime of an identical system in an identical size and shape orbit, with  $i = 28.5^\circ$ , and  $\omega = \nu = 0$ . The predicted orbital lifetime is calculated using

$$\text{Predicted lifetime} = \left( 1 + \frac{\text{Correction factor}(\%)}{100} \right) \times \mathcal{L}_{i=28.5^\circ, \omega=\nu=0} \quad (98)$$

where *Correction factor* is the network's output.

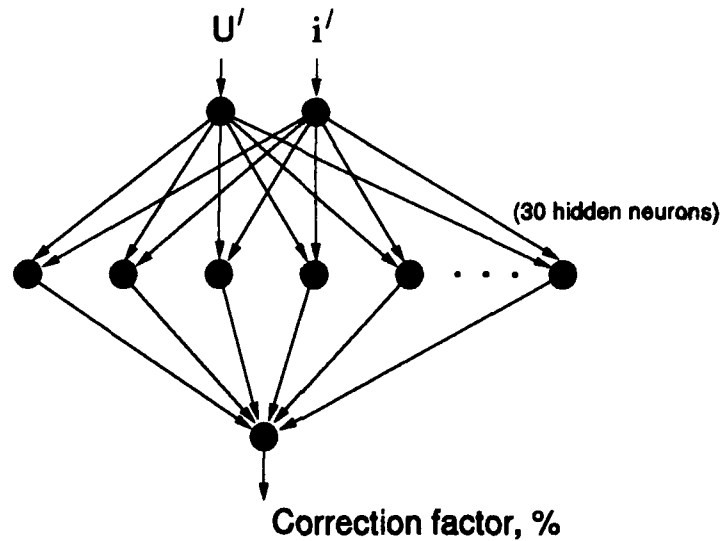


Figure 65. Orbital lifetime correction factor network structure.

**Results.** The ANN was trained using the hybrid training approach described in the **Artificial Neural Networks Chapter**. Training with the 65 point data set was continued until the network had learned to represent the mapping at each point with less than 10% error. Unfortunately, the network interpolated between given data points very poorly. Hence the training data set was expanded to include data at argument of latitude points between the original points, which were in  $45^\circ$  increments. The expanded set of argument of perigee, true anomaly, and argument of latitude points is shown in Table 9. The expanded data set consisted of 25 points at 5 inclinations, for a total of 125 data points. This number is somewhat misleading, as

each point is the average percent difference in orbital lifetime between two 28-point data sets. A total of 3,528 EPM-generated orbital lifetimes were used to obtain the 125 training data values.

Table 9. Argument of perigee and true anomaly data points. (all units degrees)

$U$	$\omega$	$\nu$	$U$	$\omega$	$\nu$
0	0	0	293	158	135
30	30	0	315	45	270
45	0	45	338	68	270
60	40	20	360	70	290
90	90	0	383	95	288
112	40	72	405	112	293
135	45	90	428	120	308
157	45	112	450	135	315
180	70	110	473	153	320
203	90	113	495	158	337
225	110	115	518	180	338
247	112	135	540	180	360
270	125	145			

Training with the expanded data set was continued until the network's representation error, at each training data point, was less than 10% of the desired value. The final weights and biases for the trained network are included in **Appendix D**.

Figure 66 shows the trained network's performance at three untrained inclinations:  $i = 10^\circ$ ,  $28.5^\circ$ , and  $70^\circ$ . The curves showing the network's output were generated for the figure using argument of latitude increments of one degree. The network results were usually well within  $\pm 10\%$  of known data point values, and interpolation performance was never more than  $\pm 15\%$  away from expected values.

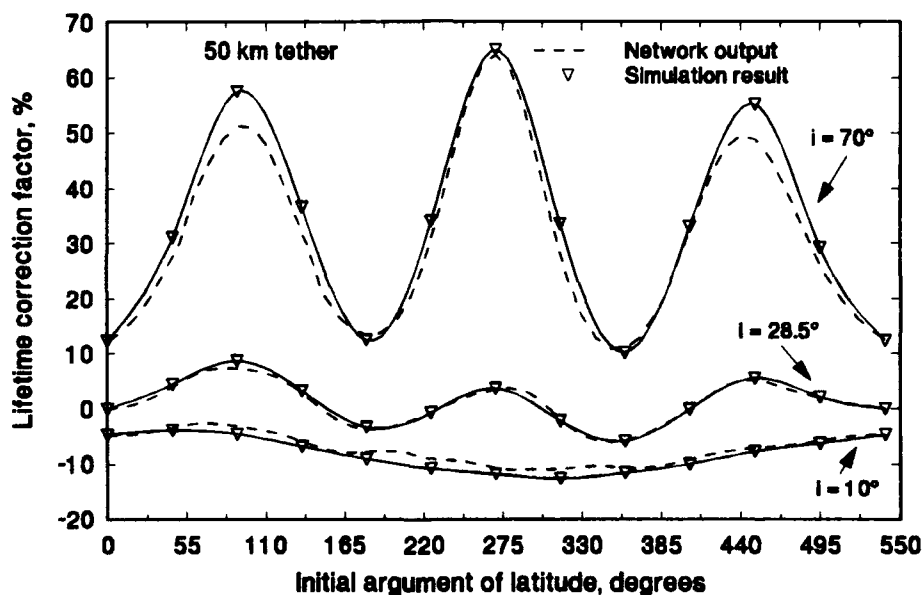


Figure 66. Correction factor network performance at untrained inclinations.

Figure 67 shows the three dimensional surface represented by the trained network. This surface was created by varying the  $U$  and  $i$  values input to the network in  $2^\circ$  increments. Each grid point in the figure represents an actual network output value - i.e., no "fictitious" points were created by the graphing procedure. Hence,

the figure is an accurate portrayal of the smoothness of the network's representation.

The 125 points composing the training data set are also shown.

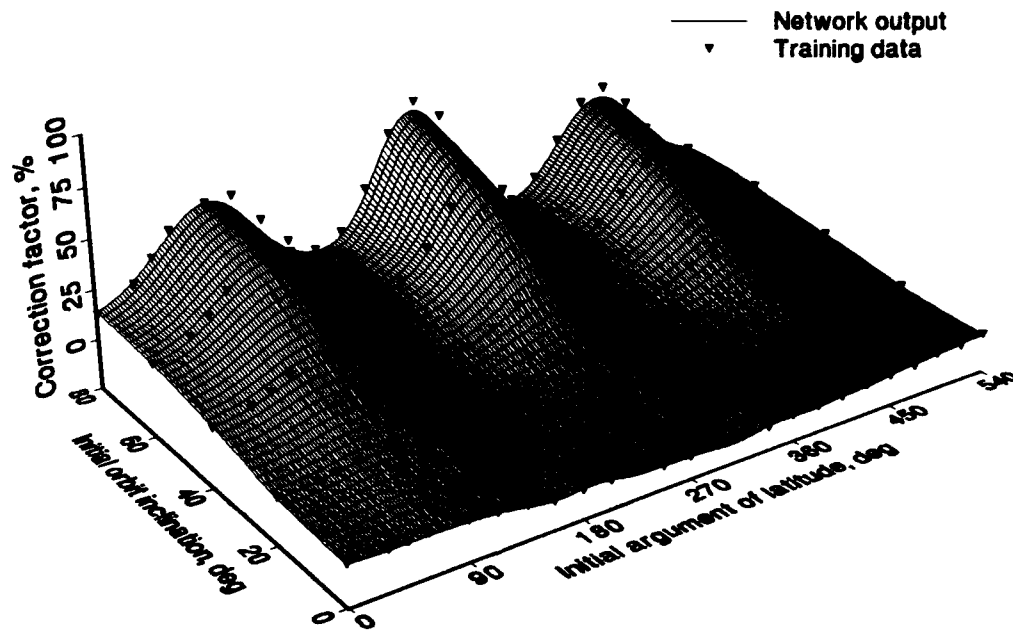


Figure 67. Network representation of orbital lifetime correction factors.

Finally, we investigated the network's ability to predict orbital lifetimes in the "worst case" scenario discussed earlier: 125 km tether,  $i = 80^\circ$ ,  $\omega = 90^\circ$ ,  $\nu = 180^\circ$ . As Figure 68 shows, the majority of the 28 orbital lifetimes predicted using a network-generated correction factor of 1.72381 are within  $\pm 20\%$  of the EPM-generated values. Specifically, only five predicted lifetimes were more than 20% different from the corresponding EPM values, and four of these occurred when  $R_p = 6578.137$  km.

The largest error was -41.5%, in a case with a predicted lifetime of 5.35 hours, and an EPM-generated lifetime of 9.14 hours. A 21.5% error occurred when the tether originated in a circular orbit of radius 6878.137 km (20.9 days vs. 17.2 days). Although this difference is slightly above the desired 20% error limit, we note that it is similar to the 22.6% deviation obtained by Hoots and France<sup>100</sup> in a case with a mean lifetime of 19.1 days.

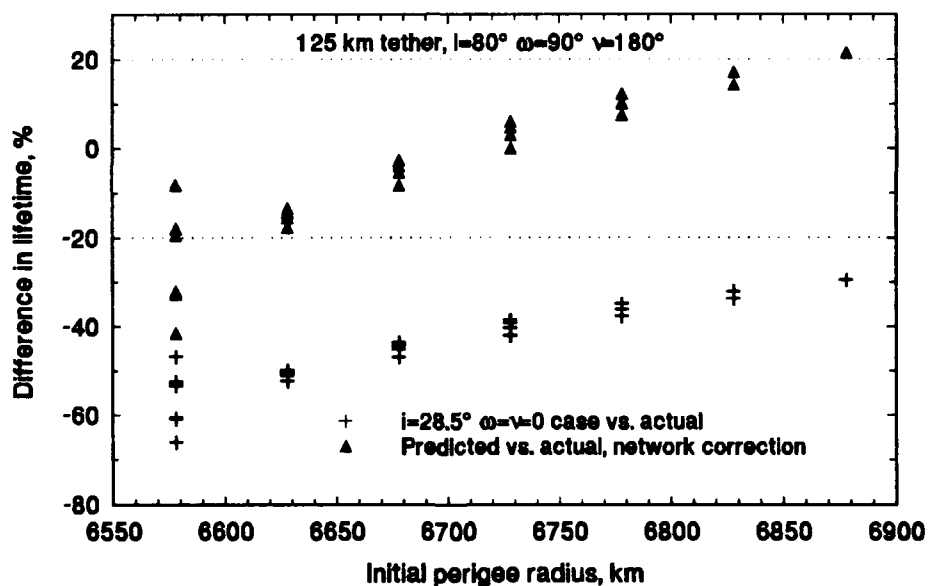


Figure 68. Correction factor network performance in "worst case" scenario.

The mean of the absolute values of the errors in the predicted lifetimes is 14.4%, with an absolute maximum of 41.5%. These statistics compare very favorably with those of the errors which result if the  $i = 28.5^\circ$ ,  $\omega = \nu = 0$  (standard) scenario

lifetimes are used, without correction, as predictions: absolute mean = 46.3%, absolute maximum = 66.1%, absolute minimum = 29.5%.

Inclination-only Correction Factors. We observe in Figure 66 that typical "average value" curves are centered at non-zero correction factor values, which are dependent upon initial orbit inclination. Hence, we can derive a simple relationship to provide an "average correction factor", as a function of inclination alone. Clearly, this average correction factor will be a better approximation in low to moderate inclination cases than it will in high inclination cases.

By finding the mean of the lifetime correction factors, for each of the five inclinations included in the network training data set, we obtain 5 points which serve as a basis for curve fitting. The correction factor means are shown in Table 10.

Table 10. Mean orbital lifetime correction factors.

Initial Orbit Inclination, degrees	Mean Lifetime Correction Factor, %
0	-9.679
20	-4.129
40	10.521
60	27.479
80	36.578

Figure 69 shows that the variation of the correction factor, as a function of initial orbit inclination, is sigmoidal.

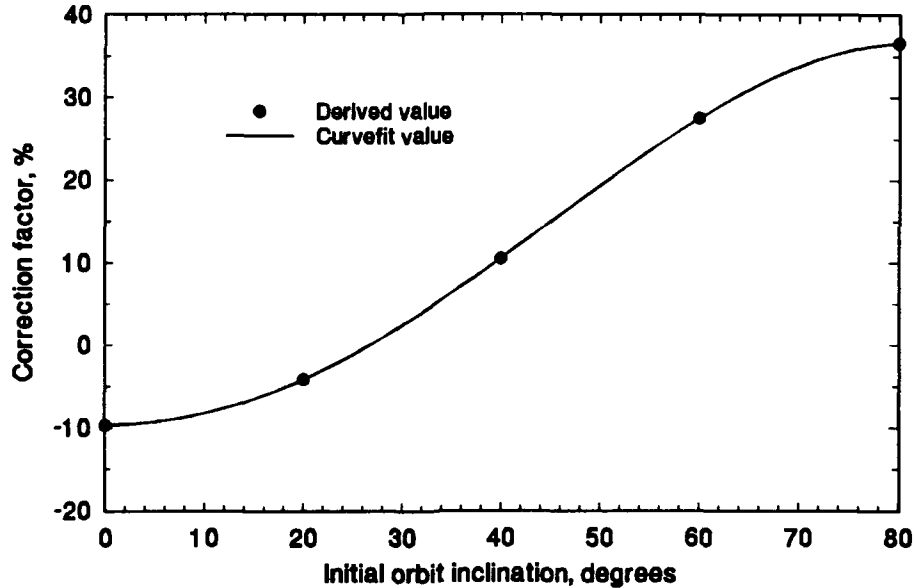


Figure 69. Inclination-only orbital lifetime correction factors.

The mean correction factor data in Table 10 was curvefit, using a least squares procedure. An equation providing a reliable representation of the data is

$$\text{Mean Correction Factor}(\%) = a + b i + c i^2 \sqrt{i} + d i^3 \quad (99)$$

where  $i$  is the initial orbit inclination, in degrees,  $a = -9.67656505$ ,  $b = 0.0476813$ ,  $c = 0.0043850397$ , and  $d = -0.00040736821$ .

Figure 70 shows the performance of the inclination-only lifetime correction factor method in the "worst case" scenario. As expected, this approach does not yield results as accurate as the correction factor network, but we see that predicted lifetimes for cases with initial perigee radii greater than or equal to 6728.137 km are

acceptable. The mean of the percent errors, which are all negative, is -26.7%; the maximum is -53.6%, and the minimum is -3.7%.

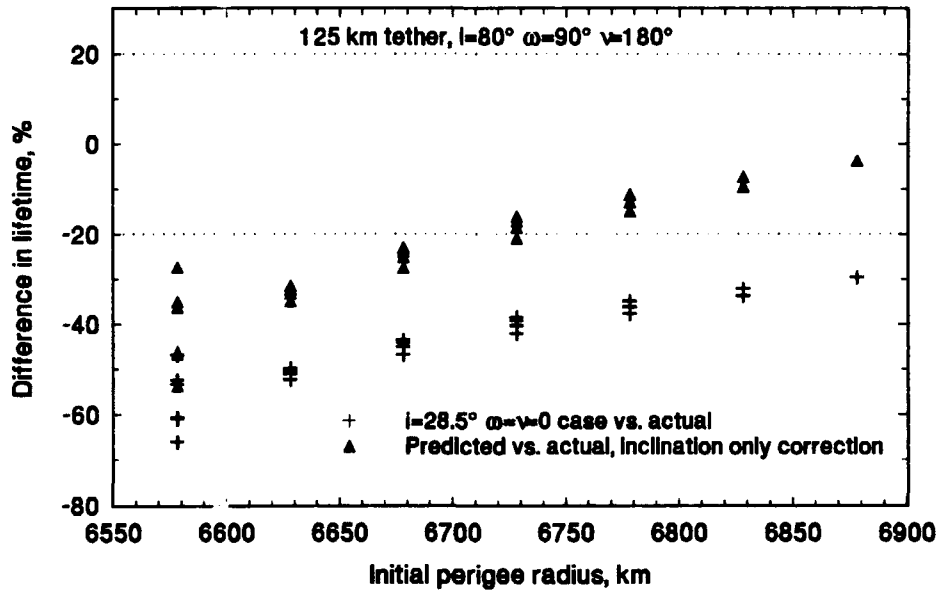


Figure 70. Inclination-only correction factor performance in "worst case" scenario.

**Postscript.** One additional aspect of the orbital lifetime correction factor method needs to be discussed. It may have occurred to the reader that all of the training data used here was derived from EPM-generated orbital lifetimes, but the trained correction factor network provides lifetime correction factors which are applied to (standard case) lifetimes produced by the orbital lifetime prediction network described earlier. Since the prediction network provides results which vary in accuracy, as compared to EPM-generated results, the correction factors derived using EPM results

may vary significantly from those which would result if, instead, the lifetime prediction network's output were used as a basis.

Fortunately, this is not the case. Comparing lifetime correction factors derived using the lifetime prediction network's output, to those obtained using EPM results, we found that the average error was 0.34%. The maximum error was 6.07%, in a scenario where the correction factor obtained using EPM results was 0.1877%, and the correction indicated using network results would have been 0.1991%. Hence, we observe that although differences exist, they are not significant. This is due to the averaging process used to obtain the correction factors.

### **Predicting the Orbital Lifetime of Tether-Trailing Satellites**

Having derived a method to predict the orbital lifetime of free tethers, we now turn our attention to developing a similar procedure for predicting the lifetimes of satellites trailing a tether.

In this section, we present results showing the effect of upward and downward deployed tethers on the orbital lifetime of single mass satellites, discuss the accuracy of single mass orbital lifetime predictions for these systems, and describe an artificial neural network trained to represent EPM-generated results.

Deployed Tether Effect on Satellite Orbital Lifetime. A deployed tether may have a profound effect on the orbital lifetime of a single-mass satellite. This type of scenario will most likely occur when either (1) a deployed subsatellite is released (or broken free) from an upward- or downward-deployed tether, leaving behind the parent and

tether, or (2) a subsatellite and tether are released (or broken free) from a parent vehicle.

The tether's mass may or may not be significant relative to that of an attached (sub)satellite, but its cross-sectional area will most likely be several times greater than that of any end-body. For example, a 20 km Kevlar 29 tether's mass is only 90.5 kg, but its cross-sectional area, assuming a 2 mm diameter, is 40 square meters (20,000 m (length)  $\times$  0.002 m (diameter)). In contrast, a 3 m diameter spherical satellite has a cross-sectional area of less than 7.1 m. Thus, due to the area difference alone, aerodynamic drag forces acting on the tether will dwarf those acting on the satellite, if all other factors are equal. Furthermore, if the tether's mass density is less than that of the satellite, which is likely, the acceleration due to drag on the tether will also be much larger than that of the satellite. Of course, the physical distribution of a deployed tether's mass will affect these results, since there may be significant variations in atmospheric mass density over the altitudes involved. Differences in drag coefficients will also have an effect.

Figure 71 shows the effects of both upward and downward-deployed tethers on the orbital decay of a 250 kg mass, 3 m diameter, spherical satellite. In each case, the satellite is initially in a 28.5° inclination orbit of radius 6728.137 km. As always, the tether is initially aligned along the local vertical, orbiting as a rigid rod. We are thus simulating the orbit evolution of a "parent" satellite trailing an upward- or downward-deployed tether. The results presented in the figure were obtained using the EPM.

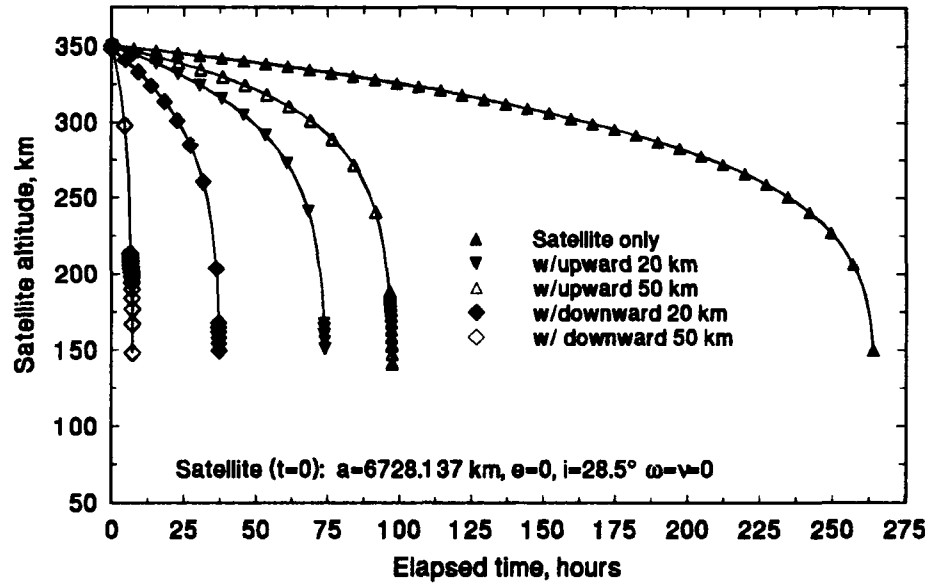


Figure 71. Effect of deployed tethers on satellite orbital decay.

The figure shows that, in each case, the tether reduced the parent satellite's orbital lifetime. As we would expect, an upward-deployed tether had less effect than an equal length downward-deployed tether, due to differences in atmospheric mass density, and the downward-deployed tethers had a very significant impact. For example, the downward-deployed 50 km tether reduced the satellite's lifetime by a ratio of more than 37 to 1 (7 hours vs. 264 hours).

A surprising result occurs in the upward-deployed cases. The figure shows that a 50 km upward-deployed tether reduced the satellite's lifetime, but not as much as the 20 km upward-deployed tether. This is the reverse of the result one would

expect based on aerodynamic drag considerations alone. The explanation for this situation is found in the initial conditions for each system's center of mass.

As the length of an upward-deployed tether is increased, so too is its mass, which shifts the system center of mass further above the satellite. Because the entire system is assumed to initially be orbiting at the parent's angular rate, i.e., the parent satellite's orbital "mean motion", all points above the parent will be moving faster than the parent. The parent is assumed to initially be in a circular orbit, and we know that as orbit radius increases the speed required to attain circular orbit decreases. The combination of these facts means that all points above the parent are initially moving at speeds greater than those required for circular orbit at their locations.

The eccentricity vector for the center of mass' initial orbit, which points from the center of the Earth toward perigee, and has a magnitude equal to the orbit's eccentricity, may be calculated from<sup>101</sup>

$$\underline{e} = \frac{1}{\mu} \left[ \left( V^2 - \frac{\mu}{R} \right) \underline{R} - (\underline{R} \cdot \underline{V}) \underline{V} \right] \quad (100)$$

where  $\underline{R}$  and  $\underline{V}$  are the center of mass' initial position and velocity vectors. Since the initial velocity is perpendicular to the position vector, and has a magnitude greater than circular orbit speed, we see that  $\underline{e}$  points in the direction of  $\underline{R}$ . That is, in an upward-deployed tether scenario, where the system is initially aligned along the local vertical and orbiting as a rigid rod, the system center of mass is initially located at perigee of an elliptical orbit, and the perigee radius is greater than the radius of the parent's initial (circular) orbit. Hence, we see that as the length of an upward

deployed tether is increased, the size of the center of mass' initial orbit is increased, leading to a longer orbital lifetime.

For example, the mass of a 20 km, 2 mm diameter (Kevlar 29) tether is 90.5 kg, and the resulting system center of mass location is 2.6574 km above the 250 kg satellite, which is in a circular orbit of radius 6728.137 km, as in Figure 71. Thus the perigee radius of the center of mass' initial orbit is 6730.79 km. The initial apogee radius,  $R_a$  may be found by calculating the initial orbit's specific mechanical energy,  $\epsilon$ , where

$$\epsilon = \frac{V^2}{2} - \frac{\mu}{R} = -\frac{\mu}{2a} \quad (101)$$

solving for the major axis length,  $2a$ , and using the relation

$$R_a = 2a - R_p \quad (102)$$

Since, by definition, apogee radius is greater than perigee radius, the system's center of mass will be in a larger initial orbit than the parent satellite. In the example scenario, the initial apogee radius is 6746.76 km.

The meaning of the upward-deployed results shown in Figure 71 now becomes clear. In these scenarios, the center of mass is initially in an orbit whose perigee and apogee radii are larger than the radius of the parent's initial (circular) orbit. This means the center of mass' initial orbit period is longer, and its altitude is always greater, than that of the parent's initial orbit. The dissipative effects of aerodynamic drag on the deployed tether cause the parent to lose altitude quicker than in the undeployed case, with the calculated lifetime resulting from the competing effects of

the drag force magnitudes and accelerations, and the size of the initial center of mass' orbit. Both of these effects result directly from the length of the deployed tether.

Exactly the opposite phenomena occurs in cases with a downward-deployed tether. The system center of mass, located below the parent satellite, is initially at apogee of an elliptical orbit, whose perigee radius is even lower. In these scenarios, the reduced radii combine with the dissipative aerodynamic drag effects to greatly reduce the system's orbital lifetime. Table 11 lists the perigee and apogee radii, and the calculated lifetimes, for each case shown in Figure 71.

Table 11. Center of mass initial orbit radii and parent satellite orbital lifetimes.

Scenario	Perigee Radius (km)	Apogee Radius (km)	Orbital Lifetime (hrs)
Parent only	6728.137	6728.137	264.2
Parent + 20 km upward deployed	6730.79	6746.76	73.9
Parent + 50 km upward deployed	6740.01	6811.89	97.3
Parent + 20 km downward deployed	6709.56	6725.48	37.2
Parent + 50 km downward deployed	6645.63	6716.26	7.1

Accuracy of Equivalent Sphere Orbital Lifetime Predictions. Following the approach utilized in the free tether studies, the EPM was used to investigate the accuracy of tether-trailing satellite lifetime predictions obtained using equivalent single-mass

satellites. Terminology used in this section will differ slightly from that of the previous section: here we will refer to a case in which a subsatellite has been downward deployed from a parent and released, trailing an "upward-deployed" tether, as a downward-deployed case; a subsatellite which has been upward deployed from a parent and released, trailing its tether, will be referred to as an upward-deployed case. Also unlike the previous section, where we assumed certain initial conditions for the parent, in these investigations we will calculate the lifetimes of systems released from identical center of mass initial conditions.

Lifetime prediction curve data points were generated for a variety of upward- and downward-deployed cases, and compared to results obtained for spheres whose cross-sectional area and mass were equivalent to that of the tethered systems. Errors in the equivalent sphere results were determined by calculating their percent difference from the "actual" tethered system lifetimes. That is, the errors in equivalent sphere lifetimes were calculated from

$$\text{Error in Lifetime (\%)} = \frac{\mathcal{L}_{\text{Equiv Sphere}} - \mathcal{L}_{\text{actual}}}{\mathcal{L}_{\text{actual}}} \times 100 \quad (103)$$

Lifetimes were calculated and compared in 8 different cases, for each of three tether lengths, assuming both upward and downward deployment. Subsatellite masses included in the study were 0, 25, 50, 100, 175, 275, 375, and 500 kg, and lifetimes were calculated using tether lengths of 20, 50, and 100 km. Except for the free tether cases (subsatellite mass = 0), a subsatellite diameter of 3 meters was assumed.

Figure 72 shows that errors in downward-deployed cases involving a 50 km tether were usually within  $\pm 20\%$ , over the entire range of subsatellite masses.

Figure 73 shows that errors occurring in cases with a 100 km tether were similar, except for small subsatellite masses. Errors in cases with a 20 km tether fell within the range  $+8.1\%$  to  $-14.1\%$ . Data was also generated assuming 1 m , 2 m and 5 m diameters, for subsatellite masses of 50, 250 and 500 kg; the resulting errors in lifetime were either within the error bands obtained for the 3 m diameter cases, or outside the limits by less than 5 percentage points.

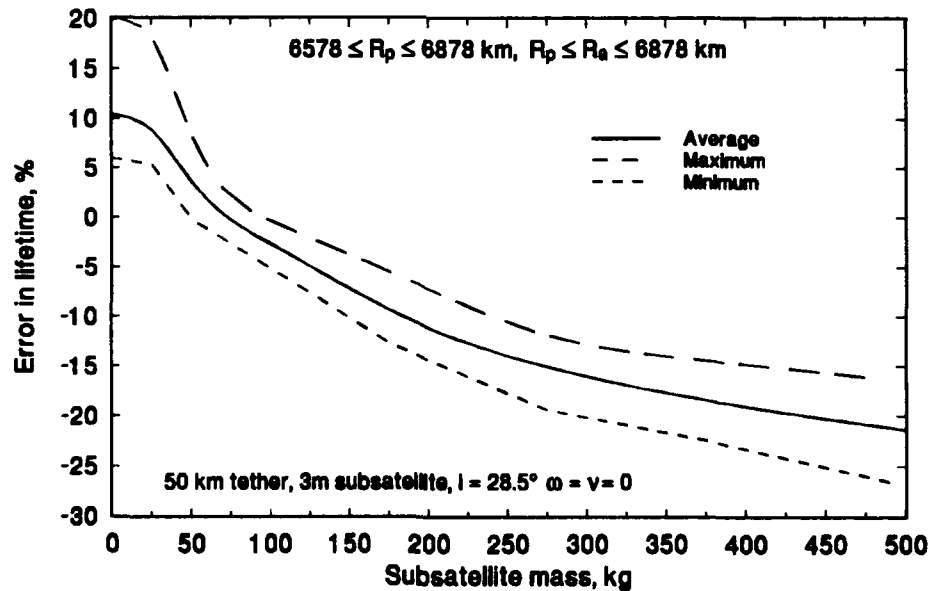


Figure 72. Error in equivalent sphere lifetime, downward-deployed 50 km cases.

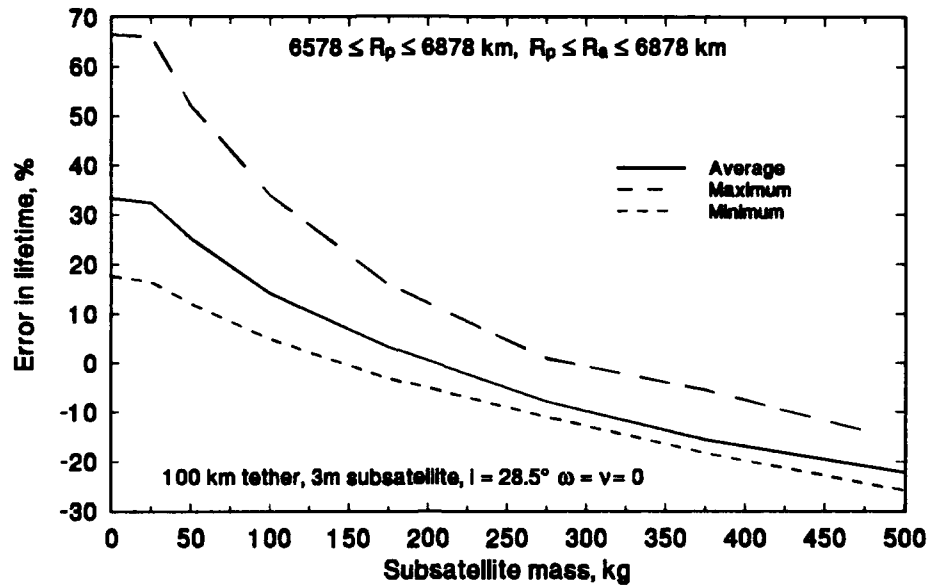


Figure 73. Error in equivalent sphere lifetime, downward-deployed 100 km cases.

Calculated errors were much larger in upward-deployed cases. As shown in Figure 74, errors in cases involving a 20 km tether ranged from a minimum of near 2%, to a maximum of over 30%. With a 50 km tether, Figure 75 shows that the minimum error exceeded 20% for subsatellite masses larger than approximately 120 kg. The average error in equivalent sphere lifetime was greater than 60% with a 500 kg subsatellite, and the maximum error was greater than 20% for all subsatellite masses. Figure 76 shows that average errors in the 100 km upward-deployed cases ranged from a low of approximately 30% to a high near 175%. Minimum error exceeded 20% for subsatellites larger than approximately 20 kg, and the maximum error was over 400% in cases involving a 500 kg subsatellite. Results were also

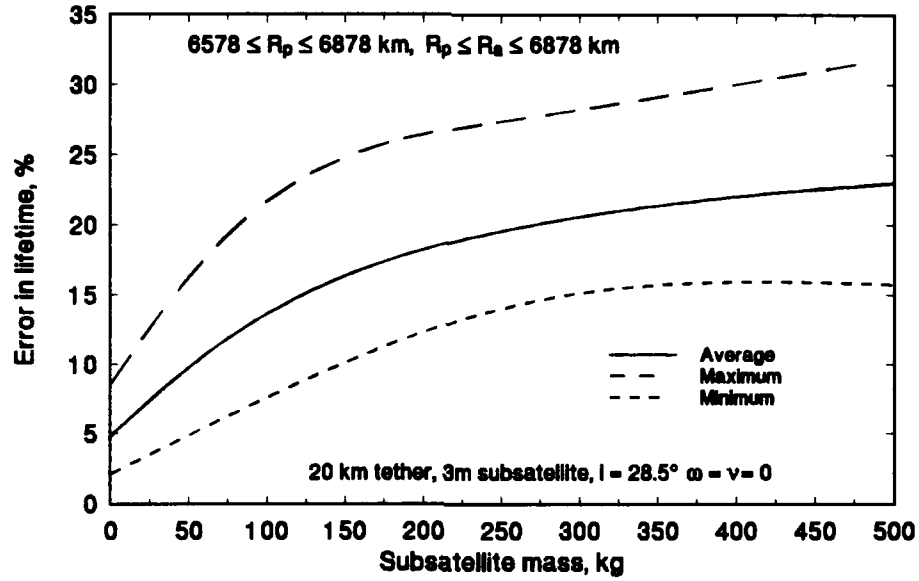


Figure 74. Error in equivalent sphere orbital lifetime, upward-deployed 20 km cases.

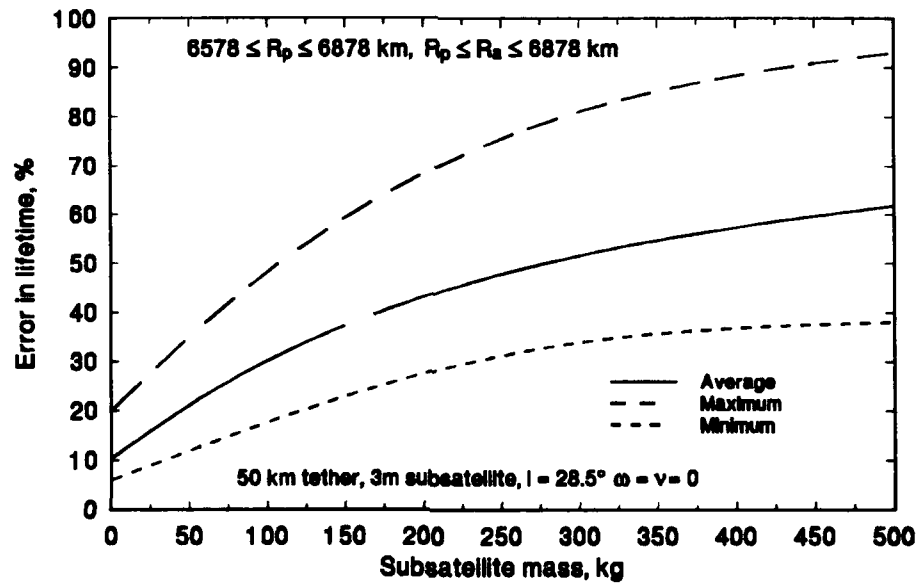


Figure 75. Error in equivalent sphere orbital lifetime, upward-deployed 50 km cases.

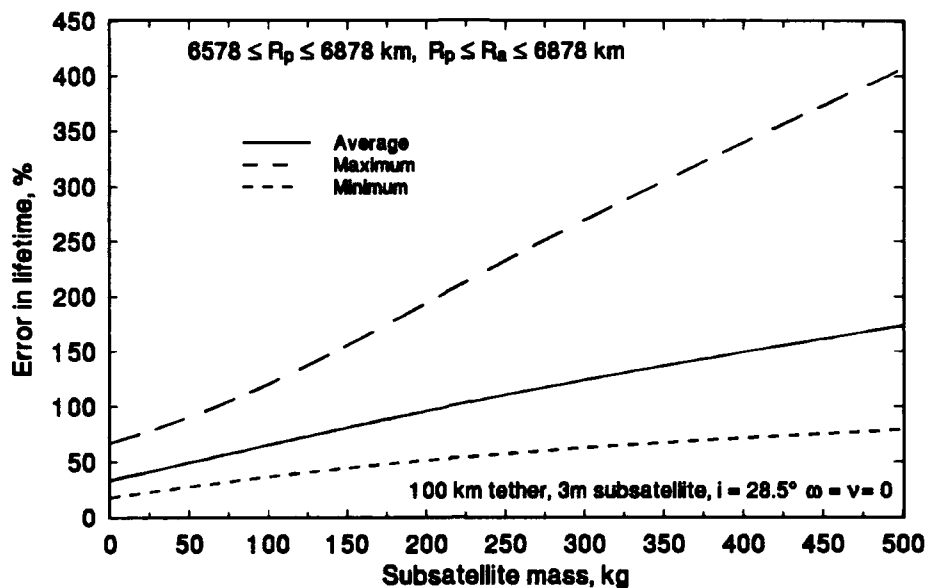


Figure 76. Error in equivalent sphere orbital lifetime, upward-deployed 100 km cases.

obtained for subsatellite masses of 50, 250, and 500 kg, with diameters of 1, 2, and 5 meters, and it was found, as in the downward-deployed cases, that errors were either within the error limits established by the 3 m diameter cases, or outside those boundaries by only a few percentage points.

A pattern is obvious in these results. It appears that equivalent sphere orbital lifetime results are acceptably accurate in many downward-deployed cases. (Notable exceptions include 100 km downward-deployed cases, with subsatellite masses smaller than approximately 150 kg.) With downward-deployed systems, increased tether length appears to cause significantly increased errors in predicted lifetimes in only the smallest mass subsatellite cases.

Conversely, errors in the upward-deployed cases are rarely tolerable. In fact, the only cases with maximum errors less than 20% were those 20 km cases with subsatellites smaller than approximately 75 kg. Increased tether length drastically increased the errors which occurred with upward-deployed subsatellites of any mass.

There is, of course, a logical explanation for this behavior. In the upward-deployed cases, a system's center of mass is located below the subsatellite, but a significant portion of the tether hangs below the center of mass location. As the system's orbit decays, the lower portions of the tether encounter the more dense regions of the atmosphere first, quickly dissipating orbit energy. However, an equivalent sphere, initially released at the system's center of mass location, may be many kilometers above the bottom of the tether, and hence will not dissipate orbital energy as quickly.

For example, the center of mass of an upward-deployed system consisting of a 100 km tether and a 250 kg subsatellite is only 32.3 km below the subsatellite, i.e., 67.7 km above the free end of the tether. Although the equivalent sphere's cross-sectional area equals that of the tether and subsatellite, it will not encounter the more dense portions of the atmosphere as early as the free end of the tether, and hence will not decay as quickly, leading to a large difference in actual and "equivalent" lifetimes.

Conversely, if the same system were downward-deployed, the equivalent sphere would be 32.3 km above the subsatellite, and would encounter the more dense portions of the atmosphere sooner than the upper 67.7 km of tether. Hence the

sphere would encounter the more dense portions of the atmosphere later than the subsatellite and the lowest portions of the tether, but before the tether's (longer) upper portion. This is apparently a fairly good tradeoff, as the results indicate that errors essentially reach a limit, near -25%, as subsatellite mass increases.

Given these findings, we chose to restrict this effort to training a neural network to predict the orbital lifetimes of upward-deployed systems. The large errors which occurred in the scenarios examined earlier indicate that single-mass orbital lifetime prediction techniques will be extremely unreliable for these types of systems..

Predicting the Orbital Lifetime of Upward-Deployed Tether-Trailing Satellites. The initial values of five independent variables dictate the orbital lifetime of tether-trailing satellites. They are: (1) the CM orbit's initial perigee radius, (2) the CM orbit's initial apogee radius, (3) the tether's length, (4) the subsatellite's mass, and (5) the subsatellite's diameter. Our objective is to train an artificial neural network to predict adequately the orbital lifetimes of upward-deployed tether-trailing satellites. In actuality, additional variables, for which we have previously made assumptions and provisions, will affect the lifetimes of these systems. These include variables such as the tether's diameter and initial orientation, the time of day and year, etc.. In this analysis, we will continue to apply all the simplifying restrictions and assumptions stated previously. The most important are that (1) the tether is initially aligned along the local vertical, unstretched, orbiting as a rigid rod, and (2) the system's CM is initially in an orbit whose inclination is  $28.5^\circ$ , and whose argument of perigee and true anomaly are zero.

As in the free tether scenarios, plotting the orbital lifetimes of tether-trailing satellites versus a factor involving the initial CM orbit's size and shape ( $R_p + (R_a - R_p) / (1 + e)$ ), on a semi-log scale, yields fairly linear curves which may be easily read.

Figure 77 shows the orbital lifetime prediction curves for a system consisting of a 500 kg, 3 m subsatellite, upward deployed on either a 50 km or 75 km tether. The figure clearly shows that increased tether length decreases orbital lifetime. This results because the portion of the longer tether below the system's CM reaches the more dense regions of the atmosphere quicker than similar portions of the shorter one.

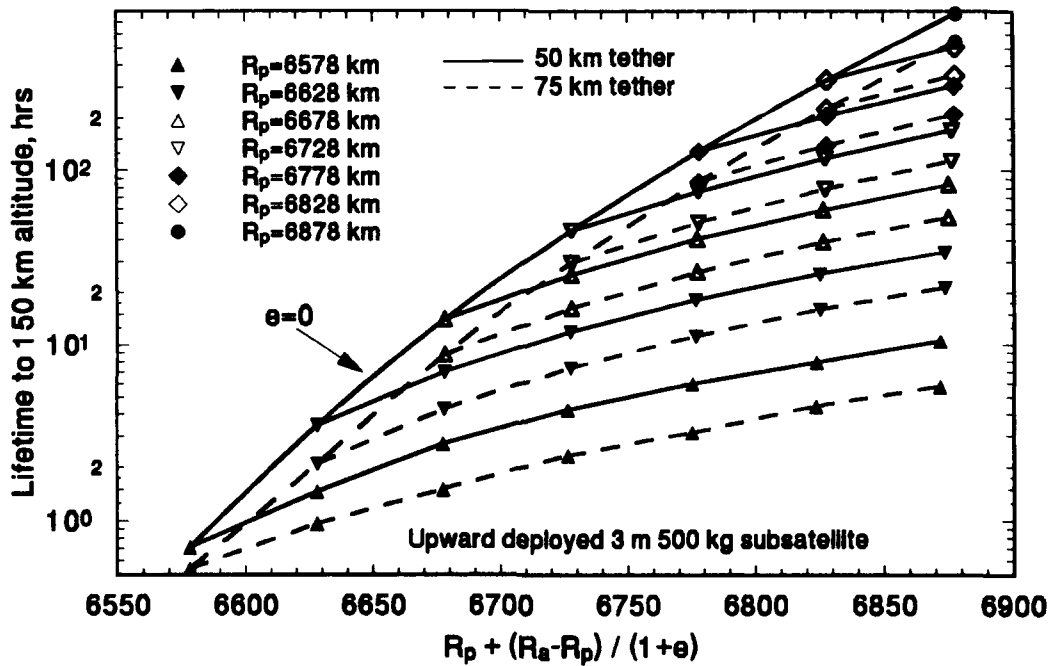


Figure 77. Effect of tether length on orbital lifetime.

For example, the lifetime of the 50 km system, when its CM is originally in a circular orbit of radius 6878.137 km, is 781 hours (32.5 days). If the 50 km tether is replaced by a 75 km tether, the lifetime is only 543 hours (22.6 days). The 50 km tether has a mass of 226 kg, and the resulting CM location is 7.8 km below the subsatellite; this means that a tether portion 42.4 km long extends below the system CM. In contrast, the 75 km tether has a mass of 339.3 kg, leading to a system CM location 15.2 km below the subsatellite. Hence, a tether portion 59.8 km long extends below the system CM in this case. We expect the increased lower portion length to have the most effect at low altitudes, and the results shown in the figure support this observation: the length-induced percent differences in lifetimes increase as the initial radius of perigee decreases.

Figure 78 shows the effect of increasing the mass of an upward-deployed subsatellite. In this scenario, a 250 kg or 500 kg subsatellite, 3 m in diameter, is deployed upward, trailing a 50 km tether. The figure shows that increased subsatellite mass leads to increased orbital lifetime. This is the result of two competing influences. First, doubling the subsatellite's mass, without changing its diameter, will halve its ballistic coefficient,  $C_D A / M$ . This means the acceleration due to drag acting on the subsatellite is also halved, which will reduce the rate of specific orbital energy dissipation. Second, increasing the subsatellite's mass moves the system CM "higher" along the tether. For example, the CM of the system with a 250 kg subsatellite is located 11.87 km below the subsatellite; with the 500 kg subsatellite it is 7.78 km below. Since lifetimes are calculated using initial CM orbit conditions, a CM location

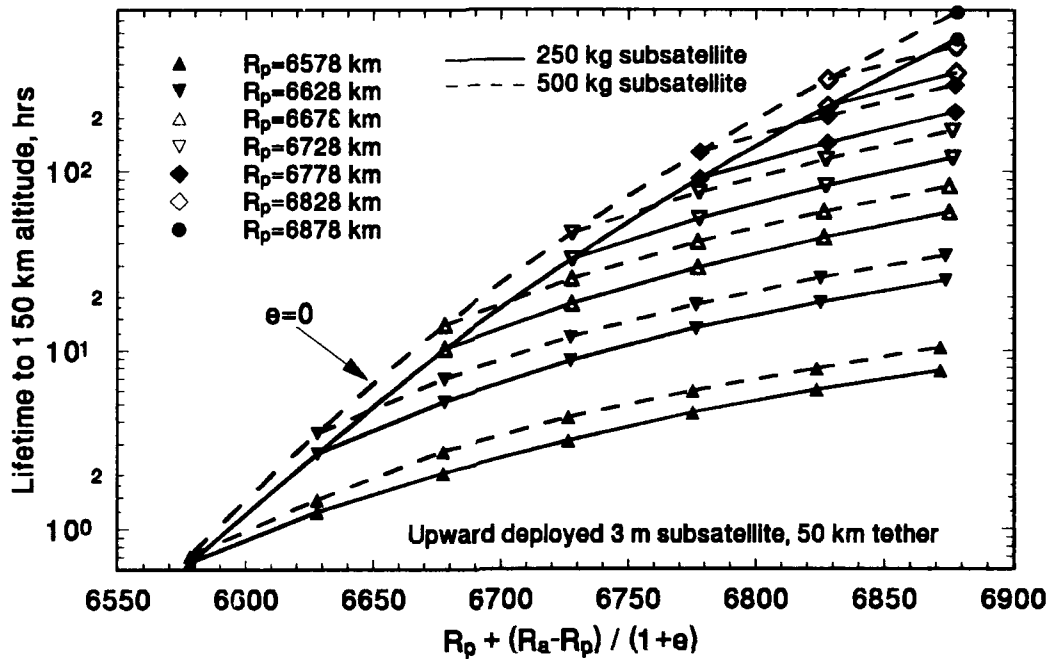


Figure 78. Effect of subsatellite mass on orbital lifetime.

closer to the top of the system (i.e., "higher") will lead to earlier dissipation of orbital energy, since the portions of the tether below the CM reach further down into the atmosphere. However, in the cases presented here, changes in subsatellite mass do not significantly alter the position of the system's CM, and the reduced subsatellite ballistic coefficient is clearly the dominant influence.

By comparing lifetime prediction curve data generated for numerous scenarios, it becomes apparent that variations in a subsatellite's diameter cause only small changes in orbital lifetimes, particularly when the trailing tether is longer than approximately 50 km. Since the realistic range of subsatellite diameters includes any

dimension up to approximately 5 meters, we compared the EPM-generated lifetimes of 1, 2, 3, and 5 m subsatellites, having masses of 50, 250, or 500 kg, trailing a 20, 50, or 100 km tether. Table 12 shows, for each tether length and all three subsatellite masses, the absolute value of the maximum percent difference in lifetimes of the 1, 2, or 5 m cases, as compared to results for the corresponding 3 m diameter case. That is, the percent differences were calculated using

$$\text{Lifetime Difference (\%)} = \frac{|\mathcal{L}_{L,d=7,M} - \mathcal{L}_{L,d=3,M}|}{\mathcal{L}_{L,d=3,M}} \times 100 \quad (104)$$

where  $L$  is the length of the trailing tether,  $d$  is the subsatellite diameter, and  $M$  is the subsatellite mass. Hence the results shown in the table are the result of comparing the lifetime prediction curve data from 36 scenarios: four subsatellite diameters, in combination with each of three subsatellite masses, with any of three tether lengths. Since each scenario includes 28 data points, the results shown in the table embody the relationships between a total of 1008 EPM-generated orbital lifetimes.

Table 12. Maximum lifetime differences caused by subsatellite diameter variations.

Tether Length (km)	Maximum Lifetime Difference (%)
20	18.1
50	6.9
100	1.3

As shown in Table 13, relatively large lifetime differences occurred in the 20 km scenarios involving all three subsatellite masses. The largest differences from the applicable 3 m results occurred in scenarios with a 5 m diameter subsatellite. This is due to the fact that the cross-sectional area of a 5 m (spherical) subsatellite ( $19.6 \text{ m}^2$ ) is nearly half that of a 20 km, 2 mm tether ( $40 \text{ m}^2$ ). In contrast, the areas of the smaller subsatellites are never more than 20% that of the tether (17.7% for a 3 m subsatellite). Thus, in the 5 m cases, the drag forces acting on the subsatellite are more significant than in the smaller diameter scenarios.

Table 13. Maximum lifetime differences with 20 km tether.

Subsatellite Diameter (m)	Subsatellite Mass (kg)		
	50	250	500
1	14.63	12.3	12.4
2	10.0	8.1	7.4
5	18.1	18.1	18.0

Since the trained ANN will be accurate to within  $\pm 10\%$  at each training data point, we can determine the agreement which must exist between different diameter scenarios to insure  $\pm 20\%$  accuracy in the network's predictions. That is, we can tolerate any predicted lifetime within the range  $\mathcal{L}_{\text{predicted}} = 1.20 \mathcal{L}_{\text{actual}}$  to  $0.8 \mathcal{L}_{\text{actual}}$ . Assuming a maximum network representation error of  $\pm 10\%$ , we see that the maximum tolerable difference due to diameter affects is  $+ 9.1\%$  or  $- 11.1\%$

( $1.1 \times 1.091 = 1.20$ ,  $0.9 \times 0.889 = 0.8$ ). Clearly, very few of the diameter - mass scenarios listed in Table 13 have even the possibility of being adequately represented by the trained ANN.

We conclude that for the subsatellite masses of interest, lifetimes obtained using a "reference diameter" of 3 m may be reliably used only in cases involving tether lengths of at least 50 km, to predict the orbital lifetimes of systems involving any subsatellite diameter up to 5 m. Clearly, the subsatellite diameter must be a contributing factor used in the prediction of the lifetimes of systems with shorter tethers, to obtain final accuracies within the desired limits.

As a result, we choose to train a neural network to predict the orbital lifetimes of upward-deployed systems involving tether lengths of at least 50 km. By making this choice, the number of independent variables is limited to just four: the CM orbit's initial radius of perigee, the initial CM orbit's size and shape factor, the length of the trailing tether, and the mass of the upward-deployed subsatellite. We also note that the end product, a trained artificial neural network, will provide results for systems whose "equivalent sphere" (i.e., single-mass) lifetime predictions are particularly unreliable (cf. Figures 74, 75, and 76).

**Neural Network Representation.** A feed-forward ANN, which mirrors the network structure previously defined and used, was trained to represent a large set of EPM-generated lifetime data for upward-deployed systems. Unlike previous networks, 100 hidden layer neurons were required to obtain the desired  $\pm 10\%$  prediction accuracy.

The network's structure is shown in Figure 79. It is composed of four linear input neurons, 100 hidden sigmoidal (logistic function) neurons, and one linear output neuron. Each of the four independent variables identified in the previous section (initial radius of perigee, initial orbit size and shape factor, tether length, subsatellite mass) were scaled to the range (0,1), and input to the network. The network's output is the system's predicted orbital lifetime, in units of hours. **Appendix E** contains exact details of the input data scaling procedures, and the weights and biases for the trained network.

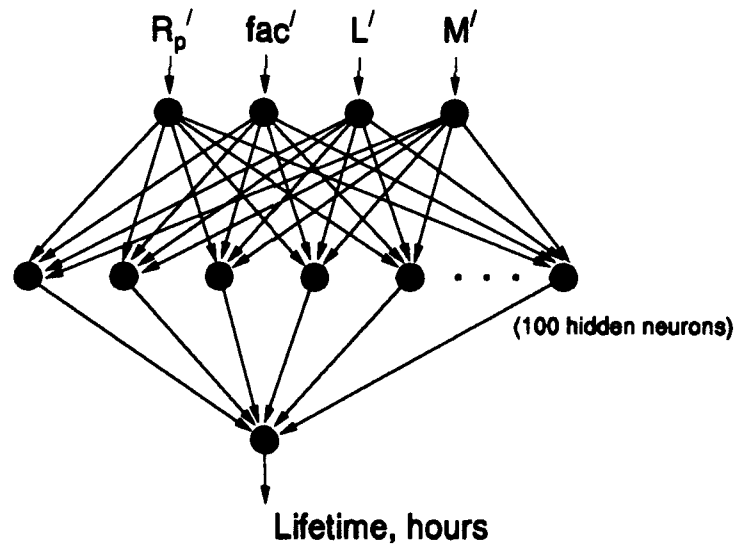


Figure 79. Upward-deployed tether-trailing satellite lifetime prediction network.

The training data set consisted of the lifetime prediction curve data for eight different subsatellite masses, trailing a tether of any of three lengths. Specifically, the

subsatellite masses included were 0, 25, 50, 100, 175, 275, 375, and 500 kg, and the three tether lengths were 50, 75, and 100 km. Hence the training data contained results obtained in 24 different subsatellite mass / tether length scenarios. Each scenario consists of 28 lifetime prediction curve data points, which means a total of 672 EPM-generated orbital lifetimes were used to train the network. The EPM results were obtained assuming a subsatellite diameter of 3 m, except in the zero (subsatellite) mass cases, when the diameter was set to zero.

The network was trained using the hybrid training approach derived earlier in this work. Training was continued until the network had learned to represent the mapping at each point with less than 10% error. The network's generalization accuracy was tested by comparing its output with EPM-generated data for tether lengths, subsatellite masses, and perigee and/or apogee radii not included in the training data. In most cases, the trained network's accuracy was significantly better than the 20% goal, and the maximum error observed in any case was less than 15%.

Figure 80 shows the network's output and EPM-generated data for a system composed of a 200 kg, 3 m upward-deployed subsatellite, trailing a 60 km tether. With the exception of the diameter, this case demonstrates the network's performance in a case that is only encompassed by the training data - the network was not shown data for this tether length or subsatellite mass during training. The network output shown in the figure was generated by varying the perigee and apogee radii in 25 km increments.

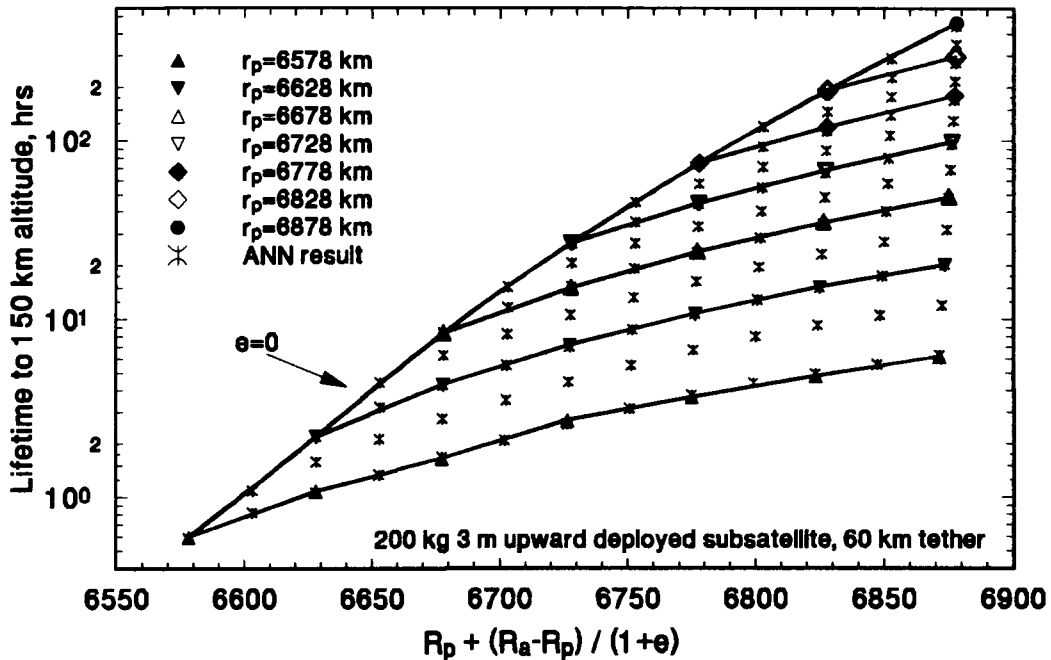


Figure 80. Network output and orbital lifetime data for 200 kg, 60 km system.

The accuracy and "smoothness" of the network's output in this case are typical. Figure 81 shows the errors in predicted versus calculated lifetimes. The maximum magnitude percent error in the network's predictions was 7.3%, and the mean of the absolute values of the errors was only 2.1%.

To further demonstrate the smoothness of the trained network's representation, Figure 82 shows, for systems including a 60 km tether and having an initial perigee radius of 6578.137 km, the variation in predicted lifetime with changes in both subsatellite mass and the initial CM orbit's apogee radius. In agreement with the trends identified earlier (Figure 78), we see that orbital lifetime increases with

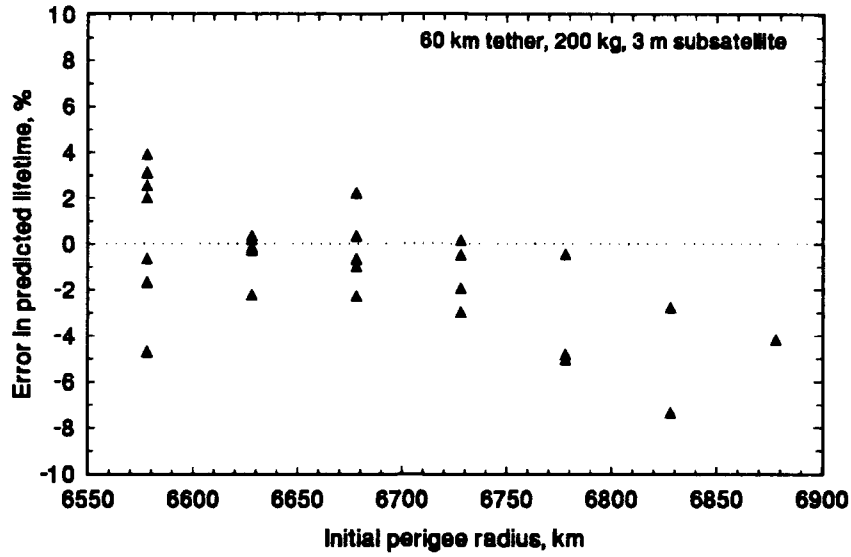


Figure 81. Network lifetime prediction accuracy, 200 kg, 60 km system.

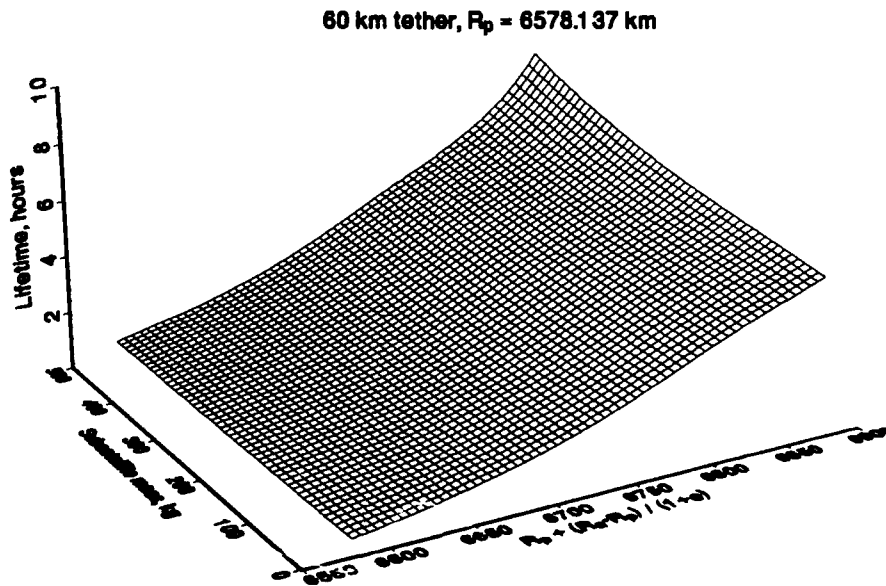


Figure 82. Predicted lifetime variations due to changes in  $R_p$  and subsatellite mass.

increases in apogee radius and/or subsatellite mass. The three-dimensional surface in Figure 82 was created by varying the CM orbit's initial apogee radius in 5 km increments, and varying the subsatellite's mass in increments of 10 kg. Hence, each grid point in the figure represents an actual network output value - i.e., there were no fictitious points created in the graphing procedure.

Figure 83 shows a similar surface, created by varying the CM orbit's initial apogee radius in 5 km increments, and varying the length of the trailing tether attached to a 300 kg subsatellite in 2 km increments. The initial perigee radius was 6578.137 km in all cases. In agreement with the trends identified earlier (Figure 77), we see that orbital lifetime increases with increases in the initial CM orbit's apogee radius, and/or decreases in trailing tether length. As before, each grid point in the figure represents an actual network output value, demonstrating the smoothness of the network's interpolation.

Based on these results, and those obtained in many other "interpolation" test cases, we believe the trained network can adequately predict the orbital lifetime of any upward-deployed tether-trailing system, within the following boundaries: subsatellite mass no greater than 500 kg, subsatellite diameter no greater than 5 m, tether length between 50 and 100 km, inclusive, initial CM orbit perigee radius no less than 6578.137 km, and initial CM orbit apogee radius no greater than 6878.137 km. Additionally, the results derived here require that the system initially be located at perigee, and that perigee be located at the ascending node of an orbit with an inclination of  $28.5^\circ$ .

In the next section of this Chapter, we will demonstrate the accuracy of lifetime predictions provided by the network in a large number of randomly chosen cases. We will also show how the network may be used to predict the orbital lifetime of systems originating in orbits whose inclinations, arguments of perigee and true anomalies are not  $28.5^\circ$ , zero, and zero, respectively.

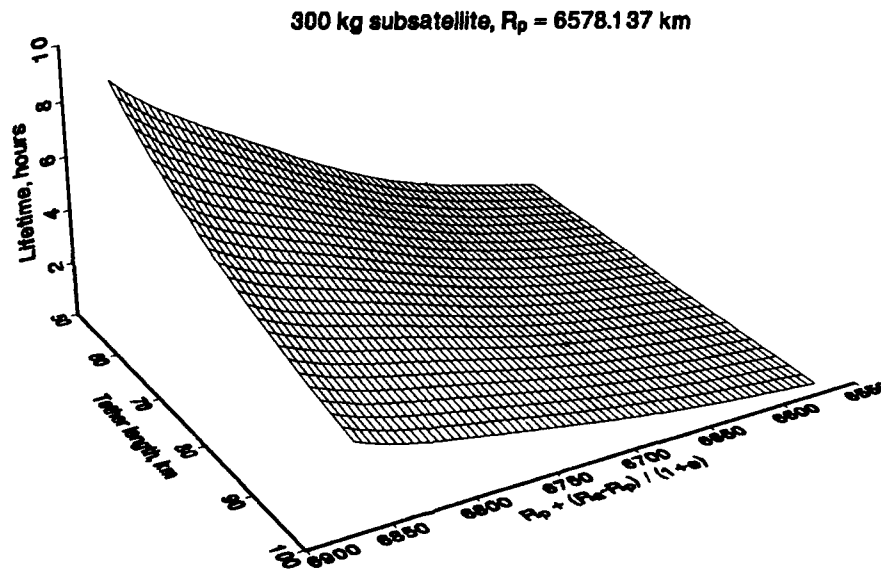


Figure 83. Predicted lifetime variations due to changes in  $R_p$  and tether length.

### Test Case Results

In this section, the utility and accuracy of the orbital lifetime prediction methods derived in this research project are demonstrated. Results of using the derived methods to predict orbital lifetimes in a total of 90 cases are presented: 45

free tether cases, and 45 (upward-deployed) tether-trailing satellite cases. In each case, some or all of the initial conditions and system physical characteristics were determined randomly. The results obtained in the test cases demonstrate

- (1) the accuracy of EPM results as compared to the MBM;
- (2) the accuracy of network lifetime predictions as compared to the MBM ( $i = 28.5^\circ$ ,  $\omega = \nu = 0$  cases);
- (3) the accuracy of lifetime predictions obtained using inclination-only correction factors, as compared to the MBM ( $i \neq 28.5^\circ$  cases);
- (4) the accuracy of lifetime predictions obtained using correction factor network results, as compared to the MBM ( $\omega, \nu \neq 0$  cases).

For each type of system, results obtained in three different scenarios are presented. The constants and variables in each scenario are listed below.

#### Free tether scenarios

- (1)  $i = 28.5^\circ$ ,  $\omega = \nu = 0$ , fixed;  $R_p$ ,  $R_a$ , tether length, variable; (10 cases).
- (2)  $i = 28.5^\circ$  fixed;  $\omega, \nu, R_p, R_a$ , tether length, variable; (15 cases).
- (3)  $i, \omega, \nu, R_p, R_a$ , tether length, variable; (20 cases).

#### Tether-trailing satellite scenarios

- (1)  $i = 28.5^\circ$ ,  $\omega = \nu = 0$ , fixed;  $R_p, R_a$ , tether length, subsatellite mass, subsatellite diameter, variable; (10 cases).
- (2)  $i = 28.5^\circ$  fixed;  $\omega, \nu, R_p, R_a$ , tether length, subsatellite mass, subsatellite diameter, variable; (15 cases).
- (3)  $i, \omega, \nu, R_p, R_a$ , tether length, subsatellite mass, subsatellite diameter, variable; (20 cases).

In each case, a random number generator, which provided random numbers between 0 and 1, inclusive, from a uniform distribution, was used to determine initial conditions, and in many cases, system physical dimensions. The random numbers,

once obtained, were mapped to the appropriate magnitude range for the variable of interest.

For example, the initial CM orbit's perigee radius,  $R_p$ , was always a randomly determined variable. To map values between 0 and 1 to the acceptable range, 6578.137 to 6878.137 (km), the operation

$$R_p = ran \times 300 + 6578.137$$

was performed, where  $ran$  is a generator-provided random number. To use values between 0 and 1 to determine subsatellite diameter, with any value up to 5 (meters) being acceptable,  $ran$  is simply multiplied by 5.0. Similar procedures were used to determine values for each variable in the various scenarios.

Results with Free Tethers, Standard Scenario. Results obtained for free tethers originating in standard scenario orbits ( $i = 28.5^\circ$ ,  $\omega = \nu = 0$ ) are shown in Table 14. In this table, the units on  $R_p$ ,  $fac$ , and tether length are kilometers, the units on lifetimes are hours, and the errors are in percent, calculated from

$$\text{Lifetime error (\%)} = \frac{\mathcal{L} - \mathcal{L}_{MBM}}{\mathcal{L}_{MBM}} \times 100 \quad (105)$$

Here,  $\mathcal{L}$  is the orbital lifetime obtained using either the EPM, or the free tether lifetime prediction network, and  $\mathcal{L}_{MBM}$  is the orbital lifetime calculated using the multi-body model. For the 10 test cases, the mean of the errors in the EPM lifetimes is -1.28%, with a maximum of -5.08%, and the mean of the errors in the network-predicted lifetimes is -2.98%, with a maximum of -8.37%.

Clearly, all results were well within the desired  $\pm 20\%$  error range, and we note that the 10 random cases included tether lengths ranging from slightly more than 15 km to over 120 km, with lifetimes varying from slightly less than 3 hours to nearly 7 days.

Table 14. Prediction method performance with free tethers, standard scenario.

$R_p$	$fac$	Length	MBM Life	EPM Life	EPM Error	Net Life	Net Error
6750.30	6766.07	31.46	40.64	40.53	-0.27	40.65	0.02
6725.23	6840.62	18.34	60.48	60.29	-0.31	58.80	-2.78
6649.36	6745.73	68.62	9.57	9.47	-1.04	9.20	-3.87
6591.36	6832.64	15.48	7.53	7.47	-0.80	6.90	-8.37
6580.73	6728.82	35.44	2.90	2.86	-1.38	2.87	-1.03
6629.49	6681.76	120.88	2.95	2.80	-5.08	2.86	-3.05
6629.74	6793.24	43.40	11.26	11.15	-0.98	10.91	-3.11
6694.69	6736.31	121.30	12.61	12.42	-1.51	12.03	-4.60
6731.71	6788.89	109.90	34.32	34.05	-0.79	33.53	-2.30
6822.18	6848.48	70.09	160.98	159.94	-0.65	159.84	-0.71

Results with Free Tethers,  $i = 28.5^\circ$ . Results obtained for free tethers originating in nonstandard orbits with a  $28.5^\circ$  inclination are shown in Table 16. Table 15 shows the randomly chosen initial conditions and tether length in each case. Errors in lifetime are listed in percent, calculated as shown in the previous section. The U-i

Table 15. Initial conditions and tether length, free tethers,  $i = 28.5^\circ$ .

Case	$R_p$ , km	$fac$ , km	$\omega$ , deg	$v$ , deg	Length, km
1	6605.62	6799.22	12.60	324.51	22.98
2	6628.54	6630.85	6.57	40.78	51.02
3	6665.86	6833.78	38.25	115.89	113.68
4	6629.37	6790.19	149.76	6.60	103.65
5	6851.71	6872.63	27.18	4.17	43.75
6	6613.73	6744.35	35.89	353.32	118.26
7	6582.82	6814.71	175.18	101.43	84.10
8	6635.89	6720.90	1.85	94.37	31.52
9	6676.93	6853.95	124.87	100.06	89.70
10	6668.80	6815.80	34.11	78.14	113.93
11	6625.12	6714.84	123.91	130.52	111.18
12	6620.71	6747.33	28.39	81.77	106.90
13	6843.47	6863.95	83.64	347.70	101.88
14	6592.12	6718.55	64.66	298.98	13.15
15	6591.46	6617.42	149.38	271.39	11.95

correction factors are also in percent, the units used by the U-i correction factor network. (Predicted lifetimes were calculated using Eq. (98), page 140.)

As shown in Table 16, results obtained with the EPM agree quite well with those obtained using the MBM. The mean percent error in the EPM results is only -4.48%, with a maximum percent error of -12.55%. Although not shown in the tables, the mean percent error in the uncorrected network-generated lifetimes,

compared to the MBM results, is -7.27%, with a maximum of -15.2%. Hence, we see that prediction errors occurring when  $i = 28.5^\circ$ , with no correction factors applied, are acceptably small. This is because the variations in orbital lifetimes caused by nonzero argument of perigee and true anomaly values are relatively small at this inclination.

As shown in Table 16, applying correction factors provided by the U-i correction factor network ("U-i Corr.") to lifetimes predicted by the standard scenario

Table 16. Prediction method performance with free tethers,  $i = 28.5^\circ$ .

Case	MBM Life	EPM Life	EPM Error	Net Life	U-i Corr.	CorrNet Life	CorrNet Error
1	7.37	7.32	-0.68	7.77	-5.47	7.35	-0.27
2	2.30	2.24	-2.61	2.15	4.46	2.25	-2.17
3	18.59	18.40	-1.02	19.55	-1.09	19.34	4.03
4	8.54	8.39	-1.76	8.13	-1.48	8.01	-6.21
5	271.81	269.01	-1.03	264.59	2.67	271.65	-0.06
6	4.21	4.05	-3.80	4.10	-2.63	3.99	-5.23
7	4.70	4.11	-12.55	4.07	3.70	4.22	-10.21
8	7.48	7.15	-4.41	6.77	7.55	7.28	-2.67
9	28.74	28.21	-1.84	29.51	-0.68	29.31	1.98
10	20.47	18.98	-7.28	17.90	6.62	19.09	-6.74
11	4.60	4.03	-12.39	4.08	2.49	4.18	-9.13
12	5.96	5.39	-9.56	5.05	6.80	5.39	-9.56
13	224.41	217.61	-3.03	211.24	4.36	220.45	-1.76
14	3.05	3.01	-1.31	3.32	-5.60	3.13	2.62
15	1.25	1.20	-4.00	1.20	2.68	1.23	-1.60

network ("Net Life") yields the lifetimes shown in the "CorrNet Life" column. This procedure reduced the mean percent error in lifetime (i.e., mean of the "CorrNet Error" column), to just -4.28%, with a maximum of -10.21%. The network-generated correction factors greatly improved the prediction network's results in this scenario.

Clearly, the EPM provided reliable results in each of the 15 nonstandard cases, and the predictions of the (standard scenario) free tether lifetime prediction network, with and without assistance from the U-i correction factor network, yielded results well within the desired  $\pm 20\%$  error tolerance. We again note the wide range of results and physical characteristics included in the test cases: lifetimes ranged from little more than one hour, to over 11 days, and tether lengths ranged from less than 12 km to over 118 km.

Results with Free Tethers, All Orbital Elements Variable. Results obtained for random length free tethers originating in randomly chosen orbits, within the constraints on the models and prediction methods, are presented in Table 17 and Table 18. Table 17 lists the randomly chosen initial conditions, tether length, MBM lifetime, EPM lifetime, and EPM error in each case. Table 18 lists the lifetimes and errors resulting from using correction factors provided by the U-i correction factor network ("CNet1 Life", "CNet1 Error") and the inclination-only procedure ("CNet2 Life", "CNet2 Error"). As before, lifetimes are in hours, and the errors in calculated and predicted lifetimes, as compared to results obtained with the MBM, are shown in percent. The units on  $R_p$ ,  $fac$ , and tether length are kilometers, and the angular orbital elements are in units of degrees.

Table 17. Initial conditions, tether length, MBM life, and EPM accuracy, free tethers.

Case	$R_p$	$fac$	$i$	$\omega$	$v$	Length	MBM Life	EPM Life	EPM Error
1	6764.96	6796.33	72.79	167.95	233.46	97.98	70.44	68.65	-2.54
2	6634.03	6744.75	19.94	124.75	218.57	55.23	6.53	6.48	-0.77
3	6603.88	6688.77	78.12	8.02	231.17	41.14	4.93	4.85	-1.62
4	6795.93	6859.92	50.63	87.03	49.38	21.87	170.78	169.42	-0.80
5	6710.50	6776.23	38.64	5.39	34.76	69.89	29.66	29.36	-1.01
6	6692.14	6840.40	45.55	124.33	296.95	53.38	43.65	43.13	-1.19
7	6655.03	6730.32	76.17	138.72	81.75	113.96	9.95	9.59	-3.62
8	6621.97	6674.29	55.44	9.52	160.64	24.10	3.85	3.80	-1.30
9	6638.02	6819.61	70.17	99.68	34.10	57.05	19.25	19.22	-0.16
10	6608.04	6801.27	68.15	137.41	90.00	100.19	8.49	8.10	-4.59
11	6687.47	6771.70	34.19	141.10	272.91	34.58	22.75	22.56	-0.84
12	6633.97	6838.91	24.01	107.51	192.61	36.63	13.94	13.89	-0.36
13	6751.99	6801.52	9.66	164.37	257.08	15.09	54.55	54.20	-0.64
14	6748.55	6768.68	78.58	11.99	300.39	93.03	48.81	48.76	-0.10
15	6655.42	6679.17	30.27	148.69	323.62	52.65	6.14	5.95	-3.09
16	6599.61	6827.12	6.79	124.29	298.18	68.66	6.07	5.90	-2.80
17	6579.32	6788.85	28.15	129.67	175.49	76.79	3.17	2.83	-10.73
18	6617.67	6735.50	26.11	20.94	54.89	51.33	6.03	5.82	-3.48
19	6843.95	6849.04	2.51	158.68	225.11	107.09	169.52	167.92	-0.94
20	6680.72	6857.85	4.32	110.37	260.99	19.01	32.17	32.05	-0.37

The mean percent error in lifetimes calculated using the EPM, as compared to those obtained with the MBM (i.e., mean of "EPM Error", Table 17), is only -2.05%,

and the maximum percent error was -10.73%. Clearly, the EPM is able to provide very acceptable results, as compared to those obtained using the MBM, for free tethers of any length, originating in any orbit within the constraints of the models.

Table 18. Prediction method accuracies, free tethers.

Case	Net Life	U-i Corr.	CNet1 Life	CNet1 Error	i-only Corr.	CNet2 Life	CNet2 Error
1	53.48	30.99	70.05	-0.55	34.91	72.15	2.43
2	7.74	-8.42	7.09	8.58	-4.17	7.42	13.63
3	3.09	52.45	4.71	-4.46	36.36	4.21	-14.60
4	145.79	20.83	176.16	3.15	19.85	174.73	2.31
5	26.68	9.57	29.23	-1.45	9.36	29.18	-1.62
6	36.79	20.94	44.49	1.92	15.40	42.46	-2.73
7	7.03	30.04	9.14	-8.14	35.97	9.56	-3.92
8	3.47	12.30	3.90	1.30	23.90	4.30	11.69
9	14.28	30.47	18.63	-3.22	33.79	19.11	-0.73
10	6.00	32.36	7.94	-6.48	32.76	7.97	-6.12
11	21.09	6.53	22.47	-1.23	5.65	22.28	-2.07
12	15.73	-2.08	15.40	10.47	-1.79	15.45	10.83
13	57.87	-8.51	52.95	-2.93	-8.31	53.06	-2.73
14	35.39	34.28	47.52	-2.64	36.41	48.28	-1.09
15	5.32	5.12	5.59	-8.96	2.57	5.46	-11.07
16	7.08	-9.55	6.40	5.44	-8.95	6.45	6.26
17	3.29	0.30	3.30	4.10	1.02	3.32	4.73
18	5.67	5.78	6.00	-0.50	-0.41	5.65	-6.30
19	185.47	-12.51	162.27	-4.28	-9.52	167.81	-1.01
20	37.26	-12.30	32.68	1.59	-9.33	33.78	5.00

The mean of the absolute values of the percent errors in lifetimes obtained using the U-i correction factor network in conjunction with the free tether lifetime prediction network (i.e., mean of errors occurring when "U-i Corr." is applied to "Net Life", Table 18) is 4.07% (i.e., mean of absolute values in "CNet1 Error", Table 18). The maximum magnitude percent error which occurred using this method was 10.47%. As these results are well within the desired  $\pm 20\%$  accuracy limits, we conclude that lifetime predictions obtained for free tethers, using the standard scenario lifetime prediction and U-i correction factor networks, are reliably accurate.

The mean of the absolute values of the percent errors in lifetimes obtained using the inclination-only correction factor function in conjunction with the free tether lifetime prediction network (i.e., mean of errors occurring when "i-only Corr." is applied to "Net Life", Table 18) is 5.54% (i.e., mean of absolute values in "CNet2 Error", Table 18). The maximum magnitude percent error which occurred using this method was 14.60%. These values are slightly higher than those obtained using the U-i correction factor network, but are still within the desired accuracy range. Six of the 20 predictions obtained using the inclination-only procedure were more accurate than those obtained using the U-i correction factor network.

Although not listed in the tables, the absolute value of the percent errors in lifetimes obtained from the (standard scenario) free tether lifetime prediction network, with no correction factors applied, as compared to those calculated with the MBM, is 16.4%. The maximum magnitude percent error was 37.2%, and 6 of the lifetimes

predicted using this approach misrepresent the corresponding MBM value by more than  $\pm 20\%$ .

The positive effects of both the U-i correction factor network and the inclination-only correction factor function are obvious: each correction factor method significantly reduced the mean percent error in the 20 cases, and, more importantly, the maximum percent errors were also greatly reduced, to values well within the maximum allowable error range. Figure 84 shows the errors in lifetime resulting from each correction factor method, as well as the error in lifetimes predicted using the standard scenario network with no corrections applied.

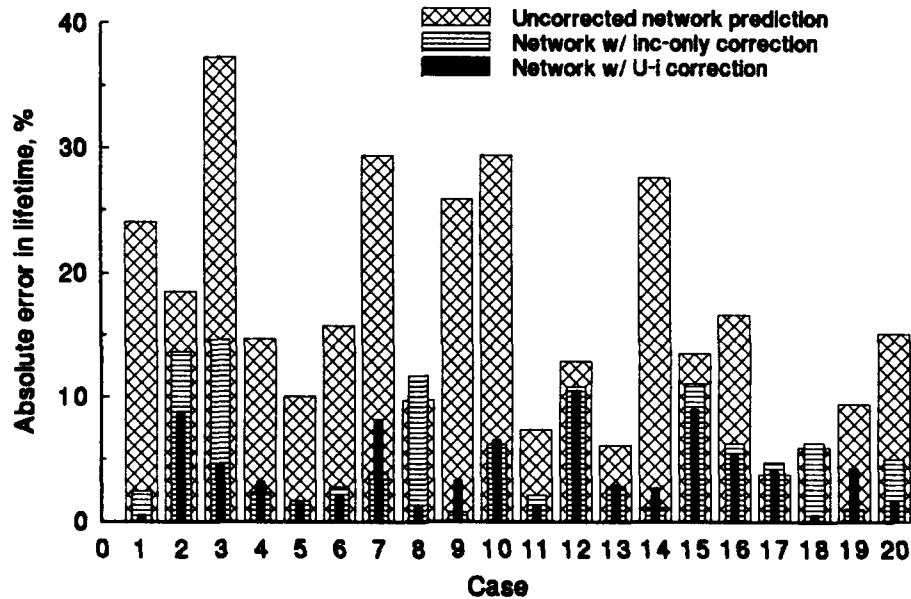


Figure 84. Errors in free tether lifetime predictions.

Results with Tether-Trailing Satellites, Standard Scenario. In this scenario, five variables were determined randomly: the CM orbit's initial perigee and apogee radii, the length of the trailing tether, and the subsatellite's mass and diameter. The CM orbit's initial inclination was  $28.5^\circ$  in each case, and the initial argument of perigee and true anomaly were zero. Table 19 contains the randomly determined initial conditions and system characteristics, and Table 20 lists the calculated and predicted orbital lifetimes, and errors, in each case. As always, the units on  $R_p$ ,  $fac$ , and tether length are kilometers, the units on the subsatellite's mass and diameter are kilograms and meters, respectively, lifetimes are given in hours, and errors are in percent.

The mean of the percent errors in EPM-calculated lifetimes is -3.35%, with a maximum percent error of -9.52%. Similarly, the mean of the absolute values of the

Table 19. Initial conditions and system dimensions, standard scenario.

Case	$R_p$	$fac$	Length	Subsat Mass	Subsat Diam
1	6595.71	6714.98	64.41	111.78	1.70
2	6710.86	6767.23	85.96	140.27	2.92
3	6622.04	6673.86	54.92	186.83	1.92
4	6653.13	6786.82	66.21	478.58	4.06
5	6792.49	6828.16	98.89	118.00	3.79
6	6697.03	6710.07	74.24	207.14	0.98
7	6657.35	6684.04	92.72	340.12	4.25
8	6649.17	6727.61	51.11	455.06	4.30
9	6707.99	6808.13	83.65	234.26	0.07
10	6587.38	6647.40	73.39	239.35	1.78

percent errors in lifetimes predicted using the trained neural network is 4.06%, and the largest percent error is -11.56%. Hence we see that both the EPM and trained lifetime prediction network provided results well within the desired  $\pm 20\%$  error tolerance.

The network was able to provide acceptable predictions even in cases with physically unrealistic subsatellite mass/diameter combinations. For example, in Case 9, an 83.65 km (51.98 mile) tether was trailing below a 234 kg (516.5 lbm), 0.07 m (0.24 ft  $\approx$  3 inches) subsatellite; the network mispredicted the MBM-calculated lifetime of 38.56 hours by slightly more than 5%, even though no similarly unrealistic examples were included in the training data set (in fact, no "unrealistic" examples were included at all). This is a good indication that the network has successfully "internalized" the

Table 20. Calculated and predicted lifetimes and accuracies, standard scenario.

Case	MBM Life	EPM Life	EPM Error	Network Life	Network Error
1	3.35	3.09	-7.76	3.09	-7.76
2	25.21	24.96	-0.99	24.86	-1.39
3	4.09	3.96	-3.18	3.88	-5.13
4	21.68	21.23	-2.08	21.36	-1.48
5	97.23	96.51	-0.74	95.86	-1.41
6	13.74	13.54	-1.46	13.32	-3.06
7	5.26	5.01	-4.75	5.10	-3.04
8	15.24	14.92	-2.10	15.32	0.52
9	38.56	38.19	-0.96	36.53	-5.26
10	1.47	1.33	-9.52	1.30	-11.56

proper rules for prioritizing its inputs in a manner that allows it to generate correct predictions.

Results with Tether Trailing Satellites,  $i = 28.5^\circ$ . Results obtained for upward-deployed tether-trailing satellites originating in nonstandard orbits (i.e., those with  $\omega, \nu \neq 0$ ) inclined at  $28.5^\circ$  are shown in Table 22. Table 21 lists the randomly generated initial conditions and system physical characteristics in each case. The units on values in both Tables are identical to those discussed in the previous section.

The mean percent error in lifetimes calculated using the EPM, as compared to those obtained using the MBM, is -4.95%, with a maximum percent error of -14.78%. Although these errors are larger than we have seen in previous scenarios, they are, nonetheless, acceptable. The EPM continues to be a reliable means of calculating orbital lifetimes of tethered systems much more quickly than is possible with the MBM.

The upward-deployed tether-trailing satellite lifetime prediction network predicted lifetimes in this scenario with percent errors ranging from -19.79%, to 1.21%. The mean of the absolute values of the percent errors is 7.62%, and the maximum magnitude percent error was 19.79%.

We note that the argument of latitude in cases 4 and 13, the cases with the maximum percent errors in predicted lifetime, are close to  $90^\circ$ . That the standard scenario lifetime prediction network mispredicted these lifetimes is not surprising, as we recall from our earlier investigation of initial inclination and argument of latitude

Table 21. Initial conditions and system dimensions,  $i = 28.5^\circ$ .

Case	$R_p$	$fac$	$\omega$	$v$	Length	Subsat Mass	Subsat Diam.
1	6584.14	6797.75	122.26	81.59	70.45	270.36	4.93
2	6609.39	6747.19	133.04	100.05	83.08	431.41	1.50
3	6601.99	6831.23	172.54	288.38	77.15	393.86	2.01
4	6798.17	6869.50	77.58	1.84	53.56	325.63	0.13
5	6644.13	6795.65	27.81	106.51	50.01	382.80	0.15
6	6740.44	6773.72	148.03	24.51	87.40	364.29	0.10
7	6812.26	6864.68	80.89	205.43	97.37	189.60	2.10
8	6755.97	6822.31	74.58	277.80	63.77	272.40	3.69
9	6622.93	6700.98	98.58	103.22	55.59	240.87	3.87
10	6752.40	6864.03	78.68	77.20	64.93	417.24	4.45
11	6641.98	6736.94	31.10	272.77	55.93	121.03	1.72
12	6735.13	6789.72	141.48	155.20	73.94	101.63	3.35
13	6621.15	6753.50	92.11	11.69	93.00	92.09	4.36
14	6625.06	6849.82	149.93	9.39	77.89	45.01	0.84
15	6784.60	6849.35	142.65	345.58	58.14	198.63	1.12

effects that  $i = 28.5^\circ$   $U = 90^\circ$  is the location of an extremum value in the variation of orbital lifetime relative to the same orbit and system's  $U = 0$  lifetime.

Figure 85 shows the relationship between errors in predicted lifetimes in this scenario and lifetime correction factors provided by the U-i correction factor network when  $i = 28.5^\circ$ . Although the U-i correction factor network was trained using results

Table 22. MBM life, EPM life, network predicted life, and errors,  $i = 28.5^\circ$ .

Case	MBM Life	EPM Life	EPM Error	Network Life	Network Error
1	4.82	4.16	-13.69	4.47	-7.26
2	5.68	5.01	-11.80	5.09	-10.39
3	9.20	7.84	-14.78	8.11	-11.85
4	307.04	293.39	-4.45	248.51	-19.06
5	25.07	24.49	-2.31	23.11	-7.82
6	43.67	43.19	-1.10	42.26	-3.23
7	181.68	174.19	-4.12	166.73	-8.23
8	92.49	91.75	-0.80	90.64	-2.00
9	5.50	5.35	-2.73	5.45	-0.91
10	143.01	141.91	-0.77	144.74	1.21
11	9.55	9.36	-1.99	9.35	-2.09
12	44.74	44.04	-1.56	43.17	-3.51
13	6.67	5.96	-10.64	5.35	-19.79
14	13.08	12.93	-1.15	12.72	-2.75
15	170.34	166.37	-2.33	146.27	-14.13

derived from free tether orbital lifetime data, we see that the correction factors would reduce prediction errors in 10 of the 15 tether-trailing satellite cases.

That the U-i correction factor network, trained using free tether data, may be of beneficial assistance in predicting the orbital lifetimes of tether-trailing satellites is not a totally illogical result. Since the lifetime prediction curves for upward-deployed

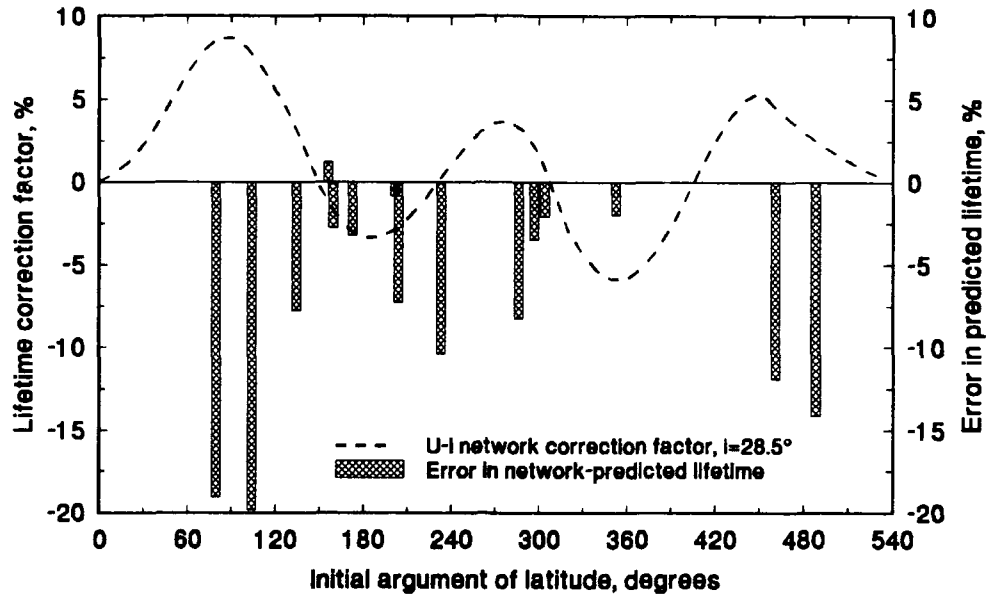


Figure 85. U-i correction factors and errors in predicted lifetimes,  $i = 28.5^\circ$ .

tether-trailing systems are essentially identical in character to those for free tethers (only the magnitudes are different), the effects of variations in initial orbit inclination and argument of latitude on orbital lifetimes should also be similar.

Figure 85 shows that the error in predicted lifetime for five of the cases in this scenario will be increased by applying the corresponding U-i correction factor (i.e., there are 5 cases in which the correction factor and the error in (uncorrected) predicted lifetime have the same sign). This results from the averaging process used to generate the correction factor values - the lifetimes in some cases and scenarios will differ from those in the standard scenario more than in others. For example, the same phenomena occurred in two free tether, nonstandard scenario cases discussed

earlier: in cases 4 and 6, Table 16, applying the appropriate U-i correction factors to predictions provided by the free tether lifetime prediction network produced results that were further from the "true" values provided by the MBM. Fortunately, the final errors were still well within the desired error limits, and the mean and maximum percent errors in the scenario were reduced, indicating the overall positive influence of the correction factors.

Table 23 contains the U-i correction factors, the resulting corrected lifetime predictions, and the errors in the corrected lifetimes, as compared to those obtained using the MBM, for the 15 cases in the current tether-trailing scenario. The mean of the percent errors is -6.8%, and the maximum percent error was reduced from -19.79% to -13.94%.

Figure 86 shows, graphically, the changes in the percent errors caused by applying the U-i correction factors to the uncorrected network predictions in each case. As expected, the correction factors worsened the prediction errors in five cases. Fortunately, as in the free tether scenario, the errors are still well below the desired 20% maximum error limit. Additionally, using the correction factors reduced the mean percent error by 1.2 percentage points, and reduced the maximum error by nearly 6 percentage points. Expecting similar results in all nonstandard scenarios, we broaden our tests to include any allowable initial orbit inclination in the next section.

Table 23. U-i correction factors, predicted lifetimes and errors,  $i = 28.5^\circ$ .

Case	U-i Correction Factor, %	Corrected Net Lifetime, hrs	Corrected Net Error, %
1	-2.87	4.34	-9.96
2	0.27	5.10	-10.21
3	4.65	8.49	-7.72
4	7.72	267.70	-12.81
5	3.14	23.84	-4.91
6	-3.38	40.83	-6.50
7	3.62	172.77	-4.90
8	-6.00	85.20	-7.88
9	-3.03	5.28	-4.00
10	-1.39	142.73	-0.20
11	0.91	9.44	-1.15
12	2.46	44.23	-1.14
13	7.23	5.74	-13.94
14	-1.95	12.47	-4.66
15	2.41	149.80	-12.06

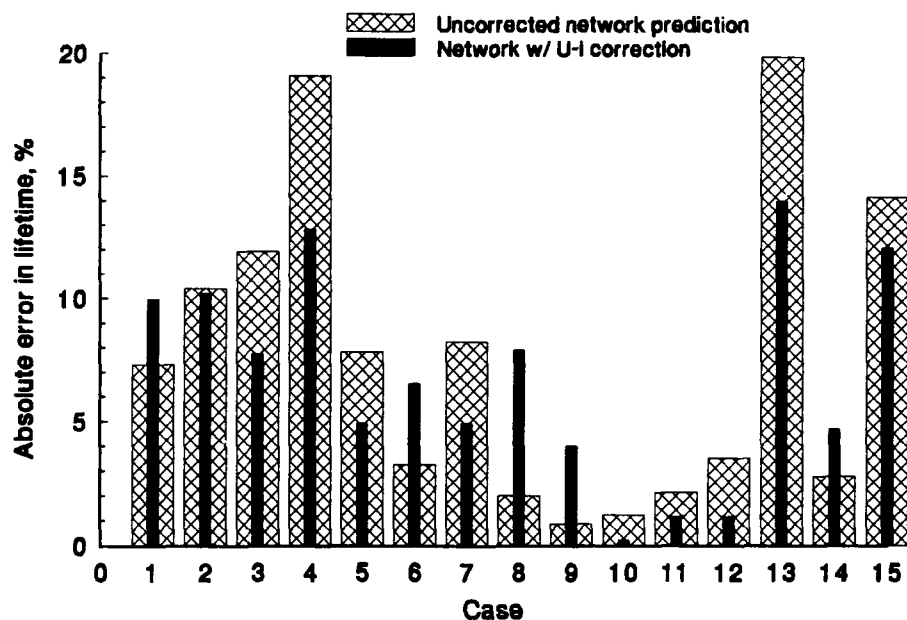


Figure 86. Errors in corrected and uncorrected predicted lifetimes,  $i = 28.5^\circ$ .

Results with Tether-Trailing Satellites, All Orbital Elements Variable. Results obtained for randomly-sized upward-deployed tether-trailing satellites, originating in randomly chosen orbits, within the constraints on the models and prediction methods, are presented in Tables 25 and 26. Table 24 lists the randomly chosen initial conditions, tether length, subsatellite mass, and subsatellite diameter in each case. Table 25 contains the MBM, EPM, and (uncorrected) network-predicted lifetimes. It also lists the percent errors in lifetimes obtained using the EPM and prediction network. Table 26 lists the U-i correction factors ("U-i Corr."), the lifetimes and errors resulting from using these correction factors ("CNet1 Life", "CNet1 Error"), the inclination-only correction factors ("i-only Corr."), and the lifetimes and errors

resulting from using these corrections ("CNet2 Life", "CNet2 Error"). The units on values in all three tables are identical to those used in the previous section.

Table 24. Initial conditions and system dimensions, upward-deployed satellites.

Case	$R_p$	$fac$	$i$	$\omega$	$v$	Length	Subsat Mass	Subsat Diam
1	6824.14	6873.19	42.11	91.28	13.64	63.67	309.39	4.15
2	6691.45	6855.33	47.59	125.74	45.05	90.18	308.82	2.01
3	6718.85	6848.27	46.95	126.63	172.56	89.18	240.19	2.46
4	6738.76	6875.86	27.03	155.17	290.58	88.56	411.87	4.22
5	6712.39	6713.89	76.12	140.77	144.16	73.48	88.27	4.26
6	6595.90	6864.56	12.51	13.01	234.48	70.39	202.60	0.37
7	6838.66	6857.92	0.95	178.56	280.78	68.92	446.48	4.87
8	6594.04	6738.29	63.29	117.28	193.20	77.79	219.08	2.84
9	6592.30	6828.20	53.87	10.05	350.01	58.26	140.83	2.25
10	6587.22	6804.55	36.71	67.40	172.89	50.42	282.38	2.51
11	6624.97	6838.17	73.66	25.14	343.11	67.12	390.60	1.17
12	6628.36	6827.54	45.03	65.54	258.06	77.74	41.94	2.92
13	6686.59	6690.88	60.69	14.47	2.06	96.29	369.59	1.07
14	6746.08	6846.17	53.61	130.85	28.10	86.64	73.13	4.71
15	6619.69	6734.55	72.84	42.77	171.90	54.63	224.84	2.19
16	6747.28	6769.10	28.21	138.13	157.57	66.88	172.27	4.16
17	6631.90	6839.81	11.57	136.39	92.41	84.04	479.40	0.14
18	6773.92	6850.35	23.37	31.08	6.56	95.30	220.56	2.01
19	6674.20	6826.27	64.91	91.77	47.73	97.84	417.86	3.12
20	6662.79	6797.55	51.60	26.49	129.33	88.54	116.52	1.43

Table 25. MBM, EPM and network lifetimes and errors, upward-deployed satellites.

Case	MBM Life	EPM Life	EPM Error	Network Life	Network Error
1	388.81	347.27	-10.68	283.73	-27.03
2	45.04	44.71	-0.73	40.67	-9.70
3	68.46	67.52	-1.37	55.18	-19.40
4	110.85	102.58	-7.46	101.72	-8.24
5	25.60	24.97	-2.46	15.12	-40.94
6	6.88	6.03	-12.35	8.38	21.80
7	317.22	301.40	-4.99	331.75	4.58
8	5.14	5.04	-1.95	3.25	-36.77
9	7.88	7.49	-4.95	7.29	-7.49
10	8.26	7.36	-10.90	7.10	-14.04
11	19.76	19.28	-2.43	16.49	-16.55
12	12.29	12.27	-0.16	11.83	-3.74
13	9.96	9.54	-4.22	7.83	-21.39
14	77.31	76.83	-0.62	70.33	-9.03
15	10.00	9.55	-4.50	7.09	-29.10
16	47.83	47.02	-1.69	45.33	-5.23
17	14.59	13.60	-6.79	15.64	7.20
18	107.39	106.01	-1.29	102.87	-4.21
19	33.84	33.18	-1.95	24.90	-26.42
20	18.09	17.97	-0.66	15.80	-12.66

Table 26. Prediction method accuracies, upward-deployed satellites.

Case	U-i Corr.	CNet1 Life	CNet1 Error	i-only Corr.	CNet2 Life	CNet2 Error
1	21.86	345.75	-11.07	12.37	318.83	-18.00
2	8.59	44.16	-1.95	17.20	47.67	5.84
3	24.68	68.80	0.50	16.64	64.36	-5.99
4	3.92	105.71	-4.64	0.22	101.94	-8.04
5	63.14	24.67	-3.63	35.96	20.56	-19.69
6	-8.69	7.65	11.19	-7.45	7.76	12.79
7	-9.38	300.63	-5.23	-9.63	299.80	-5.49
8	29.35	4.20	-18.29	29.80	4.22	-17.90
9	7.96	7.87	-0.13	22.60	8.94	13.45
10	9.48	7.77	-5.93	7.72	7.65	-7.39
11	12.69	18.58	-5.97	35.22	22.30	12.85
12	8.40	12.82	4.31	14.94	13.60	10.66
13	13.84	8.91	-10.54	27.98	10.02	0.60
14	13.95	80.14	3.66	22.39	86.08	11.34
15	23.81	8.78	-12.20	34.93	9.57	-4.30
16	2.33	46.39	-3.01	1.06	45.81	-4.22
17	-8.77	14.27	-2.19	-7.76	14.43	-1.10
18	0.32	103.20	-3.90	-2.19	100.62	-6.30
19	25.61	31.28	-7.57	30.86	32.58	-3.72
20	13.91	18.00	-0.50	20.69	19.07	5.42

The mean percent error in lifetimes calculated using the EPM, as compared to those obtained using the MBM (i.e., mean of "EPM Error", Table 25) is -4.11%, with

a maximum percent error of -12.35%. Hence the EPM has again proven to be a reliable means of quickly calculating orbital lifetimes.

The upward-deployed, tether-trailing satellite lifetime prediction network provided predicted lifetimes with percent errors ranging from -40.94% to 7.20% ("Network Error", Table 25). The mean of the absolute values of the percent errors is 16.30%, and the predicted lifetimes in 7 of the 20 cases were in error by more than  $\pm 20\%$ . These results are not surprising, since the (uncorrected) network predicts orbital lifetimes assuming a standard scenario ( $i = 28.5^\circ$ ,  $\omega = \nu = 0$ ).

Applying correction factors provided by the U-i correction factor network reduced the mean of the absolute values of the percent errors to just 5.82%, with a maximum magnitude percent error of 18.29% ("CNet1 Error", Table 26). Percent errors ranged from -18.29% to 11.19%.

Using correction factors provided by the inclination-only correction factor function yielded a mean (absolute) percent error in predicted lifetime of 8.75%, with errors ranging from -19.69% to 13.45% ("CNet2 Error", Table 26).

Clearly, both correction factor techniques, derived using free tether results, were successful in significantly reducing the errors in predicted lifetimes of tether-trailing satellites. These results are noteworthy, in addition to those obtained in the previous ( $i = 28.5^\circ$ ) section, because they demonstrate the capability of the techniques over a wide range of initial orbit inclinations. Initial inclinations in this scenario ranged from a low of only  $0.95^\circ$ , to  $76.12^\circ$  (Table 24).

Figure 87 shows the relationships between the errors in lifetimes produced by each of the three prediction approaches: the prediction network with no corrections applied, the inclination-only correction factor approach, and the U-i correction factor approach. In four cases (8, 13, 15, 17) the inclination-only method yielded smaller magnitude percent errors than the U-i method. However, the differences were only significant in Case 15 (-4.30% vs. -12.20%) and Case 13 (0.60% vs. -10.54%). The inclination-only method worsened the error in predicted lifetime in 6 of the 20 cases, two of which were significant (9, 12), as compared to only 2 cases worsened by the U-i correction factors, neither of which were significant. Despite the "incorrect corrections", all errors were within the desired limits.

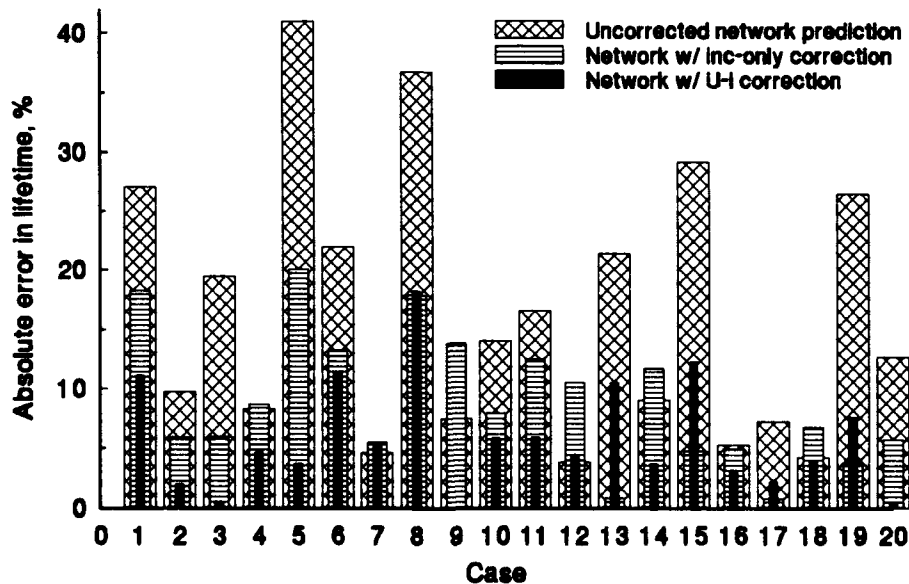


Figure 87. Errors in tether-trailing satellite lifetime predictions.

Both correction factor methods appear to provide an acceptable means of assisting the lifetime prediction network in calculating predicted lifetimes of upward-deployed tether-trailing satellites originating in nonstandard orbits. However, we must caution that although the inclination-only correction factor function led, with less effort, to acceptable lifetime predictions in the random test cases studied here, this may not always be the case.

Because the initial argument of latitude may cause significant variations about the mean correction factor, at any given inclination, but particularly at the higher inclinations, it is more likely that correction factors obtained using the inclination-only approach will be inadequate, as initial orbit inclination increases, than those obtained using the U-i correction factor network. Because this situation is a result of natural phenomena (i.e., the shape of the Earth and atmosphere), this caution applies to lifetime predictions for both free tethers and tether-trailing satellites.

## CONCLUSIONS AND RECOMMENDATIONS

In 1988, King-Hele and Walker, two of the world's foremost authorities on predicting the orbital lifetimes of single-mass Earth satellites, stated, "Accurate prediction of the lifetimes of satellites decaying naturally under the action of air drag is one of the most difficult problems of orbital dynamics".<sup>102</sup> The objective of this research project was to develop a method for predicting the orbital lifetimes of uncontrolled free tethers and tether-trailing satellites, systems whose dynamics and physical properties are, in many respects, more complex than those of single-mass satellites.

The general approach to solving the problem has been the application of the so-called empirical method. Mathematical functions, in the form of trained artificial neural networks, have been derived from data produced by a dynamical system model.

Using an extensive multibody model (MBM), which includes tether elasticity and attitude variation effects, the effects of various assumptions on calculated orbital lifetimes were investigated. It was shown that modeling drag coefficients as Knudsen number-dependent variables, as compared to setting them to commonly used constant values, has a significant effect on calculated lifetime. We also found that assuming an oblate Earth and a rotating, oblate atmosphere had a discernible effect on calculated lifetimes.

An orbital element propagation model (EPM), using Gauss' form of Lagrange's planetary equations, in terms of equinoctial elements, was developed. The EPM provides very accurate orbital decay results, as compared to the more rigorous multi-body model, very quickly. The EPM's accuracy was demonstrated in scenarios involving free tethers, upward- and downward-deployed subsatellites trailing a tether, and also with a system consisting of a tethered pair. In 90 randomly chosen test cases (45 free tethers, 45 upward-deployed tether-trailing satellites), errors in lifetimes calculated with the EPM, using results obtained with the MBM as truth, were always smaller than  $\pm 15\%$ . In 80 of the 90 test cases, the errors were less than  $\pm 10\%$ . In each case, the EPM reduced computer simulation time by a ratio of over 300 to 1. Hence we have developed a new and original technique for reliably simulating the orbital decay of tethered systems, very quickly.

It was shown that lifetimes calculated using an equivalent (mass and area) sphere in the place of a tethered system were only sometimes reliable. The most severe errors occurred with free tethers longer than approximately 50 km, and upward-deployed subsatellites trailing a (downward-deployed) tether longer than approximately 50 km. The focus of the research project was hence narrowed to provide prediction techniques for free tethers and upward-deployed tether-trailing satellites. It is these systems whose lifetimes will be very poorly predicted by the various single-mass orbital lifetime prediction methods used today.

We derived an algorithm to train feed-forward artificial neural networks by minimizing a cost function based on the sum of the percentage errors which occur in a

network's representation of a training data set. This algorithm has proven to be very effective in training networks to represent orbital lifetime data spanning many orders of magnitude. The "standard" backpropagation training algorithm is often unable to train a network to accurately represent widely-spread real-valued data, as it seeks to minimize a cost function based on the summation of the squares of the magnitude errors. A hybrid training approach was also described and demonstrated. This combination of the derived Minimum Percent Error (MPE) and standard backpropagation training algorithms is often able to significantly reduce training time while producing a network which generalizes well.

The MPE training algorithm and hybrid training approach were used to train three networks: one to predict the orbital lifetimes of free tethers, one to predict the orbital lifetimes of upward-deployed tether-trailing satellites, and one to provide correction factors for predicted lifetimes, which account for variations in initial orbit inclination and argument of latitude.

The lifetime correction factors, which vary as functions of both initial inclination and initial argument of latitude, were derived using an averaging approach. Although derived using lifetime data for a 50 km free tether, the corrections were shown to be dramatically effective in modifying the predicted lifetimes of tethers and upward-deployed systems of various dimensions.

There are some cases in which the correction factor will not modify a predicted lifetime enough to place its accuracy within the desired  $\pm 20\%$  error range, but we have observed that essentially all of these occurrences involve relatively short

lifetimes. The most common cases in which this deficiency occurs are those involving an initial perigee radius of 6578.137 km. Lifetimes in these cases typically range from one-half hour to approximately 10 hours.

An inclination-only lifetime correction factor function was also derived. This function provides a relatively easy and quick way to approximate differences in lifetimes caused by differences in initial orbit inclination. As inclination increases, the function-provided correction factors become less reliable, since variations in initial argument of latitude cause larger and larger deviations from the mean (inclination-driven) difference in lifetime. However, as we demonstrated in 40 randomly-generated test cases (20 free tether cases, 20 upward-deployed tether-trailing satellite cases), the inclination-only function provides satisfactory results in many instances, even at high inclinations.

There are quite a few effects that were not investigated in this research project. One possibly significant area for further research is the effect of material properties on orbital lifetimes. It is likely that tether properties, such as mass density, elasticity, and the coefficient of thermal expansion, may have a discernible, if not significant, affect on lifetimes. The material properties of any attached end-body, such as surface reflectivity, absorptivity, etc., may also cause significant changes in calculated lifetimes. Variations in end-body shape and orientation may also significantly affect orbital lifetimes.

Extending the models to simulate the orbital evolution of systems originating in higher altitude orbits, which hence have longer lifetimes, is another area of possibility.

To be done reliably, this will require, at a minimum, that the Sun's gravitational forces be added to the force model developed in this work.

The initial state of a deployed tether will definitely affect a system's orbital lifetime. Lifetimes undoubtedly will vary notably if a deployed tether is initially stretched significantly, or is not nearly straight, or is not aligned along the local vertical. Any of these initial conditions will probably render results obtained with the EPM, in its present form, woefully inaccurate. However, it may be possible, by simply modifying the (constant) tether shape and orientation assumed in the model, to continue to use the orbital element propagation approach reliably.

In addition to providing mathematical models and trained neural networks which can be used by others to calculate and predict the orbital lifetimes of various tethered systems, we have also demonstrated a very powerful approach to solving "difficult" problems. Although the empirical method is centuries old, the ability of artificial neural networks to develop, autonomously, their own internal rules and representations, simply by repeatedly viewing and attempting to emulate a training data set, is a current capability that greatly simplifies a researcher's task. This capability is especially valuable in situations involving multidimensional data, as a priori knowledge of the form of an appropriate function is not required. We have also demonstrated the ability of neural nets to learn to quite accurately represent widely-spread real-valued data.

Whether or not tethered satellites ever become commonplace in Earth orbit, and whether or not an operational need to predict the lifetime of an uncontrolled

system ever arises, the use of artificial neural networks as an integral part of the empirical method is surely an approach whose value and power are just beginning to be realized. The neural network training techniques derived and applied in this research project will undoubtedly be appropriate for future applications in various fields of study and endeavor.

## REFERENCES

<sup>1</sup>Tsiolkovsky, K. E., *Grezy O. Zemle i nebe (i) Na Veste (Speculations between earth and sky, and on Vesta: science fiction works)*, Isd-vo AN-SSSR, 1895 (reprinted in 1959), pg. 35.

<sup>2</sup>Bekey, I., "Tethers Open New Space Options", *Astronautics and Aeronautics*, Vol. 21, No. 4, April 1983, pp. 32-40.

<sup>3</sup>Artsutanov, Y., "V Kosmos na Electrovoze: Komsomolskaya", *Pravda*, July 31, 1960 (summarized in English in *Science*, Vol 158, pp. 946-947).

<sup>4</sup>Carroll, J. A., "Tether Applications in Space Transportation", *Acta Astronautica*, Vol. 13, No. 4, 1986, pg. 165.

<sup>5</sup>Carroll, pg. 165.

<sup>6</sup>Misra, A. K., and Modi, V. J., "A Survey on the Dynamics and Control of Tethered Satellite Systems", *Advances in the Astronautical Sciences*, Vol. 62, 1987, pg. 668.

<sup>7</sup>Grossi, M. D., "Tether History and Historiography", *Proceedings of the 2nd International Conference on Tethers in Space*, October, 1987, pp. 3-8.

<sup>8</sup>Colombo, G. "Shuttle-borne 'Skyhook': A New Tool for Low Orbital Altitude Research", *Smithsonian Astrophysical Observatory Report*, 1974.

<sup>9</sup>Carroll, pg. 165.

<sup>10</sup>Penzo, P. A., and Ammann, P. W. (Co-Eds.), *Tethers in Space Handbook*, Second Edition, NASA Office of Space Flight, May 1989, pg. 3.

<sup>11</sup>Penzo and Ammann, pg. 6.

<sup>12</sup>*Tethered Satellite System 2 Planning Guide*, NASA Office of Aeronautics and Space Technology, May 1989, pp. 21-22.

- <sup>13</sup>Bergamaschi, S., and Morana, M., "Order of Magnitude Evaluation of the Lifetime of a Free Tether in Orbit", *Proceedings of the 2nd International Conference on Tethers in Space*, October, 1987, pp. 453-460.
- <sup>14</sup>Bergamaschi, S., "Orbit Evolution and Decay of Tether Launched Space Systems", *Proceedings of the 3rd International Conference on Tethers in Space*, May, 1989, pp. 178-183.
- <sup>15</sup>King-Hele, D. G., *Satellite Orbits in an Atmosphere: Theory and Applications*, Blackie and Son Ltd., Glasgow, Scotland, 1987.
- <sup>16</sup>Incropera, F. P., and DeWitt, D. P., *Fundamentals of Heat and Mass Transfer*, Second Edition, John Wiley & Sons, New York, 1985, pp. 311-312.
- <sup>17</sup>Incropera and DeWitt, pp. 311-403.
- <sup>18</sup>Masterton, W. L., and Slowinski, E. J., *Chemical Principles*, Third Edition, W. B. Saunders Co., Philadelphia, PA, 1973, pp. 92-99.
- <sup>19</sup>Penzo and Ammann, pp. 37-38.
- <sup>20</sup>Misra, A. K., and Modi, V. J., "Dynamics and Control of Tether Connected Two-Body Systems - A Brief Review", AIAA Paper 82-315, Presented at the 33rd Congress of the International Astronautical Federation, Sept. 27-Oct. 2, 1982.
- <sup>21</sup>Bergamaschi and Morana, 1987, pg. 456.
- <sup>22</sup>Simpson, P. K., *Artificial Neural Systems*, Pergamon Press, Elmsford, NY, 1990, pg. 136.
- <sup>23</sup>Strachey, J., *The Standard Edition of the Complete Psychological Works of Sigmund Freud: Vol. I, Pre-Psycho-Analytic Publications and Unpublished Drafts*, The Hogarth Press, London, England, 1966, pp. 295-343.
- <sup>24</sup>Simpson, pg. 136.
- <sup>25</sup>Russell, S. B., "A Practical Device to Simulate the Working of Nervous Discharges", *The Journal of Animal Behavior*, Vol. 3, 1913, pp. 15-35.
- <sup>26</sup>McCulloch, W., and Pitts, W., "A Logical Calculus of the Ideas Immanent in Nervous Activity", *Bulletin of Mathematical Biophysics*, Vol. 7, 1943, pp. 115-133.
- <sup>27</sup>Simpson, pg. 136.
- <sup>28</sup>Hebb, D., *Organization of Behavior*, John Wiley & Sons, New York, 1949.

- <sup>29</sup>Simpson, pg. 136.
- <sup>30</sup>Bernstein, J., "Profiles: Marvin Minsky", *The New Yorker*, December 14, 1981, pp. 50-126.
- <sup>31</sup>Simpson, pg. 137.
- <sup>32</sup>Simpson, pg. 137.
- <sup>33</sup>Bernstein, pg. 69.
- <sup>34</sup>Simpson, pg. 137.
- <sup>35</sup>Simpson, pg. 136.
- <sup>36</sup>Simpson, pg. 30.
- <sup>37</sup>Rumelhart, D. E., Hinton, G. E., and Williams, R. J., "Learning Representations by Back-Propagating Errors", *Nature*, Vol. 323, October 1986, pp. 533-536.
- <sup>38</sup>Rumelhart, D. E., Hinton, G. E., and Williams, R. J. "Learning Internal Representations by Error Propagation", *Parallel Distributed Processing*, Vol. 1, MIT Press, Cambridge, MA, 1986, pp. 319-362.
- <sup>39</sup>Simpson, pg. 120.
- <sup>40</sup>Hecht-Nielson, R., "Theory of the Backpropagation Neural Network", *Proceedings of the 1989 IEEE INNS International Joint Conference on Neural Networks*, Vol. I, SOS Printing, San Diego, CA, 1989, pg. I-593.
- <sup>41</sup>Hecht-Nielson, R., "Neurocomputing: Picking the Human Brain", *Artificial Neural Networks: Theoretical Concepts*, Computer Society Press, Washington, DC, 1988, pp. 16-17.
- <sup>42</sup>Yoon, B. L., "Neural Networks: Still Looking Good", *Aerospace America*, Vol. 29, No. 10, October 1991, pp. 48-50.
- <sup>43</sup>Lapedes, A., and Farber, R., "How Neural Nets Work", *Evolution, Learning and Cognition*, World Scientific Publishing Co., London, England, 1988, pp. 331-346.
- <sup>44</sup>Sietsma, J., and Dow, R. J. F., "Creating Artificial Neural Networks That Generalize", *Neural Networks*, Vol. 4, No. 1, 1991, pp. 67-79.
- <sup>45</sup>Sietsma and Dow, pg. 67.

- <sup>46</sup>Sejnowski, T., and Rosenberg, C., "Parallel Networks That Learn to Pronounce English Text", *Complex Systems*, Vol. 1, No. 1, 1987, pp. 145-168.
- <sup>47</sup>Lapedes and Farber, pg. 344.
- <sup>48</sup>Bate, R. R., Mueller, D. D., and White, J. E., *Fundamentals of Astrodynamics*, Dover Publications, New York, 1971, pp. 2-3.
- <sup>49</sup>King-Hele, 1987, pg. 10.
- <sup>50</sup>Kaplan, M. H., *Modern Spacecraft Dynamics and Control*, John Wiley & Sons, Inc., New York, 1976, pg. 282.
- <sup>51</sup>*The Astronomical Almanac For The Year 1989*, Nautical Almanac Office, United States Naval Observatory, U.S. Government Printing Office, Washington D.C., 1989, pg. E88.
- <sup>52</sup>Regan, F. J., *Re-Entry Vehicle Dynamics*, AIAA, New York, 1984, pp. 203-206.
- <sup>53</sup>Minzner, R. A., *The 1976 Standard Atmosphere Above 86-km Altitude*, NASA, Washington, D.C., 1976, pp. 31-38.
- <sup>54</sup>Regan, pg. 219.
- <sup>55</sup>Harvey, J. K., "Rarefied Gas Dynamics For Spacecraft", *Hypersonics*, Vol. 1, Edwards Brothers, Inc., Ann Arbor, Michigan, 1989, pp. 493-497.
- <sup>56</sup>Koppenwallner, G., "Rarefied Gas Dynamics", *Hypersonics*, Vol. 1, Edwards Brothers, Inc., Ann Arbor, Michigan, 1989, pp. 525-531.
- <sup>57</sup>Koppenwallner, G., and Legge, H., "Drag of Bodies in Rarefied Hypersonic Flow", *Thermophysical Aspects of Re-Entry Flows*, Vol. 103, AIAA, New York, 1986, pp. 50-52.
- <sup>58</sup>Koppenwallner and Legge, 1986, pg. 51.
- <sup>59</sup>Koppenwallner, 1989, pg. 529.
- <sup>60</sup>Harvey, 1989, pp. 497-499.
- <sup>61</sup>Koppenwallner, G., "Drag and Pressure Distribution of a Circular Cylinder at Hypersonic Mach Numbers in the Range Between Continuum Flow and Free Molecular Flow", *Rarefied Gas Dynamics*, Vol. 1, (Proceedings of the Sixth International Symposium on Rarefied Gas Dynamics), Academic Press, New York, 1969, pp. 739-750.

<sup>62</sup>Legge, H., and Koppenwallner, G., "Sphere Drag Measurements in a Free Jet and a Hypersonic Low Density Tunnel", *Rarefied Gas Dynamics*, Vol. 1, (Proceedings of the Seventh International Symposium on Rarefied Gas Dynamics), Editrice Tecnico Scientifica, Pisa, Italy, 1971, pp. 481-488.

<sup>63</sup>Rees, D., Barnett, J. J., and Labitzke, K. (Co-Eds.), "COSPAR International Reference Atmosphere: 1986, Part I: Thermosphere Models", *Advances in Space Research*, Vol. 8, No. 5-6, 1988, pp. (5)9-(5)326.

<sup>64</sup>Rees, D., Barnett, J. J., and Labitzke, K. (Co-Eds.), "COSPAR International Reference Atmosphere: 1986, Part II: Middle Atmosphere Models", *Advances in Space Research*, Vol. 10, No. 12, 1990, pp. 12(1)-12(10).

<sup>65</sup>Whitten, R. C., Champion, K. S., Reid, R., and Vaughan, W. W. (Co-Eds.), *American National Standard Guide to Reference and Standard Atmosphere Models*, AIAA, 1990, pp. 3-4, 47-49.

<sup>66</sup>1986 COSPAR International Reference Atmosphere, Part II, pg. (12)3.

<sup>67</sup>Gersten, R. H., "Geodetic Sub-Latitude and Altitude of a Space Vehicle", *The Journal of the Astronautical Sciences*, Vol. VIII, No. 1, Spring, 1961, pp. 28-29.

<sup>68</sup>1989 *Astronomical Almanac*, pg. K6.

<sup>69</sup>*Mathematical Foundation For SCC Astrodynamic Theory*, NORAD Technical Publication TP SCC-008, Headquarters, North American Aerospace Defense Command, 6 April 1982, pg. 109.

<sup>70</sup>Kane, T. R., Likins, P. W., and Levinson, D. A., *Spacecraft Dynamics*, McGraw-Hill, Inc., New York, 1983, pg. 296.

<sup>71</sup>Gere, J. M., and Timoshenko, S. P., *Mechanics of Materials*, Second Edition, Wadsworth, Inc., Belmont, California, 1984, pg. 21.

<sup>72</sup>James, M. L., Smith, G. M., and Wolford, J. C., *Applied Numerical Methods for Digital Computation*, Second Edition, Harper & Row, New York, 1977, pg. 404.

<sup>73</sup>Bate, Mueller and White, pp. 387-389.

<sup>74</sup>Battin, R. H., *An Introduction to the Mathematics and Methods of Astrodynamics*, AIAA, New York, 1987, pg. 473.

<sup>75</sup>Battin, pg. 471.

<sup>76</sup>Battin, pg. 471.

- <sup>77</sup>Battin, pp. 476-484.
- <sup>78</sup>Taff, L. G., *Celestial Mechanics*, John Wiley & Sons, New York, 1985, pp. 300-316.
- <sup>79</sup>Battin, pp. 490-494.
- <sup>80</sup>Bergamaschi and Morana, 1987, pp. 453-460.
- <sup>81</sup>Battin, pg. 494.
- <sup>82</sup>Battin, pg. 494.
- <sup>83</sup>Muller, B., and Reinhardt, J., *Neural Networks*, Springer Verlag, Inc., New York, 1990, pg. 45.
- <sup>84</sup>Cybenko, G., "Approximation by Superpositions of a Sigmoidal Function", *Mathematics of Control, Signals, and Systems*, Vol. 2, Springer Verlag Inc., New York, 1989, pp. 303-314.
- <sup>85</sup>Simpson, pp. 113-114.
- <sup>86</sup>Rumelhart, Hinton, and Williams, October, 1986, pp. 533-536.
- <sup>87</sup>Minai, A. A., and Williams, R. D., "Acceleration of Back-Propagation through Learning Rate and Momentum Adaptation", *Proceedings of the 1990 International Joint Conference on Neural Networks*, Vol. I, Lawrence Erlbaum Associates, Hillsdale, NY, 1990, pp. I-676 - I-679.
- <sup>88</sup>Bergamaschi and Morana, 1987, pp. 453-460.
- <sup>89</sup>Sterne, T. E., *An Introduction to Celestial Mechanics*, Interscience Publishers, Inc., New York, 1960, pp. 116-150.
- <sup>90</sup>Liu J. J. and Alford, R. L., "Semianalytic Theory for a Close-Earth Artificial Satellite", *Journal of Guidance and Control*, Vol. 3, No. 4, July-August, 1980, pp. 304-311.
- <sup>91</sup>King-Hele, 1987, pp. 230-258.
- <sup>92</sup>Penzo and Ammann, pg. 7.
- <sup>93</sup>Hoots, F. R., and France, R. G., "Uncertainty Estimation for Satellite Lifetime Prediction", AAS Paper 91-431, August, 1991. (Presented at the AAS/AIAA Astrodynamics Specialist Conference, Durango, Colorado, 19-22 August 1991)
- <sup>94</sup>Liu and Alford, pp. 304-311.

<sup>95</sup>Whitten, Champion, Reid, and Vaughan, pp. 39-40.

<sup>96</sup>Hoots and France, pg. 2.

<sup>97</sup>Hoots and France, pg. 7.

<sup>98</sup>Hoots and France, pg. 10.

<sup>99</sup>Beyer, W. H. (Ed.), *CRC Standard Mathematical Tables*, 25th Edition, CRC Press, Inc., West Palm Beach, FL, 1978, pg. 175.

<sup>100</sup>Hoots and France, pg. 8.

<sup>101</sup>Bate, Mueller, and White, pg. 62.

<sup>102</sup>King-Hele, D. G. and Walker, D. M. C., "Predicting the Orbital Lifetimes of Earth Satellites", *Acta Astronautica*, Vol. 18. Pergamon Press, Oxford, England, 1988, pp. 123-131.

## **APPENDIX A**

### **Atmosphere Model**

Atmospheric Mass Density Model. The algorithm used to model the 1986 COSPAR International Reference Atmosphere mass density is presented below. The equations were derived using a least squares method. To maximize curvefit accuracy, the data were separated into six altitude segments. Each equation requires that altitude (*alt*) be input in kilometers, and yields the mass density in kg/m<sup>3</sup>.

For 50.0 km ≤ altitude < 70.72 km,

$$density = \left( \frac{a + c \cdot alt + e \cdot alt^2}{1 + b \cdot alt + d \cdot alt^2 + f \cdot alt^3} \right)^2$$

where

$$\begin{aligned} a &= -0.013334132 & b &= -0.062682054 & c &= 0.00010393496 \\ d &= 0.001238967 & e &= 1.108105 \times 10^{-7} & f &= -9.6011459 \times 10^{-6} \end{aligned}$$

For 70.72 km ≤ altitude < 103.319 km,

$$density = \exp\left(a + b \cdot alt^3 + \frac{c}{alt}\right)$$

where

$$a = -13.2408775 \quad b = -4.9112657 \times 10^{-6} \quad c = 386.6494328$$

For 103.319 km ≤ altitude < 125 km,

$$density = a + b \cdot alt + \frac{c}{alt} + \frac{d}{alt^{1.5}} + \frac{e}{alt^2}$$

where

$$a = -0.0017583229$$

$$b = 2.8715758 \times 10^{-6}$$

$$c = 0.646620178$$

$$d = -7.63995073$$

$$e = 26.45513632$$

For 125 km  $\leq$  altitude < 200 km,

$$\text{density} = \left( \frac{a + c \cdot \text{alt}}{1 + b \cdot \text{alt}} \right)^2$$

where

$$a = -3.144972 \times 10^{-5}$$

$$b = -0.0096872241$$

$$c = 7.9433967 \times 10^{-8}$$

For 200 km  $\leq$  altitude < 500 km,

$$\text{density} = \exp\left(a + b \cdot \text{alt} + \frac{c}{\text{alt}}\right)$$

where

$$a = -22.6805231$$

$$b = -0.01319637$$

$$c = 663.289123$$

For 500 km  $\leq$  altitude  $\leq$  1000 km,

$$\text{density} = \exp\left(a + b \cdot \text{alt}^2 + c \cdot \text{alt}^2 \cdot \ln(\text{alt})\right)$$

where

$$a = -21.5579663$$

$$b = -0.00014824362$$

$$c = 1.9745928 \times 10^{-5}$$

Figures A-1 through A-5 show the smoothness of the fit between data points and at altitudes where there is a transition from one equation to the next. Figure A-6 shows the atmospheric mass density over the altitude range 50 km to 1000 km, and Figure A-7 shows the accuracy of the curvefit. Curvefit error is less than  $\pm 4\%$  at any altitude up to 1000 km, and less than  $\pm 2\%$  over the altitude range 50 km to 500 km.

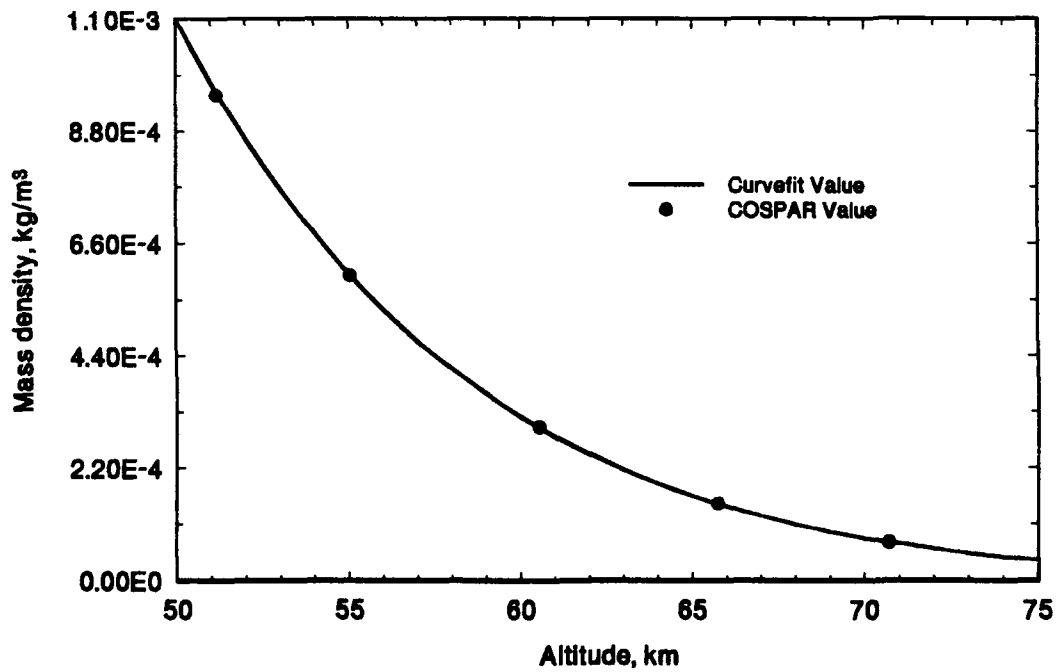


Figure A-1. Atmospheric mass density, 50-75 km.

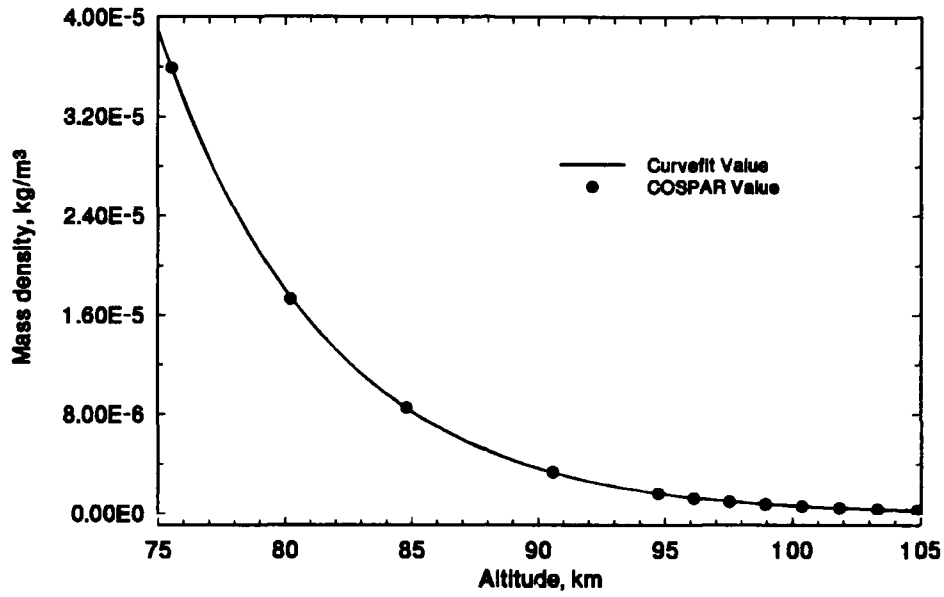


Figure A-2. Atmospheric mass density, 75-105 km.

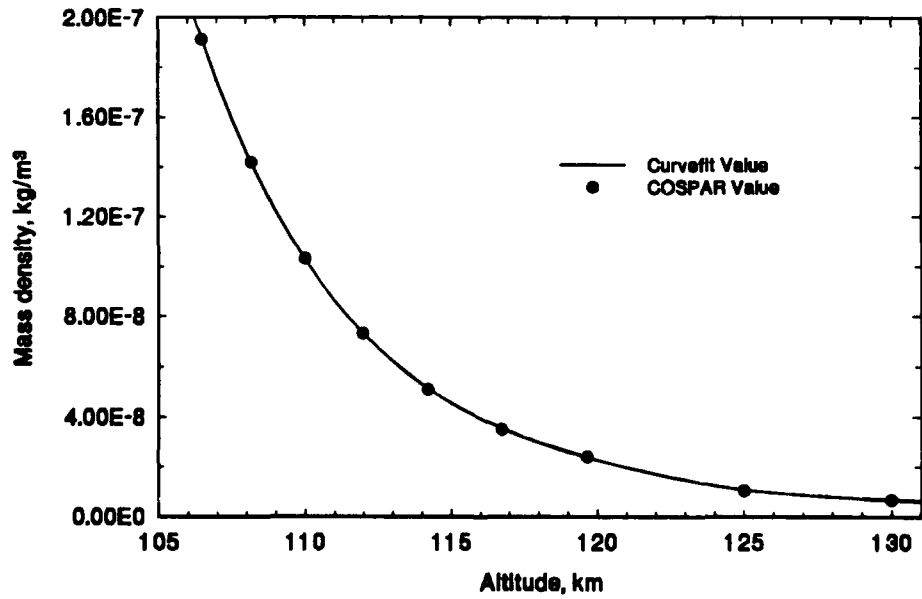


Figure A-3. Atmospheric mass density, 105-130 km.

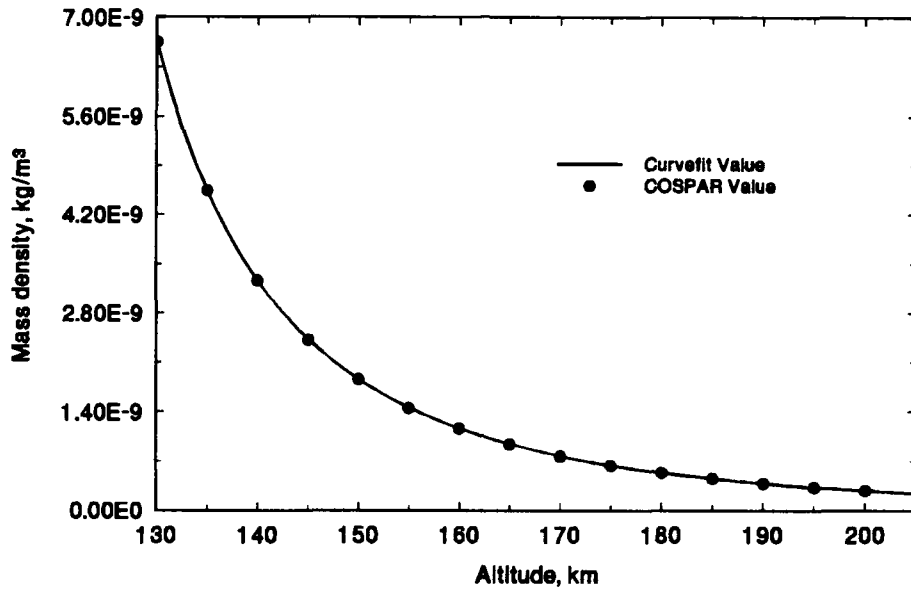


Figure A-4. Atmospheric mass density, 130-200 km.

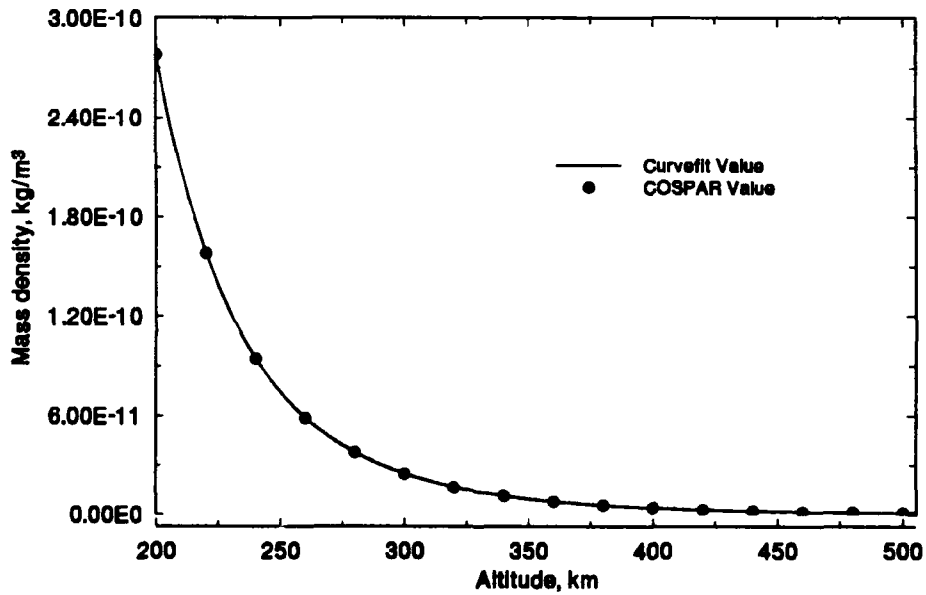


Figure A-5. Atmospheric mass density, 200-500 km.

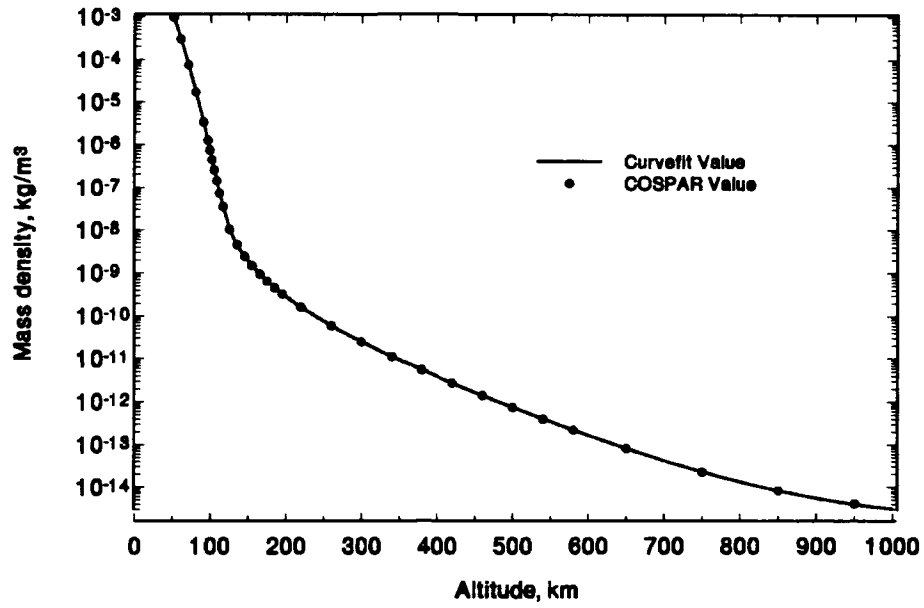


Figure A-6. Atmospheric mass density, 50-1000 km.

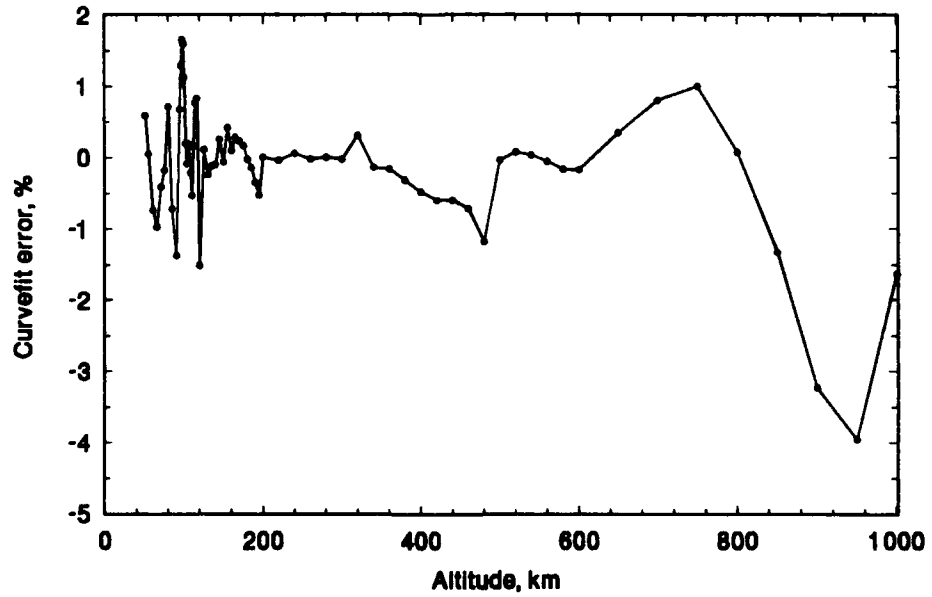


Figure A-7. Atmospheric mass density curvefit accuracy, 50-1000 km.

Molecular Mean Free Path Model. Mean free path data derived from the 1986 COSPAR International Reference Atmosphere is modeled in four altitude segments. The maximum altitude modeled is 200 km, since the largest body included in the present work (a 5 meter sphere) experiences free molecular flow conditions prior to reaching this height. The equations were derived using a least squares method. Each requires the altitude (*alt*) in kilometers, and yields the mean free path (*mfp*) in meters. For 50 km ≤ altitude ≤ 70.72 km,

$$mfp = \frac{a + c \cdot alt}{1 + b \cdot alt + d \cdot alt^2}$$

where

$$a = -1.6333717 \times 10^{-5}$$

$$b = -0.025658961$$

$$c = 5.2525786 \times 10^{-7}$$

$$d = 0.00016667317$$

For 70.72 km < altitude ≤ 103.319 km,

$$mfp = \left( \frac{a + c \cdot alt}{1 + b \cdot alt + d \cdot alt^2} \right)^2$$

where

$$a = -0.006307417$$

$$b = -0.017378386$$

$$c = 0.00016634472$$

$$d = 7.6539008 \times 10^{-5}$$

For 103.319 km < altitude ≤ 125 km,

$$mfp = \frac{a + c \cdot \ln(alt) + e \cdot (\ln(alt))^2}{1 + b \cdot \ln(alt) + d \cdot (\ln(alt))^2}$$

where

$$a = 0.877984043$$

$$b = -0.40954511$$

$$c = -0.38755049$$

$$d = 0.041951477$$

$$e = 0.042777741$$

For 125 km < altitude ≤ 200 km,

$$mfp = \left( \frac{a + c \cdot alt}{1 + b \cdot alt} \right)^2$$

where

$$a = -9.09341521$$

$$b = -0.0020986475$$

$$c = 0.088170734$$

Figures A-8 through A-11 show the smoothness of the fit between data points and at altitudes where there is a transition from one equation to the next. Figure A-12 shows the molecular mean free path over the altitude range 50 km to 200 km. As shown in Figure A-13, the curvefit absolute error is less than 3% over the modeled altitude range.

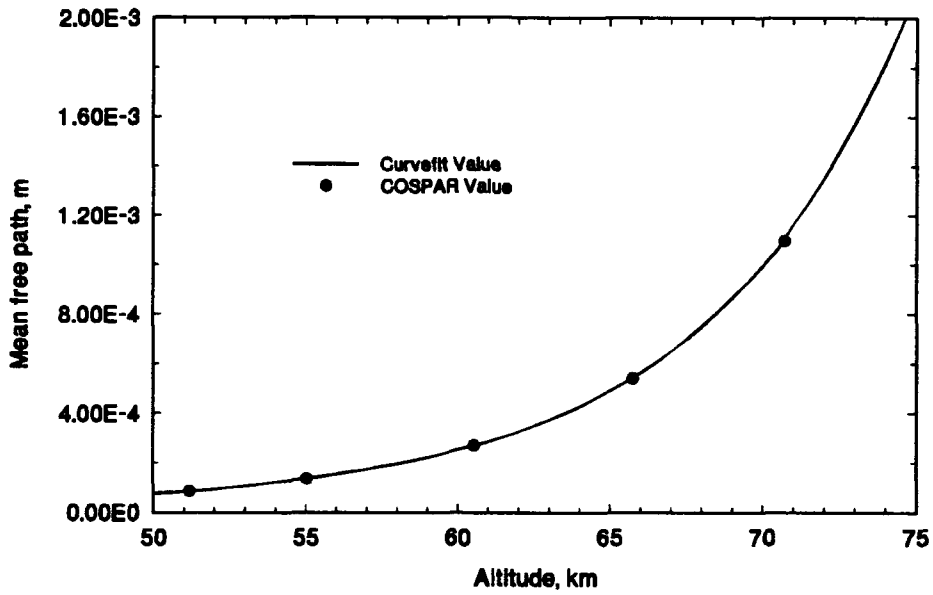


Figure A-8. Mean free path, 50-75 km.

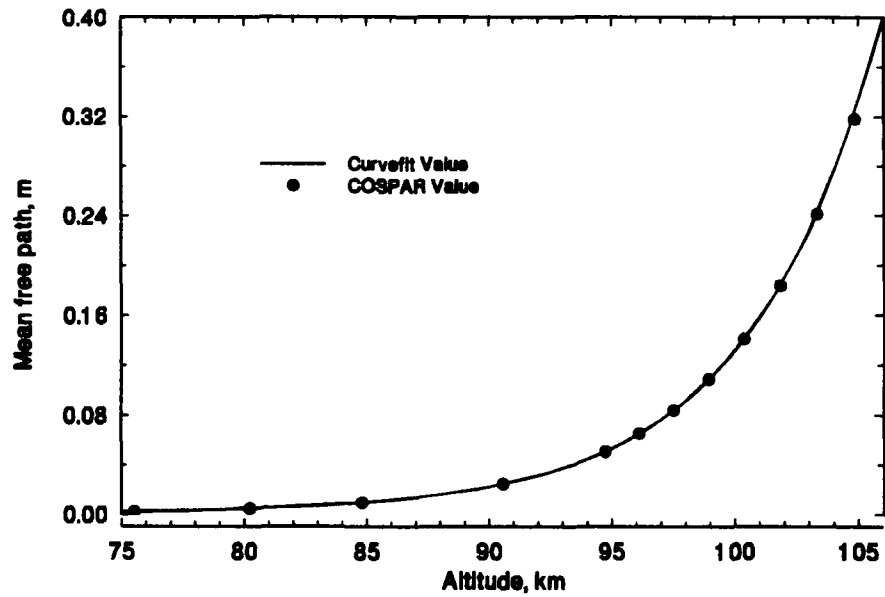


Figure A-9. Mean free path, 75-105 km.

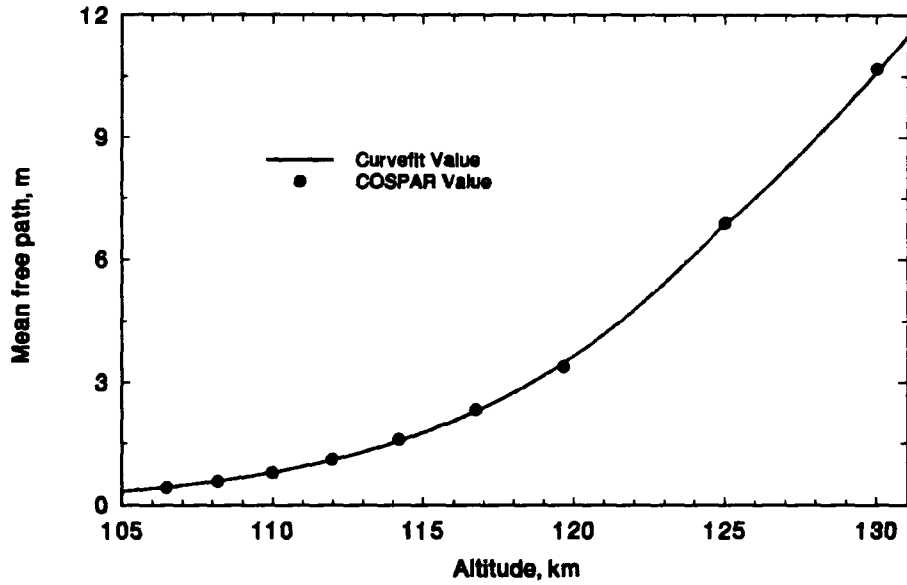


Figure A-10. Mean free path, 105-130 km.

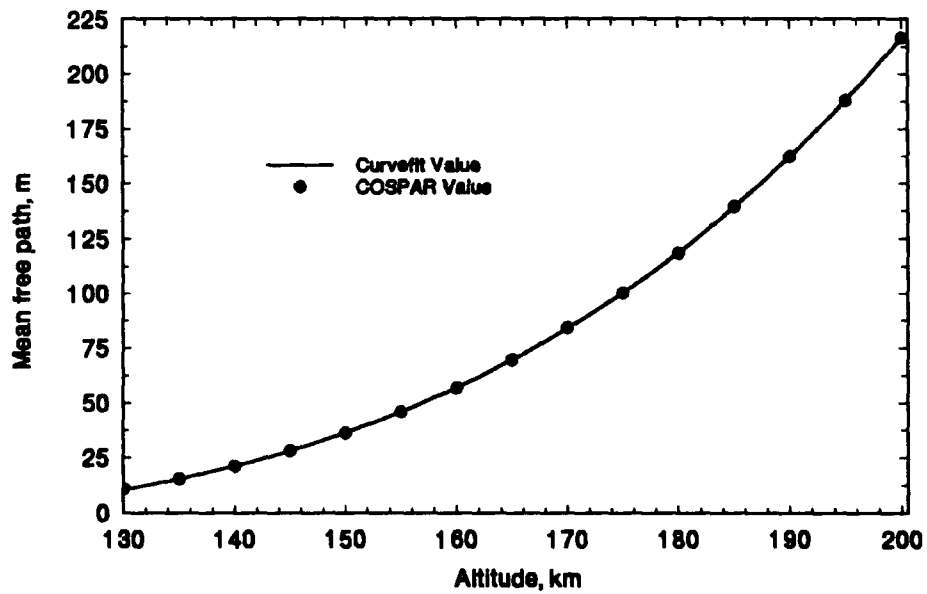


Figure A-11. Mean free path, 130-200 km.

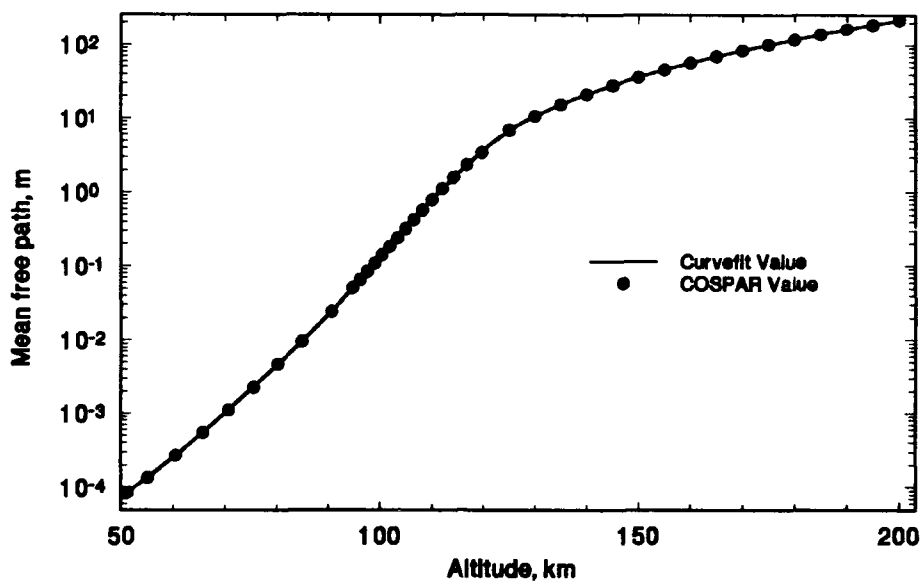


Figure A-12. Mean free path, 50-200 km.

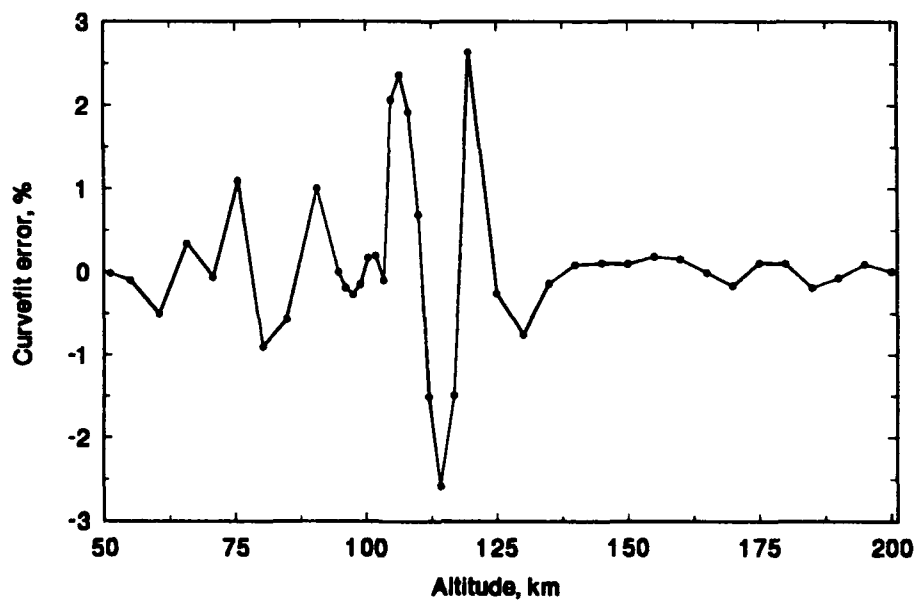


Figure A-13. Mean free path curvefit accuracy, 50-200 km.

## **APPENDIX B**

### **Drag Coefficient Models**

Circular Cylinder Drag Coefficient. The algorithm used to model the variation of the aerodynamic drag coefficient of a circular cylinder is presented below. The equation that links the free molecular and continuum flow regimes was derived using a least squares method. The independent variable is the dimensionless Knudsen number ( $Kn$ ), formed by dividing the free stream molecular mean free path by the cylinder diameter.

For  $Kn \leq 0.01$ ,

$$C_D = 1.24$$

For  $0.01 < Kn < 10$ ,

$$C_D = a + b \ln(Kn) + c (\ln(Kn))^2 + \frac{d}{\sqrt{Kn}}$$

where

$$a = -0.0017583229$$

$$b = 2.8715758 \times 10^{-6}$$

$$c = 0.646620178$$

$$d = -7.63995073$$

For  $10 \leq Kn$ ,

$$C_D = 2.80$$

Figure B-1 shows the curvefit results and the empirical data.

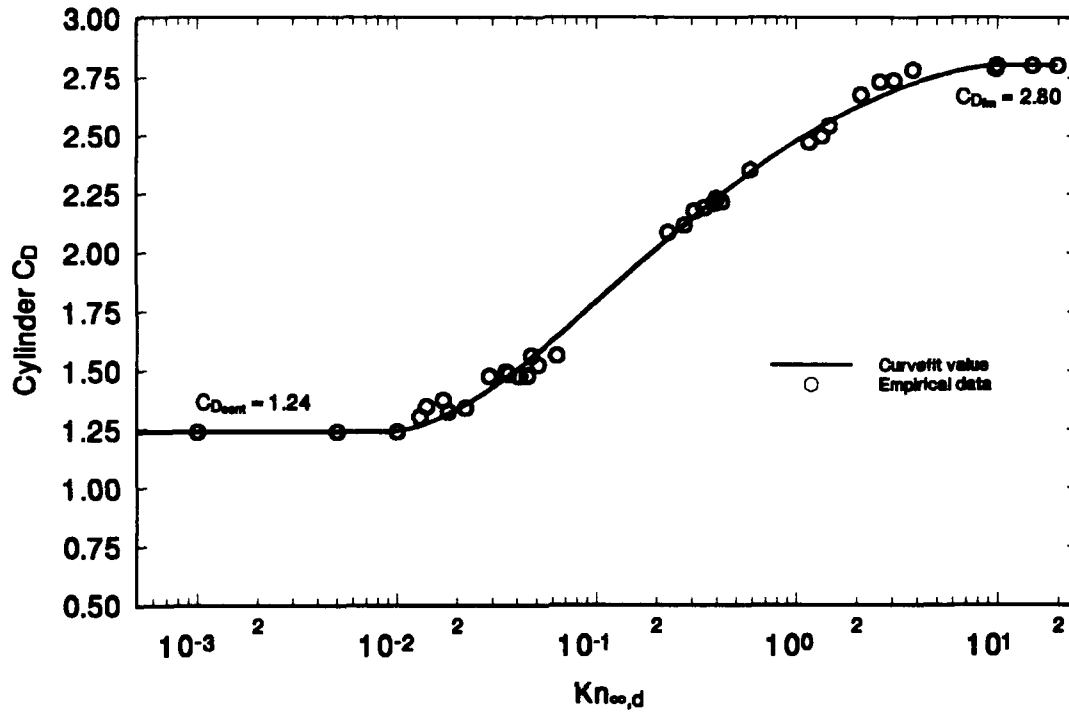


Figure B-1. Circular cylinder drag coefficient variation.

**Sphere Drag Coefficient.** The algorithm used to model the variation of a sphere's aerodynamic drag coefficient is presented below. The equation that links the free molecular and continuum flow regimes was derived using a least squares method. The independent variable is the dimensionless Knudsen number ( $Kn$ ), formed by dividing the free stream molecular mean free path by the sphere diameter.

For  $Kn \leq 0.001$ ,

$$C_D = 0.92$$

For  $0.001 < Kn < 10$ ,

$$C_D = \frac{a + c \ln(Kn) + e (\ln(Kn))^2 + g (\ln(Kn))^3 + i (\ln(Kn))^4}{1 + b \ln(Kn) + d (\ln(Kn))^2 + f (\ln(Kn))^3 + h (\ln(Kn))^4 + j (\ln(Kn))^5}$$

where

$$a = 2.466284047$$

$$b = 0.369700078$$

$$c = 1.194683231$$

$$d = 0.14802969$$

$$e = 0.368965697$$

$$f = 0.027107488$$

$$g = 0.062605796$$

$$h = 0.00092770392$$

$$i = 0.0041343789$$

$$j = -0.00012474748$$

For  $10 \leq Kn$ ,

$$C_D = 2.70$$

Figure B-2 shows the curvefit results and the empirical data.

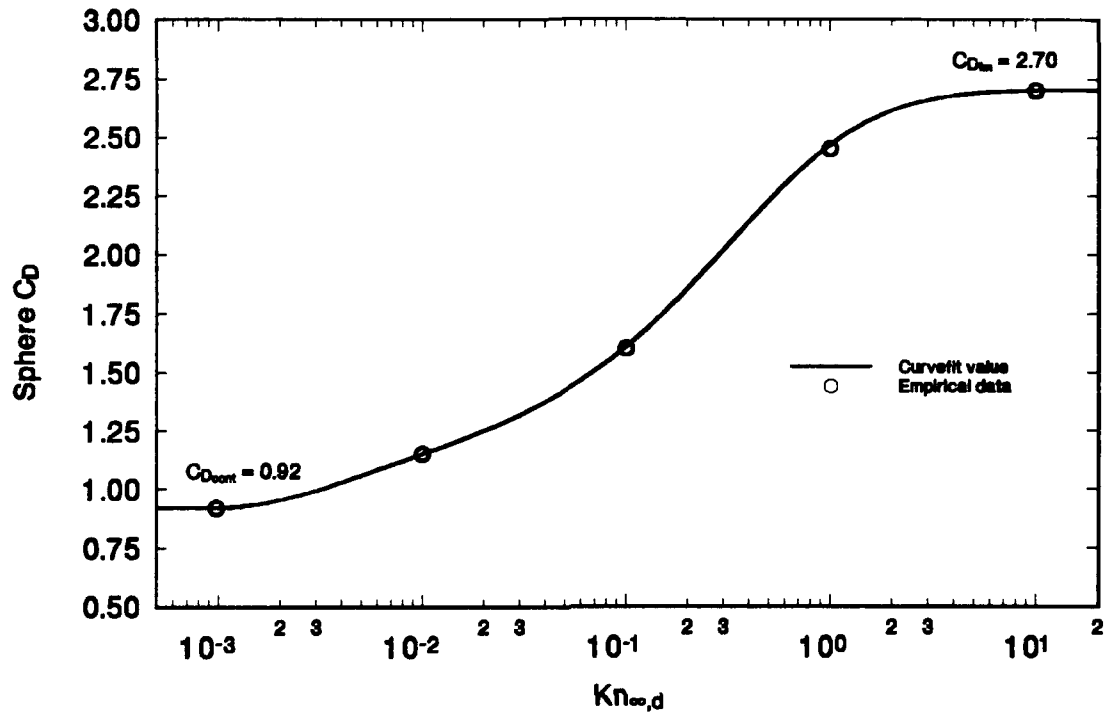


Figure B-2. Sphere drag coefficient.

## **APPENDIX C**

### **Network Constants - Free Tether Orbital Lifetime**

This Appendix contains the values of the weights and biases used in the free tether orbital lifetime prediction network. The network consists of 34 neurons arranged in 3 layers (input-hidden-output). The 3 input neurons and single output neuron are linear elements, while the 30 hidden neurons use the sigmoidal logistic function. The input values must be properly scaled and applied to the correct input neuron. The network's output is the approximate lifetime (elapsed time for the tether center of mass to reach 150 km altitude) of the free tether, in hours. The lifetime prediction assumes the tether center of mass is initially in a 28.5° inclination orbit with argument of perigee and true anomaly both equal to zero.

Units and Limits. The network requires that a scaled radius of perigee ( $R_p'$ ) be provided to Input Neuron 1, a scaled size and shape factor ( $fac'$ ) be provided to Input Neuron 2, and a scaled tether length ( $l'$ ) be provided to Input Neuron 3.  $R_p'$  and  $fac'$  describe aspects of the tether center of mass' initial orbit.

Input to Input Neuron 1:

$$R_p' = (R_p(\text{km}) - 6578.137) \div 300, \quad 6578.137 \text{ km} \leq R_p \leq 6878.137 \text{ km}$$

Input to Input Neuron 2:

$$fac' = (fac(\text{km}) - 6578.137) \div 300, \quad 6578.137 \text{ km} \leq fac \leq 6878.137 \text{ km}$$

$$fac \doteq R_p + \frac{R_a - R_p}{1 + e}, \quad e \doteq \frac{R_a - R_p}{R_a + R_p}$$

Input to Input Neuron 3:

$$l' = \frac{\text{length}(\text{km})}{100 \text{ km}}, \quad 10 \text{ km} \leq \text{length} \leq 125 \text{ km}$$

Connection Weights from Input Neurons to Hidden Neurons ( $W_{ij}$ ).

Hidden Unit #	Weight from Input Unit 1 ( $Rp'$ )	Weight from Input Unit 2 ( $fac'$ )	Weight from Input Unit 3 ( $l'$ )
1	10.3444915859	8.2527591085	-0.6751672663
2	6.2333808295	5.9146212372	-0.2813545438
3	4.9317921366	3.0737802825	-0.5340004101
4	-0.2713022307	0.3241286937	-0.2267440989
5	6.3103255220	6.0044604626	-0.2978133929
6	1.8701164555	7.4375496959	-0.2822153247
7	-0.6691715619	-0.0542085754	0.5526113910
8	5.1297754736	3.4118906609	-0.5134497213
9	-4.1934406968	-1.5832846711	-2.1211700006
10	6.1931646191	5.8388058457	-0.2571912350
11	6.9713464320	6.5285636816	-0.3933455083
12	-0.1599688473	-0.0303760751	-0.3664126540
13	0.5447138619	0.5011952513	1.6290742099
14	2.4783489123	2.0368718709	-4.1100527207
15	11.0113111674	8.6482262431	-0.7046314917
16	6.9010939576	5.2474031080	-0.4247669835
17	-0.9767128223	1.3047661034	4.0733606760
18	0.3102134131	0.8164468535	0.1965550481
19	-3.1537052259	10.0224136902	-0.6928904359
20	8.8229666635	7.4819011876	-0.5815027101
21	2.3815726950	1.3011267816	-0.6969581403
22	-6.5519738882	-5.0081203823	0.4082005928
23	8.3018994362	7.2358437489	-0.5380372513
24	7.4483683550	2.3540628074	-0.4323303364
25	5.9153979386	-6.6892904207	0.0376885535
26	-2.2425243319	7.2488943483	0.3431325889
27	11.9394594358	9.2843448882	-0.7381789263
28	8.6287280208	7.3903233795	-0.5660893863
29	1.9414716365	1.1795956443	4.0024544434
30	0.1094380036	0.6506214195	-0.1892025399

Biases on Hidden Neurons ( $v_j$ ).

Hidden Unit #	Bias	Hidden Unit #	Bias
1	16.8077610465	16	8.1577406761
2	10.1679628840	17	0.6701441975
3	5.8456202221	18	0.7682754851
4	0.9967226979	19	8.5789296376
5	10.4010601127	20	14.6006452581
6	6.3201548074	21	2.5648353952
7	2.4460679242	22	-7.9065621340
8	6.2410283199	23	13.8467621879
9	0.4461119653	24	4.6899025883
10	9.9165711091	25	-3.2369315023
11	11.7617874295	26	3.3734023560
12	1.1354550692	27	19.2968728600
13	0.1312053257	28	14.3210171070
14	-0.5810254700	29	7.8210828708
15	17.8174365290	30	0.4219097122

Bias on Output Neuron ( $v_k$ ).  $v_k = 0.8827370959$

Connection Weights from Hidden Neurons to Output Neuron ( $W_{jk}$ ).

Hidden Unit #	Connection Weight	Hidden Unit #	Connection Weight
1	30.3956513227	16	16.6699114935
2	22.4919846679	17	4.3335399014
3	9.3395399204	18	0.7648396518
4	-0.0464153938	19	-12.7884580003
5	22.7118252621	20	27.2339012791
6	13.9857769386	21	3.2066533761
7	-1.3283093900	22	-15.4657532622
8	10.2027996201	23	26.2887461808
9	4.1950648661	24	17.8527651477
10	22.3088900623	25	9.8722456181
11	23.9435997555	26	7.8464704176
12	-0.6626808404	27	34.8665680420
13	2.6674574948	28	26.8772946996
14	3.7104488603	29	-5.2674438644
15	32.1030342755	30	0.3218249791

## **APPENDIX D**

### **Network Constants - Lifetime Correction Factor**

This Appendix contains the weights and biases used in the lifetime correction factor network. The network consists of 33 neurons arranged in 3 layers (input-hidden-output). The 2 input neurons and single output neuron are linear elements, while the 30 hidden neurons use the sigmoidal logistic function. The input values must be properly scaled and applied to the correct input neuron. The network's output is the approximate percent difference of the current system's lifetime from the lifetime of the same system if it were initially in a 28.5° inclination orbit with argument of perigee ( $\omega$ ) and true anomaly ( $v$ ) both equal to zero.

Units and Limits. The network requires that a scaled orbit argument of latitude ( $U'$ ) be provided to Input Neuron 1, and a scaled orbit inclination ( $i'$ ) be provided to Input Neuron 2. Both values describe the initial orbit of a tethered system's center of mass.

Input to Input Neuron 1:

$$U' = U(\text{degrees}) \div 540^\circ, \quad U \doteq \omega + v$$

$$0 \leq \omega \leq 180^\circ, \quad 0 \leq v \leq 360^\circ$$

$$(\text{If } \omega > 180^\circ, \text{ set } \omega = \omega - 180^\circ)$$

Input to Input Neuron 2:

$$i' = i(\text{degrees}) \div 80^\circ, \quad 0 \leq i \leq 80^\circ$$

Connection Weights from Input Neurons to Hidden Neurons ( $W_{ij}$ ).

Hidden Unit #	Weight from Input Unit 1 ( $U'$ )	Weight from Input Unit 2 ( $i'$ )
1	30.5971515814	4.2154281069
2	1.5359433496	0.6645087827
3	18.9948056456	4.0498542229
4	10.0200398651	1.0408554490
5	7.5347850384	5.5977041680
6	9.9459586415	4.0703293434
7	12.7259687199	-0.4073947197
8	-27.5303599618	-1.2033839472
9	20.9967550767	-0.2315195436
10	21.7885288593	3.9151261135
11	40.2950097475	0.1027142209
12	34.5586443769	-3.8599055824
13	0.7048572069	-0.2148552433
14	-23.9673056492	-5.6658241090
15	21.8685301844	3.2099527177
16	30.0194869073	-3.2641333936
17	24.4330317432	-4.3340278336
18	-3.4042577277	-11.0525781328
19	-3.0450950244	-0.3284852997
20	1.8134324339	0.5183198298
21	-4.0943983506	8.8564511168
22	4.4311867542	-12.4286344356
23	24.9048656402	-2.6994067402
24	33.6455529543	-3.5856185612
25	14.7544079852	-1.1853701692
26	28.0974456648	0.2034712477
27	30.0344602034	1.1562867808
28	6.3292649168	5.6642145314
29	-29.9038184209	-1.3838931026
30	25.4266943025	-0.4043601786

Biases on Hidden Neurons ( $v_i$ ).

Hidden Unit #	Bias	Hidden Unit #	Bias
1	17.6093087286	16	23.7873981681
2	3.8006133494	17	16.6318756999
3	16.2289117587	18	-7.3090861636
4	9.5084719397	19	2.4766336145
5	4.1932369682	20	6.4882973551
6	20.3962096358	21	11.0650263849
7	10.7107124618	22	-4.5731277922
8	-7.2868966611	23	2.9744167747
9	13.8476381791	24	13.4642458356
10	12.2005467111	25	9.9150583278
11	22.6092819297	26	12.5408367960
12	15.9861404286	27	24.3205943278
13	4.5737809755	28	11.6239406257
14	-22.3438917670	29	-3.3418628694
15	6.0985060360	30	18.0221365072

Bias on Output Neuron ( $v_k$ ).  $v_k = 5.9924819741$ .

Connection Weights from Hidden Neurons to Output Neuron ( $W_{ji}$ ).

Hidden Unit #	Connection Weight	Hidden Unit #	Connection Weight
1	56.3522660224	16	-30.2499663020
2	0.7295784261	17	-26.7571804965
3	-14.3285007883	18	-10.8642652415
4	-8.4412121825	19	-4.2988860191
5	-11.5107482830	20	-4.5700306676
6	9.3185889284	21	17.1121581216
7	-7.7946318494	22	-10.6115295797
8	57.3059464346	23	-24.4499393519
9	-16.5019528754	24	-31.6767497174
10	-15.2759689874	25	10.3384517394
11	-31.0423967532	26	57.8360370860
12	-32.3281387432	27	39.0244463608
13	-4.0524857910	28	-6.7327232342
14	-15.8510865448	29	-18.7580187996
15	67.3870802586	30	38.1790378863

## **APPENDIX E**

### **Network Constants - Upward-Deployed Tether-Trailing Satellite Orbital Lifetime**

This Appendix lists the weights and biases used in a network trained to predict the orbital lifetimes of upward-deployed tether-trailing satellites. The network consists of 105 neurons arranged in 3 layers (input-hidden-output). The 4 input neurons and single output neuron are linear elements, while the 100 hidden neurons apply the sigmoidal logistic function. The input values must be properly scaled and applied to the correct input neuron. The network's output is the approximate system lifetime (elapsed time for the system center of mass to reach 150 km altitude), in hours. The lifetime prediction assumes the system's center of mass is initially in a 28.5° inclination orbit with argument of perigee and true anomaly both equal to zero. Although not an input to the network, the subsatellite's diameter should be no more than 5 m.

Units and Limits. The network requires that a scaled radius of perigee ( $R_p'$ ) be provided to Input Neuron 1, a scaled size and shape factor ( $fac'$ ) be provided to Input Neuron 2, a scaled tether length ( $l'$ ) be provided to Input Neuron 3, and a scaled subsatellite mass ( $m'$ ) be provided to Input Neuron 4.  $R_p'$  and  $fac'$  describe aspects of the system's center of mass initial orbit.

Input to Input Neuron 1:

$$R_p' = (R_p(\text{km}) - 6578.137) \div 300, \quad 6578.137 \text{ km} \leq R_p \leq 6878.137 \text{ km}$$

Input to Input Neuron 2:

$$fac' = (fac(\text{km}) - 6578.137) \div 300, \quad 6578.137 \text{ km} \leq fac \leq 6878.137 \text{ km}$$

$$fac \doteq R_p + \frac{R_a - R_p}{1 + e}, \quad e \doteq \frac{R_a - R_p}{R_a + R_p}$$

Input to Input Neuron 3:

$$l' = \frac{\text{length}(\text{km})}{100 \text{ km}}, \quad 50 \text{ km} \leq \text{length} \leq 100 \text{ km}$$

Input to Input Neuron 4:

$$m' = \frac{\text{mass}(\text{kg})}{500 \text{ kg}}, \quad 0 \leq \text{mass} \leq 500 \text{ kg}$$

Connection Weights from Input Neurons to Hidden Neurons ( $W_{ij}$ ).

Hidden Unit #	Weight from Input Unit 1 ( $Rp'$ )	Weight from Input Unit 2 ( $fac'$ )	Weight from Input Unit 3 ( $l'$ )	Weight from Input Unit 4 ( $m'$ )
1	3.8304109785	2.1283882083	-1.5953995074	1.0388837505
2	6.6771622814	4.8239132702	-6.0781793491	2.8720276291
3	4.1517471753	2.9931136185	-0.9268389978	0.8121063827
4	6.3315124888	4.4878045212	-4.9244508365	2.4976508234
5	9.6182565842	1.7968282685	-2.2628064870	0.3977966238
6	8.4247519244	3.9704171172	-4.7606592013	1.7941595688
7	6.2091720617	4.4200179985	-6.1031471404	2.6947993015
8	8.3662335333	5.3499817134	-9.0050298632	3.7640240781
9	5.4081827193	4.3758476090	0.1065743273	0.4221847542
10	6.8187009211	5.0331215690	-6.2125680537	2.9517643400
11	10.7886131846	6.3836069003	-0.0647634430	0.3786433702
12	6.0654024261	4.7812414783	1.7934039533	-0.6310976473
13	-5.6604996777	-2.9062716984	12.2768961492	4.3149460411
14	6.4177837595	5.7787446634	-1.1650118122	1.0665634771
15	6.1423889328	5.1218303522	0.8945095104	0.0300039942
16	6.8586479922	5.2355560723	-4.1983060338	2.2994389073
17	5.9865847581	4.1574324597	-5.0307394937	2.4422995553
18	5.4409211357	4.2847248878	0.5685184030	0.1085729250
19	6.3455844172	4.8760528680	-3.8242925683	2.1616027304
20	7.3477416419	5.0472018383	-7.1286850358	3.2745207403

Connection Weights from Input Neurons to Hidden Neurons, continued.

Hidden Unit #	Weight from Input Unit 1 ( $Rp'$ )	Weight from Input Unit 2 ( $fac'$ )	Weight from Input Unit 3 ( $l'$ )	Weight from Input Unit 4 ( $m'$ )
21	8.7051751997	3.4985978108	-2.8879668124	0.9759321006
22	4.8793339135	3.8304929555	-0.4996792039	0.7139517580
23	6.7658830391	4.9864272832	-5.9004309289	2.8789694563
24	5.3478442794	4.2608917852	0.3055423183	0.2761590710
25	4.9892716391	3.9910612023	-0.8708736231	0.9410736066
26	6.8332179671	5.0159825068	-6.4859851604	2.9955665331
27	1.1161934457	1.0115731055	-5.9848274428	-6.2919063102
28	5.4792029952	4.1677846148	1.2045747901	-0.3566681495
29	5.8971343638	4.6409340257	1.4624097934	-0.4316879128
30	5.8517264705	4.7908394540	0.7392491569	0.0787246610
31	6.3309056755	5.2749936762	-2.5245739128	1.6001494970
32	7.0101064667	5.3508802294	-4.2736424087	2.3258123216
33	8.1322711146	4.9525449870	-8.2225018327	3.6128066932
34	6.2454201901	4.3087962825	-6.4618415748	2.7446363458
35	5.8036465543	4.7815136432	0.4767047094	0.2450486773
36	5.8893713156	4.9003380614	0.4714280781	0.2635023210
37	8.6312756151	5.2240463686	-8.2996459836	3.7745682221
38	4.7794125730	3.7350156996	-0.8003643375	0.8693981518
39	6.3297162480	5.1198172892	1.8769209785	-0.6192664151
40	6.7817690722	4.8457316719	-7.2362798963	3.0528221960
41	7.4852375242	5.3089419720	-7.3660843176	3.3591590327
42	4.0898279791	1.9278521554	-0.9182705328	4.7979939127
43	7.1194916442	5.3654465437	-6.8719827220	3.1659463460
44	9.5494620414	3.4920899228	-2.6312509643	0.6722894688
45	4.9038493150	3.0050644687	-2.3380042802	1.3292331668
46	7.0625009385	5.4517267639	-6.8467375411	3.1412316053
47	5.3100698539	4.3081180883	-0.1285123191	0.5582117522
48	5.4344903044	3.8598230416	4.5920766557	-2.9622475616
49	4.4407191340	3.2972044450	-1.4662021831	1.1381277056
50	1.5607667552	5.8854659108	-1.0132879678	1.2401548774
51	6.8728706830	5.1876477186	-6.7295383526	3.0448219367
52	4.6329821023	3.5442109638	-0.6277456861	0.7407901091
53	7.0409744913	3.1996099364	-3.2949510876	1.3815393681
54	4.3442507416	-5.7277039357	-0.1386501077	-0.7552146444
55	4.7877871168	3.7425095344	-0.8528451291	0.9023647458
56	3.3925243397	2.0567816170	-1.5012549764	1.0509363023
57	6.5606351579	4.9526897969	-6.4074868851	2.8794163834
58	8.6693249349	5.5829780000	-7.7365014128	3.7731582519
59	7.3140146079	6.1626334531	-2.5666988732	1.4377828932
60	4.4540711020	3.2783276423	-1.5508702552	1.1562760427

Connection Weights from Input Neurons to Hidden Neurons, continued.

Hidden Unit #	Weight from Input Unit 1 ( <i>Rp'</i> )	Weight from Input Unit 2 ( <i>fac'</i> )	Weight from Input Unit 3 ( <i>l'</i> )	Weight from Input Unit 4 ( <i>m'</i> )
61	8.6959212457	4.3950183481	-8.2673306988	3.3192308882
62	6.8590926498	5.2338174366	-5.3405761556	2.7861951046
63	5.5994531908	4.6946420631	-1.7528378392	1.3502764435
64	5.6507880054	4.2901177736	1.6111305022	-0.6173450499
65	4.7596039195	3.6873145888	-1.4026155634	1.1576116484
66	1.5322861201	0.9955594749	-0.9159873188	1.0631366131
67	4.7618314328	3.7148943228	-0.9220009948	0.9330239177
68	8.2518982245	5.2725598407	-7.7335781499	3.6354808011
69	4.1793682965	2.8983033426	-1.8301438017	1.2188452214
70	5.6455006847	4.5576487840	0.5542505322	0.1635146386
71	6.0820238134	4.2346587627	-5.6684518822	2.5831522040
72	6.1199028710	5.2432863710	0.3763180753	0.3559834331
73	7.0134737566	5.0167486276	-7.8778213613	3.2050323987
74	6.5966265270	5.7140595089	0.9666081947	0.0521330191
75	5.4508729468	4.5839156275	-1.0174090984	1.0471314124
76	3.9018611602	3.8107505551	-0.0501000366	-1.1389385025
77	6.9931828239	5.1634096155	-6.0556878775	3.0008769132
78	6.2590998975	4.3603643615	-5.8268508139	2.6685738433
79	6.3538981122	3.2020413800	-2.9933639430	1.4000415759
80	8.4178665012	3.9971090470	1.9594292023	-1.8501740849
81	6.3568724295	4.5836397608	-6.5263535369	2.8050457456
82	6.3022447962	4.5825292820	-5.3884750169	2.6213133419
83	6.3022382011	4.6930406963	-7.1424952991	2.8487860622
84	7.1079702177	5.3203489057	-6.5932349020	3.1276953049
85	4.4011932965	3.2800096569	-0.9625560987	0.8865704864
86	9.5780537903	4.9033176001	-5.5896673521	2.0727212982
87	7.7379219211	3.8283715970	-4.0923533274	1.6471480063
88	7.2067107805	6.9537653962	-0.6046491660	0.8229259356
89	6.5416804319	4.4061988382	-4.0134558238	2.0649929871
90	7.0783982740	5.2496992668	-7.2857696589	3.1883183489
91	6.7766766820	5.8539016913	1.5895922140	-0.3121058771
92	6.2067047984	5.0202030275	1.5641355297	-0.4244327819
93	9.2693599530	3.0437628971	-3.0765241096	1.6746848317
94	6.5662417511	5.8702358520	0.2979481310	0.4363396330
95	13.6475761078	-5.6215885360	-1.4613683496	0.5651192968
96	3.9832471962	2.8093751134	-1.2043265351	0.9341126802
97	5.3480019567	4.3962446288	-0.4170058165	0.7363097022
98	4.3559304429	3.1642052412	-1.6185308875	1.1770222128
99	7.4229247461	2.7710850246	-2.3014639552	0.8614948768
100	5.6887938998	4.5307969197	0.8361197493	-0.0257557078

Biases on Hidden Neurons ( $v_j$ ).

Hidden Unit #	Bias	Hidden Unit #	Bias	Hidden Unit #	Bias
1	3.8082978778	36	11.4490031228	71	9.3746573732
2	10.3827263545	37	12.4159486739	72	11.7998732100
3	8.2342276793	38	9.2613897556	73	10.5543215515
4	9.6004124394	39	12.7953539213	74	12.8843729046
5	2.1611620231	40	10.3361298015	75	10.0329477753
6	6.6521768535	41	11.4403615513	76	3.0214452234
7	9.6383318459	42	7.5011797723	77	11.0109747355
8	11.9453852910	43	11.1959711572	78	9.6060069085
9	10.5664333268	44	5.5920255013	79	5.7924893923
10	10.6984298582	45	6.0684955542	80	8.3565889830
11	12.7232380537	46	11.2181047045	81	9.8600384143
12	12.2457506141	47	10.3395526220	82	9.8798151795
13	1.2809154763	48	11.6874407070	83	9.8403545342
14	11.2138004972	49	8.0937826602	84	11.1980331865
15	12.7334581360	50	4.3946611150	85	8.5809225207
16	9.9513223032	51	10.8220438593	86	7.9453609498
17	9.2008549431	52	9.1816159673	87	6.5699684714
18	10.7543296531	53	5.5659243474	88	13.0935492282
19	9.7060501240	54	-5.4732187486	89	8.3928981750
20	11.1379096222	55	9.2422660706	90	10.9651077721
21	5.7547505213	56	3.7399966944	91	13.5733451152
22	9.5873879323	57	10.3896402644	92	12.4274343852
23	10.6197606295	58	12.9493986637	93	4.5230084596
24	10.5552988578	59	10.7661643415	94	12.5166609376
25	9.5025851321	60	7.8908816703	95	3.6861536064
26	10.6667428820	61	7.6312123549	96	7.5938679165
27	3.3443466308	62	10.8447662360	97	10.2487885590
28	10.9839431056	63	9.6989032004	98	7.6700255334
29	11.8162697291	64	11.3996039797	99	4.8281690495
30	11.5023890494	65	8.7120620413	100	11.2422092308
31	9.9273277679	66	2.7699274071		
32	10.0170524457	67	9.1479903510		
33	11.6470873879	68	12.2077450117		
34	9.5105163373	69	6.8620764800		
35	11.3060943415	70	11.0819772712		

Bias on Output Neuron ( $v_k$ ).  $v_k = 28.3367468575$ .

Connection Weights from Hidden Neurons to Output Neuron ( $W_{jk}$ ).

Hidden Unit #	Connection Weight	Hidden Unit #	Connection Weight	Hidden Unit #	Connection Weight
1	2.6729999225	36	12.4315557302	71	14.1253511700
2	15.1194407352	37	18.4897487160	72	13.0293023108
3	8.5552947983	38	9.9317787892	73	16.5700592492
4	13.9590698688	39	13.8385077874	74	14.1936774149
5	5.5335396520	40	15.8135810714	75	11.8391901533
6	12.2497764944	41	16.9405366010	76	5.9229796697
7	14.6893595598	42	-4.2066273085	77	15.8084811382
8	18.6973734504	43	16.5481008570	78	14.2768198629
9	11.2916414428	44	8.5648175983	79	8.3123169811
10	15.6512757220	45	7.3530880231	80	9.0727104768
11	15.8048209389	46	16.6384138832	81	15.0403111451
12	13.0919133607	47	11.0915559557	82	14.3721521872
13	14.5485329654	48	13.2811287233	83	15.6975325900
14	13.5238570569	49	9.2043937661	84	16.3065792836
15	13.1746955903	50	8.4310567872	85	9.0410607670
16	14.3195935709	51	16.1447813862	86	13.1192371213
17	13.5664876232	52	9.6792589772	87	8.8235816060
18	11.5606103726	53	6.9280990274	88	15.4509507307
19	13.5651066988	54	13.9973174624	89	12.8430716235
20	16.4027285361	55	10.3218015290	90	16.6194152856
21	8.8460528317	56	2.3858103664	91	14.8577833182
22	10.2847334196	57	15.4804082069	92	13.4323065546
23	15.4047730470	58	18.7909152553	93	9.2025920052
24	11.0505598811	59	14.2774263642	94	14.1139245073
25	10.8101008187	60	8.7819946954	95	-16.7518735253
26	15.7110461447	61	13.8985728007	96	7.9649137692
27	7.5576619301	62	15.3771433466	97	11.4296690910
28	11.7229894086	63	12.1427437987	98	8.6036649471
29	12.5376381170	64	12.0736708497	99	4.8996634236
30	12.1687296792	65	10.2682684512	100	12.0673856518
31	13.3675326534	66	1.1309499541		
32	14.5104669236	67	10.0464564065		
33	17.5598706747	68	17.8946024102		
34	14.6682644458	69	7.7338246795		
35	12.2114058466	70	11.8485674966		